Doctoral Dissertation
Doctoral Program in Civil and Environmental Engineering (33rd Cycle)

Surface wave methods for mineral exploration

Myrto Papadopoulou

* * * * * *

Supervisors
Prof. Laura Valentina Socco, Supervisor

Politecnico di Torino
2021

I hereby declare that, the contents and organisation of this dissertation constitute my own original work and does not compromise in any way the rights of third parties, including those relating to the security of personal data.

…….....

Myrto Papadopoulou

Turin, 2021

Acknowledgment

There are no words to express my gratitude to my supervisor, Prof. Laura Valentina Socco. I thank her for the opportunity, for being there through this journey with her loving and bold advice, as a devoted academic supervisor, as a mentor, a friend, my family in Torino. Thanks for pushing me beyond what I though was the limit.

To Prof. Deyan Draganov, for his welcoming support during the time I spent in Delft and ever since.

To our group at Polito for the priceless support, all the wonderful hours of brainstorming. Farbod, Federico, Chiara, Karim, Shufan, Binbin, Diego you have been the best team possible.

To my family, for their endless support, love and their smiles. To my friends, for putting up with my bad moments. To a couple of you who ended up learning something about surface waves.

I sincerely thank the outstanding group of professionals who took part in Smart Exploration for the mind-opening cooperation. Special thanks to the project's coordinator, Alireza Malehmir, for always having time for advice and help. To Emilia Koivisto and Bojan Brodic for the excellent collaboration and their help with the computation of the stacked sections shown in the thesis. To George Apostolopoulos, for still calling me his student.

I would like to thank Nordic Iron Ore AB (NIO) and Yara Suomi Oy for their kind hospitality, as well as Uppsala University, TUBAF and Geopartner for providing their equipment for the data acquisition. Uppsala University and NIO for providing access to the raw seismic data, in the framework of the Smart Exploration.

Smart Exploration project has received funding by EU's Horizon 2020 research and innovation programme under grant agreement No. 775971.

Contents

List of Symbols and Acronyms

SW	Surface waves
BW	Body waves
DC	Dispersion curve
MASW	Multichannel Analysis of Surface Waves
SASW	Spectral Analysis of Surface Waves
W/D	Wavelength-Depth relationship
S/N	Signal to noise ratio
MUSIC	MUltiple SIgnal Classification
QC	Quality control
V_S	S-wave velocity
V_{Sz}	Time-average S-wave velocity
V_P	P-wave velocity
V_{Pz}	Time-average S-wave velocity
V_R	Rayleigh-wave velocity
V_g	Group velocity
ν	Poisson's ratio
ν_z	Apparent Poisson's ratio
f	Frequency
λ	Wavelength
ρ	Mass density
h	Layer thickness
k	Wavenumber
p	Slowness or ray parameter
τ	Intercept time
x	Distance
Δx	Receiver separation
x_1	Source-first receiver offset
L	Array length
ω	Angular frequency
φ	Phase
u	Seismic trace
t	Time
SR	Temporal sampling rate
θ	Azimuth
A	Amplitude
E	Energy
γ	Decay exponent

α_f	Attenuation coefficient
G_i	Autospectral density
QI	Quality index
z	Depth
z_d	Datum depth
t_d	One-way traveltime (static shift)
R	Receiver
S	Shot
d	Path length
N_T	Trace length
$\mathbf{t}_L$	Time-lag vector
$\mathbf{C}$	Cross-correlation matrix
$\mathbf{cc}$	Cross-correlation amplitude
$\mathbf{f}_{CB}$	Common frequency band
q	Candidate DC
A_{CC}	Integral of the cross-correlation amplitude
$\mathbf{bp}$	Breaking points
$\mathbf{V}$	Voxel space
μ	Median
$\mathcal{H}$	Hodges–Lehmann median estimator
ε	Median-estimator error
A_{effec}	Effectiveness ratio
S_{ind}	Similarity index
$l_{R_1R_2}$	Receiver path
$\mathbf{m}$	Model
Q	Misfit function
$\mathbf{d}_{obs}$	Vector of observed slowness
$\mathbf{C}_{obs}$	Covariance matrix of the experimental uncertainties
$\mathbf{C}_{Rp}$	Covariance matrix of the regularization strength
$\mathbf{G}$	Sensitivity matrix
λ_d	Damping parameter
e	Experimental uncertainty
P	Power-spectral density
G	Green's function
S_0	Autocorrelation function
C	Cross-correlation panel

Chapter 1

Introduction

1.1 Motivation

Worldwide consumption of raw materials presents constantly increasing trends which, within the EU, are predicted to persist in the following decades (OECD, 2019). As a result, the need for secure and sustainable supply of mineral resources, becomes critical, increasing the significance of mineral exploration.

Exploration for minerals is challenging, since new prospects are currently pursued at increasing depths (Decrée & Robb, 2019) and often, in the proximity of existing mines, where noise, accessibility and environmental-impact issues exist. To be successful, modern mineral exploration methods should become technologically advanced, ensuring high efficiency, economic viability and environmental sustainability. Compared to the geophysical techniques traditionally employed in mineral exploration (mainly magnetic, gravity, EM, GPR), seismic methods, can provide higher resolution even at great depths, but are less common due to their higher costs. Therefore, the development of innovative, low-cost and environmentally-friendly seismic-processing methods, adapted to the characteristics of mineral exploration sites, is necessary.

Smart Exploration is a project funded by the EU's Horizon 2020 research and innovation programme, with the aim of developing cost-effective and environmentally friendly geophysical tools and methods for mineral exploration

(www.smartexploration.eu). Its main focus is the development of advanced seismic (active and passive), electromagnetic and potential-field processing and modelling methods and novel instrumentation, suitable for near-mine acquisitions. In addition, the project aims at generating new exploration targets, by re-processing available legacy data and combining them with data acquired through pioneering field experiments into 3D common Earth models. In total, 27 partners (universities and research institutions, SMEs and mining and civil stakeholders) from nine EU countries, including Politecnico di Torino, are involved in the project.

The current thesis belongs to the project's outcomes, and has supported the development of innovative seismic-processing methods, tailored to mineral exploration, as part of WP3 (work-package 3) of Smart Exploration, as well as the development of new exploration targets, related to WP4. In particular, the thesis focuses on one of the key-steps of the land seismic-processing workflow, the characterization of the near surface, and aims at innovative, low-cost and low-impact solutions, which can provide information also on deeper structures, including the exploration targets.

The shallow subsurface is typically characterized by low-velocity and highly heterogeneous (weathered) layers, which can affect the imaging of the deeper structures, if not properly accounted for (Sheriff, 2002). This problem is normally mitigated through the application of static corrections (statics), which correct for the wave travel-times within the weathering layer, based on a shallow velocity model (i.e., based on the thickness and velocity of the weathering layer, as well as topography). The accuracy of the static corrections, depends on the accuracy of the estimated velocity model and can affect the effectiveness of the subsequent processing steps (e.g., velocity analysis, NMO correction, migration) and the quality of the final seismic images and interpreted models (Marsden, 1993a; Cox, 1999).

Apart from statics, the estimation of the near-surface velocities can be valuable in several other stages of the seismic processing workflow. For example, it can be used to optimize the velocity model used in migration or of the initial model used in Full Waveform Inversion. Moreover, in the context of mineral exploration, the knowledge of the near-surface conditions is necessary also for purposes related to mine planning. For instance, possible shallow weakness zones, such as faults and fractured zones, can pose hazards during excavation (Donnelly, 2018) and should

be properly predicted during the mine-safety assessment. Estimation of the near-surface lithology can help to properly organize the mine infrastructure and select the appropriate excavation techniques and gear, predict the most suitable mine-waste disposal locations, avoid possible environmental impacts from acid mine drainage, etc.

Finally, accurate shallow velocity models can assist the construction of high-quality, reliable geological models and the relevant interpretation.

In mineral exploration, near-surface characterization with seismic methods is a challenging task. Mineral-exploration sites are typically characterized by hard-rock geology, which is usually highly complex, presenting high degree of heterogeneity. As addressed widely in literature (e.g., Eaton et al., 2003, and references therein), these types of settings are inherently related to complex propagation phenomena causing high levels of noise in the data.

In such conditions, body-wave (BW) seismic methods routinely used to estimate the statics (e.g., uphole methods, various refraction-based methods), can prove inefficient. Most of these methods require the picking of first breaks, which can be a demanding, time-consuming and, therefore, costly process (Marsden, 1993b), especially for noisy data. In addition, these methods present intrinsic limitations in presence of lateral heterogeneity and low-velocity anomalies, such as the common faulting and fracturing of the hard rock (Buske et al., 2015), which challenge their overall applicability to mineral exploration.

In this work, an alternative approach to characterize the near surface, based on surface waves (SW), is proposed. These waves travel along the free surface in/through the shallowest portions of the subsurface, carrying high energy. In vertically heterogeneous media, their propagation velocity depends on the frequency (geometric dispersion). This property can be extracted from the seismic data in the form of dispersion curves (DCs) (Aki & Richards, 1980) and can be used to estimate the subsurface velocities. In exploration, SW are typically considered as noise (groundroll) to be removed, since they can mask BW reflections. However, their sensitivity to the near-surface properties and their high energy makes them ideal candidates for the characterization of the weathering layer. Successful applications of SW methods to retrieve V_S and V_P static corrections in hydrocarbon exploration (e.g., Roy et al., 2013; Boiero et al., 2011; Douma & Haney, 2011; Miao et al., 2016), serve as proof of concept.

Besides resource-exploration, SW methods are popular in numerous near-surface applications, such as engineering investigations, environmental studies etc. The most common SW analysis tools are the so-called multichannel SW methods (or MASW, Park et al., 1998; Xia et al., 1999), for which, the DCs are retrieved from the seismic traces of arrays of receivers, regularly positioned in-line with a common source. The picked DCs are considered local and 1D and they are inverted, by means of 1D forward modelling, to retrieve 1D V_S models. To map the lateral-property distribution, the usual approach is to apply spatial windowing on the records and invert the windowed data separately, to retrieve an ensemble of laterally distributed 1D models (Miller et al., 1999; Xia et al., 2004).

On a different scale, in global seismology, SW generated by earthquakes or ambient noise have been widely used to map the laterally varying structure of the Earth's crust and mantle (e.g., Ritzwoller & Levshin, 1998; Kennett & Yoshizawa, 2002; Sabra et al., 2005; Shapiro & Campillo, 2004). In this case, the most popular SW method is SW tomography, for which the input DCs are retrieved between different pairs of receivers and are inverted in a tomographic approach to estimate 2D/3D (depending on the receiver geometry) velocity distributions. In SW tomography, the adopted forward modelling is also 1D, and therefore, the tomographic models are laterally distributed 1D models (quasi-2D/3D). However, the DCs are not considered local but as average between the receiver pairs and are inverted in a manner which allows the estimation of the local V_S at several grid points (Kennett & Yoshizawa, 2002). Depending on the spatial and wavelength DC coverage and the superposition between different receiver-pair paths, high resolution can be achieved (Yin et al., 2016).

In hard-rock sites, the use of SW remains under-exploited, as suggested by the sparsity of relevant literature (8% in the last five years). The so-far experience has shown that for SW, these sites are indeed a challenge, since the DCs retrieved from hard rock are of low quality, noisy, narrow-banded and poorly dispersive, affecting the possibility of extracting high-quality velocity models (e.g., Pileggi et al., 2011).

In mineral exploration, the difficulties for SW methods are amplified, since acquisition usually takes place in the vicinity of active mines, where the mining operations increase the levels of noise in the data. This is a critical challenge for SW processing, especially when the DCs are extracted with two-station approaches,

for which the contribution of each seismic trace to the picked DCs is high, making the method highly unstable (Socco et al., 2014; Ikeda & Tsuji, 2018).

Moreover, man-made structures, related to the mining infrastructure, act as sharp lateral variations, which cannot be described by the existing SW modelling tools. Lithological variability is a challenge, particularly for the processing and inversion scheme of MASW, for which the lateral resolution depends on the width of the spatial window used in the DC extraction. The minimum window size is, in turn, bounded by the data quality and spectral resolution (e.g., Foti et al., 2015), and therefore adequate lateral resolution might not be possible.

Mineral exploration is an industrial application, the task of which is to facilitate investment decisions and mine-development strategies. This narrows the data-processing time availability and is a challenge, particularly for SW tomography, for which a large number of DCs between several receiver pairs are extracted from the data. The inherent 2π ambiguity of the two-station method (e.g., Bloch & Hales, 1968), coupled with the instability of the DCs (e.g., Socco et al., 2014), demands high levels of experienced-user intervention during data processing (Lin et al., 2017), which decrease the objectiveness of the obtained results and make the method difficult to be automated.

An additional source of ambiguity is the selection of the processing parameters, i.e., the source-first receiver offset and the minimum and maximum receiver separation. SW processing assumes plane-wave propagation, which is valid only if the traces are outside the near-field region (Richart et al., 1970; Wielandt, 1993), while if the receivers are too far from the source (in the far-field), low-quality traces, suffering from attenuation, might be introduced in the DC extraction, reducing its quality (Bullen & Bolt, 1985). Although relevant also in multichannel processing, near- and far-field effects are particularly disruptive when only two receivers are used for the DC extraction (Foti, 2002; Lin et al., 2017). To avoid them, various empirical relationships between the optimal offset with respect to the measurable wavelength have been proposed, but no common consensus on a globally-acceptable rule has been reached (Foti et al., 2018). Several literature examples have shown that these rules are inadequate and that these phenomena are, instead, data and site dependent (e.g., Yoon, 2005; Ivanov et al., 2008; Bodet et al., 2009). A common recommendation is to select the processing parameters based on tests on data samples (Park et al., 1999) which, however, requires high levels of

expertise and increased processing times, introducing additional obstacles towards the automation and objectiveness of the DC extraction.

A critical limitation of all SW methods is that the DCs are mainly sensitive to V_S, while in exploration V_P statics are required. The commonly adopted solution, is to assume an *a priori* value of the Poisson's ratio (ν) during V_S inversion, and then use it to convert the V_S model into V_P (e.g., Strobbia et al., 2010). However, this approach includes the risk of wrong *a priori* assumptions, which can affect the estimation of V_S and V_P (Foti & Strobbia, 2002; Ivanov et al., 2019). Moreover, it can substantially increase the costs, since it requires additional data and/or supplementary processing stages to obtain a reliable *a priori* ν estimate (e.g. Abudeif, 2016).

Last but not least, mining industry is driven by high sustainability and environmental standards, often legally formulated, as well as safety and social approval criteria. To this end, the use of passive-seismic sources for exploration is a promising tool. This approach, removes the need for active-seismic sources, making exploration more environmentally friendly and less disruptive, as well as cheaper and feasible also in areas where accessibility issues exist, and therefore an active source cannot be easily transported and operated. An additional advantage of passive-seismic data is that they usually contain lower frequencies, with respect to the signal generated by active sources, which allows the measurement of longer SW wavelengths. In the framework of SW analysis, since the penetration depth of SW depends on their wavelength, this translates to deeper investigation.

Nevertheless, the extraction of high-quality DCs from passive-source data is not straightforward. The direction of propagation of SW with respect to the receivers' location is unkown, while the data usually contain low-energy SW signal. To ensure that useful information is contained in the data, the field measurements are usually performed over long time periods, leading to large datasets which are difficult to be processed, especially when a manual DC picking is adopted. Finally, ambient noise usually lacks high-frequency SW information, impeding the retrieval of accurate velocity estimates at shallow depths.

The current thesis addresses these limitations through novel methodological implementations, to further develop SW methods and improve their applicability to mineral exploration.

The methodological advancements proposed in the thesis can be summarized as:

- A multichannel SW-based method for the estimation of V_P statics, referred to as *SW direct statics estimation method.* The method uses as input the groundroll portion of the seismic measurements, without the need of any additional information. Its core is the Wavelength-Depth method (Socco et al., 2017; Socco & Comina, 2017), a SW technique based on the the skin-depth of SW, which allows the direct transformation of the DCs into V_S and V_P models and statics.
- A high-resolution V_P statics estimation method, named as *SW tomostatics estimation method*. The method combines a fast, suitable for exploration, SW tomography, which provides a high-resolution V_S model, with the W/D method, which provides ν. Also this workflow is solely based on SW and is applicable to both 2D and 3D, active- and passive-source seismic datasets.
- A data-driven, fast and almost fully automatic, method for the optimized selection of the processing parameters (source-receiver offset and receiver distance), which does not involve any empirical criteria or subjective decisions.
- A fully automatic, data-driven two-station SW processing method, designed to provide a large number of DCs at minimal time-requirements without any operator-involvement costs.
- An automatic passive-source seismic data pre-processing method, which allows to detect and isolate the time-windows of the passive records which contain useful SW information and estimate the direction of SW propagation within each time-window.

The proposed methods are tested on synthetic data and applied on three seismic exploration datasets, acquired in two of the validation sites of "Smart Exploration": A legacy (acquired in 2016) 2D active-seismic and a newly (2019) acquired 3D active-seismic dataset from the iron-oxide mining site of Ludvika (central Sweden) and a 2D/3D active- and passive-seismic dataset acquired in 2018 in the apatatie mine of Siilinjärvi in Finland. The results are validated in the thesis through comparison with independently derived information (geological models and traditional BW-based statics estimation methods).

Finally, in addition to our SW analysis, we also exploit the possibility of using seismic interferometry for the retrieval of seismic reflections from mineral-exploration passive-source seismic data. Since ambient-noise data are typically dominated by SW, we test and optimize a strategy to efficiently pre-process the data and isolate the portions of the noise which contain BW signal.

1.2 Structure of the thesis

The second chapter of the thesis, presents the fundamentals of SW propagation and the typical stages of the most common SW-analysis schemes. Particular focus is given on the stage of SW processing, applied for the extraction of the SW DCs from the raw seismic data.

Chapter 3 discusses the significance of mineral exploration in Europe and its current status, as well as the role of "Smart Exploration" project in the on-going effort of optimize the state-of-the-art exploration methods. The seismic datasets, acquired at two mining sites associated to "Smart Exploration" and used in this thesis, are also presented. The challenges of hard-rock sites and their impact to SW analysis is discussed along with a relevant state of the art.

The fourth chapter presents the proposed *SW direct statics estimation* method. It is applied on the 2D datasets from the mining sites of Ludvika and Siilinjärvi. The statics and resulting seismic sections, are compared with the ones retrieved with standard BW-based methods.

Chapter 5 presents the novel, fully automatic two-station processing method. The proposed data-driven technique for the detection and exclusion of near- and far-field effects is also presented in this chapter. The methods are applied on a synthetic dataset and on the 3D dataset from the mining site of Ludvika.

The sixth chapter presents the *SW Tomostatics* method. Statics are computed for the same datasets used in Chapter 4, and the results of both methods are compared.

In Chapter 7, we present the fully automatic passive-source seismic data pre-processing scheme. The method is applied on portion of the 3D passive-seismic dataset from the mining site of Siilinjärvi. The retrieved DCs are inverted jointly with curves extracted from active-seismic measurements on the same area, to retrieve a 3D V_S model at a wide depth range. In the same chapter, we also present

and apply the method to isolate BW-dominated portions of the record and retrieve the reflections with seismic interferometry.

The final chapter presents the most important conclusions derived by the work of the thesis and provides recommendations for future work.

Chapter 2

Surface-wave methods

Surface waves (SW) are seismic waves which travel only within the shallowest layers of the subsurface. In vertically heterogeneous media, their propagation is characterized by geometric dispersion, represented by curves relating the SW phase velocity and frequency (dispersion curves – DCs). Most SW methods use this property to infer the subsurface characteristics: the wavefield, generated by active (man-made) or passive (ambient noise or earthquakes) seismic sources and measured by a set of receivers undergoes a stage of processing, to extract one or more DCs. The DCs are inverted to estimate the subsurface seismic velocities.

Regardless how they are inverted, the core of the different methods is the extraction of the DCs from the raw seismic data. In this chapter, focusing on SW processing, the most common SW methods are demonstrated and compared.

2.1 Fundamentals of surface-wave propagation

Surface waves are seismic waves which exist only in the presence of an interface, such as the earth's surface. Their energy propagates in a direction parallel to the surface with a cylindrical wavefront and reduces exponentially with the distance from the surface, becoming negligible at a depth which depends on their wavelength. Their propagation is, therefore, affected only by the properties of a

limited subsurface portion with thickness depending on the propagating wavelength.

For a source that acts on the surface, most of the generated energy is transformed into SW, rather than BW (Richart et al., 1970). In addition, since SW energy spreads with a cylindrical wavefront only in the direction of propagation, their geometric attenuation is significantly lower than the one of BW, which propagate with a spherical wavefront (Aki & Richards, 1980). For these reasons, SW usually dominate the seismic records.

Since the depth of penetration of SW depends on their wavelength (frequency), different propagating SW frequencies sample different depths. In a homogeneous medium, SW velocity is constant and depends on the medium properties, and mainly on V_S. In particular, the phase velocity of SW is lower than V_S, and for Rayleigh waves propagating in a homogeneous medium, the phase velocity (V_R) is in the range of $0.87V_S < V_R < 0.96V_S$, depending on ν (Richart et al., 1970).

If the medium is vertically heterogeneous (layered, Figure 2.1a), different SW frequencies are influenced by materials with different V_S, and therefore their phase velocities vary. This phenomenon is called "geometric dispersion" and it is represented by curves which relate the phase velocity of SW with their frequency, called dispersion curves (DCs, Figure 2.1b).

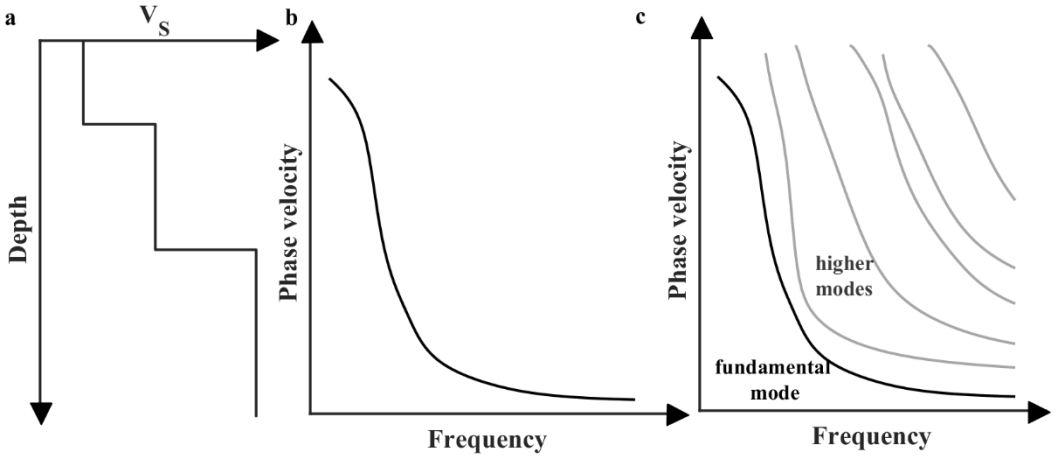

Figure 2.1: Surface-wave dispersion. a) Vertically heterogeneous V_S model. Dispersion curve a) fundamental mode and b) fundamental (black) and higher (grey) modes.

Mathematically, SW are solutions to the elastic equations of motion, under the assumptions of zero stress at the surface and zero stress and strain at infinity (boundary conditions). Their description forms the basis of SW forward modelling. In a linear elastic, homogeneous medium, the SW solution is relatively simple since there exists only one value of velocity for each frequency which satisfies the boundary conditions. In a vertically heterogeneous medium, closed-formed solutions have been found only for a medium which is layered and isotropic, with a free surface parallel to the plane of isotropy.

Assuming continuity of strains and stresses at the layer interfaces, the equations of motion can be described as an eigenvalue problem for which, a non-trivial solution exists if and only if the wavenumbers and frequencies obey the following relationship, known as Rayleigh secular function:

$$F_R\left[\lambda(z), G(z), \rho(z), k_j, f\right] = 0 \qquad (2.1),$$

where f is the frequency, G and λ are the Lame parameters, ρ is the mass density, k is the wavenumber:

$$k = \frac{2\pi f}{V_R} \qquad (2.2),$$

while the subscript j corresponds to different modes of SW propagation, occurring due to the constructive interference of the waves at the boundaries of the layers. For a layered medium consisting of a finite number of homogeneous layers overlying a homogeneous half-space, finite number of modes are possible (Figure 2.1c). At the lowest frequencies, only the lowest-velocity mode, called fundamental, is present while the higher modes, corresponding to higher velocities, appear only above specific cut-off frequencies.

Different methods exist to solve the eigenvalue problem, the most popular ones being the propagator matrix algorithms. In this family, the approach firstly introduced was the transfer matrix method of Thomson (1950) and Haskell (1953), which has been subsequently improved by Knopoff (1964) and Dunkin (1965). Other methods of this type are the stiffness matrix method (Kausel & Roësset, 1981) and the method of reflection and transmission coefficients (Kennett, 1974),

while several optimizations of all these algorithms also exist (e.g., Wang & Rokhlin, 2001; Liu, 2010; Ke et al., 2011; Harvey, 1981). Apart from their differences, all matrix-based methods describe the elastic wave propagation in the layered model as a matrix equation, formed by the properties of the layer materials and solved by imposing the SW boundary conditions and layer-continuity.

The Thomson-Haskell method (used in this work), models the subsurface as a stack of laterally homogeneous linear elastic or viscoelastic layers, characterized by their V_S, V_p, ρ and h. The stresses and strains in each layer are described in terms of these parameters, and dependency of the layers among each other (continuity conditions) and from the free surface and infinite half space (boundary conditions) is forced. This forms a single matrix equation for the entire system. The secular function can be found by imposing the matrix determinant equal to zero. The roots of the secular function provide the modal DC.

The computed modes are theoretically possible but their existence in the seismic data also depends on the energy characteristics of the system, which are not described in the secular function. In many situations, the energy partitioning between the modes does not allow the recognition of all of them in the data. Their energy distribution depends mainly on the energy of the source and on the velocities and attenuation of the layers and, often, especially in stratigraphic conditions where the velocity increases with depth, only the fundamental mode is detectable. However, higher modes might also be energetic and the possibility to separate them depends on the similarity of their velocities and on the resolution of the measured wavenumbers, which in turn, depends on the test configuration and processing method (see Section 2.2). If the difference of the velocities is lower than the wavenumber resolution, the separation of the modes is not possible and the measured DC is a superposition of the different modes: it is an apparent DC (Socco & Strobbia, 2004).

Therefore, a complete modelling of SW should account also for the energy, frequency and geometrical characteristics of the simulated source-receiver configuration and the dissipative phenomena within the layers. However, due to the complexity of this simulation, most SW methods assume that the measured DCs coincide with the ones computed numerically and often consider only the fundamental mode.

Apart from the phase velocity, SW are also characterized by a group velocity (V_g) which is the velocity of their waveform envelope. In a vertically heterogeneous medium, also group velocity is dispersive and multimodal and its value, at each frequency, is related to phase velocity according to

$$V_g = \frac{d\omega}{dk(\omega)} = V_R\left(1 - k\frac{dV_R}{d\omega}\right)^{-1} \qquad (2.3).$$

From eq. 2.3 it is clear that if the phase velocity decreases with frequency (normal dispersion), group velocity is lower than the phase velocity.

2.2 Surface-wave acquisition

The purpose of acquisition is to measure the signal of the propagating SW, by recording the wavefield generated by a seismic source. In land seismic surveys, the signal can be generated on purpose, using an active seismic source (e.g., weight drops, explosives, vibrating sources) or, in the case of passive seismic acquisition, it can have a natural origin, such as earthquakes or ambient noise. The signal is recorded by a system of receivers (typically geophones in land seismics), deployed together with the sources (if present) along a line (2D acquisitions, e.g., Figure 2.2) or spread over an area in regular or irregular carpets (3D acquisitions).

In seismic reflection for resource-exploration, the acquisition is typically not optimized for SW retrieval, since exploration methods are usually based on the analysis of BW, while SW are considered as noise to be removed. Due to their energy dominance, though, the measurement of SW does not impose severe acquisition requirements, and high-quality SW can usually be extracted from common exploration datasets, assuming that no analog filtering techniques to remove them (e.g., receiver groups, low-cut filters) have been applied during acquisition.

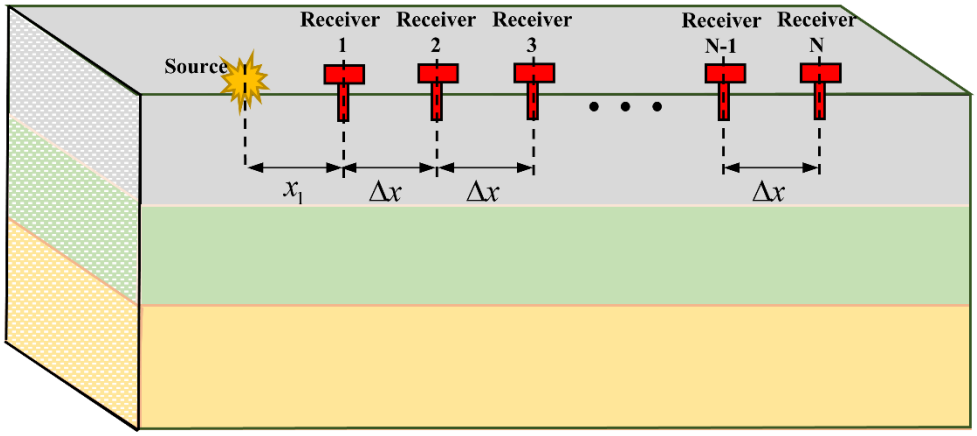

Figure 2.2: Illustration of a typical 2D active-seismic acquisition configuration.

Moreover, the frequency content of the signal generated by the exploration-seismic sources and measured by the receivers, usually allows the extraction of broadband DCs. Both vibrating and impulsive sources, typically used in exploration, produce frequencies which are usually considered adequate for near-surface characterization (Foti et al., 2015). Explosive sources might not be ideal for SW analysis, due to their necessary burying, although several examples have shown that broadband SW signal can be retrieved also with this source type (Foti et al., 2018).

Passive-seismic sources (ambient noise or earthquakes) usually generate lower frequencies (Park et al., 2005). In the context of SW analysis this is beneficial, since it leads to longer propagating SW wavelengths and, thus, deeper investigation. Nevertheless, due to their common lack in high frequencies, resolution at shallow depths cannot be achieved from passive SW measurements.

From the receiver standpoint the, common in exploration, vertical geophones are considered acceptable (Socco & Strobbia, 2004). MEMs and accelerometers can also be used, and are usually characterized by a flat frequency response in a wider frequency band with respect to geophones. Nevertheless, they present the disadvantage of lower S/N (Hons & Stewart, 2008).

The adopted acquisition parameters might also influence the quality of the DCs. As it will be discussed in Section 2.3, the extraction of the DCs with SW processing is based on spectral analyses of the continuous wavefield generated by the source, assuming that it is energetically dominated by its SW component. The continuous

SW wavefield can be described as the contribution of m different modes (Aki & Richards, 1980) according to

$$u(x,t) = \frac{1}{2\pi} \int_{-\infty}^{+\infty} \sum_{m} A_m(\omega, x) e^{i(\omega t - k_m(\omega)x)} d\omega \qquad (2.4),$$

where x is the distance from the source and ω is the angular frequency. A_m is the amplitude term, which depends on the source spectrum ($P(\omega)$), the instrument ($I(\omega)$) and site ($R_m(\omega)$) response, the attenuation coefficient ($a_m(\omega)$) and the geometric attenuation ($1/\sqrt{x}$) and is equal to (Aki & Richards, 1980)

$$A_m(\omega, x) = I(\omega) P_m(\omega) R_m(\omega) \frac{e^{-a_m(\omega)x}}{\sqrt{x}} \qquad (2.5),$$

while phase term ($\varphi(\omega, x)$) is equal to

$$\varphi(\omega, x) = -k(\omega) x \qquad (2.6).$$

In terms of signal processing, the acquisition is a discrete sampling and windowing, in space and in time, of the wavefield and, similar to any sampling procedure, the fidelity of the reconstructed signal depends on the sampling parameters.

Time sampling usually has a minor effect (Socco & Strobbia, 2004), since the time windows used in exploration are normally long enough to contain the entire SW traveltimes. In addition, the temporal *SR* is usually high, allowing the retrieval of the high-frequency components of the signal, in accordance with the Nyquist sampling criterion.

On the other hand, space sampling, defined by the position and number (N) of the receivers, can have a more severe effect on the reconstructed signal, due to the finite number of receivers typically used. The properties of the retrieved DCs, influenced by the space sampling parameters, are the frequency band and spectral resolution of the curves as well as their ability to describe only SW propagation phenomena, excluding possible artefacts.

2.2.1 Receiver spacing

The receiver spacing is the spatial sampling rate which defines the maximum wavenumber and, as a consequence, the minimum wavelength that can be reliably measured. If the receiver separation is Δx, the Nyquist theorem states that

$$k_{Nyquist} = \frac{1}{2}\frac{2\pi}{\Delta x} \quad (2.7),$$

and therefore, the maximum wavenumber that can be sampled ($k_{\max}$) is

$$k_{\max} = \frac{\pi}{\Delta x} \quad (2.8),$$

and the minimum wavelength that can be reliably retrieved is $\lambda_{\min} = 2\Delta x$. In practice, this theoretical lower wavelength limit is rarely reached in SW processing due to the fast attenuation of high frequencies and the achievable $\lambda_{\min}$ of the DCs is usually data and site dependent (Foti et al., 2018). Nevertheless, if shorter wavelengths are expected, spatial aliasing can be overcome with dedicated acquisition schemes and/or processing techniques (Foti et al., 2002), or based on *a priori* information (see Section 2.3.5).

2.2.2 Array length

Even though no theoretical upper limit on the measurable wavelengths exists, the possibility to retrieve long wavelengths from the records is related to the quality of the signal recorded far from the source, due to geometric attenuation. In this sense, the array length, which affects the distance of the farthest geophone from the source, has an impact on the retrievable frequency band. Several empirical rules suggest that the maximum wavelength which can be measured in the data equals the receiver array length (e.g., Park & Carnevale, 2010). Nevertheless, such empirical rules are not universal and the longest measurable wavelength is also a factor of the offset, energy and frequency band of the source, as well as the medium velocities and attenuation (e.g., Ivanov et al., 2008).

Furthermore, in signal processing terms, the receiver array is a window in space, the length of which (L) defines the achievable wavenumber resolution, necessary to discriminate different SW modes. In particular, according to the

Rayleigh criterion, the wavenumber resolution equals $2\pi/L$, which means that longer receiver windows provide higher resolution. An additional effect of spatial windowing is that the convolution of the window spectrum with the spectrum of the signal can produce spectral leakage and artefacts (e.g., due to the main and side-lobes of the spectrum of the window). This, in turn, affects the possibility to resolve small wavenumber differences, i.e., to properly measure the phase velocities. A longer window produces less artefacts and is, therefore, preferable in terms of wavenumber resolution.

Finally, the optimal array length is also related to the expected lateral subsurface-property variability and might affect the possibility of retrieving a DC which is representative of the actual subsurface conditions. When a long array is deployed, its location is more likely to cross a laterally heterogeneous area, which cannot be described by the theoretical assumptions of SW modelling. Therefore, with respect to the assumption of lateral homogeneity, the shorter the receiver array, the more accurate the DC.

2.2.3 Source-receiver offset

The distance between the source and the nearest receiver (x_1) is a parameter that can severely influence SW processing, since it is related to the possible presence of near-field and far-field effects. The term near-field describes the area in the vicinity of the seismic source, where Rayleigh waves are not fully developed into plane waves (Richart et al., 1970; Wielandt, 1993). If measurements in this area are used for SW analysis, the plane wave-propagation assumption of SW modeling is violated, causing wrong model estimations. In addition, in the near-field, strong interference of BW might be present, since BW can be highly energetic in the vicinity of the source, even though their geometrical spreading is greater with respect to SW. Therefore, assuming that SW are dominant in the near-field can produce errors in the estimation of the DCs (typically underestimation of the phase velocities, Zywicki & Rix, 2005; Strobbia & Foti, 2006).

The far-field effects describe the reduction of the S/N of the SW signal far from the source due to the geometrical attenuation (Bullen & Bolt, 1985), which might reduce the quality of the retrieved DCs and estimated models (Park, 2011).

Due to the dispersive nature of SW, these phenomena are frequency dependent, and the near-field and far-field offset regions vary for different wavelengths (e.g., Bodet et al., 2009). The wavelength values affected by the near- and far-field effects, are usually estimated based on empirical rules of thumb, in relation with the source offset. The most commonly accepted definitions of the near- and far-field are summarized in Table 2.1 and plotted in Figure 2.3. The variability of these rules shows that such an empirical approach lacks reliability and several studies have shown that near- and far-field offset ranges are data and site dependent (e.g., Yoon, 2005; Ivanov et al., 2008; Tremblay & Karray, 2019) and cannot be defined universally.

Table 2.1: *Commonly used empirical relationships for the determination of the near- and far-offset regions*.

	Near-offset	Far-offset
Heisey et al. (1982)	$\lambda < 3x_1$	$\lambda > \frac{x_1}{2}$
Sánchez-Salinero (1987)	$\lambda < \frac{x_1}{2}$	
Gucunski & Woods (1991)	$\lambda < 2x_1$	
Ganji et al. (1998)	$\lambda < 3x_1$	$\lambda > \frac{x_1}{2}$
Park et al. (1999)	$\lambda < 2x_1$	
Foti et al. (2015)	$\frac{x_1}{2} < \lambda < 2x_1$	$\lambda > \frac{x_1}{3}$

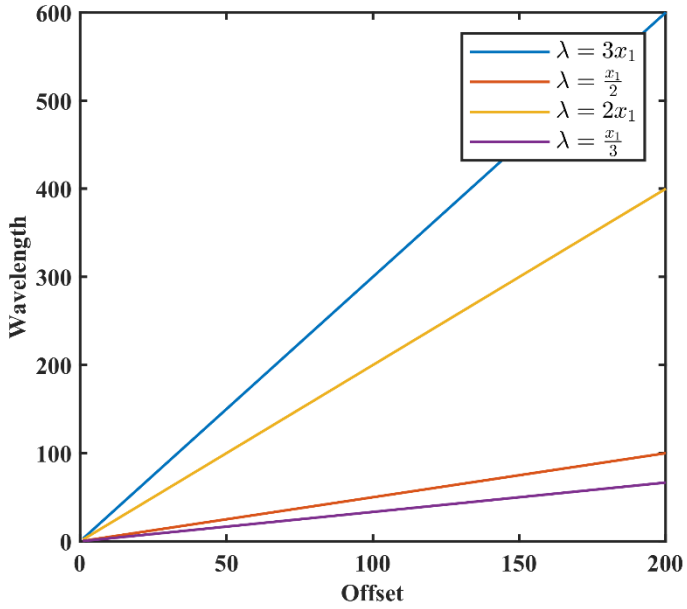

Figure 2.3: Commonly used empirical relationships for the determination of the near- and far-offset regions.

2.3 Surface-wave processing

The aim of processing is to estimate the DCs from the acquired data and, ideally, it should provide DCs which are broadband, accurate, and representative of SW propagation within the measured subsurface portion, to ensure that the inversion will provide a reliable velocity estimate.

Processing allows the extraction of both group and phase-velocity DCs. The retrieval of group velocity is based on computing the peaks of the envelope of the SW signal, measured by at least one receiver. The measurement of phase velocity is based on the computation of the phase or phase-velocity difference of different frequencies of the SW signal, between at least two positions. Group velocity DCs are rarely used in exploration, mainly because group velocity is influenced by a shallower subsurface portion than phase velocity (e.g., Ritzwoller et al., 2001), and therefore, phase velocity DCs allow deeper subsurface investigation. On the other hand, group velocity can be valuable for the optimization of the phase velocity retrieval, if the separation of different SW modes is challenging. Therefore, this section focuses on the phase-velocity processing, but a method to isolate SW modes using the group velocity information is also discussed in Section 2.3.5.

Regarding the extraction of phase velocity DCs, several processing methods exist, and they are commonly classified in two categories:

- multichannel methods, which are based on the analysis of the wavefield sampled by multiple receivers;
- two-station methods, for which the DC is estimated using the recordings of two receivers only.

In the following, the most popular processing techniques will be demonstrated and compared, adopting the aforementioned distinction, even though, it will be shown that multichannel and two-station processing is mathematically equivalent. For the demonstration, we will initially refer to a simple 2D active-seismic acquisition configuration (Figure 2.2), while the applicability of the methods to 3D acquisition setups and to passive-source data will be discussed in Section 2.3.4.

All methods assume a laterally homogeneous subsurface model, plane wave propagation and dominance of the fundamental mode of SW in the records. Discussion on the performance of the methods when these are not fully respected is given in Section 2.3.5.

Finally, it is important to note that here we address only the most fundamental SW processing methods. Based on the same basic principles, a great variety of more advanced processing tools have been developed, but their analysis is out of the scope of this dissertation. An extensive overview can be found in Park & Ryden (2007), Socco et al. (2010) and Pelekis & Athanasopoulos (2011).

2.3.1 Multichannel processing methods

Multichannel methods are based on the application of a wavefield transform on a gather recorded by a receiver array, to convert it from its original space-time ($x-t$) domain, into a different domain (usually frequency – wavenumber or $f-k$, frequency – slowness or $f-p$, and frequency – phase velocity or $f-v$). In the new domain, the data appear as an image of the energy distribution (dispersion image) where, due to the high energy of SW and their characteristic dispersive pattern, the DC can be identified and picked as the coordinates of the spectral maxima.

2.3.1.1 Analysis in the f-k domain

Seismic data processing in the $f-k$ domain is commonly applied as a filtering technique in seismic exploration, mainly for the removal of the groundroll from the

recorded data, since in exploration SW are considered as coherent noise. It was proposed as a method to extract the SW DCs by Nolet & Panza (1976), and it has been used as the basis of several more elaborated, high-resolution SW processing techniques (e.g., Serdyukov et al. 2019).

Referring to Figure 2.2, we assume a linear receiver array, composed by N receivers at a constant spacing of Δx. The length of the receiver spread is $L=(N-1)\Delta x$. The wave is generated by an impulsive source, in-line with the receiver array, at offset x_1 from the first receiver. The N-channel record is denoted as $u(x_i,t)$, where $x_i = x_1 + (i-1)\Delta x$ is the distance of the i-th ($i=1,2...N$) receiver from the source and t stands for time.

The simplest implementation of the $f-k$ transform is a 2D (temporal and spatial) discrete Fourier transform of the wavefield $u(x_i,t)$. First, the temporal discrete Fourier transform is applied to $u(x_i,t)$.

$$U(x_i,f)=\sum_{i=1}^{N} u(x_i,t)e^{-j2\pi f x_i} \tag{2.9},$$

and its subsequent spatial Fourier transform computes the $f-k$ spectrum, which can be described as

$$\hat{U}(f,k)=\sum_{i=1}^{N} U(x_i,f)e^{(-jk(f)x_i)} \tag{2.10},$$

where $j=\sqrt{-1}$. Plotting the amplitude of $\hat{U}(f,k)$ provides an image of the energy density as a function of f and k, where the DC is picked as the coordinates of the spectral maxima (f_{DC} and $k(f)_{DC}$). From these, the phase velocity of the DC can be computed as

$$v_{DC}(f)=\frac{2\pi f_{DC}}{k(f)_{DC}} \tag{2.11}.$$

2.3.1.2 Analysis in the f-p domain

The transformation in the $f-p$ domain has been proposed as a method to estimate the SW DCs by McMechan and Yedlin (1981). It is a two-step process, based on two linear transformations: the application of a slant stack transformation on the wavefield $u(x,t)$, and its subsequent temporal Fourier transform.

The first step, the slant stack transform (also known as Linear Radon or $\tau-p$ transform), converts $u(x,t)$ from its original domain into the domain of slowness (or ray parameter) p and intercept time, τ. The slowness equals the inverse of the velocity and corresponds to the slope of $u(x,t)$ with respect to its x direction. The transformation is performed by steering the record with different values of slowness (p_T), which are chosen according to the range of the expected velocities. At each step, all the traces of $u(x,t)$ are summed along slope p_T at all intercept times, converting the original wavefield into a new domain, the $\tau-p$ domain:

$$\bar{u}(\tau, p_T) = \sum_{i=1}^{N} u(t = \tau + p_T x_i, x_i) \qquad (2.12).$$

In the second step, temporal (along τ) Fourier transform is applied on each trace of the $\bar{u}(\tau, p_T)$ gather, resulting in the $\hat{U}(f, p_T)$ spectrum:

$$\hat{U}(f, p_T) = \sum_{i=1}^{N} \bar{u}(\tau, p_T) e^{(-j2\pi f\tau)} \qquad (2.13).$$

The peaks of the amplitude of the $\hat{U}(f, p_T)$ spectrum (f_{DC}, p_{DC}), corresponding to the DC, are picked and the phase velocity is computed as

$$v_{DC}(f) = \frac{1}{p_{DC}} \qquad (2.14).$$

2.3.1.3 Analysis in the f-v domain - Phase Shift method

The Phase Shift method (Park et al., 1998) is a special implementation of the $f-p$ transform, the basic difference being that the slant stack is performed after the temporal Fourier transform.

Considering the representation of the spectrum $U(x_i, f)$ in terms of amplitude A_i and phase $\Phi_i(f)$:

$$U(x_i, f) = \sum_{i=1}^{N} A_i e^{-j\varphi_i(f)} \quad (2.15),$$

the only variable that contains information on the velocity ($v(f)$) is the phase term which can be defined as

$$\varphi_i(f) = \varphi_I(f) - k(f)x_i = \frac{2\pi f x_i}{v(f)} \quad (2.16),$$

where, $\varphi_I(f)$ is the phase of the source. Assuming different testing phase velocities v_T, a phase shift is computed for each trace and frequency as:

$$\varphi(f)_{Ti} = \frac{2\pi f x_i}{v_T} \quad (2.17),$$

and applied on the $U(x, f)$ wavefield. Slant stacking along all v_T values, leads to the estimation of the summed amplitude:

$$\hat{U}(f, v_T) = \sum_{i=1}^{N} U(x_i, f) e^{-j\varphi(f)_{T_i}} \quad (2.18).$$

The value of v_T for which $\hat{U}(f, v_T)$ is maximized, corresponds to the phase velocity (v_{DC}) of the DC at each frequency.

2.3.1.4 Equivalence between the multichannel methods

The spectral estimators of the three fundamental multichannel SW processing techniques presented in this chapter ($f-k$, $f-p$ and $f-v$) are summarized in Table 2.2. Recalling that $t = \tau + px$ and that, $\varphi(f) = 2\pi fpx = k(f)x$, it is evident that the three transforms are mathematically equivalent.

Table 2.2: *Summary of the common multichannel spectral estimators*

Method	Spectral Estimator
$f-k$	$\hat{U}(f,k)=\sum_{i=1}^{N}U(x_i,f)e^{(-jk(f)x_i)}$
$f-p$	$\hat{U}(f,p_T)=\sum_{i=1}^{N}\overline{u}(\tau,p_T)e^{(-j2\pi f\tau)}$
$f-v$	$\hat{U}(f,v_T)=\sum_{i=1}^{N}U(x_i,f)e^{-j\varphi(f)_{T_i}}$

2.3.2 Two-station processing methods

Two station methods allow the estimation of the phase velocity, by measuring the time at which different frequencies of the highest-amplitude event recorded by two receivers, in-line with a common source and located at known distance Δx from each other, become in-phase. Therefore, two-station methods include two basic operations: the analysis of a pair of traces in different frequencies, by means of a temporal Fourier transform, and the measurement of their phase difference at different time lags. The most common approach to measure the phase difference is cross-correlation, which provides a measure of the similarity of two waveforms, reaching its maximum when the two highest-amplitude events are in-phase. Depending on whether cross-correlation of the traces is applied in frequency or in time domain, different implementations of the two-station method have been developed.

2.3.2.1 Frequency-domain cross-correlation

The two-station method in the frequency domain was introduced by Sato (1955) and has been widely used as a tool to extract phase velocity DCs from both active and passive (e.g., Meier et al., 2004; Fry et al., 2010) SW measurements. The method assumes the wavefield $u(x_i,t)$, $i=1,2$ measured by two receivers only. If $U(x_i,f)$ is the corresponding temporal Fourier transform, the cross-power spectrum can be computed as:

$$\begin{aligned} C_{12}(f) &= U_1(f)^* U_2(f) \\ &= A_1(f) e^{-j[\varphi(f)+k(f)x_1]} A_2(f) e^{j[\varphi(f)+k(f)x_2]} \\ &= A_1(f) A_2(f) e^{jk(f)(x_2-x_1)} \\ &= A_1(f) A_2(f) e^{j\Delta\varphi} \end{aligned} \quad (2.19),$$

where $*$ denotes the complex conjugate, $\varphi(f)$ is the phase of the source, $\varphi_i(f) = k(f)x_i$ $(i = 1,2)$ is the phase of the i-th trace and $\Delta\varphi(f) = \varphi_1(f) - \varphi_2(f)$ is the phase difference between the two traces at each frequency. The (unknown) phase difference can be computed from the cross-power spectrum according to

$$\Delta\varphi(f) = \arctan \frac{\mathrm{Im}\left[C_{12}(f)\right]}{\mathrm{Re}\left[C_{12}(f)\right]} \quad (2.20).$$

allowing the computation of the phase velocity, according to

$$v(f) = \frac{2\pi f\left(\Delta x\right)}{\Delta\varphi(f)} \quad (2.21).$$

2.3.2.2 Time-domain cross-correlation

Bloch & Hales (1968) proposed an alternative implementation of the two-station method, based on the time-domain cross-correlation of the two traces. For this approach, the wavefield $u(x_i,t)$, $i = 1,2$ is decomposed into monochromatic traces of different frequencies $f_0 \in [f_{\min}, f_{\max}]$, and cross-correlation is performed on the filtered traces, frequency by frequency. For the decomposition in different frequencies, one of the most common approaches is the multiple filtering technique (MFT) of Dziewonski & Hales (1972). For this method, each trace is Fourier-transformed and then analysed into harmonics by means of a series of narrow-banded Gaussian band-pass filters. The filters are centered at different frequencies f_0, ranging within a user-defined limit $[f_{\min}, f_{\max}]$ and have the following form:

$$H(f_0, f) = e^{-\alpha\left(\frac{f-f_0}{f}\right)^2} \quad (2.22),$$

where, α is a constant describing the size and rate of decay of the Gaussian filter.

The filter is multiplied by the spectrum of the traces, and by means of inverse Fourier transform, a harmonic, containing amplitudes only at f_0 can be retrieved:

$$u_0(x_i,t) = \frac{1}{2\pi}\int_0^{\infty} U(x_i,f)H(f_0,f)e^{ift}df \tag{2.23}$$

Cross-correlation of the $u_0(x_i,t)$ trace pairs is performed for all the central frequencies $u_0(x_i,t)$. The results are combined into a matrix containing the cross-correlation amplitudes computed for each frequency and time lag, onward referred to as cross-correlation matrix. The maxima of the matrix, indicating the SW arrival-time (t_{DC}) at each frequency, are picked and the DC is computed as

$$v_{DC} = \frac{\Delta x}{t_{DC}} \tag{2.24}.$$

Assuming that the gaussian window used in the MFT is narrow enough, not to oversmooth the spectrum of each trace, the method is equivalent to the frequency-domain cross-correlation. Let $u_0(x_1,t)$ and $u_0(x_2,t)$ be two monochromatic ($\omega = \omega_0$) signals, resulting after application of MFT to $u(x_i,t)$. Their cross-correlation yields

$$u_{12}(t) = A_1 e^{-j(\varphi_1+\omega_0 t_1)} A_2 e^{j(\varphi_1+\omega_0 t_1)} \tag{2.25},$$

and is maximized when

$$\begin{aligned} \varphi_1 + \omega_0 t_{DC1} &= \varphi_2 + \omega_0 t_{DC2} \\ t_{DC2} - t_{DC1} &= \frac{\varphi_1 - \varphi_2}{\omega_0} \\ \frac{\Delta x}{v_{DC}} &= \frac{\Delta\varphi}{\omega_0} \\ v_{DC} &= \frac{\omega_0 \Delta x}{\Delta\varphi} \end{aligned} \tag{2.26},$$

which is identical to eq. 2.21.

2.3.2.3 Surface-wave interferometry

The cross-correlation of two traces approximates the Green's function that would be measured at one of the two receivers, if a source was located at the position of the other (e.g., Weaver & Lobkis, 2001; Wapenaar, 2004). This principle is the basis of seismic interferometry, a method that has been developed and received increasing attention in the last 20 years, primarily because it allows to construct virtual-source seismic datasets, even in the absence of an actual active source (passive data). The estimation of DCs from the SW component of the Green's function with SW interferometry is essentially equivalent to the DC estimation with the two-station methods, and is widely applied to earthquake (e.g., Shapiro & Campillo, 2004; Shapiro et al., 2005), ambient-noise (e.g., Yao et al., 2006) and active-source seismic data (e.g., Halliday et al., 2010).

2.3.3 Equivalence between multichannel and two-station methods

Several experimental studies have shown that multichannel and two-station methods provide DCs of great similarity (e.g., Martin, 2011; Garofalo et al., 2016; Sasanakul et al., 2019). Here, their mathematical comparison is performed, using the expression of the DC computed for only two traces by all the presented methods.

Two-station f-k transform

Considering only two traces, corresponding to a distance $x_i\,(i=1,2)$ from a common source, the expression of the $f-k$ transform (eq. 2.9) becomes:

$$\widehat{U}(f,k)=\sum_{i=1}^{2}U(x_i,f)e^{-jk(f)x_i} \tag{2.27},$$

which, in terms of amplitude (A_i) and phase ($\varphi_i(f)$) spectrum, can be expressed as

$$\begin{aligned}\widehat{U}(f,k)&=\sum_{i=1}^{2}A_i e^{-j\varphi_i(f)}e^{-jk(f)x_i}\\&=\sum_{i=1}^{2}A_i e^{-j(\varphi_i(f)+k(f)x_i)}\end{aligned} \tag{2.28}.$$

Eq. 2.28 is maximized when

$$\varphi_1(f)+k_{DC}(f)x_1=\varphi_2(f)+k_{DC}(f)x_2 \tag{2.29},$$

and therefore

$$k_{DC}(f) = \frac{\varphi_1(f) - \varphi_2(f)}{x_2 - x_1} \tag{2.30}.$$

Since $k = \frac{2\pi f}{v}$

$$v_{DC}(f) = \frac{2\pi f(x_2 - x_1)}{\varphi_1(f) - \varphi_2(f)} = \frac{2\pi f(\Delta x)}{\Delta\varphi(f)} \tag{2.31}.$$

Two-station f-p transform

The $f - p$ transform (eq. 2.21) of two traces ($N = 1, 2$) can be expressed as

$$\begin{aligned} \hat{U}(f, p_T) &= \sum_{i=1}^{2} \bar{u}(t = \tau + p_T x_i, p_T) e^{-j2\pi f\tau(f)} \\ &= \sum_{i=1}^{2} \bar{u}(t = \tau + p_T x_i, p_T) e^{-jt} e^{j2\pi f p_T(f) x_i} \end{aligned} \tag{2.32}.$$

and in terms of amplitude and phase spectrum as

$$\hat{U}(f, p_T) = \sum_{i=1}^{2} A_i e^{\varphi(f)_i} e^{j2p_T(f)x_i} \tag{2.33}.$$

Eq. 2.33 is maximized when

$$\varphi_1(f) + 2\pi f p_T(f)_{DC} x_1 = \varphi_2(f) + 2\pi f p_T(f)_{DC} x_2 \tag{2.34}.$$

from which, the slowness corresponding to the DC is given by

$$p_{DC}(f) = \frac{\varphi_1(f) - \varphi_2(f)}{2\pi f(x_2 - x_1)} \tag{2.35},$$

and the phase velocity of the DC equals

$$v_{DC}(f) = \frac{2\pi f(x_2 - x_1)}{\varphi_1(f) - \varphi_2(f)} = \frac{2\pi f(\Delta x)}{\Delta\varphi(f)} \tag{2.36}.$$

Two-station f-v transform

The $f-v$ transform (eq. 2.26) for $N=1,2$ is given by

$$\hat{U}(f,v_T)=\sum_{i=1}^{2}U(x_i,f)e^{-j\varphi_{T_i}(f)} \tag{2.37},$$

or, in terms of amplitude and phase spectrum

$$\hat{U}(f,v_T)=\sum_{i=1}^{2}A_i e^{-j\varphi_i(f)}e^{-j\varphi_{T_i}(f)} \tag{2.38}.$$

$\hat{U}(f,v_T)$ is maximized when

$$\varphi_1(f)+\varphi_{T_1}(f)=\varphi_2(f)+\varphi_{T_2}(f)$$

$$\varphi_1(f)+\frac{2\pi f x_1}{v_{DC}(f)}=\varphi_2(f)+\frac{2\pi f x_2}{v_{DC}(f)}$$

$$v_{DC}(f)=\frac{2\pi f(x_2-x_1)}{\varphi_1(f)-\varphi_2(f)}=\frac{2\pi f\Delta x}{\Delta\varphi(f)} \tag{2.39}.$$

Eq. 2.31, 2.36 and 2.39 are identical to the expression of v_{DC} retrieved by the presented two-station methods (eq. 2.21 and 2.26). Therefore, under the assumptions of lateral homogeneity and plane wave propagation, in the absence of noise and other recorded events and if only two traces are considered, the DCs estimated by the two-station and multichannel methods are equivalent.

Their equivalence can be proven also for DCs estimated from more than two traces, as we will demonstrate here for the $f-k$ transform. The derivation for any other multichannel processing method is straightforward. Let N be an arbitrary number of receivers located at $x_{n1},...,x_{nN}$, with $x_{n1}=x_1$ and $x_{nN}=x_2$. The $f-k$ spectrum is maximized when

$$\varphi_{n_1}(f)+k_{DC}(f)x_{n_1}=\varphi_{n_2}(f)+k_{DC}(f)x_{n2}=...=\varphi_{n_N}(f)+k_{DC}(f)x_{n_N} \quad (2.40).$$

As a result, for any $l,m\in[1,2,...,N]$, the expression of the phase velocity remains equal to the one of eq. 2.21:

$$v_{DC}(f)=\frac{2\pi f(x_l-x_m)}{\varphi_m(f)-\varphi_l(f)}=\frac{2\pi f(x_2-x_1)}{\varphi_1(f)-\varphi_2(f)}=\frac{2\pi f(\Delta x)}{\Delta\varphi(f)} \qquad (2.41),$$

and since a laterally homogeneous medium is assumed, $v_{DC}(f)$ is also equal to the average of all the individual receiver pair contributions

$$v_{DC}(f)=\frac{2\pi f}{K}\sum_{l,m=1}^{N}\frac{x_l-x_m}{\varphi_m(f)-\varphi_l(f)} \qquad (2.42).$$

where $K=\frac{N(N-1)}{2}$ is the number of the possible receiver pairs.

Eq. 2.41 and 2.42 show that in a laterally homogeneous medium, the DC extracted from any pair of traces or by any combination of multiple traces of the considered record is always identical and equal to the average DC of the individual pairs of races. The only difference is that the simultaneous processing of the N traces, leads to the estimation of one DC for which the contribution of the K possible pairs is averaged (Figure 2.4a). On the other hand, if N receivers are available, the use of only two traces at a time allows the extraction of K DCs (Figure 2.4b). Nevertheless, the resulting N-channel DC and the K two-station DCs, carry the same information content: the contribution of the K trace couples.

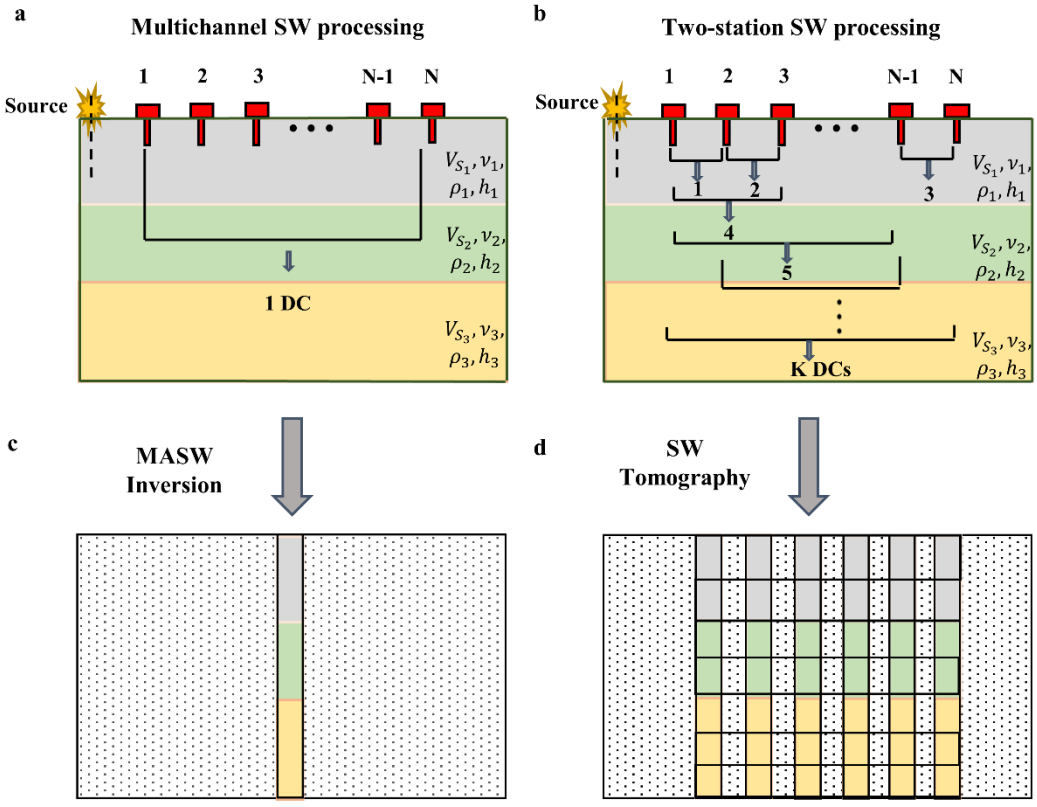

Figure 2.4: Simplified scheme of a) Multichannel and b) Two-station SW processing, and of c) MASW inversion and d) of SW tomography.

2.3.4 Applicability to irregular source-receiver geometries, 3D seismic acquisition setups and to passive-source seismic data

We have demonstrated the mathematical background of the most fundamental SW processing techniques, using as reference a regular 2D active-seismic acquisition setup. For 2D profiles with non-uniform receiver spacing, the use of the 2D Fourier transform to compute the $f-k$ spectrum, presented in Section 2.3.1, is restricted. In this case, the $f-k$ spectrum can be computed with more complicated algorithms (e.g., the MUltiple SIgnal Classification (MUSIC) algorithm - Schmidt, 1986). The rest of the presented multichannel and two-station methods do not present any mathematical limitation with respect to the receiver spacing, and are therefore directly applicable to **irregular 2D profiles**.

Concerning the processing of **3D active-seismic data**, the application of two-station methods is straightforward, as long as the acquisition spread contains pairs of receivers, in-line with common shots. The application of multichannel

processing is also possible, but requires a form of data rearrangement based on the source-receiver offset (e.g., Boiero et al., 2011; Wang et al., 2015).

Regarding **passive-source data**, a difference with respect to real-data processing is that the position of the passive source is unknown (see Chapter 7 for details). In this case, the SW propagation direction should be estimated prior to the DC extraction, otherwise the measured velocity will correspond to a projection of the true phase velocity on the receiver array (Boschi et al., 2013). For this reason, for passive-source SW analysis, the data are usually collected by areal arrays of receivers and are processed with methods which allow the estimation of the SW propagation direction. The DCs are then extracted, considering only the portions of the data which have been recorded by receivers in-line with the estimated SW propagation azimuth.

Such a method, used in this dissertation, has been proposed by Zywicki (1999). It is a special implementation of the $f-k$ transform, based on the conventional frequency-domain beamforming method (Johnson & Dudgeon, 1993). For this method, the $f-k$ spectrum is computed by steering the receiver coordinates towards different azimuths and phase velocities (or, equivalently, towards different values of the k_x and k_y components of wavenumber) using the following steering vector:

$$\mathbf{e}(\mathbf{k}) = [e^{-j\mathbf{k}\mathbf{x}_1}, ..., e^{-j\mathbf{k}\mathbf{x}_N}] \tag{2.43},$$

where $\mathbf{k}$ is the vector of testing wavenumbers and $\mathbf{e}$ is the phase shift corresponding to each testing $\mathbf{k}$. The beamformer applies a phase shift $\mathbf{e}(\mathbf{k})$ on the temporal Fourier transform of the original record $u(x_i, t)$, which in vector notation is given as

$$\mathbf{U}(f) = [U(x_1, f), \ldots, U(x_N, f)]^T \tag{2.44},$$

and T denotes the vector transpose. The output of the beamformer is expressed as

$$Z(\mathbf{k}, f) = \mathbf{e}^H \mathbf{W}\mathbf{U} \tag{2.45},$$

where $\mathbf{W} = \begin{bmatrix} w_1 & 0 & 0 \\ 0 & \ddots & 0 \\ 0 & 0 & w_N \end{bmatrix}$ is the Hermitian transpose and $\mathbf{W}$ is a diagonal matrix containing shading weights w_i, which control the contribution of each receiver in the spectral estimation:

$$\mathbf{W} = \begin{bmatrix} w_1 & 0 & 0 \\ 0 & \ddots & 0 \\ 0 & 0 & w_N \end{bmatrix} \quad (2.46).$$

The conventional frequency domain beamforming applies uniform and equal to unity shadowing for all sensors. Zywicki (1999) recommends for Rayleigh-wave analysis the use of shading weights based on the approximation of their geometrical spreading ($w_i = \sqrt{x_i}$). This geometrical spreading normalization or similar amplitude or energy normalizations are customary in SW analysis and, for generality, will be omitted in the following demonstrations.

The power spectrum of Z ($P(\mathbf{k}, f)$) provides the value of the energy associated with each azimuth and wavenumber at each frequency. Neglecting $\mathbf{W}$, the power spectrum can be computed as

$$\begin{aligned} P(\mathbf{k}, f) &= \mathbf{Z}\mathbf{Z}^{\mathrm{H}} \\ &= \mathbf{e}(\mathbf{k})^{\mathrm{H}}\mathbf{U}(f)\mathbf{U}(f)^{\mathrm{H}}\mathbf{e}(\mathbf{k}) \\ &= \mathbf{e}(\mathbf{k})^{\mathrm{H}}\mathbf{R}\mathbf{e}(\mathbf{k}) \end{aligned} \quad (2.47),$$

where $\mathbf{R}$ is the spatiospectral correlation matrix, containing the cross-power spectra between all possible couples of observations:

$$\mathbf{R} = \begin{bmatrix} U(f)_1 U(f)^*_1 & U(f)_1 U(f)^*_2 & \cdots & U(f)_1 U(f)^*_N \\ U(f)_2 U(f)^*_1 & U(f)_2 U(f)^*_2 & \cdots & U(f)_2 U(f)^*_N \\ \vdots & \vdots & \ddots & \vdots \\ U(f)_N U(f)^*_1 & U(f)_N U(f)^*_2 & \cdots & U(f)_N U(f)^*_N \end{bmatrix} \quad (2.48),$$

and * indicates the complex conjugate.

The peaks of $P(\mathbf{k}, f)$ at each frequency provide the magnitude of $\mathbf{k}$, which can be used for the estimation of the phase velocity according to eq. 2.9. The

direction of $\mathbf{k}$ indicates the azimuth of the dominant energy, which can be computed as

$$\theta = \arctan\left(\frac{k_x(f)}{k_y(f)}\right) \tag{2.49}.$$

Therefore, the transform allows to estimate, apart from the phase velocity, also the direction of the propagating SW energy. If the position of the source is known, as in the linear array example of Figure 2.1, the beamformer output can be expressed in a simplified form as

$$Z(k,f) = \sum_{i=1}^{N} U(x_i, f) e^{jk(f)x_i} \tag{2.50},$$

which is equivalent to the $f-k$ spectrum retrieved by the simple 2D Fourier transform (eq. 2.9).

2.3.5 Implementation to real-data processing

It has been demonstrated that under the assumptions of plane wave propagation, laterally homogeneous velocity distribution and dominance of the fundamental SW mode in the recorded data, the basic SW processing methods are mathematically equivalent. Nevertheless, due to the discrete nature of real-data processing and because the aforementioned assumptions might not always be fully respected, differences among the methods may arise.

Among the various multichannel techniques, although numerous studies on synthetic and real data (e.g., Tran, 2008; Martin, 2011; Zhao, 2012) have shown that the retrieved DCs are often very similar, choices during the method **implementation**, such as the discretization of the testing velocity or slowness values applied for the computation of the $f-p$ and $f-v$ slant stacked amplitudes, or different amplitude normalization or geometrical spreading compensation factors, might produce minor differences in the quality of the retrieved images (e.g., Dal Moro et al., 2003). Nonetheless, these kinds of operations do not alter the actual data content of the transformed dispersion image, which, as shown in this chapter, is identical for all multichannel methods.

Regarding two-station methods, their practical implementation might give rise to certain challenges. One of the most widely discussed shortcomings is related to the effect of **spatial aliasing** (e.g., Al-Hunaidi, 1992; Rosenblad & Bertel, 2008; Foti et al., 2011). Due to the use of the arctangent function in eq. 2.20, the computed $\Delta\varphi$ is a wrapped phase, having an uncertainty of one cycle (2π). To estimate the unwrapped phase, an integer n of 2π should be added to $\Delta\varphi$, prior to the application of eq. 2.21, in the following manner:

$$\Delta\varphi_{unwrapped}(f) = \Delta\varphi_{wrapped}(f) \pm 2n\pi \tag{2.51}$$

The decision of a proper n value is not straightforward, and in practice, the correct DC is typically estimated by computing with eq.2.21 several values of $v(f)$ using different n values. The $v(f)$ curves, are visually compared with a reference on the expected phase velocities in the investigated area, which can be retrieved for instance by previous studies (e.g., Lin et al., 2008) or based on the known velocity distribution in the area (e.g. Bakırcı et al., 2012; Boschi et al., 2013). Throughout the thesis, we will use as reference a DC resulting from multichannel processing of the same dataset. Multichannel DCs are considered reliable references (e.g., Ikeda & Tsuji, 2020), since the inclusion of a high number of receivers in the spectral computation, and therefore the denser spatial discretization, makes them less prone to spatial aliasing. Once the reference DC has been obtained, the $v(f)$ curve which is nearest to the reference is selected as the estimated two-station DC, v_{DC}.

Since reliable *a priori* knowledge of the expected phase velocities is not always realistic, especially in heterogeneous sites, the two-station method carries a high degree of uncertainty. Moreover, an additional manual quality control is usually necessary, to ensure that for the entire frequency band, the picked phase velocities follow the same cycle and portions of the DC are manually deleted if they present "jumps" to wrong cycles (Lin & Chang, 2004).

Similar manual "cleaning" operations are normally performed also during multichannel SW processing, to remove portions of the DCs falling on undesired spectral maxima (Foti et al., 2018). Nevertheless, due to the lower number of DCs, such a **manual intervenion** is not critical, as opposed to the increased processing-time and operator-intervention requirements of two-station processing, which make this approach ill-suited to large-scale applications.

Another critical limitation of the two-station methods is their inability estimate the desirable phase velocities (usually corresponding to the fundamental SW mode), if several SW modes or other recorded events, such as BW or noise, are dominant in the data. The cross-correlation function of the two traces is maximized when the highest-amplitude events of both traces are in-phase, regardless the nature of these events. If **higher SW modes or other types of waves** are highly energetic, the maximum amplitude might be related to a different event for each trace, leading to a wrong estimation of the phase velocity.

A possible solution is to filter the traces prior to the computation of the cross-power spectrum, in order to isolate the fundamental mode, based on its group velocity. A common method for the computation of the group velocity is based on the MFT, described in Section 2.3.2. With this method, the traces can be decomposed into monocromatic signals, u_0, containing energy only around f_0. For the group velocity estimation, the quadrature of each u_0 trace is computed as

$$u_{q0}(x_i,t) = -\mathrm{Im}(u_0(x_i,t)) \tag{2.52},$$

where $u_0(x_i,t)$ is the Hilbert transform of $u_0(x_i,t)$, and its envelope as

$$E_0(x_i,t) = \sqrt{\left(u_0(x_i,t)\right)^2 + \left(u_{q0}(x_i,t)\right)^2} \tag{2.53}.$$

The value of time, corresponding to the maximum value of the envelope, equals the group arrival time ($t_g(f_0)$) from which, the group velocity can be computed as

$$v_g(f_0) = \frac{x_i}{t_g(f_0)} \tag{2.54}.$$

Repeating the same computation for all $f_0 \in [f_{\min}, f_{\max}]$, allows the estimation of the group velocity DC for each original trace. To filter the traces, before the application of the two-station processing, a time-window centered at the group arrival time is applied on each trace, ensuring that cross-correlation will be performed only for fundamental mode. For processing also higher modes, different pre-processing techniques can be adopted (e.g., Khosro Anjom et al., 2021).

To avoid numerical artefacts in the computation of the phase velocity, Yao et al. (2005) recommend to filter around the group velocity using a time-window with cosine shoulders:

$$w(t,f_0)=\begin{cases} 1 & \text{if} \quad t_g(f_0)-\dfrac{n}{f_0}<t<t_g(f_0)+\dfrac{n}{f_0} \\ \cos\left(\pi\dfrac{\left|t-t_g(f_0)\right|+\dfrac{2}{f_0}}{\dfrac{1}{f_0}}\right) & \text{if} \quad -\dfrac{2}{f_0}<\left|t-t_g(f_0)\right|<\dfrac{2}{f_0} \\ 0 & \text{elsewhere} \end{cases} \tag{2.55}$$

where n is the (constant) ratio between the half-window length and the period of interest and, according to Yao et al. (2005) should be in the range of 2-3.

For multichannel processing, such a filtering is not necessary since, assuming adequate spectral resolution, all multichannel methods allow the separation of the different modes in the spectra. In particular, if sufficiently energetic, higher modes appear as separate spectral maxima at distinct velocities, with respect to the fundamental mode, and can be picked to obtain a multimodal DC (e.g., Tselentis & Delis 1998; Park et al., 1999).

An additional challenge for two-station methods is the presence of **random noise** in the data. In presence of noise, the use of a large number of receivers in the spectral computations can be advantageous since, according to eq. 2.42, the contribution of each individual trace in the multichannel DC computation is statistically reduced with increasing number of receivers. Therefore, using a large number of receivers, reduces the influence of low S/N traces in the spectrum and makes multichannel processing more stable. For the same reason, also near/far-field effects are expected to be less damaging in multichannel processing (Foti et al., 2002).

Finally, an important apsect to be considered is the effect of **lateral variations** in the subsurface velocity. Boiero and Socco (2010) have shown that two-station and multichannel methods are equivalent also in the case of smooth (linear) lateral variability, as long as the same subsurface portion is covered by the receivers. In this case, the DC measured for any number of receivers covering the entire path, is equal to the average slowness (velocity) along the path.

On the other hand, two-station and multichannel methods are not anymore equivalent if sharp lateral variations are present in the subsurface. Depending on their properties, such discontinuities might act as strong impedance contrasts, causing the back-reflection or attenuation of the energy of the propagating SW (Hyslop & Stewart, 2015). This introduces a complexity on the measured wavefield, (Lin & Lin, 2007; Roy et al., 2013; Evangelista & Santucci de Magistris, 2015), and regardless the processing method and number of traces, the measured phase velocity cannot be easily interpreted in relation to any specific subsurface velocity. Therefore, sharp lateral variations are a challenge for SW processing and should be detected and filtered out from the data, prior to the DC extraction. Methods to detect the presence and location of sharp lateral variations are discussed in Section 4.1.

2.4 Surface-wave inversion

Surface-wave inversion leads to the estimation of the subsurface properties based on the information contained in the experimental DCs. The inversion estimates the parameters (commonly the layer V_S and thickness) of a synthetic layered model of which the forward response (synthetic DC) closely matches the experimental one. It can therefore be regarded as the solution to an optimization problem, of which the objective function is a measure of the distance between the synthetic and experimental DCs.

Several approaches can be adopted for the solution of the inverse problem. The, widely used, local-search algorithms start from an initial (trial) synthetic velocity model, compute the corresponding synthetic DCs, and update the model based on the comparison of the synthetic DCs with the experimental ones. These methods are fast, but suffer from a well-known disadvantage. They may converge to local minima, different than the optimal solution (global minimum), which makes them highly dependent on the choice of the initial model. Global-search algorithms, on the other hand, look for the best-fitting model, over a wide range of possible parameters within a predefined model space. Detailed reviews of the most common algorithms in SW analysis can be found in Foti et al. (2011).

Regardless the specific algorithm, used to minimize the objective function, a distinction between the existing SW inversion schemes can be made, based on

whether the measured DCs are considered in the inversion as local properties or as average along the receiver paths. Concerning this aspect, two popular SW inversion schemes exist:

- the scheme which assumes local DCs and velocity models and,
- the scheme of SW tomography, which assumes path-average distribution of the phase velocities.

Traditionally, regardless the mathematical equivalence of the various DC-estimation techniques, the SW processing method associated to these schemes differs.

DCs resulting from multichannel SW processing are usually inverted as 1D curves, with a method commonly referred as MASW (Multichannel Analysis of Surface Waves- Park et al., 1998; Xia et al., 1999), an acronym which was established for a specific processing and inversion method, but is widely used as a general term to describe any type of multichannel processing and 1D inversion combination. The same generalization will be made in the current thesis.

For MASW, a DC estimated from an array of receivers is considered local and 1D, located at the center of the array. Possible lateral heterogeneity of the medium below the receivers is neglected and the inverse problem is solved assuming a 1D layered model, based on the forward modelling algorithms discussed in 2.1.1. Due to the lower sensitivity of the DCs to V_P and ρ (Nazarian & Stokoe, 1984; Xia et al., 1999), the values of these parameters are assigned *a priori*, and inversion is run only for the layer thickness and V_S. Therefore, the typical output of MASW is a 1D V_S model, located at the center of the receiver array (Figure 2.4c).

The method is a standard investigation tool in several engineering applications, such as bedrock mapping (Miller et al., 1999), soil classification (Kanlı et al., 2006; García Nieto et al., 2018), road construction (Park et al., 2018), pavement testing (e.g., Ryden et al., 2003; Ryden & Park, 2004). In exploration, where the multifold acquisition schemes are favorable for multichannel DC extraction, MASW is gaining increasing interest as a method to estimate the static corrections (e.g., Roy et al., 2010; Miao et al., 2016).

In principle, since multichannel and two-station methods are equivalent, a DC extracted from a two-station processing method could be inverted as a 1D curve. In

fact, SASW (Nazarian & Stokoe, 1984), the precursor of MASW in the field of geotechnical engineering, is based on the extraction of the DCs with the two-station methods and their inversion as local curves, outputting a 1D V_S model. Several experimental studies have shown that the retrieved models from MASW and SASW are equivalent (e.g., Garofalo et al., 2016). Nonetheless, in the field of engineering, MASW is gaining increasing interest over SASW, due to the higher reliability of the DCs retrieved by multichannel processing (Park & Ryden, 2007).

The inversion scheme of SW tomography is almost exclusively associated with two-station SW processing. SW tomography is a well-established method in regional and global-scale studies, where it is commonly applied for the determination of 3D models of the earth's structure, using SW generated from ambient noise or earthquakes (e.g., Ritzwoller & Levshin, 1998; Kennett & Yoshizawa, 2002; Shapiro & Campillo, 2004; Sabra et al., 2005). The method is less common in the scale of exploration, even though successful applications on active (e.g., Swoboda et al., 2013; Socco et al., 2014) and passive (Picozzi et al., 2009) seismic exploration data have proven its validity as an exploration tool.

The input to SW tomography is a set of DCs, corresponding to different crossing paths between pairs of receivers. In this case, the experimental DCs are not treated as local 1D curves, but their path-average nature is accounted for, in a manner which allows the estimation of the local distribution of V_S. Kennett & Yoshizawa (2002), provide a comprehensive description of this technique, formulating the classic SW tomography as a two-step process: The first step (tomography), assumes that the local properties of the medium between two stations have a linear contribution to the average phase velocity measured by the DC and therefore, that strong velocity contrasts are absent (see Section 2.3.3.1). The area between the receivers is discretized into a grid, and the grid (local) phase velocities at a given frequency (or period) along a specific receiver path are estimated as the ones that average into the observed DC. Since each grid point might belong to multiple crossing receiver paths, its velocity should be tuned, to satisfy all the corresponding observed DCs. Therefore, the final result is, for each frequency, a map of the local phase velocities for the entire grid, which all satisfy the entire set of path-average DC. In the second stage, the local DCs, corresponding to each grid

position, are inverted to estimate local 1D models, using a 1D forward model (Figure 2.4d).

To improve its efficiency, several authors (e.g., Boschi & Ekström, 2002; Boiero, 2009; Fang et al., 2015; Mohammadi et al., 2020; Zhang, 2020) proposed modifications of SW tomography, to avoid the intermediate stage of phase-velocity map building, and invert the path-average DCs directly for local V_S models. The method of Boiero (2009), used in this thesis and described in detail in Chapter 6, computes the path-average phase velocity distribution resulting from an assumed local V_S distribution, and updates the V_S model to fit the path-average DCs.

In all SW tomography approaches, the achievable lateral resolution of the produced velocity model depends on the spatial coverage of the DC paths and, in general, a dense coverage allows higher lateral resolution (Bijwaard & Spakman, 2000). To optimize the vertical resolution and investigation depth, a wide distribution of path lengths is necessary, since different receiver separations are responsible for different frequencies (wavelengths) of the DCs (see Section 2.2).

Considering the equivalence of all the SW processing methods, a set of multichannel DCs could be used as input to SW tomography, possibly with higher reliability, since the multichannel DCs are more stable in presence of other recorded events and noise (see Section 2.3.5). Such an approach has been recently proposed by (Hu et al., submitted) for a 2D velocity model estimation. However, using multiple receivers for each path and at the same time achieving a high degree of path overlap and azimuth coverage, necessary for 3D SW tomography, would require a larger number of receivers than typically available. Therefore, the common convention, which associates MASW with DCs retrieved from multiple receivers and SW tomography with DCs retrieved by two-station methods and is adopted in the following chapters.

2.5 Conclusion

Surface-wave methods are based on the extraction of DCs from the acquired seismic data with SW processing, and the subsequent inversion of the DCs to retrieve V_S models. Depending on how the DCs are measured and inverted, SW methods can be categorized under the schemes of MASW and SW tomography.

In this chapter it has been shown that the DCs are mathematically equivalent, regardless the number of receivers and data processing applied for their computation. The main difference between MASW and SW tomography is the manner in which the DCs are treated in the inversion. In MASW, a multichannel DC is inverted as a 1D curve, to estimate a 1D velocity model, characterizing the entire subsurface portion below the array. SW tomography uses DCs measured from several pairs of receivers and inverts them simultaneously as path-average curves. Being based on 1D forward modelling algorithms, MASW and SW tomography, should, if the assumption of laterally homogeneous subsurface models is respected, output the same V_S model.

In real-world applications, the theoretical hypotheses of SW analysis are seldom met entirely, and the choice and implementation of the method to be used should consider the intended application and site conditions.

Chapter 3

Background

3.1 Mineral Exploration in Europe - Smart Exploration

"Metallis ex usu hominum sublatis, tollitur omnis ratio & tuendæ sustentandæ ualetudinis, & tenendi cursum uitæ cultioris. Etenim homines fSdissimam et miserrimam uitam degerent inter feras, ni metalla essent, redirent ad glandes at syluestria poma & pruna: herbis & radicibus euulsis uescerentur, unguibus foderent speluncas, in quibus noctu iacerent, interdiu in syluis & campis passim more bestiarum uagarentur, quæres quia hominis ratione, prestantissima & optima naturæ dote, prorsus est indigna, adeóne quisquam erit stultus aut pertinax, ut metalla ad uictum uestitum necessaria esse, & ad uitam hominum tuendam pertinere, non concedat?"

"If we remove metals from the service of man, all methods of protecting and sustaining health and more carefully preserving the course of life are done away with. If there were no metals, men would pass a horrible and wretched existence in the midst of wild beasts; they would return to the acorns and fruits and berries of the forest. They would feed upon the herbs and roots which they plucked up with their nails. They would dig out caves in which to lie down at night, and by day they would rove in the woods and plains at random like beasts, and in as much as this condition is utterly unworthy of humanity, with its splendid and glorious natural endowment, will anyone be so foolish or obstinate as not to allow that metals are necessary for food and clothing and that they tend to preserve life?"

GEORGIUS AGRICOLA, De Re Metallica (Translated from the first edition)

The famous quote from the "'Father of Mineralogy'", dating back to more than half a millennium ago, can be fairly considered valid today. Mined raw materials lie on the technological root of all modern industrial societies, and one could reasonably argue that the history of human civilization, starting from the "stone age" and reaching to the "Fourth Industrial Revolution", projects the advancement of mining endeavour. Man, as a "tool making animal" was, is and will be irrevocably connected to the extraction of mineral resources.

The importance of mining grows rapidly with the evolution of technology and today, the extraction of mineral resources is the basis of a wide range of production activities, such as the energy and construction industry, the production of chemicals and fertilizers, automotive and aerospace products, electronics etc. (Azapagic, 2004; Dubiński, 2013). The increasing complexity of the produced goods makes the supply of diverse mineral resources critical. Even though recycling is gaining increasing attention as a source of materials, relevant projections show that mining will continuously rise in the coming decades. For instance, OECD predicts that in the forthcoming 40 years, the global demand for raw materials will increase to more than twice its current levels (OECD, 2019), and in economic developed regions (Europe and OECD America), mining is predicted to undergo a 70%-80% increase of its current levels. The same analysis forecasts that also recycling will face a rapid growth, but will not be sufficient to mitigate the projected increase of demand. Thus, the stability of the future economic and social growth depends to the effective exploitation of current mining resources and the discovery of new raw-material deposits.

Being the cradle of the modern industrialized economy, Europe has been a mineral-exploitation pioneer for decades. In the 20th century, though, with new "players" emerging in the global economic stage, ore extraction in Europe started to face a downturn and has been gradually replaced by -more competitive- global market imports (DW, 31/01/2007; Schüler et al., 2017; Ritchie, 2019)

Nonetheless, the economic conditions present constant and rapid changes. International competition, increasing demand in ores and high market friction, point out to the necessity of a secure raw material supply within the EU. In this context, since 2008, the EU has adopted the "raw materials initiative", which comprises of three major pillars: a) fair and sustainable supply of raw materials from global markets, b) sustainable supply of raw materials within the EU and c) resource

efficiency and supply of ‘secondary raw materials' through recycling (European Commission, 2008).

To promote the second pillar, a quantum leap in the efficient use of land, materials and labour in the industry is necessary to make the intra-EU raw materials market sustainable and competitive. To this end, the development of advanced and more efficient mineral exploration methods is of utmost importance.

“Smart Exploration” is a project funded by the EU’s Horizon 2020 research and innovation programme, for the development of cost-effective and environmentally friendly mineral exploration solutions (www.smartexploration.eu). The project was initiated in November 2017 and has been active until November 2020, focusing on the development of measuring systems and geophysical methods (mainly seismic, electromagnetic and potential-field). The project engaged 27 seven partners, including research institutions, SMEs, and stakeholders (mining companies and one municipality), based in 9 EU countries and six green-field and brown-field validation sites, located in Sweden, Finland, Greece, Kosovo and Portugal.

Politecnico di Torino, has been one of the project partners since the initiation of the project and was involved in the development of novel seismic processing methods, optimized for mineral exploration. The research work of the current thesis was conducted in association with Smart Exploration, and has been used for the geophysical characterization of two sites among the six pilots associated to the project.

3.2 Mining site of Blötberget in Ludvika, central Sweden

3.2.1 Study area and geology

The first site, Blötberget, is located in the mining area of Ludvika in central Sweden (Figure 3.1) and belongs to one of the country’s most significant mineral districts, Bergslagen. The iron ores of Bergslagen have been exploited for centuries, supporting fundamental sectors of the Swedish industrial activity, and mainly the production of steel.

The Bergslagen district belongs to the Svecokarelian orogen in the Fennoscandian Shield. The iron ore comprises mainly of banded iron formations, skarn-type and apatite-rich iron oxides, among which, the apatite-rich iron oxides are dominant (Geijer and Magnusson, 1944). It exists as sheet-shaped horizons,

formed within dacitic to andesitic, feldspar porphyritic metavolcanic host rocks. Both the host rocks and the mineralization have been intruded by dacitic, andesitic and basaltic dykes and subvolcanic and synvolcanic, granitic to intermediate plutonic rocks. Additional post-mineralization intrusions of granite–aplite–pegmatite and metamorphism are present and are responsible for severe deformation of the rocks (Allen et al., 1996).

The area of focus, Blötberget, is known for its high-quality apatite-rich iron-oxide deposits. The mineralization consists mainly of magnetite and hematite with presence of apatite and quartz-silicate minerals. Magnetite is the dominant mineral of the ore and it is distinguished from hematite, which has a slightly different mineralogy, having a higher content in quartz and feldspar. Both magnetite and hematite appear as separate horizons, which present a steep dip (approximately 45°) towards the south-southwest down to a depth of 500 m. At this depth, the dip becomes less abrupt until a depth of at least 800 m – 850 m.

The Blötberget ores have been subject to mining since the sixteenth century. In 1979, all mining activities were ceased, due to a significant drop in the price of iron, which severely affected the production of this commodity in Europe. Recently, favorable economic conditions have led to a renewed interest and in 2010 permits for exploration and production were given to Nordic Iron Ore (NIO). The company (www.nordicironore.se) estimates the mineral resources (down to 800 m) to be: 45.4 million tons of 41.7 % iron (estimated), 9.6 million tons of 36.2 % iron (indicated) and 11.8 million tons of 36.2 % iron (proven). The initiated activities focus on increasing the existing knowledge on the depth and lateral extent of the deposits. This information is critical for the economic assessment of the ores and for planning the mine-facility installation.

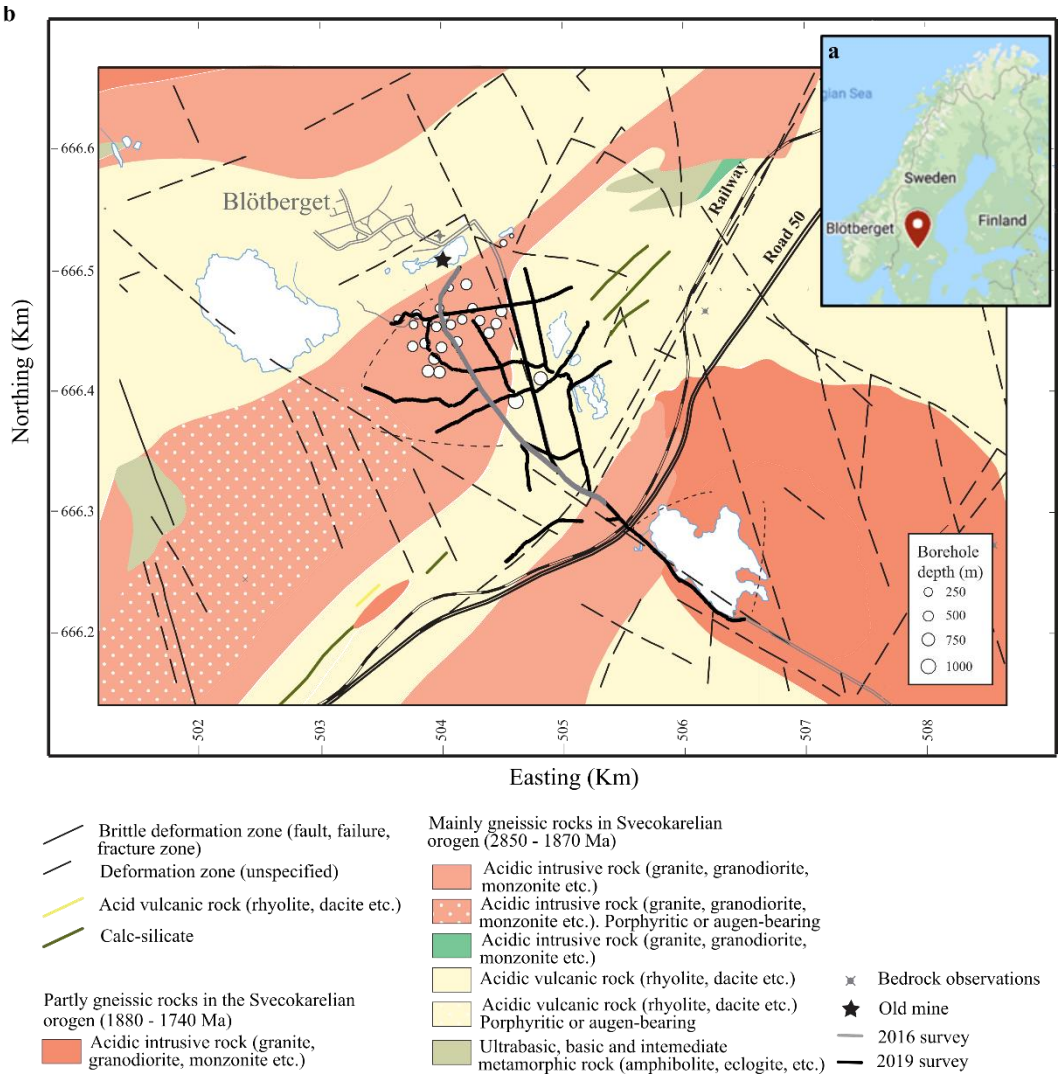

Figure 3.1: a) Map pointing to the area of interest. b) Geological map of the Blötberget area in central Sweden, where the seismic survey lines of the 2016 (grey) and 2019 (black) are shown. The map was reprinted with the kind permission of the Geological Survey of Sweden.

3.2.2 Earlier studies

Maries et al. (2017) present and extensive study of the physical properties of the mineralization and host rocks in Blötberget, based on downhole and laboratory measurements. Triple-sonic full-waveform logging, performed in four of the existing boreholes (white dots in Figure 3.1b), showed that all lithological units, including the near-surface, present high seismic velocities, with V_P ranging between 5000 m/s and 6500 m/s and V_S in the range of 3000 m/s and 4000 m/s. Laboratory measurements on core samples indicated that the mineralized bodies

present significantly higher densities (> 4000 Kg/m^3) than the host rock, leading to high values of acoustic impedance, which justify the suitability of reflection seismic to detect the mineralization.

Regarding the near-surface lithology, the logging measurements showed that the first 100 m consist mainly of metasedimentary argillitic rocks and granite, the density values of which vary between 2500 and 3000 Kg/m^3. These lithological units appeared in several boreholes as outcrops and no core samples or measurements indicated the existence of soft unconsolidated materials. Nonetheless, the existence of soft sediments on the surface is possible, since Blötberget is known for its swampy environment.

In total, three high-resolution active-source seismic field campaigns (in 2015, 2016 and 2019) have been conducted, with the target of increasing the existing knowledge on the extension of the mineralization. The acquisition details and processing results of the 2015 survey are presented in Malehmir et al. (2017). The results of the 2015 dataset processing provided confirmation of the suitability of reflection seismic for this site, since strong reflections appeared in correspondence with the known location of the mineralized bodies. Moreover, the resulting unmigrated sections provided evidence of deeper continuation of the mineralized horizons, which led to the campaigns of 2016 and 2019 (both used in this work) for further investigation.

3.2.3 Seismic dataset of 2016

The acquisition parameters of the 2016 survey are summarized in Table 3.1. The data were recorded within a period of five days, along the profile shown in grey in Figures 3.1b and 3.2. The line had a total length of approximately 2200 m, and was deployed in a direction which crosses the known mineralization, as indicated by the total-field aeromagnetic data map of Figure 3.2, acquired by the Geological Survey of Sweden. The map presents strong magnetic anomalies intersecting the line in two zones (yellow dashed circles in Figure 3.2). The seismic recording equipment included 427 cabled geophones (10 Hz) spaced at 5 m, and 24 wireless stations (10 Hz) spaced at 10 m, while the seismic shots were stroke with a 500-Kg mini skid-steer mounted vertical drop-hammer, along the profile plotted in red in

Figure 3.3a. The recording time made available was 10 s (reduced to 2 s for processing) and the SR was 1 ms.

Table 3.1: *Acquisition and recording parameters of the 2016 and 2019 seismic surveys in the Blötberget mining area in Sweden.*

	September 2016	April-May 2019
Type of survey	Active-source 2D	Active-source 2D
Acquisition system	Sercel Lite 428	Sercel Lite 428
Number of profiles	1	11 (receivers in 9, shots in 11)
Receivers	427 cabled and 24 wireless (10 Hz)	Cabled and wireless 10 Hz
Number of receiver locations	451	1266
Receiver interval	5 m (cabled) - 10 m (wireless)	10 m – 20 m
Source	500-kg mini skid-steer mounted vertical drophammer	32 t vibrator (20 s sweep length, 10-160 Hz linear sweeps)
Number of shot locations	387 (times 3 shots per location)	1051 (times 3 sweeps per location)
Shot interval	5 m	10 m – 20 m
Record length	10 s (reduced to 2 s for processing)	5 s (reduced to 2 s for processing)
Sampling rate	1 ms	1 ms (resampled at 2 ms)

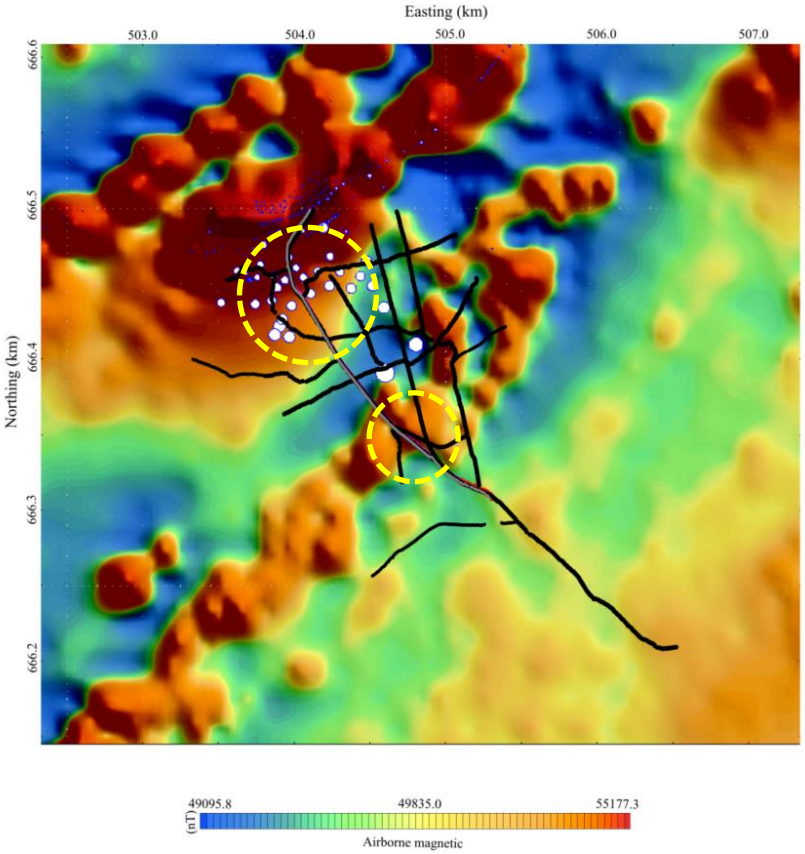

Figure 3.2: Total-field aeromagnetic map of the area in central Sweden showing the location of the 2016 (grey) and 2019 (black) seismic profile and existing boreholes (white dots). The total-field magnetic map was kindly provided by the Geological Survey of Sweden.

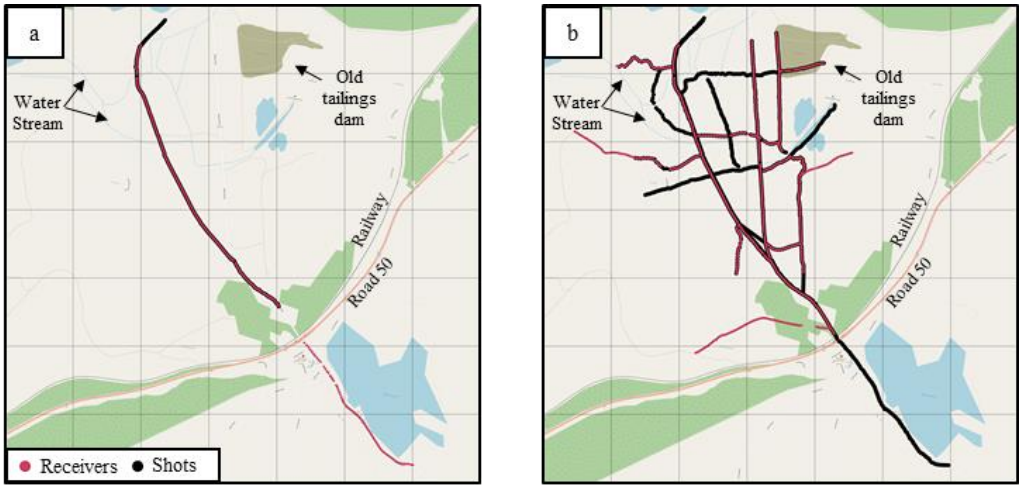

Figure 3.3: Source and receiver geometry of the seismic data acquired in a) 2016 and b) 2019.

The dataset of 2016 has served as a validation dataset to benchmark, compare and combine a variety novel exploration solutions developed within Smart Exploration by various research groups. Balestrini et al. (2020) applied an interferometric method to suppress the SW contained in the data, improving the retrieval of BW reflections. Even though their target was to remove the groundroll contained in the data, they showed that SW are highly energetic and broadband, an encouraging finding with respect to the work of the current thesis, which focuses on the use of groundroll as the input signal to SW analysis.

The high SW contamination has been addressed also in the conventional processing of Markovic et al. (2020). Their work resulted in the migrated stacked section shown in Figure 3.4. The section indicates the existence of two SE-dipping reflectors ("M1" and "M2" in Figure 3.4), which match the position of the known mineralized bodies (blue and red surfaces in Figure 3.4). The section shows that the mineralization probably extends deeper than the known depth of 850 m, by approximately 350 m. This implies a 30 % increase of the resources, if the thickness and lateral extent are assumed constant. Supplementary reflections in the footwall of the known mineralization were also detected, and may be related to additional ore bodies. Apart from the mineralization, a set of NW-dipping reflectors ("R1", "R2" and "R3" in Figure 3.4) were detected and have been interpreted as lithological contacts (faults).

Bräunig et al. (2020) applied an advanced prestack depth imaging workflow, which led to an improved mapping of the structure of the mineralization. Their result fortified the indications that the mineralization extends deeper than originally known and that subvertical faults exist, showing that the faults probably cross-cut the mineralization. In their work, they addressed the issue of near-surface imaging, showing that shallow layers are characterized by a complex system of faulting and fracturing, leading to severe scattering of the BW signal. To better account for this complexity, Bräunig et al. (2020) performed first-break tomography and retrieved a high-resolution shallow velocity model, which was fed to their final migrated model, improving its quality.

The current work focuses on an improved characterization of the complex near-surface environment of Ludvika and the estimation of static corrections. Chapters 4 and 6 present two novel SW-based static solutions and their application on the 2016 dataset. The first workflow, is a fast statics estimation method, based

on multichannel SW DC estimation, limited inversion steps and simple data transform methods. The second workflow is a high-resolution statics estimation method, based on SW tomography. The two workflows have been validated within Smart Exploration and compared with the results of conventional approaches. They have both been included in a complete seismic imaging workflow presented in the deliverable "D10" of the project.

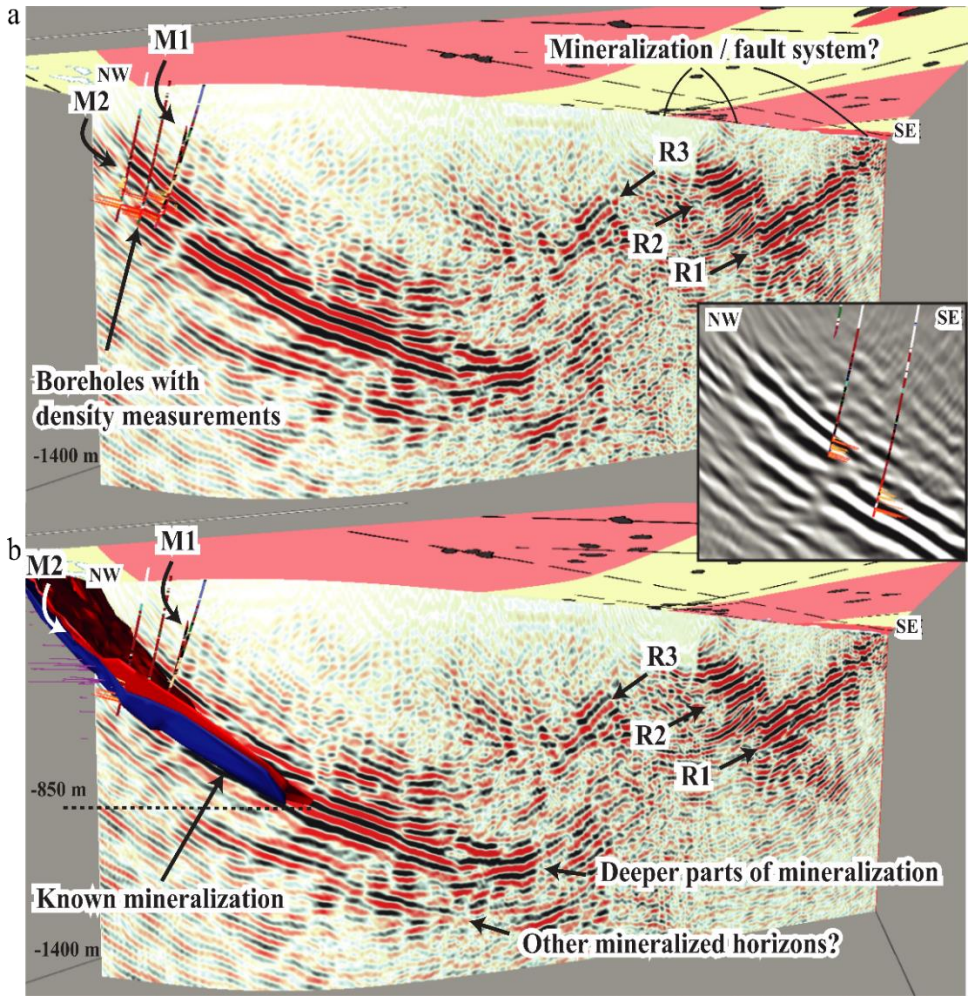

Figure 3.4: Migrated seismic section which resulted from the conventional reflection seismic processing of the Ludvika legacy dataset with (a) density logs (zoomed on the right side) and (b) the ore bodies (blue and red horizons). The section suggests the mineralization probably continues deeper than the known depth (850 m), to a depth of approximately 1200 m. Supplementary reflections in the footwall of the known ore bodies could be additional resources (from Markovic et al., 2020))

3.2.4 Seismic dataset of 2019

The survey of 2019 was conducted within Smart Exploration, in order to estimate the 3D geometry of the mineralization, and to confirm its depth extension (see for details Malehmir et al., 2021). An additional task was to investigate further the number and geometry of the cross-cutting faults indicated in 2016 data processing. This information is critical, not only for the estimation of the complete internal structure of the mineralization -and therefore of the existing reserves- but also for planning the mine infrastructure, since the existence of such weakness zones in the near-surface affects the safety during the exploitation phase of the mine.

The acquisition parameters of 2019 are shown in Table 3.1. The acquisition (black in Figures 3.1b and 3.2 and black and red in Figure 3.3), included 1266 cabled and wireless receivers deployed along 9 lines, and 1051 shot positions shot along 11 lines. The receivers and source points were uniformely spaced along each line, at 10 or 20 m distance. A broadband (10 Hz -160 Hz) linear 32 t vibrator was used as source, performing 3 sweeps at each source location. Each shot was recorded by all the receivers, in order to achieve cross-line azimuth coverage. In total, the 3D dataset included 1,330,566 traces which, after resampling to a *SR* of 2 ms and a record length of 2 s, sized 15.1 GB of computer memory.

The dataset is currently being reprocessed by various groups of Smart Exploration. In the current work, high resolution 3D V_S and V_P models have been estimated through SW analysis and are presented in Chapters 5 and 6.

3.3 Mining site of Siilinjärvi, eastern Finland

3.3.1 Study area and geology

The Siilinjärvi mine is located in the municipality of Siilinjärvi, 20 km north of city of Kuopio in Finland (Figure 3.5a). It is the only operating mine producing phosphorus within the EU. Phosphorus is a commodity listed as one of the 27 critical raw materials for the EU, necessary for the production of agricultural fertilizers (European Commission, 2017). The production activities on the site date back to 1979, when open-pit extraction was initiated by Kemira Oy. Since 2007,

the mine has been operated by Yara International and its current annual production is approximately 11 Mt of ore (O'Brien et al., 2015).

In Siilinjärvi, the phosphorus-bearing mineral is apatite, found within a carbonatite-glimmerite complex (Figure 3.5b). The apatite is currently extracted from two open pits: the main pit, called Särkijärvi (Figure 3.5b) and a satellite pit, named Saarinen, and is processed to produce phosphoric acid on-field, in a concentrator installed in the proximity of the Särkijärvi pit. A significant by-product of the mine is gypsum, which is currently deposited on a 2 × 1 km wide pile, on the southwest of the Särkijärvi pit (Figure 3.5b).

Intrusions of basaltic diabase dykes and a tonalite-diorite body can be found within the carbonatite-glimmerite complex. The tonalite-diorite intrusion is located southwestern of the main mine pit, while the intruded diabase dykes are present throughout the entire ore body. The thickness of the dykes varies within a range of a few centimeters to several meters and most of them present a steep dip (Mattsson et al., 2019). Their dominant orientations are northwest–southeast and north–northwest/south–south. Towards the south of the main pit, the diabase dykes intersect each other and the tonalite-diorite body, creating a complex structural environment.

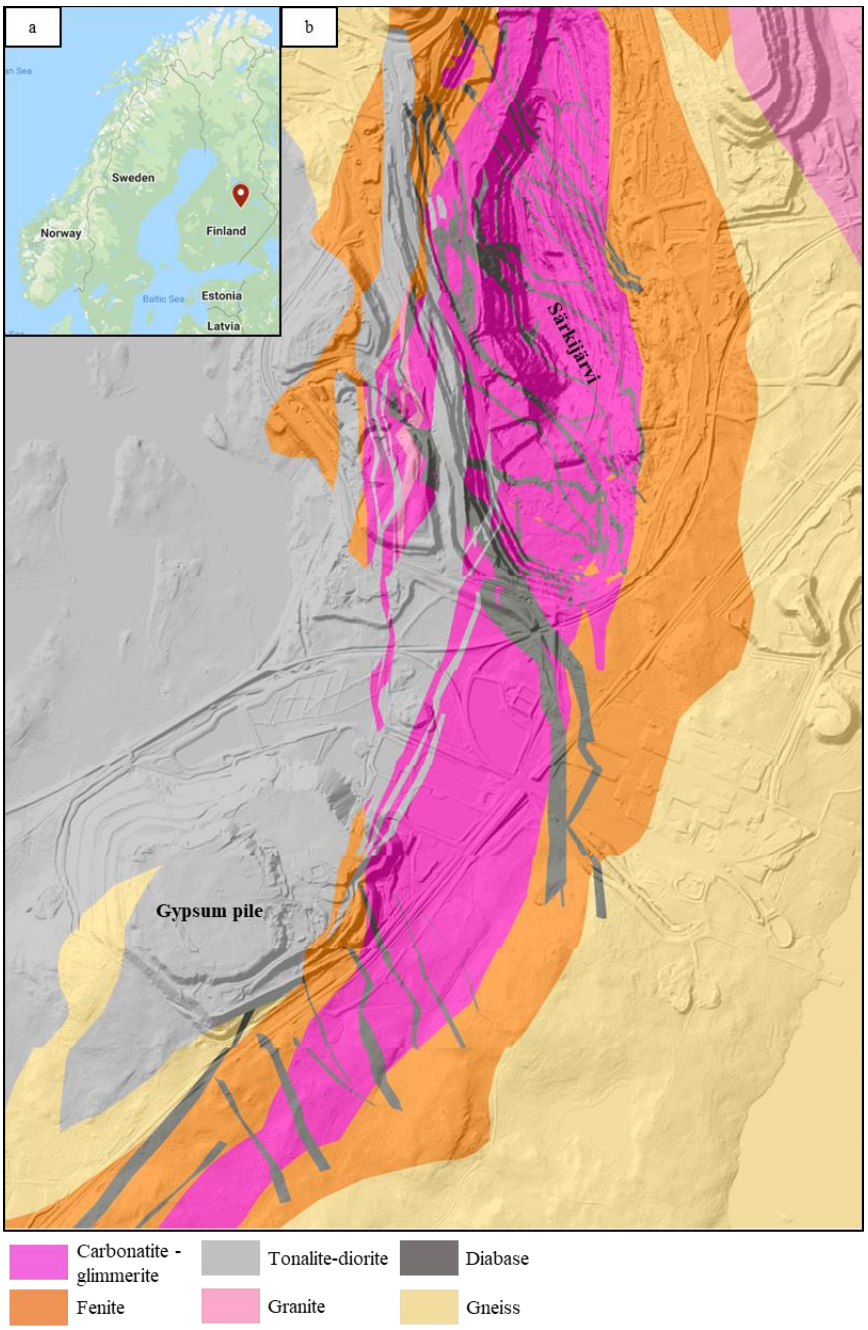

Figure 3.5: a) Map pointing to the area of interest. b) Map of the geology of the area south of the Särkijärvi pit. The geological map has been kindly provided by Yara. Base map: Elevation model, 2008-2019, 2 m x 2 m © National Land Survey of Finland.

3.3.2 Earlier studies

A wealth of information related to the structure and seismic properties of the mineralization and surrounding rocks is available from earlier studies. Malehmir et

al. (2017) present the results of downhole logging (full-waveform sonic, magnetic susceptibility, formation resistivity, temperature, fluid conductivity and natural gamma) and laboratory measurements. In the same work, also the data and results of a seismic survey performed at the site in 2014 are presented. The purpose of their study was to identify the physical properties of the rocks, identify potential weakness zones and gain knowledge on the extension of the mineralization, towards the south of the main mine pit.

The laboratory measurements showed that the P-wave velocities of diorite and fenite fall within 5400 m/s – 6100 m/s and 5300 m/s – 5800 m/s, respectively. The carbonatite-glimmerite and the diabase dykes were found to present a larger variability of V_P, between 4800 m/s and 6500 m/s. The dykes were found to present the highest density values (2750 kg/m^3 – 3050 kg/m^3) and the fenite the lowest ones (2580 kg/m^3 – 2680 kg/m^3). The values of density measured for the carbonatite-glimmerite were found to range between 2800 kg/m^3 - 2950 kg/m^3 and for diorite between 2650 kg/m^3 and 2900 kg/m^3.

The sonic logs indicated in-situ P-wave velocities between 2500 m/s and 7000 m/s, with the highest values corresponding to diabase and diorite. The lowest ranges were associated with carbonatite, which was found to be highly fractured in various zones and different depths. Based on these measurements, Malehmir et al. (2017) concluded that the carbonatite could potentially be reflective.

The seismic survey consisted in four lines, two of which were deployed inside the Särkijärvi pit and two towards the south of the pit. The data were processed for seismic reflection and first-break tomography. The tomographic velocity models presented several low-velocity zones, which were associated with thin (a few meters) glacial-rock overburden layers (blue in Figure 3.6). Deeper low velocity anomalies were found in the area towards the east of the pit, and were associated to the shearing of the ore body, due to intrusion of the tonalite-diorite and diabase dykes. The location of these anomalies was confirmed by the seismic reflection results, which at the same positions revealed strongly dipping (> 70^o) reflectors.

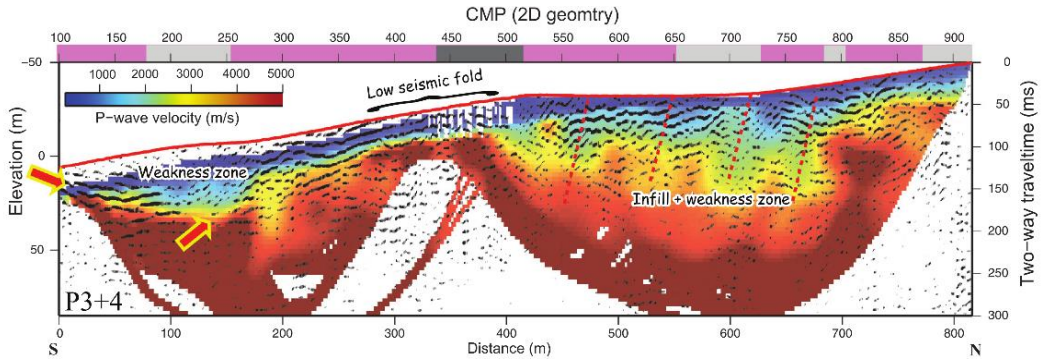

Figure 3.6: P-wave tomography and unmigrated 2D reflection processing results of two seismic lines acquired in 2014 inside the Särkijärvi pit (from Malehmir et al., 2017)

Malehmir et al. (2017) pointed out that the low S/R of the data, the high near-surface variability and the presence of dipping reflectors, imposed challenges to the data processing. Nonetheless, the final results were consistent with the known geology of the area, confirming the suitability of seismic methods to characterize the site.

In summary, so far it has been shown that the carbonatite-glimmerite orebody is expected to present lower density and, due to fracturing, lower seismic velocities with respect to the ones of the host rocks and to the tonalite-diorite and diabase-dyke intrusions.

3.3.3 Seismic dataset of 2018

Between September 20 and October 5 of 2018, a 2D/3D active- and passive-source seismic field campaign was conducted in Siilinjärvi, in the framework of Smart Exploration. A crew of more than 20 members (mainly young professionals) belonging to several partner-affiliations of Smart Exploration was involved in the seismic data acquisition (Figure 3.7). Apart from the seismic measurements, also Ground Penetrating Radar (GPR) and magnetic total field data were collected during the same period and Unmanned Aircraft Vehicle (UAV) based magnetic data are planned to be acquired in the future.

The aim of the seismic survey was: a) to study the lateral and depth extent of the ore body, the knowledge of which is vital for the further development of the mine; b) to assess the distribution of the diabase dykes, which are waste for the mine production and their total volume affects the total reserves, and c) to estimate

potential weakness zones, critical for the safety of the mining activity and its environmental impact. Therefore, the area of the survey included (Figure 3.8):

- A) The area in the of the main mine pit, where the focus was to map the extension of the mineralized body, especially towards the south of the main pit, and possible subsurface structures, which could affect the stability of the pit.
- B) The forest area of the mine which is an area of great interest for the reserve estimation and long-term planning of the mine.
- C) The area of the gypsum pile, where the target was to map the continuation of the mineralized body beneath the pile and possible fractured zones, which would allow the infiltration of the highly acid (pH < 2) drained water from the gypsum pile.

Considering the areas of interest and logistical restrictions, the equipment was deployed, as shown in Figure 3.8: a) three source-receiver lines, named as SM1, SM2 and SM3 in Figure 3.8 (the red stars show the position of the shots); b) an irregular carpet of receivers, recording both active shots and ambient noise (black dots in Figure 3.8); c) additional shots within the area of the open pit (blue stars in Figure 3.8); d) four calibration shots (yellow stars in Figure 3.8). During the striking of all the shots (along the three lines, within the pit and the calibration shots), all the receivers in the irregular carpet were active.

Figure 3.7: Members of the Smart Exploration crew participating in the seismic field survey in Siilinjärvi in 2018.

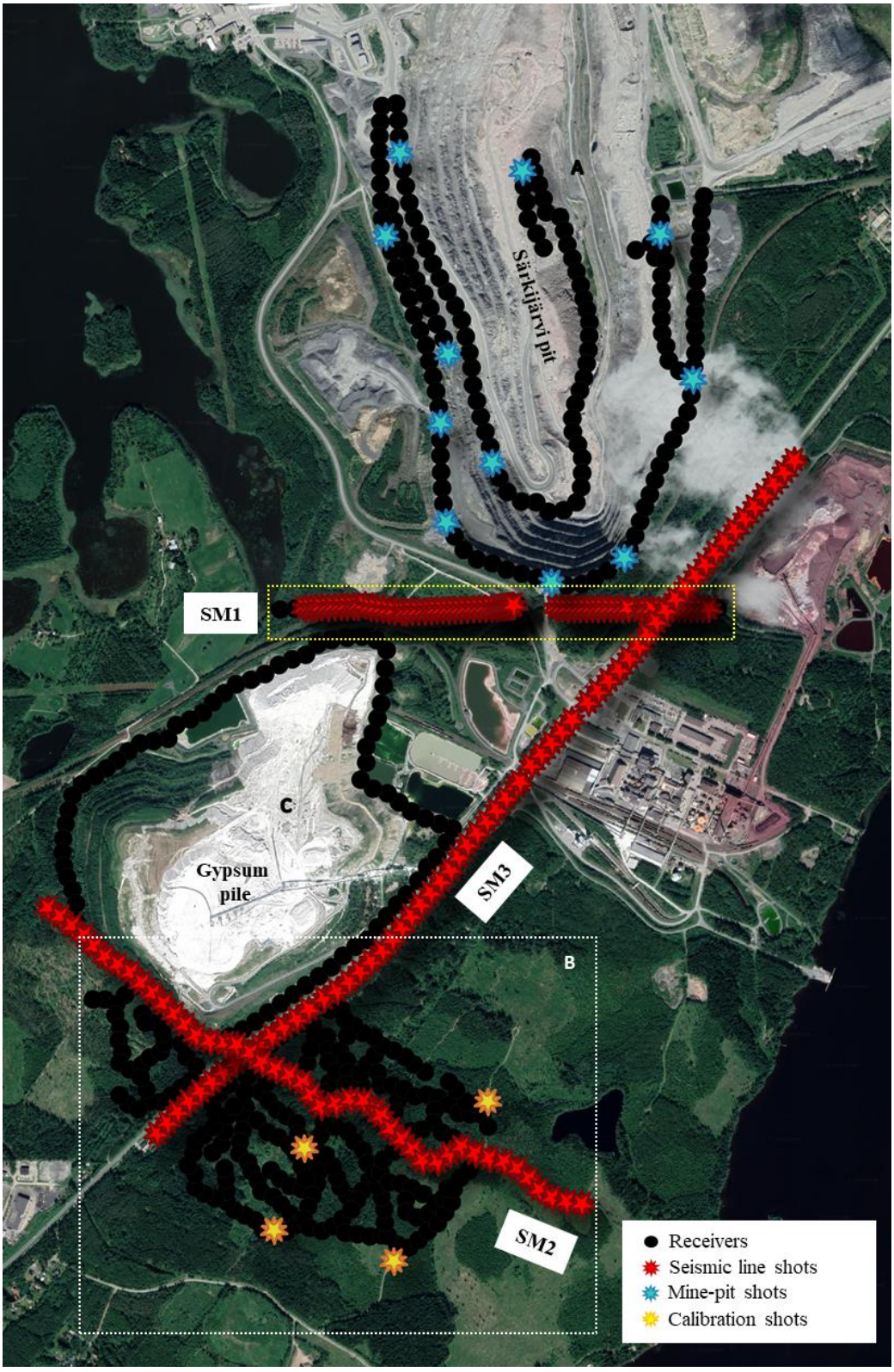

Figure 3.8: Map of the Siilinjärvi survey area. Black dots correspond to the receivers, red stars show the position of the shots along the seismic lines, blue stars show the shots in the main mine pit, and yellow stars indicate the four calibration blasts in the forest. The dashed yellow and white rectangle indicate the two areas of focus of this work.

The purpose of the joint use of the seismic lines and the irregular receiver carpet was to provide a detailed imaging, at different scales, of the subsurface beneath the survey area. The 2D lines were aimed at retrieving a high-resolution depth image of the mineralization along the profiles, and were designed with a dense source-receiver geometry. A combination of 10-Hz cabled and wireless geophones were used, spaced at 5 m (SM1) and 10 m (SM2 and SM3), while the shot spacing was equal to 20 m for all the lines.

The irregular receiver carpet was designed for a wide spatial coverage, necessary to image the continuity and shape of the mineralization. It consisted of 578 10-Hz vertical geophones (Figure 3.9) connected to wireless stations, which contained a GPS locator, a transmitting antenna and an analogue-to-digital converter. In order to continuously transmit the data of each station to the central recording van, the wireless stations had to communicate with each other. To ensure this, two neighboring stations had to be at a maximum distance of 50 m from each other, which was the main constraint given by the equipment in use.

In presence of obstacles (e.g. vegetation), this distance had to be further reduced to approximately 40 m. The array was aimed at recording both ambient noise and the active data. Hence, it recorded continuously for 13 days during which period the active shots were blasted. The data were recorded with a sampling rate of 2 ms and stored in 1-minute segy files, having a total size of almost 800 Gb. The active shots were tracked in the records based on their known time occurrence and stored as separate 6 s-long shot gathers.

In this work, we use the data from line SM1 and the forest area to test the proposed SW workflows since they are of great interest for the near-future development of the mine. Processing of the remaining portions of the survey is planned for the future.

Figure 3.9: A planted 10-Hz geophone connected to a wireless station, belonging to the irregular grid of receivers of the 2018 Siilinjärvi seismic survey.

Acquisition of the active-seismic data in line SM1

The source-receiver layout of SM1 is shown in zoom in Figure 3.10, and its acquisition parameters are given in Table 3.2. The line had a total length of 1360 m and consisted of 262 geophones (combination of cabled and wireless, shown in light and dark blue in Figure 3.10 and Figure 3.11a). A number of 59 explosive shots (magenta in Figure 3.10) and 10 shots stroke by a 520-Kg mini skid-steer mounted vertical drophammer (yellow in Figure 3.10) at a spacing of 5 m, in the locations where it was not possible to use explosives, due to safety reasons, were used. The gap of the receiver- and source-positions at distance 750 m - 840 m from the first receiver, was caused by an intersecting railway and an adjacent to it road, where the equipment could not be deployed. A narrower gap at distance 1200 m – 1230 m from the first receiver was caused by an intersecting dirt road.

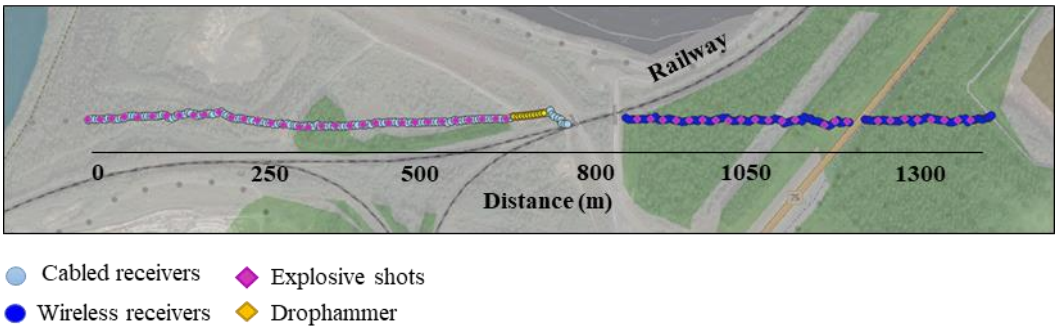

Figure 3.10: Map of the Siilinjärvi survey area, zoomed around active line SM1.

Table 3.2: *Acquisition and recording parameters of the seismic data acquired along line SM1 in Siilinjärvi.*

2018 seismic survey – line SM1	
Type of survey	Active-source 2D
Number of active channels	262 (147 cabled and 115 wireless)
Receiver interval	5 m
Receiver frequency	10 Hz
Source	Explosives and 500-kg mini skid-steer mounted vertical drophammer
Number of shot locations	387 (times 3 shots per drophammer-shot location)
Explosive charge weight	125 or 250 g
Shot-hole depth	2-3 m
Bobcat source pattern	4-5 shots per location
Shot interval	20m (explosives) /5 m (drophammer)
Record length	6s
Sampling rate	1 ms

Figure 3.11: Members of the Smart Exploration crew in the Siilinjärvi mining area a) deploying the cabled receiver system along line SM1 and b) gathering the wireless recorders used in the active seismic lines.

Acquisition of the active and passive-seismic data in the forest area

The survey map, focused around the forest area, is shown in Figure 3.12 and the acquisition and recording parameters are summarized in Table 3.3. The array comprised of 273 receivers, which were deployed considering the requirements of SW tomography: for this method, as discussed in Chapter 2, a widespread source-receiver azimuth distribution and separation between receiver pairs (path length) is desirable. Nonetheless, in the forest area of Siilinjärvi a perfectly uniform distribution was not possible, due to logistical constraints. The main challenge was the density of the forest and its slippery terrain, which posed limitations to the deployment of the equipment. Therefore, for safety reasons and for the effectiveness of the deployment and recollection of the equipment, most of the receivers were placed along or as close as possible to the paths of the forest and only few receivers were located out of the paths, to guarantee optimal subsurface illumination given the position of the sources.

To assess the suitability of this deployment, the azimuthal illumination of the shots towards the array (polar histogram in Figure 3.13a) and the distribution of the length of all the available paths (histogram in Figure 3.13b) were estimated. The paths were well distributed over all azimuths and the path length was well distributed around a maximum of 300 m.

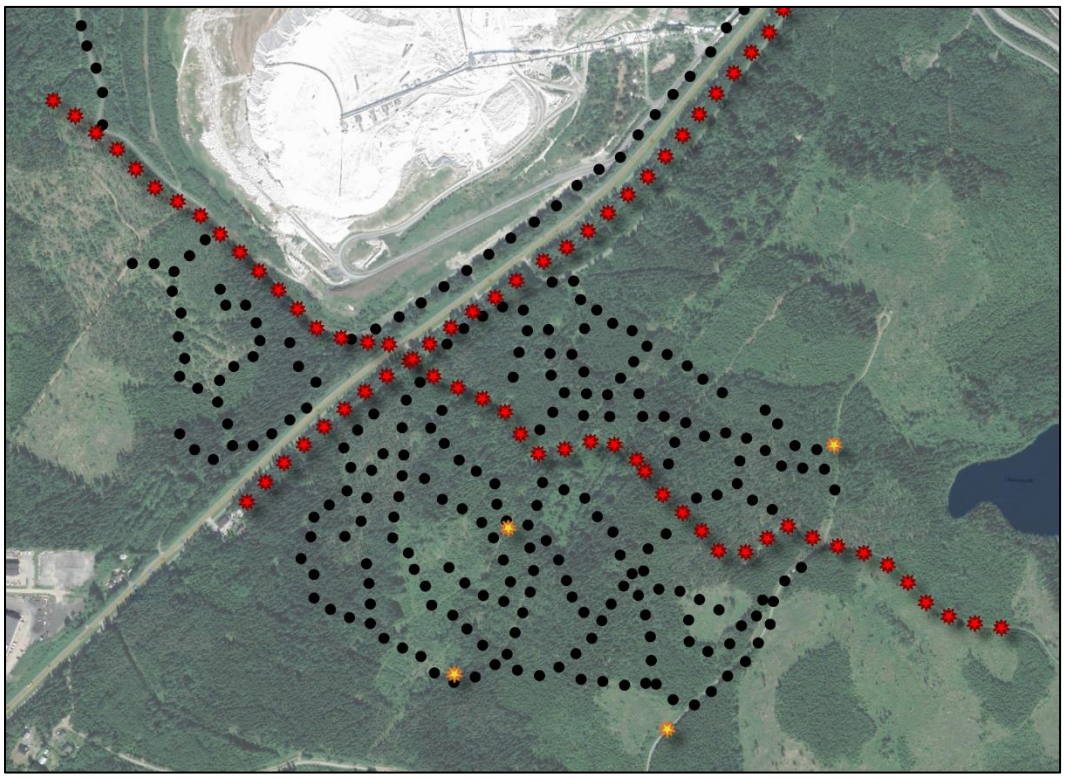

Figure 3.12: Map of the Siilinjärvi survey area, zoomed around the forest region.

Table 3.3: *Acquisition and recording parameters of the active- and passive-source seismic data acquired in the forest area in Siilinjärvi*

2018 seismic survey – forest area		
Type of survey	Active-source 3D	Passive-source 3D
Number of active channels	273	273
Receiver frequency	10 Hz	10 Hz
Number of shot locations	103 (along SM2), 50 (along SM3) and 4 calibration shots	-
Source	Explosives	-
Charge weight	125 or 250 g	-
Shot-hole depth	2-3 m	-
Record length	6s	13 days
Sampling rate	2 ms	2 ms

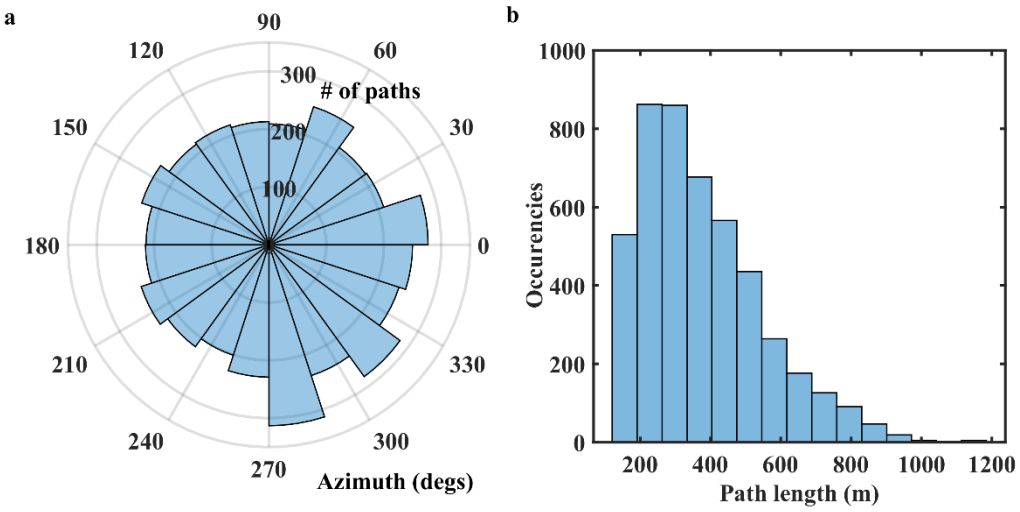

Figure 3.13: Design of the 2018 Siilinjärvi seismic survey in the forest area. a) Polar histogram of the total azimuthal coverage given by all the used shots and the receivers. b) Histogram of the path length distribution.

3.4 State of the art

Mineral-exploration sites are commonly characterized by hard-rock (crystalline) geology. The potential of seismic-exploration methods to characterize such environments is a scientific topic which has received increasing attention in the last three decades, in parallel with the growing interest towards deeper mineralizations, which makes seismic methods more and more attractive.

Numerous examples (extensive reviews can be found in e.g., Eaton et al., 2003; Malehmir et al., 2012; Buske et al., 2015), have shown that seismic methods can provide high-resolution images of the mineralization targets and host rocks and assist mine-planning. Nevertheless, with respect to the sedimentary environments of hydrocarbon exploration, for which most seismic exploration methods have been developed and tested, hard-rock environments are characterized by higher geological complexity. They are typically related to significant heterogeneity, ranging from fine-scale discontinuities, such as cracks (Levander et al., 1994; Holliger, 1997), to larger-scale rock-property alternations (L'Heureux et al., 2009). As a result, rocks act as highly scattering environments which can distort the propagating seismic wavefield (amplitude, traveltime and spectral distortions), causing increased levels of background noise in the recorded data (Cheraghi et al., 2013).

In addition, local discontinuities related to tectonic activities (Eaton, 1999), such as vertical and sub-vertical faults and fractures are also common. Together with the, rugged topography, velocity contrasts (Bona et al., 2013), overburden materials (Hobbs, 2003) and rock anisotropy, caused by metamorphism or tectonic processes (Salisbury et al., 2003; Bongajum et al., 2012), they have also been associated to reductions of the S/N.

Such low-data quality affects also the results of SW processing, causing the DCs obtained from hard-rock sites to be noisy, discontinuous, narrow-banded and poorly dispersive. This behaviour can be observed in Figure 3.14a, where we show literature examples (reproduced from Hollender et al., 2017) of dispersion images obtained from a hard-rock site. Considering that the quality of the inverted models depends on the bandwidth and quality of the DCs (see Section 2.4), the retrieval of accurate models can be a challenge. This is not the case with the DCs from soft sites, encountered in most SW applications, where the DCs are typically characterized by smooth dispersive patterns and broad frequency band (e.g., Figure 3.14b, reproduced from Olafsdottir et al., 2018).

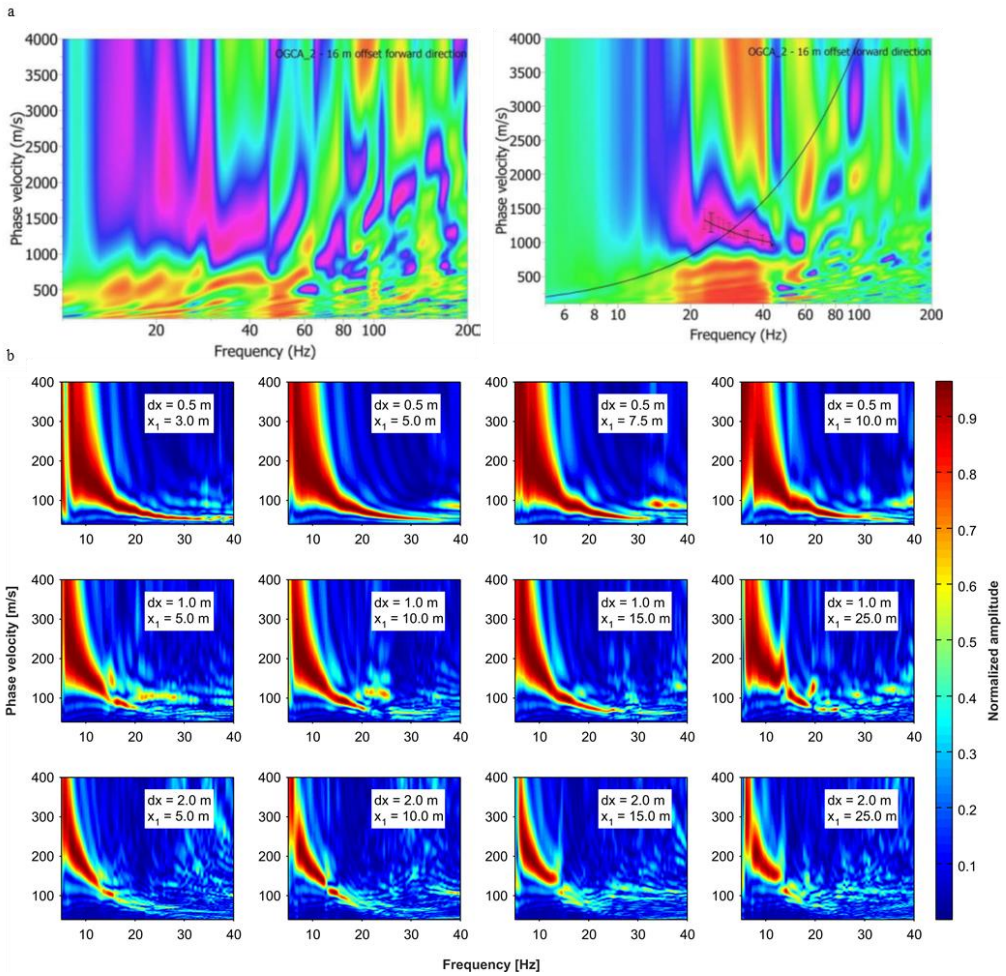

Figure 3.14: Example dispersion images, extracted from a) a hard-rock site (reproduced from Hollender et al., 2017) and b) a soft site (reproduced from Olafsdottir et al., 2018).

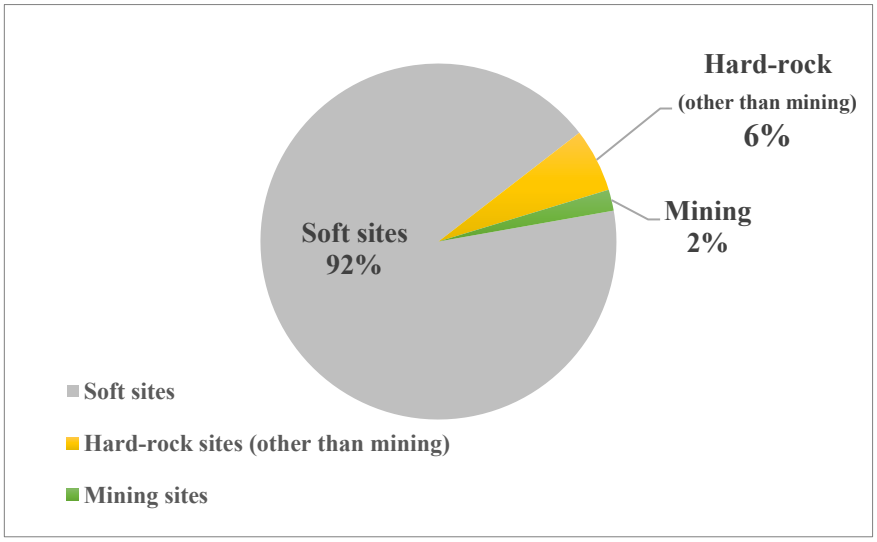

Figure 3.15: Publications (journal papers and expanded abstracts) on EAGE's "Earthdoc" and "SEG digital library" from January 2014 to December 2018.

As a cosequence, although SW methods are very popular in near-surface characterization, their application to crystalline environments remains limited and only a few literature examples have dealt with SW analysis in hard-rock sites. From an extensive literature review in the most common repositories for applied geophysics (SEG Digital Library and EAGE's EarthDoc), between 2014 and 2018 only 8 % of the SW-related literature refers to hard-rock applications (Figure 3.15). Most of these works concern seismic-site characterization, where hard-rock geology is common, while only 2 % of the recent publications refer to mineral exploration (Figure 3.15).

In the field of seismic-site characterization, examples have shown that apart from the low data quality, additional challenges should be expected. Strong impedance contrasts due to soft overburden layers overlying the hard rocks (e.g., Albarello, 2011) are challenging for SW processing and inversion. According to Bergamo et al. (2011) and Pileggi et al. (2011), if the overlying layers are sufficiently thick, higher modes should be expected. Other challenges are velocity inversions and strong heterogeneity (Ladak, 2020) as well as the possible inadequacy of the acquisition parameters to properly measure the long wavelengths caused by the high seismic velocities (Pileggi et al., 2011).

Nevertheless, previous experiences show that SW can provide valuable information at hard-rock sites. For example, Albarello & Gargani (2010) showed that SW DCs can be used effectivelly for soil classification, while Pileggi et al. (2011) and Picozzi et al. (2009) showed that SW analysis at hard-rock sites benefits from the longer propagating wavelengths, which allow deeper investigation (80–100 m in their examples). Useful guidelines were proposed by Cercato et al. (2010), who dealt with shallow-bedrock examples, and proposed muting the data to separate the SW fundamental mode from other waves that are generated due to the property contrast. Casto et al. (2009) underlined the need to use all available a priori information, to better constrain the bedrock depth in SW inversion. Foti et al. (2011) discussed that the high achievable lateral resolution of SW tomography can be valuable to delineate the lateral variability of hard-rock sites, stressing though the need to account for the presence of sharp lateral variations.

Concerning mineral exploration, Hollis et al. (2018) showed that the long wavelengths retrieved from ambient-noise and inverted with SW tomography can delineate the geological boundary of a mineral deposit. Sharma et al. (2018)

confirmed that ambient-noise SW records provide great investigation wavelengths and estimated a 1D V_S profile at a mineral-exploration site. Several case studies dealt with the existence of sharp lateral heterogeneities and showed that they can be delineated with SW. For example, Rector et al. (2015) applied active SW tomography to image old mine workings, introducing a new acquisition scheme. They showed that SW phase velocities and amplitudes are sensitive to the presence of voids. Similar conclusions about the sensitivity of SW to lateral variations were made by Sherman et al. (2014) and Ivanov et al. (2016), who applied SW-based methods for locating voids and mine workings in historical mining sites.

Nevertheless, apart from hard-rock geology, the characteristics and operational requirements of mineral exploration impose additional challenges which should be overcome to efficiently apply SW methods.

When the data are acquired in the vicinity of active mines (brown fields), noise due to the production or supporting activities of the mine (Adam et al., 2000) can severely degrade the quality of the recorded data (e.g., Harrison, 2009; Ahmadi, 2015) and, therefore, the possibility of extracting high-quality DCs. Typical noise sources are the transportation and production vehicles and in-mine ore-processing facilities. Due to the variability of these sources and their short distance from the acquisition sites, the noise filtering and separation from the SW signal can be challenging (e.g., Adebisi, 2012). On the other hand, several examples have shown that the BW (e.g., Cheraghi et al., 2013) and SW (e.g., Sharma et al., 2018) created by these sources can be used as useful signal by acquiring passive-source data.

Being driven by the industrial interests of the mining sector, and with usually lower available budgets than the ones invested in hydrocarbon-exploration, mineral exploration demands SW methods to be cost-effective. This imposes that the operational time and computational resources used for SW analysis should be minimized.

Moreover, sustainable, resource-efficient and environmentally friendly development strategies are necessary to receive “social license” to operate. This can impact seismic exploration since the data acquisition, commonly utilizing active-seismic sources (e.g., explosives), might be restricted by legislation and safety regulations. Moreover, exploration might not be welcome by the local communities, due to the generated noise and disturbance of the surrounding

industrial and civil activities. This can lead to data acquired with sources providing low S/N or using irregular layouts, which requires the design of customized processing solutions.

Finally, a challenge for SW methods, when used for exploration, is that they should be able to provide V_P models, to be compatible with reflection-seismic workflows (e.g., for statics estimation). On the other hand, SW propagation is mainly sensitive to V_S (Section 2.4). This is usually solved by assuming *a priori* values of ν in the DC inversion and use it to convert the inverted V_S model into V_P. However, this approach is prone to errors for both V_S and V_P (Foti & Strobbia, 2002; Karray & Lefebvre, 2008; Ivanov et al. 2019) estimations. To avoid them, the *a priori* selection of ν is usually performed with caution, on the basis of independent information (e.g., geological maps and previous studies), or performing additional investigations, such as borehole measurements or other geophysical methods (Ivanov et al., 2000; Strobbia et al., 2010; Abudeif, 2016; Anukwu et al., 2020). Nevertheless, even such an informed selection of ν is risky and can introduce uncertainties due to inherent limitations of the performed methods. Moreover, the acquisition of additional data and/or the performance of extra processing steps might increase the overall costs.

To overcome these challenges, novel SW methodologies, tailored to mineral exploration, are proposed in the following chapters.

3.5 Conclusion

Mineral exploration is of paramount importance for Europe's current and future financial and social growth. Seismic methods, although still infrequent in the exploration for minerals, can be valuable to provide high-resolution images of the ore bodies, which are currently sought at great depths. The use of SW methods, rarely applied to such challenging hard-rock settings, as tools to characterize the near-surface and improve target prospecting can be valuable in this contecxt. Considering that the hard-rock geology can trigger long SW wavelengths, potentially reaching to the mineralization targets, increases the importance of developing SW techniques, tailored to these environments.

We have presented the seismic datasets which will be used throughout the thesis to demonstrate the developed methodological tools. The datasets have been acquired at two mineral exploration sites of great significance within the EU. Apart from the importance of the datasets for the validation of novel methods, developed within the thesis and in Smart Exploration, their size and unique characteristics make them important sources of information on Europe's mineral deposits. To this end, the new data and target generation and integration objective is one of the values of Smart Exploration.

Chapter 4

Multichannel SW analysis for mineral exploration – SW direct statics estimation method

4.1 Introduction

In this chapter, we propose a method to estimate the statics based on multichannel SW processing, onward referred to as "SW direct statics estimation method". The proposed technique is designed to overcome the limitations of multichannel SW processing in presence of sharp lateral variations, as well as the low sensitivity of the DCs to V_P and it can provide the statics in a fast and efficient manner, avoiding excessive inversion steps.

The method is applied to two seismic mineral exploration datasets, acquired at the iron-oxide mining site of Ludvika (Sweden) and at the apatite mine of Siilinjärvi (Finland). The output statics and resulting stacked sections are compared with the ones retrieved by routinely used BW-based methods and with existing geological information.

4.2 Method

A schematic representation of the SW direct statics estimation method is presented in Figure 4.1 and its basic steps (labelled as “A”-“F”) are described in the following paragraphs.

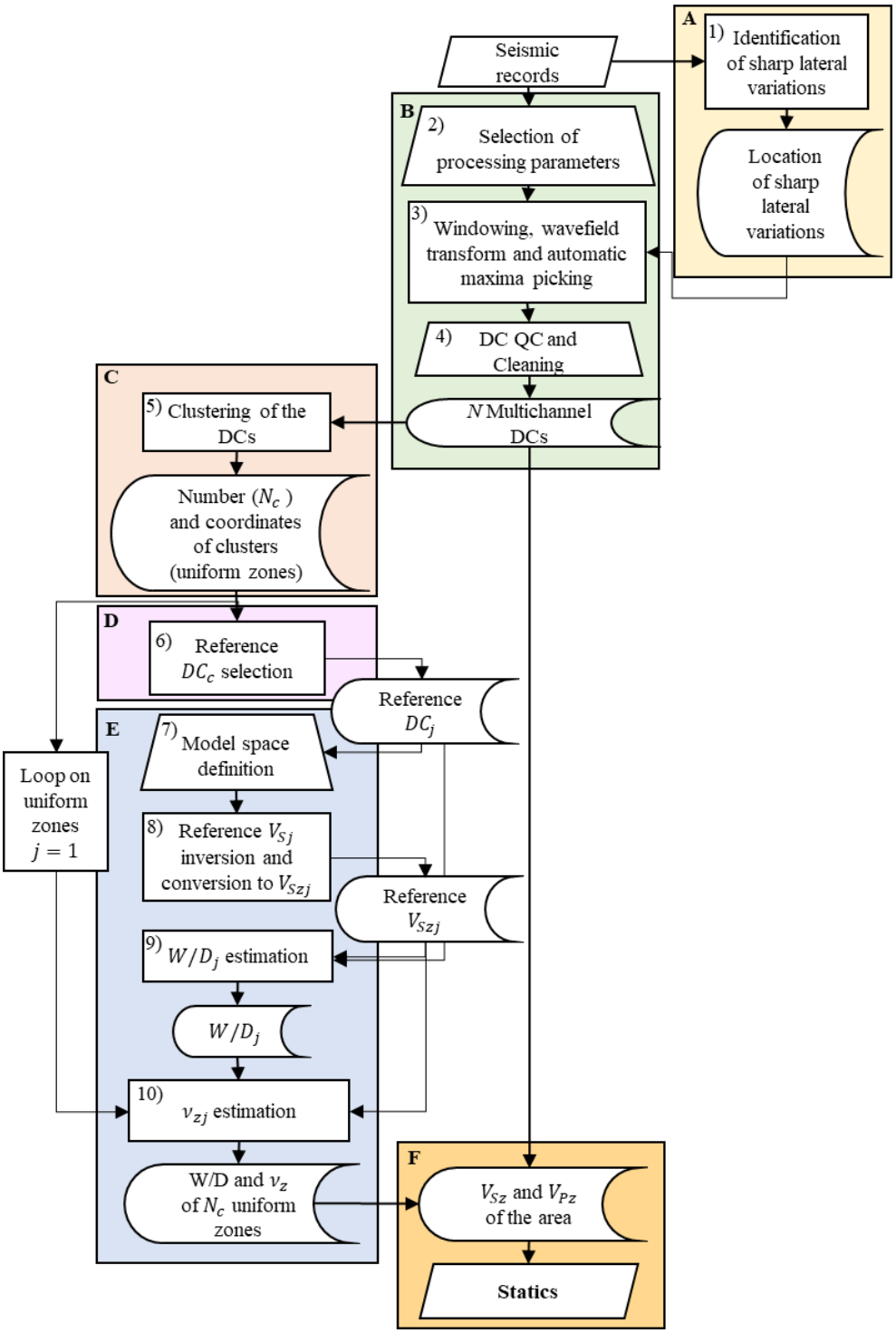

Figure 4.1: Scheme of the proposed SW direct statics estimation method.

A. Identification of sharp lateral variations

The first step of the workflow is the identification of possible sharp lateral variations and the estimation of their position (process #1), to avoid the extraction of DCs from windows which cross sharp discontinuities in the following step "B".

The key-concept behind the employed methods is that, regardless the inability of the existing SW modelling tools to describe them, sharp lateral variations affect significantly the propagation of SW. In particular, when SW, propagating parallel to the surface, encounter a subsurface target, back-reflections or trapping of their energy within the discontinuity might be caused. These phenomena, affect significantly the measured energy of the SW signal, causing local decays or amplifications at the position of the discontinuity. Therefore, SW energy can be regarded as an attribute of the recorded data, which is highly sensitive to the presence of sharp lateral variations in the near-surface and can be used to estimate their location.

Four methods based on the measurement of SW energy from multichannel seismic data are included in the workflow: the method of a) Energy, b) Decay exponent, c) Attenuation coefficient and d) Autospectrum. The methods have been originally introduced in the works of Nasseri-Moghaddam et al. (2005), Zerwer et al., (2005) and Bergamo & Socco (2014), and further optimized by Colombero et al. (2019). All methods are directly applicable to raw data, without the need of pre-processing or availability of *a priori* information on the subsurface structure.

The MATLAB codes used in this work have been implemented by Bergamo & Socco (2014) and by Colombero et al. (2019). They involve fast computations and are mostly automatic, apart from the selection of a limited number of processing parameters, necessary for the computation of the decay exponent and the attenuation coefficient, which is based on manual testing.

a) Energy

The computation of the energy of the seismic traces has been introduced as a technique for the detection of sharp lateral variations by Nasseri-Moghaddam et al. (2005). The energy of the traces is obtained for each receiver i of a shot gather as

$$E_i = \sum_f \left| A_{f,i} \right|^2 r_i \qquad 4.1,$$

where $A_{f,i}$ is the amplitude of the trace at frequency f and the factor r_i is the distance of the receiver, applied to compensate for the SW geometrical spreading.

Once the value of E_i of each trace has been retrieved, it is normalized to the maximum E_i of all traces. Following Colombero et al. (2019) the computation of 4.1 is repeated for all shots and the results for each receiver and each shot are stacked, normalized to the global maximum and visualized into an energy-distance ($E-r$) plot. This is done because, according to Colombero et al. (2019), stacking enhances the relative impact of the actual subsurface structure on the $E-r$ plot. If a localized target exists in the subsurface, the plot is expected to present sudden increases or decays, due to the back-reflections of the waves on the target's boundaries or the amplification of energy within the target. A search for such strong energy anomalies allows the estimation of the target's location.

b) Energy decay exponent

The decay exponent method has been introduced and implemented to multifold data by Bergamo & Socco (2014). It is based on the computation of the energy decay exponent (γ) of the recorded data, which can be defined as

$$\frac{E_{i+1}}{E_i} = \left(\frac{r_{i+1}}{r_i} \right)^{-\gamma} \quad (4.2),$$

where E_i and E_{i+1} are the values of energy of the traces i and $i+1$, respectively, and r_i and r_{i+1} are their distance from the shot. In a laterally homogeneous medium with no intrinsic attenuation, the value of γ corresponding to SW is equal to one, following the equation of geometrical spreading (Richart et al., 1970); compensating for the geometrical spreading, γ becomes zero. Strong deviations from this theoretical value can be associated with back-reflections of the waves and/or trapping of their energy caused by subsurface discontinuities and can be, therefore, indicative of their location.

In practice, after the value of E_i of all the traces has been obtained with eq. 4.1, a spatial window is applied and shifted along the seismic line. At each position, γ

is computed as the slope of the $E-r$ plot in bilogarithmic scale, according to (Bergamo & Socco, 2014):

$$\log\left(\frac{E_{i+1}}{E_i}\right) = -\gamma \log\left(\frac{r_{i+1}}{r_i}\right) \tag{4.3}.$$

The size of the window is a compromise between the S/N of the final computation and the lateral resolution. For each window, the values of γ from all available shots are averaged and the related standard deviation is computed for positive and negative offsets. If the plot of the resulting γ presents strong fluctuations, having higher magnitudes than the standard deviation and presenting opposite trends for positive and negative offsets, these can be associated with the location of subsurface discontinuities, which interfere in the propagation of waves and cause local attenuation or amplification of energy.

c) Attenuation coefficient

Bergamo & Socco (2014) proposed the use of the trace energy to estimate the attenuation coefficient α_f, which can also be used as an indicator of the location of sharp lateral variations. Compensating for the geometrical attenuation, α_f can be defined from

$$E_{f,i+1} = E_{f,i} e^{-2\alpha_f (r_{i+1} - r_i)} \tag{4.4},$$

where $E_{f,i+1}$ and $E_{f,i}$ are the values of energy recorded at each frequency f by two receivers, located at distances r_{i+1} and r_i from the shot, respectively. Its value is a measure of the attenuation of energy at different frequencies and offsets and is expected to present significant fluctuations in the presence of local subsurface discontinuities.

For the computation of α_f from multichannel data, Bergamo & Socco (2014) propose the application of a moving spatial window on the recorded gathers, in a similar manner as in the method of the energy decay exponent. The window is moved along the seismic line and, at each position, α_f is computed from the slope of the $E-r$ plot, considering natural logarithmic scale in E:

$$\ln\left(\frac{E_{f,i+1}}{E_{f,i}}\right) = -2\alpha_f\left(r_{i+1} - r_i\right) \tag{4.5}$$

The local slope at all i positions within the window is averaged, and the resulting mean attenuation coefficient of the window ($\overline{a_{f,w}}$) is normalized with respect to the global (along the whole line) average ($\overline{a_f}$) and to the related standard deviation ($std\left(\overline{a_f}\right)$):

$$\overline{\Delta a_{f,w}} = \frac{\overline{a_{f,w}} - \overline{a_f}}{std\left(\overline{a_f}\right)} \tag{4.6}$$

According to Colombero et al. (2019), this nosrmalization allows sudden variations of a_f to be highlighted, providing a robust estimation of the position and shape of subsurface targets.

Finally, if more than one shots are available, $\overline{\Delta\alpha_{f,w}}$ is computed for all the shots, following Colombero et al. (2019), the resulting absolute $\overline{\Delta\alpha_{f,w}}$ values are stacked to provide a single $\overline{\Delta\alpha_{f,w}}$ image, as a function of offset and frequency.

d) Autospectrum

The method has been introduced by Zerwer et al. (2005) and is based on the measurement of the autospectral density G_i of the seismic traces at each receiver position i, which can be obtained as the sum of the squares of the real and imaginary parts of the discrete Fourier transform of each trace, Y_i, according to

$$G_i(f) = \left\{\mathrm{Re}\left[Y_i(f)\right]\right\}^2 + \left\{\mathrm{Im}\left[Y_i(f)\right]\right\}^2 \tag{4.7}$$

The plot of G_i is an alternative way to visualize the energy content of the seismograms as a function of offset, which provides information also on its frequency (or wavelength) distribution. Similar to the previous methods, if more than one shots exist, the G_i of all the shots can be summed, to enhance the S/N. If a subsurface target is present along the seismic line, the G_i plot is expected to

exhibit sudden accumulations or decays at the target's position and only within the frequency bands affected by it. This, apart from the location of the targets, provides a qualitative imaging of the shape and depth extent of the anomaly, since the penetration depth of SW is proportional to their wavelength.

B. Extraction of the dispersion curves

Once the location of the sharp lateral variation has been estimated, a set of DCs along the investigated area is extracted. We adopt the method and corresponding MATLAB code of Socco et al. (2009), which allows the retrieval of a set of local DCs, by applying a moving spatial window on the traces.

First, the necessary processing parameters (the window length, the minimum and maximum source-receiver offset and the step of the moving window) are chosen by the user (process #2), on the basis of tests on sample shot records. An optional user-defined parameter, used as input to the method, is a "mask", outlining the spectral region where the energy maxima corresponding to the DC lie. The "mask" ensures that during the following automatic DC picking (process #3), only the spectral region of interest is used for the extraction of the DCs.

Based on these parameters, the entire dataset undergoes a fully automatic DC picking (process #3). For each window position and each shot (within the selected offset range), a wavefield transform is applied on the windowed data, and the maxima of the spectrum corresponding to each shot (further individual DC), inside the pre-defined "mask", are picked and saved. To account for possible irregularities in the data geometry, all the computations were carried out in the $f-v$ domain (see Section 2.3.4 for details).

The spectral computation is repeated for all the shots, within the selected offset range, and the resulting spectra are stacked, to increase the S/N. The maxima of the stacked spectrum provide the stacked DC corresponding to the specific window, while its assigned position is the centre of the spatial window.

To improve the quality of the DCs, once all the curves have been estimated, an optional manual quality control is performed and, if necessary, parts of the picked DCs, which do not correspond to SW, are deleted (process # 4). Although manual, this step has been implemented into an efficient procedure, requiring minimal user intervention, involving a selection of the undesirable parts of the DC directly on the

spectral image. Given the low number and high quality of the DCs typically resulting from multichannel processing (see Section 2.3.5), process # 4 is expected to be a fast and straightforward step.

Finally, a set of N stacked DCs (and N subsets of individual DCs) is retrieved, each one located at the centre of the window used for its estimation.

C. Clustering of the dispersion curves

A clustering algorithm is applied to the estimated DCs, to divide them into sets of curves which present uniform distributions of the phase velocities (process # 5). This allows stage "E", where the W/D and ν_z are estimated for the site, to be performed only for a reference DC from each cluster (Socco et al., 2017), and reduce the time and computational costs of the workflow. Alternatively, process # 5 can be avoided and stage "E" can be performed for the total of N DCs, output from stage "B".

The clustering method adopted here has been proposed by Khosro Anjom et al. (2017). It is a hierarchical clustering algorithm which does not require any *a priori* information on the number of clusters (uniform zones) and their location. The definition of the clusters is based on the dissimilarity of the DCs, measured as the Euclidean distance between the phase velocities at each frequency, within the common frequency band of all the DCs. As a linkage criterion between the DCs of the clusters, the average distance of each component of a cluster with respect to the distance of each component of all the other clusters is used. The algorithm outputs a dendrogram, indicating the number (N_c) of the clusters (uniform zones) and the DCs allocated to each one of them.

D. Reference curve selection

For the estimation of the W/D, the necessary inputs are a single DC from each cluster (considered as a reference DC) and its corresponding V_{Sz} model.

Socco et al. (2017) have shown that the estimation of the W/D of a cluster is stable and rather independent on the choice of the reference DC. In particular, they have proven that the impact of the reference DC selection on the final time-average velocity estimate of the entire cluster (stage "F") is low (2 % –10 %), even at sites where V_S varies laterally (up to 150 %).

For optimal results, an automatic *QC* method (Karimpour, 2018) is applied to allow the highest-quality DC to be used as reference. For each DC, the method computes the following quality index (*QI*):

$$QI = 1 - \frac{(NSD + ND_{PN} + NFB)}{\max(NSD + ND_{PN} + NFB)} \quad (4.8),$$

where NSD is the standard deviation of each DC, with respect to the DCs of the individual shots used for spectral stacking, summed for all frequency components and normalized to the maximum standard deviation; $NDPN$ is the difference of the average DCs extracted from positive- and negative-offset shots, summed for each frequency and normalized to the maximum difference and NFB is the reciprocal of the frequency band (FB) of each DC, normalized to the maximum FB of all the DCs. The DC having the maximum QI is selected as reference for each cluster j.

Reference Monte Carlo V_S inversion, reference V_{Sz}, W/D and ν_z estimation

The second input to the W/D computation is a V_{Sz} model associated to the DC. Any reliable information on the V_{Sz} distribution, such as logging information or borehole measurements, can be used as input. Alternatively, V_{Sz} can be obtained directly from the data, by inverting the reference DC_j of each cluster to estimate a 1D V_S profile at the position of the curve.

For the inversion, we use the Monte Carlo algorithm of Socco & Boiero (2008), which is an efficient global-search inversion method that performs an optimized random sampling of the model parameter space, based on the scale properties of the DCs. The layer V_S, h and ν are randomly sampled over a user-defined model space, and the layer ρ is assumed constant (process # 7). The synthetic DCs, corresponding to the generated models, are computed based on the Haskell and Thompson forward modeling (Thomson, 1950; Haskell, 1953) and the best-fitting V_S model is retrieved based on a statistical Fisher test (process # 8). The inverted V_S model is then transformed into V_{Sz} according to

$$V_{Sz} = \frac{\sum_n h_i}{\sum_n \frac{h_i}{V_{Si}}} \quad (4.9),$$

where h_i is the thickness and V_{Si} is the S-wave velocity of the i-th layer, while n is the number of layers down to the depth (z) of the profile.

Once both the reference DC_j of each cluster j and its corresponding V_{Sz_j} model have been retrieved, the experimental W/D is estimated (process # 9) following Socco et al. (2017): an automatic search tool, compares the V_{Sz} and the DC (in the domain of wavelength and phase velocity), identifying couples of wavelength and depth, for which the phase velocity is equal to the V_{Sz}. The couples are interpolated with a polynomial fit, resulting in a continuous relationship of the wavelength and depth, the W/D relationship.

Once the W/D_j of the cluster has been retrieved, the estimation of the corresponding ν_{z_j} is achieved by means of an automatic sensitivity analysis (process # 10). Using the reference V_{S_j} model of each cluster and trial values of ν, a set of synthetic DCs is retrieved by means of forward modelling. These are used, together with the reference V_{Sz_j} model, to compute a set of simulated W/D curves, each one corresponding to a different value of ν. An automatic comparison of the simulated W/D curves with the experimental one is performed, and value of ν is retrieved as the ν of the synthetic W/D that matches the experimental W/D. This process is repeated for all depth values of the experimental W/D, leading to the estimation of the ν_{z_j} profile of the cluster.

E. Wavelength–depth transformation, time-average S-wave and P-wave velocity and statics estimation

The W/D_j relationship of each cluster is used to transform all the DCs of the cluster into V_{Sz} with a simple transformation of the coordinates of the DC. In particular, the wavelength components of each DC are converted into depth values, based on the cluster's W/D_j, and the phase velocities are set equal to V_{Sz}. This process results in a set of N 1D V_{Sz} profiles, located at the same positions as the DCs.

Subsequently, the estimated ν_{z_j} of each cluster is used to convert the estimated V_{Sz} profiles belonging to the cluster into V_{Pz}, following Socco & Comina (2017):

$$V_{Pz} = V_{Sz}\sqrt{\frac{2\nu_z - 2}{2\nu_z - 1}} \tag{4.10}.$$

Finally, the computation of the one-way time (static shift) at the selected (floating) datum plan z_d is carried out using the values of each 1D V_{Pz} profile, resulting from eq. 4.10, at z_d :

$$t_d = \frac{z_d}{V_{Pz=z_d}} \tag{4.11},$$

where t_d is the one-way time at datum depth z_d . To obtain the source and receiver statics, the one-way times are interpolated at the source and receiver positions, respectively.

4.3 Case study 1: Seismic line from the Ludvika mining site, Sweden (2016)

We present the application of the direct statics estimation method on the portion of the seismic line of Ludvika (2016), shown in green in Figure 3.3a. All the computations of the workflow were performed by a standard single-core commercial laptop.

4.3.1 Workflow application and results

Figure 4.2 illustrates the results of the sharp lateral variation detection methods. The plot of the normalized E, stacked for all the shots, is given in Figure 4.2a. After testing windows with length between 10 m and 70 m, the decay exponent and attenuation coefficient were computed using a window of 55 m. The plot of γ, stacked for all the negative-offset shots (γ_{neg}, blue) and for all positive-offset shots (γ_{pos}, red) is shown Figure 4.2b, where the error bars denote the corresponding standard deviation. The plot of $\overline{\Delta\alpha_{f,w}}$ as a function of frequency and distance is given in Figure 4.2c. Finally, the autospectrum method, applied to the individual traces of each gather, provided the stacked normalized G plot of Figure 4.2d.

The results of the four methods were examined together, to identify the most critical zones, indicating possible presence of sharp lateral variations.

Two, particularly strong, localized anomalies were identified by all the methods, and are marked by the black lines labelled as "2" and "3" in Figure 4.2. Between them, the plots of E and G present a strong peak, indicating the possible presence of a local target. At its boundaries, γ_{pos} and γ_{neg} (Figure 4.2b) show prominent peaks, while the plot of $\overline{\Delta\alpha_{f,w}}$ (Figure 4.2c) presents sharp increases. Such a pattern can be associated with the presence of sudden changes in the subsurface due to localized targets (e.g., fractured zones, changes in lithology and man-made structures), and therefore, their positions (Table 4.1) were stored, to be excluded from the extraction of the DCs.

The same pattern can be recognized in the plots of γ and $\overline{\Delta\alpha_{f,w}}$, at additional locations, labelled as "4" - "8" in Figures 4.2b and 4.2c, which are not associated with any significant variation in the plots of E and G. Nevertheless, due to the strong signature and correspondence on the plots of γ and $\overline{\Delta\alpha_{f,w}}$, their locations were considered reliable and were also stored for further use.

Since these anomalies affect low frequencies (mostly < 40 Hz), they are probably related to deep subsurface structures. Considering that a water stream crosses the line at between the locations "2"-"5" (Figure 3.1a), we can conclude that these anomalies are all probably related to the fracture-system of the river. The area between lines "6" and "7", due to its longer lateral extent, could be related to shallow fracturing of the rock. The energy anomaly of line "8" presents a narrower separation between γ_{pos} and γ_{neg}, with respect to all the other black lines, and the plot of $\overline{\Delta\alpha_{f,w}}$ presents a peak only at high frequencies (> 30 Hz), meaning that the heterogeneity is shallow. A possible cause can be the local reduction of the bedrock depth, creating a velocity contrast at shallow depths.

Coherent in the results of all methods appear the larger-scale anomalies, indicated by the green and orange boxes in all panels of Figure 4.2. The green box marks an area 316 m long, where the plot of E (Figure 4.2a) presents continuous peaks, terminating at the location labelled as "1" in Figure 4.2a. In the same area, the plot of γ_{pos} (red Figure 4.2b) presents constant fluctuations, while γ_{neg} (blue

Figure 4.2b) preserves positive values, indicating strong energy attenuation. Inside the green box, the plots of $\overline{\Delta\alpha_{f,w}}$ (Figure 4.2c) and G (Figure 4.2d) show strong and almost continuous anomalies.

Similarly, the orange box in all panels of Figure 4.2 depicts an area where all the methods presented significant and continuous abnormalities.

Due to their long lateral extent, both these anomalies are probably related to large-scale geological features. A comparison with the total-field aeromagnetic data map of Figure 3.2 reveals that at the NW and SE ends, the selected portion of the seismic line intersects two magnetic lineaments, which correspond to oxide-bearing formations, in the positions shown by the yellow circles in Figure 3.2. Hence, we can assume that the energy anomalies are related to the shallow expression (highly fractured zones) of deeper iron-oxide bodies.

Due to their consistency in all plots of Figure 4.2, the boundaries of the two boxes, labelled as “1” and “9”, were stored, to be omitted from the DC extraction.

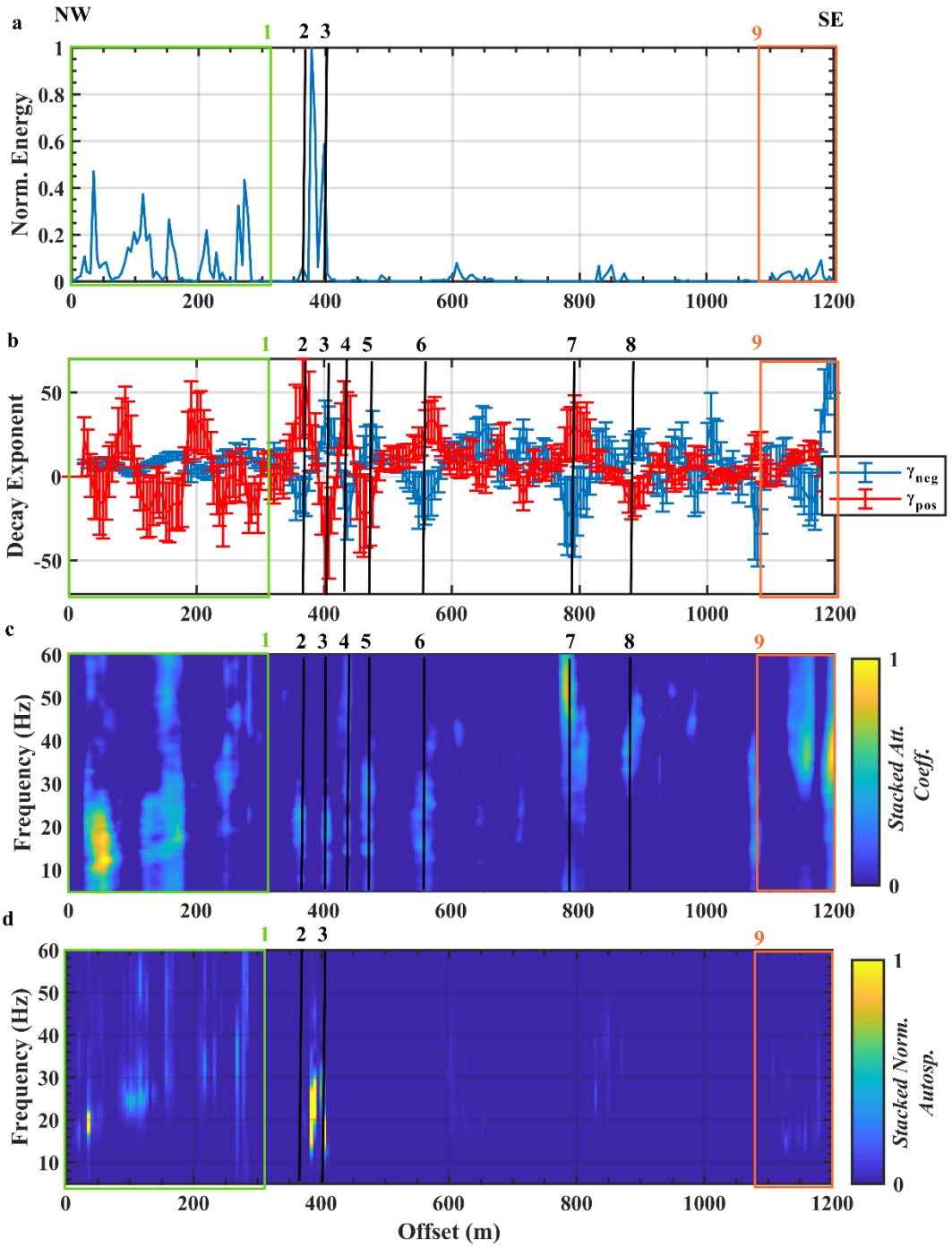

Figure 4.2: Sharp lateral variation detection on the Ludvika 2016 dataset. Plot of the a) stacked normalized energy, b) average decay exponent for positive-offset (blue) and negative-offset traces (red), c) stacked normalized attenuation coefficient and d) stacked normalized autospectrum. The error bars in panel (c) indicate the standard deviation. The estimated positions of the sharp lateral variations are labelled as "1"- "9" and are listed in Table 4.1.

Table 4.1: *Locations of the sharp lateral variations estimated for the processed portion of the Ludvika 2016 seismic line.*

Sharp lateral variation	Position on the seismic line (m)
1	316
2	366
3	407
4	436
5	461
6	567
7	792
8	881
9	1074

The sample shot records, used to test the optimal processing parameters, were randomly chosen from three different areas along the line, located between 0–365 m, 568–791 m and 882–1073 m, to avoid the effect of lateral variations. The parameters that provided the optimal results and were chosen for the DC extraction are presented in Table 4.2.

An example stacked $f-v$ spectrum, computed from the receiver window centred at 1190 m, is plotted in Figure 4.3a. The spectral "mask", manually drawn by the operator around the spectral maxima and automatically applied on the entire dataset, is depicted in black in Figure 4.3b. The automatically picked DC before the manual cleaning is plotted in grey in Figures 4.3c and 4.3d, and the cleaned DC, which was the final output of this step, is plotted in black in Figure 4.3d.

Table 4.2: *Windowing parameters for the DC extraction*

Processing parameter	Value
Window size	75 m
Step	15 m
Minimum offset	10 m
Maximum offset	300 m

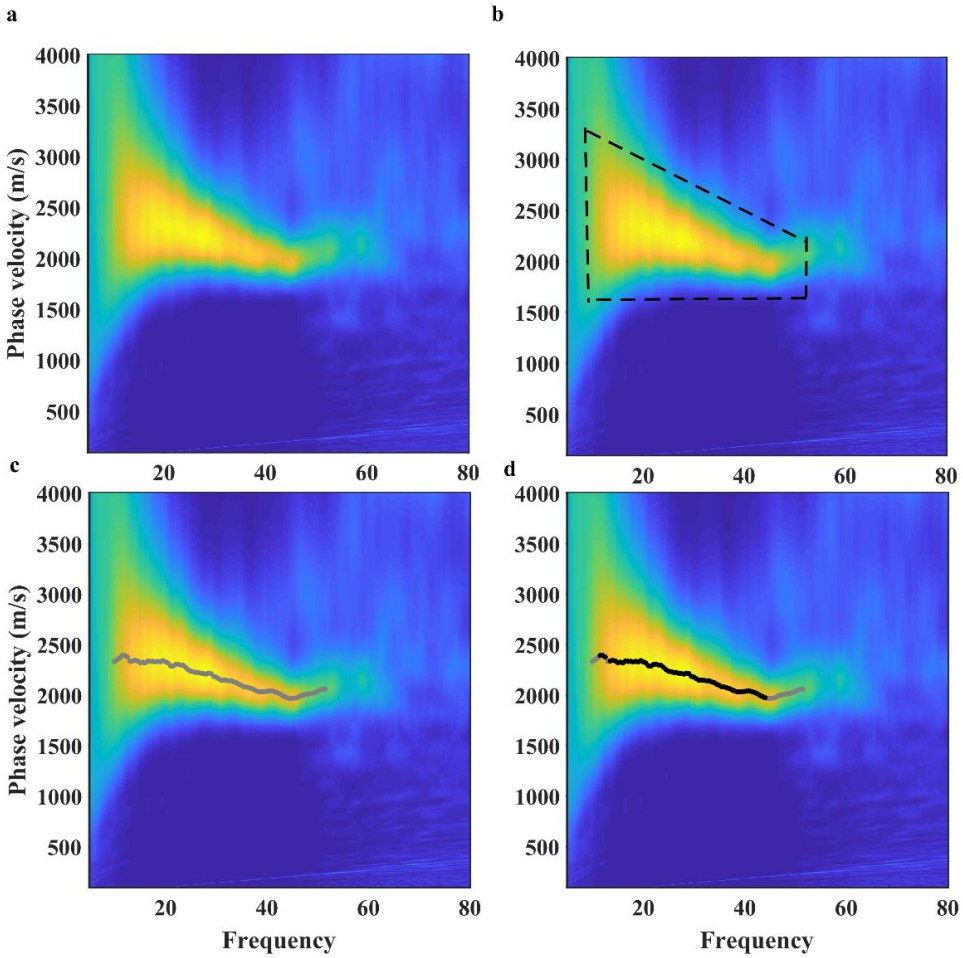

Figure 4.3: Example a) stacked $f-v$ spectrum, with b) the user-defined spectral "mask" (dashed). c) In grey, the automatically picked spectral maxima and, d) in black, the picked DC after cleaning.

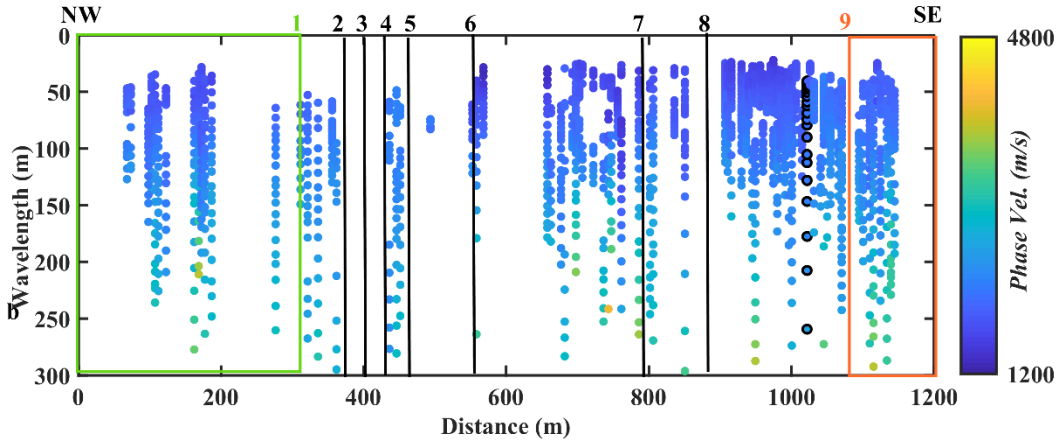

Figure 4.4: Multichannel DCs picked from the Ludvika 2016 dataset. The vertical axis represents the wavelength. The colour scale provides the phase velocity, given by the colour bar. The reference DC is highlighted in black. The estimated positions of the sharp lateral variations are labelled as "1"- "9".

Repeating the same operation for all window positions, except those in Table 4.1, a set of 80 DCs were automatically extracted along the line. In Figure 4.4, the DCs are plotted as a pseudo-section, in the wavelength-phase velocity domain: each DC is plotted at the location corresponding to the centre of the window, and the vertical axis represents the wavelength. The phase velocity is given by the colour scale.

Observation of the pseudo-section of Figure 4.4 shows that the spatial distribution of the DCs varies significantly along the line, and there exist several gaps. Some of them correspond to the positions of the sharp lateral variations (Table 4.1), and the rest are positions where the spectra did not present clear maxima and, therefore, no DC could be picked.

In Figure 4.5a, the DCs are plotted in the frequency–phase velocity domain. The DCs are all concentrated in one frequency and phase–velocity region, with no obvious separation in different groups and the variability of the phase velocity (indicative of the lateral variability of V_S) is, at maximum, 80% (Figure 4.5b). Their clustering (Figure 4.5c), did not present any separation in groups and, therefore, it was decided to consider only one reference DC.

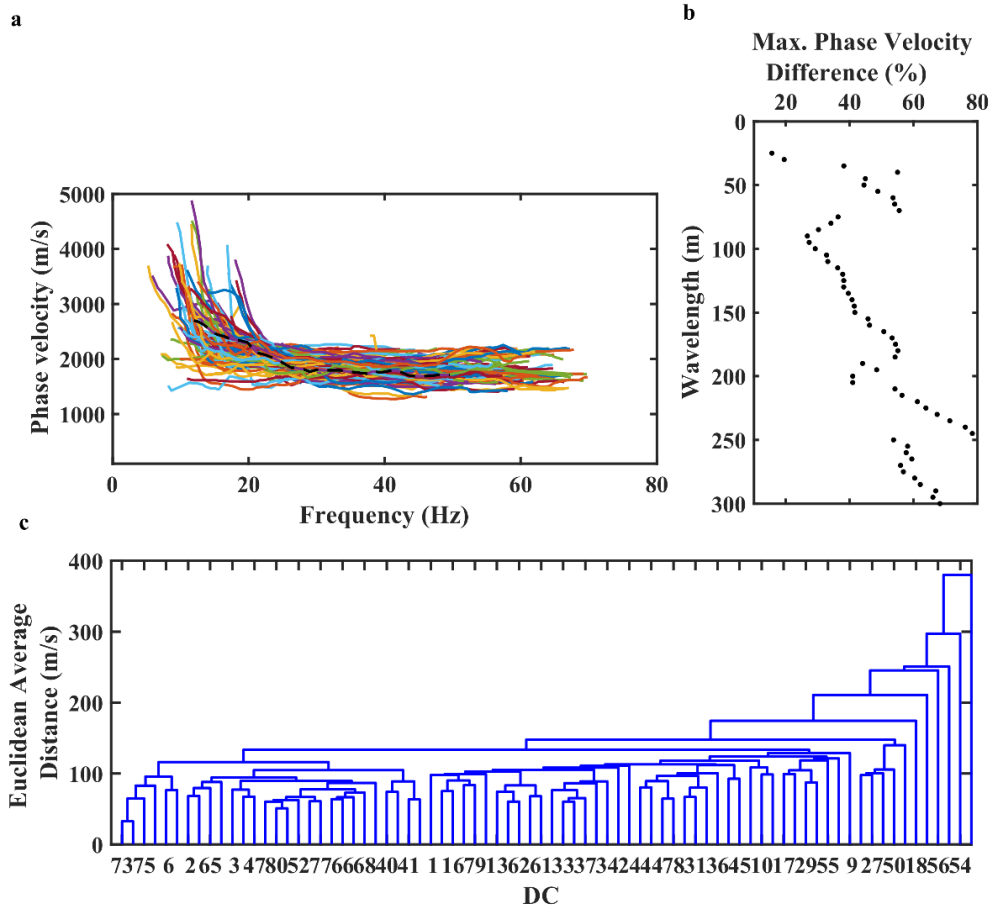

Figure 4.5: a) The multichannel DCs. Different colours correspond to different positions and dashed black to the reference DC (located at 1022 m). b) Maximum phase velocity variability at each wavelength of all the extracted DCs. c) Result of the DC clustering.

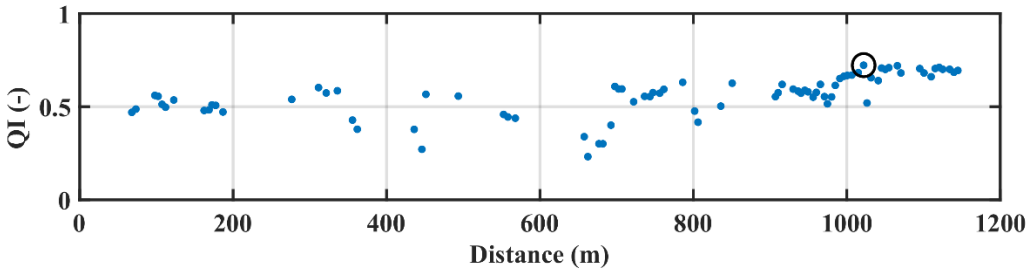

Figure 4.6: Quality index (*QI*) of the extracted DCs. The highest *QI* value is circled in black.

For the reference DC selection, the *QI* was computed according to eq. 4.8, for each DC and the results are plotted against the DC position in Figure 4.6. The DC with the highest *QI* was the one at position 1022 m (circled in Figure 4.6, black in Figure 4.4 and black dashed in Figure 4.5a), and it was the one chosen as reference.

For the Monte Carlo inversion of the reference DC, one million profiles were randomly generated simulating a three-layered model (two layers plus half space). The layer thickness and V_S were randomly sampled, within the model space boundaries, plotted in Figure 4.7a (dashed blue). The value of ρ was fixed at 2000 kg/m^3 for the shallow layers and 2800 kg/m^3 for the half space. The value of ν for all the layers was randomly sampled from a wide range (0.1 – 0.45), which is reasonable for typical near-surface materials (e.g. Gercek, 2007).

In Figure 4.7a, the accepted models are presented in a colour scale that indicates the misfit between their synthetic DCs and the experimental DC. The DCs of the best-fitting models are presented in Figure 4.7b (using the same colour scale) and are compared with the experimental one (black dots).

Using eq. 4.9, the best-fitting model (red in Figures 4.7a and 4.8a) was transformed into the V_{Sz} model shown in black in Figure 4.8a. The V_{Sz} model was then compared with the reference DC (black dots in Figure 4.8a) to obtain the W/D relationship, which is plotted in Figure 4.8b.

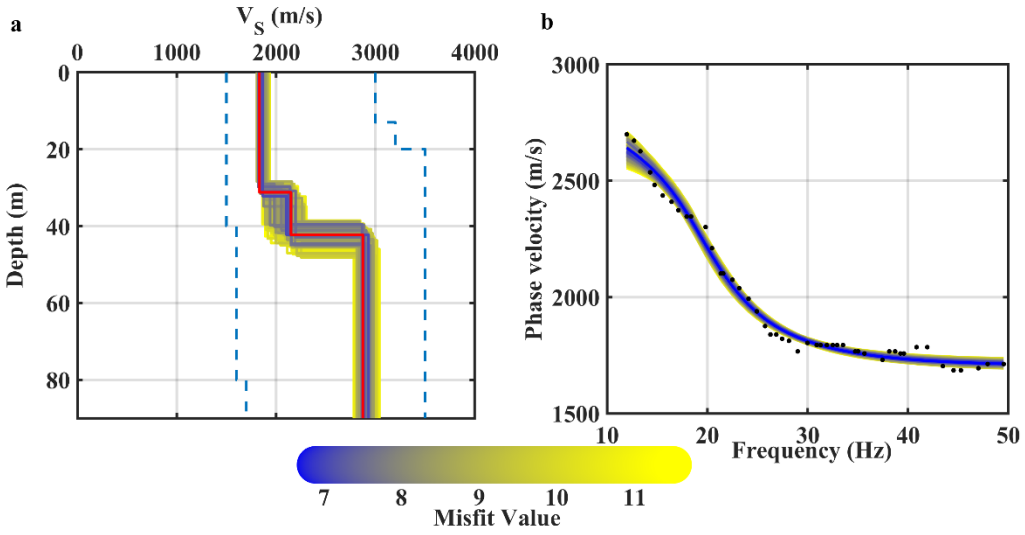

Figure 4.7: Monte Carlo inversion results. a) Best-fitting models. In red, the reference V_S profile, and in dashed blue, the model parameter space. b) Synthetic DCs of the best-fitting models compared with the experimental DC (black points). The colour scale indicates the misfit and is given by the colour bar.

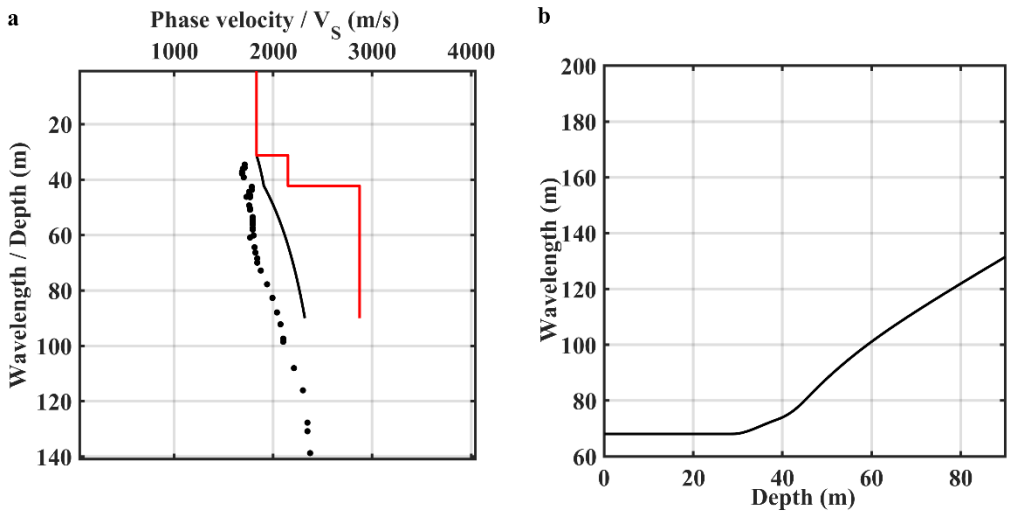

Figure 4.8: a) Reference 1D V_S model (red), reference V_{Sz} model (black line) and reference DC (black dots). b) Experimental W/D curve.

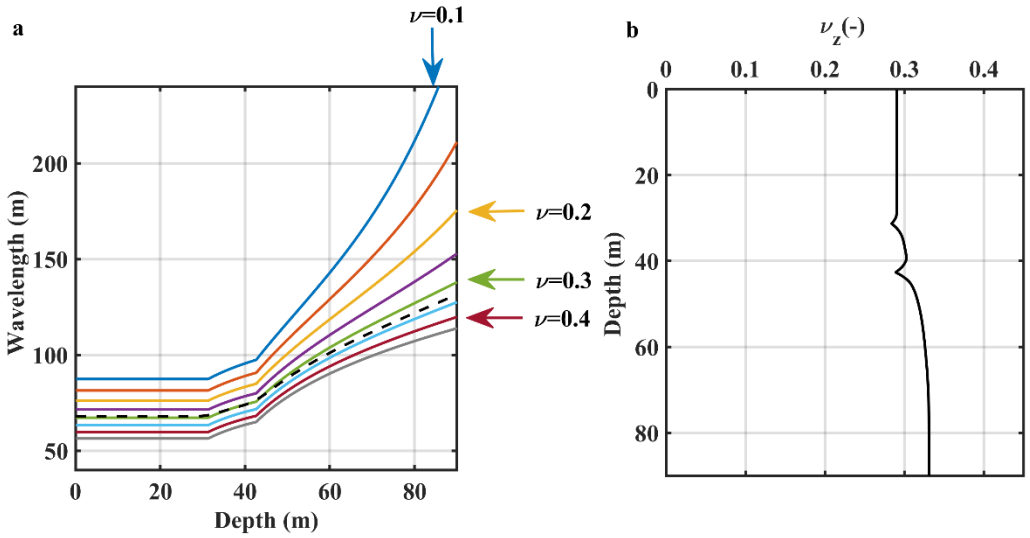

Figure 4.9: a) Experimental (black dashed) and synthetic W/D curves (different colours, depending on ν). b) Estimated ν_z.

Figure 4.9a reports the sensitivity analysis performed to retrieve ν_z: using the V_S profile of Figure 4.8a (red), a set of synthetic W/D relationships (different colours in Figure 4.9a) were computed, changing the value of ν from 0.1 to 0.45 with a step of 0.05. Comparison of the synthetic W/D curves with the experimental one (black dashed in Figure 4.9a) led to the estimation of the ν_z profile, plotted in Figure 4.9b. Its value cannot be directly compared with local log measurements,

since it is a smooth profile. Nevertheless, it lies within reasonable values, according to Maries et al. (2017).

The W/D relationship of the reference DC was used to transform all the other DCs into V_{Sz}. The resulting 1D V_{Sz} profiles are plotted in Figure 4.10a, at the positions of their corresponding DCs. The vertical axis represents the depth and the value of V_{Sz} is given by the colour scale, while the depth of each profile depends on the wavelength of its corresponding DC. It can be observed that the estimated values (between 1400 m/s and 2500 m/s) suggest the presence of near-surface materials of high V_S and are in agreement with the geological information on the site (Maries et al., 2017).

The V_{Pz} model, estimated from the V_{Sz} 1D profiles (Figure 4.10a) at each position and the ν_z (Figure 4.9b) according to eq. 4.10, is plotted in Figure 4.10b. Figure 4.11 reports the estimated one-way traveltime (static shift), computed with eq. 4.11. for different datum depths, down to the investigation depth of the V_{Pz} model of Figure 4.10b (90 m).

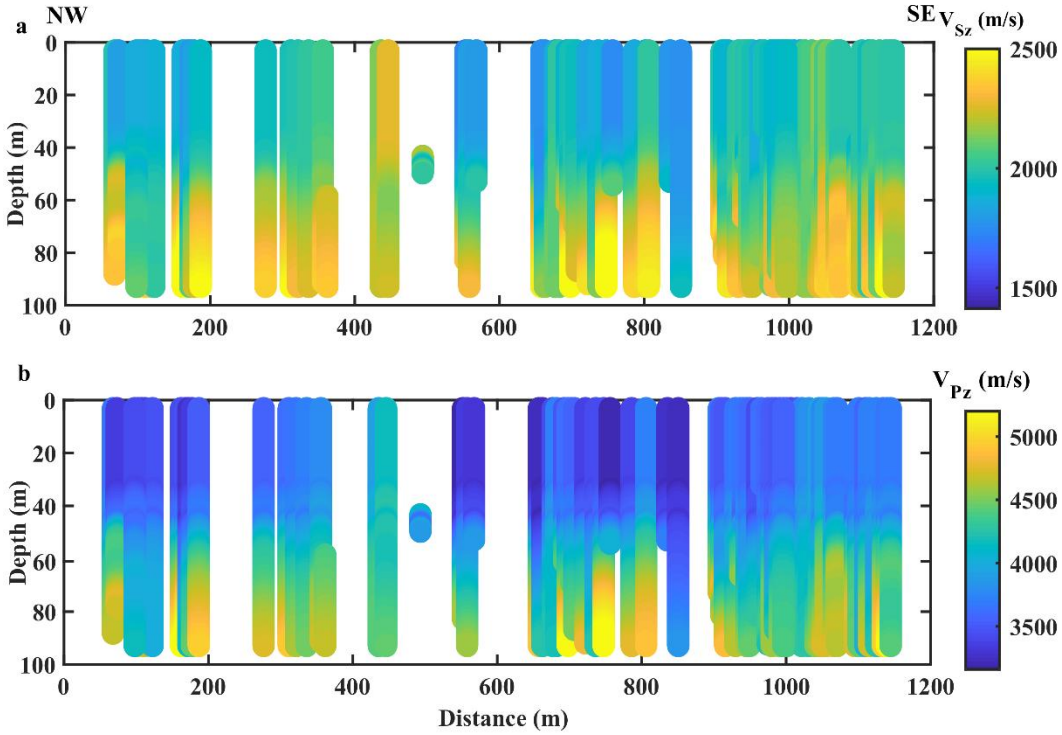

Figure 4.10: Pseudo-2D a) V_{Sz} and b) V_{Pz} model. The thickness of the 1D profiles is illustrative.

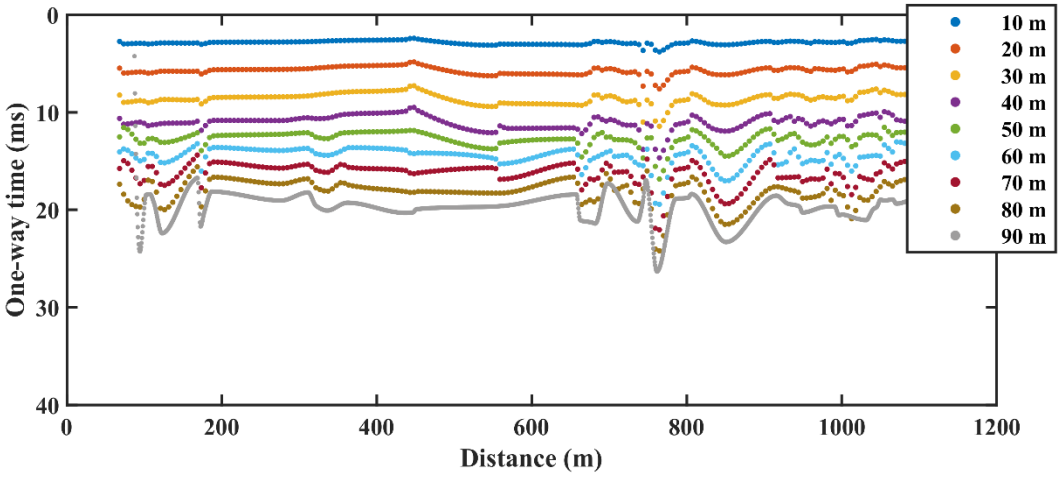

Figure 4.11: One-way time (static shift) at various datum depths (indicated in different colours).

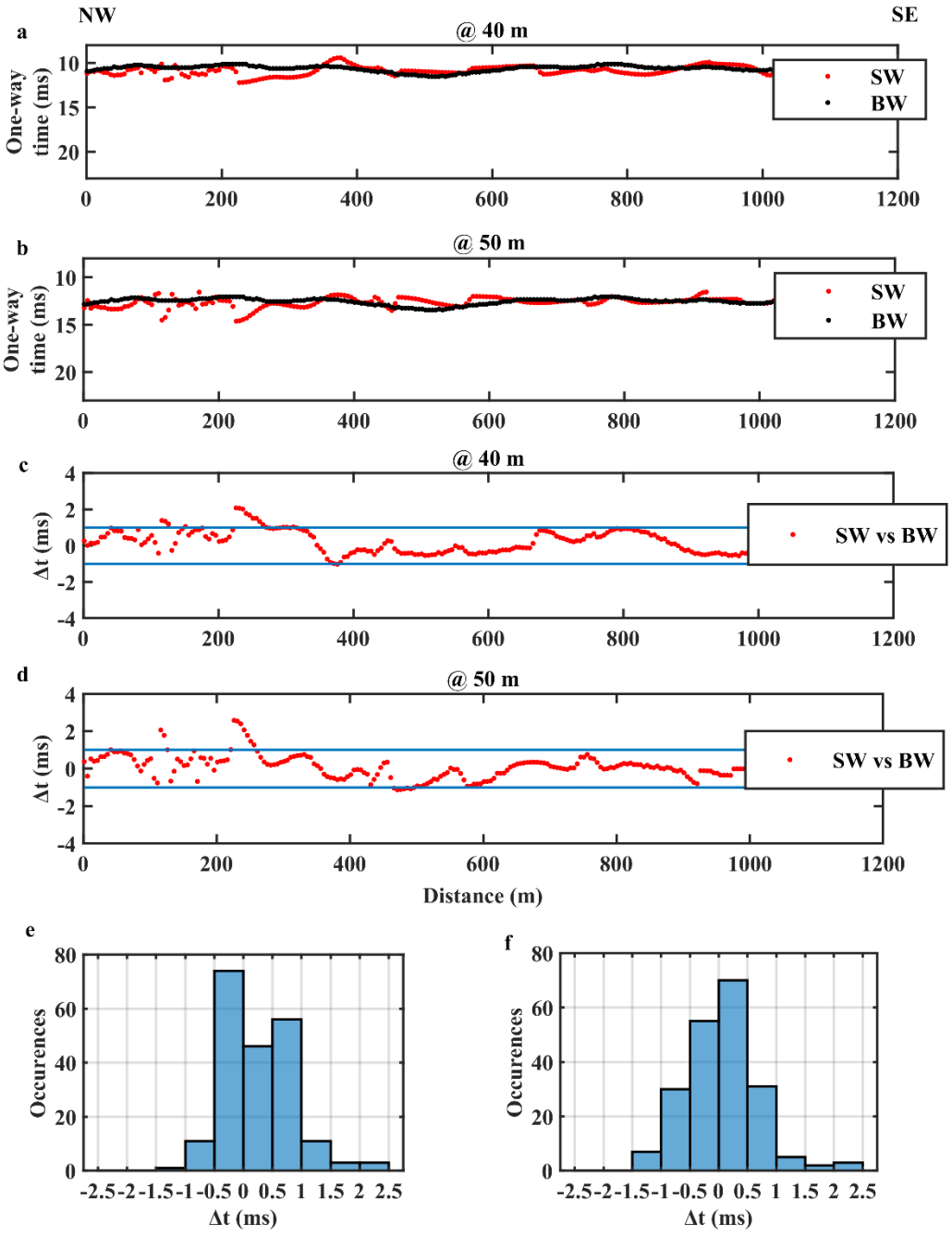

Figure 4.11: One-way time (static shift) at a datum depth of a) 40 m and b) 50 m. In red, the SW direct statics and in black, the BW tomostatics (Bräunig et al., 2020). One-way time difference between SW direct statics and BW tomostatics at a datum depth of c) 40 m and d) 50 m. Distribution of the one-way time difference (Δt) between the SW direct statics and BW tomostatics at a datum depth of e) 40 m and f) 50 m. The sum of occurrences in (e) and (f) is 205.

Evidently, the lateral resolution of our estimated statics depends on length of the spatial window used for the DC extraction (75 m). To evaluate the quality of

the result, we compare the retrieved statics with the ones retrieved by a standard BW tomography by Bräunig et al. (2020) for the same dataset. Being an accepted method for near-surface V_P estimation, BW tomography serves as a benchmark.

The statics are compared at two datum plans (40 m, shown in Figure 4.11a and 50 m, shown in Figure 4.11b), which were chosen as examples, because they are deeper than the known depth to the bedrock. The SW direct statics are shown in red and the ones resulting from BW tomography are shown in black. Their difference at the two datum depths, is plotted in Figures 4.11c and 4.11d, respectively, where in blue we define the interval of ± 1 ms (equal to the *SR*), within which the difference is considered negligible. According to the histogram of Figure 4.11e, 7.8% of the measurements present a difference that is out of the range of ± 1 ms for the computation at 40 m datum, while for the 50 m datum, 8.29% are out of ± 1 ms range (Figure 4.11f). The comparison confirms that the direct SW statics estimation presents a low error with respect to the benchmark.

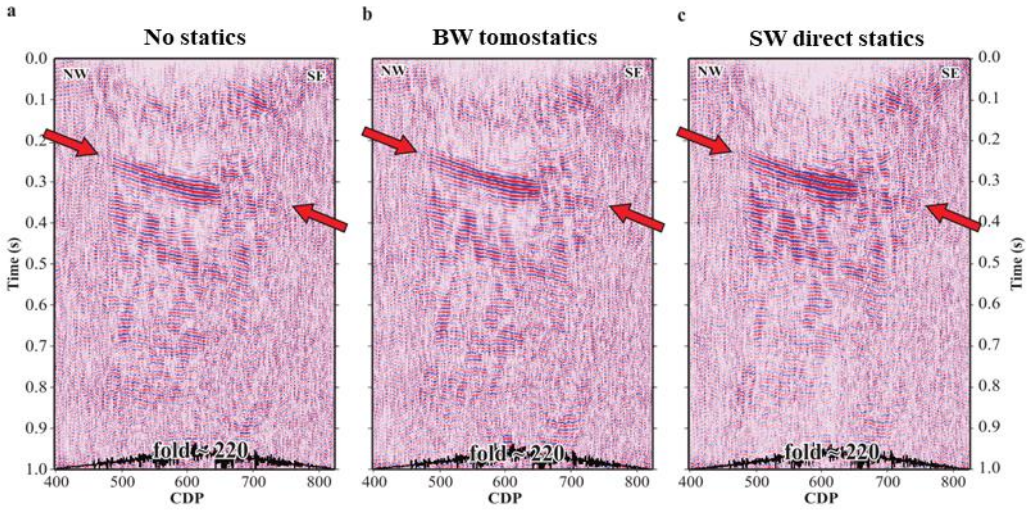

Figure 4.12: Brute stack a) before any statics, b) after application of P-wave traveltime tomostatics and c) after application of SW direct statics. The red arrows indicate a strong reflector.

Figure 4.12a presents the stacked section before any statics. The resulting brute stacks, after the application of the BW tomostatics and the SW direct statics at 40 m datum, are shown in Figures 4.12c and 4.12d, respectively. It can be observed that the SW direct statics resulted in an improved coherency of the reflector (indicated by the red arrows) with respect to the section with no statics, and similar quality with respect to the BW tomostatics.

This comparison shows that the proposed SW-based workflow can provide statics which are of similar quality with the ones achieved by a method routinely used in seismic exploration. Therefore, it can be regarded as a valid alternative to estimate the statics, which is completely independent from BW data and, therefore, can be useful when obtaining BW is less effective (e.g. when first-break traveltimes cannot be easily picked due to noise).

Table 4.4: *Breakdown of the time requirements of the SW direct statics estimation for the processed portion of the Ludvika 2016 dataset.*

Workflow stage	Automation level	Time
A. Identification of sharp lateral variations	Automatic, only a manual selection of window length for γ and α computation	10 min
B. Extraction of the dispersion curves		
• Selection of processing parameters	Manual	20 min
• Windowing, wavefield transform and automatic maxima picking	Automatic	10 min
• DC *QC* and cleaning	Manual	10 min
C. Clustering of the dispersion curves	Automatic	<1 min
D. Reference curve selection and Monte Carlo inversion, reference, W/D and estimation		
• Reference DC selection	Automatic	<1 min
• Model space definition	Manual	<1 min
• Reference V_S inversion and conversion to V_{Sz}	Automatic	~120 min
• W/D estimation	Automatic	< 1 min
• ν_z estimation	Automatic	< 1min
E. Wavelength–depth transformation, V_{Sz}, V_{Pz} and statics estimation	Automatic	2 min
		Total: ~175 min

The time requirements and automation level of the different stages of the workflow for this dataset are listed in Table 4.4. In total, from raw data to statics delivery, the workflow required approximately 175 min to run on a standard

commercial laptop from which, only a limited fraction (< 35 min) required the work of an operator. Compared to the conventional method (BW tomostatics), which requires a long and highly operator-dependent stage of first-break picking and the computationally demanding first-break tomography, the proposed statics estimation is considerably faster. Moreover, it is faster than most typical SW methods, since most of the processes (estimation of the W/D relationship and the ν_z, transformation of all the DCs into V_{Sz} and V_{Pz}, computation of statics) are automatized and based only on data transforms, requiring very little computational effort. The methods for the detection of sharp lateral variations and the process for the extraction of the DCs are completely automatic, except for some preliminary tests required for processing parameter selection, and an optional manual cleaning of the DCs. The only computationally demanding, but completely automatic, task is the inversion of the reference DC, which required 2 hours to run on a commercial laptop.

4.4 Case study 2: Seismic line SM1 from the Siilinjärvi mining site, Finland (2018)

We present the application of the method to the active 2D seismic dataset of line SM1 from the Siilinjärvi mining site in Finland (Section 3.3.3). According to our *a priori* knowledge on the site, the near-surface is expected to be highly variable, since intense lithological variability has been mapped at the location of line SM1 (Figure 2.10). Specifically, it is known that towards the south of the main mine pit, where line SM1 is located, shallow intrusions of vertical and sub-vertical diabase dykes are present within the mineralization, while the work of Kauti et al. (2019) has shown that also horizontal dykes are present within the ore body.

4.4.1 Workflow application and results

The results of the sharp lateral variation detection step of the workflow are presented in Figure 4.13. Figure 4.13a, shows the resulting stacked and normalized E. The results of the decay exponent and the attenuation coefficient methods, for a window length of 100 m, are shown in Figures 4.13b and 4.13c, respectively, while Figure 4.13d presents the stacked normalized G. We note that the colour

scale of Figures 4.13c and 4.14d is exaggerated, to enhance the visualization of the results.

All methods indicated the presence of sharp lateral variations, since abrupt changes in the measured quantities can be depicted in all the plots of Figure 4.13. Their appearance, though, lacks coherency among the different methods and their identification, particularly in the plots of $\overline{\Delta\alpha_{f,w}}$ and G, is highly ambiguous, due to their low contrast with respect to the background values. Nevertheless, simultaneous examination of all the results allowed the detection of some interesting features that could be reliably associated with local subsurface targets. In particular, the plots of E and G present large-scale anomalies at the eastern end of the line, highlighted by the black box in Figures 4.13a and 4.13d. In this area, the plots of $\overline{\Delta\alpha_{f,w}}$ and γ do not present any reliable results, probably due to the lack of positive-offset shots at the eastern portion of the seismic line (Figure 3.10). Nevertheless, due to the coherency of the anomalies within the black box in the plots of E and G, its western boundary ("3" - 1064 m) was disregarded from the DC extraction. Smaller-scale anomalies can be depicted in the plots of γ and $\overline{\Delta\alpha_{f,w}}$, at the locations outlined by the black dashed lines ("1" at 252 m, and "2" at 359 m) in Figures 4.13b and 4.13c, while the G plot provides an interesting feature corresponding to position "2" only. The locations of the black dashed lines were also saved and omitted during the DC extraction.

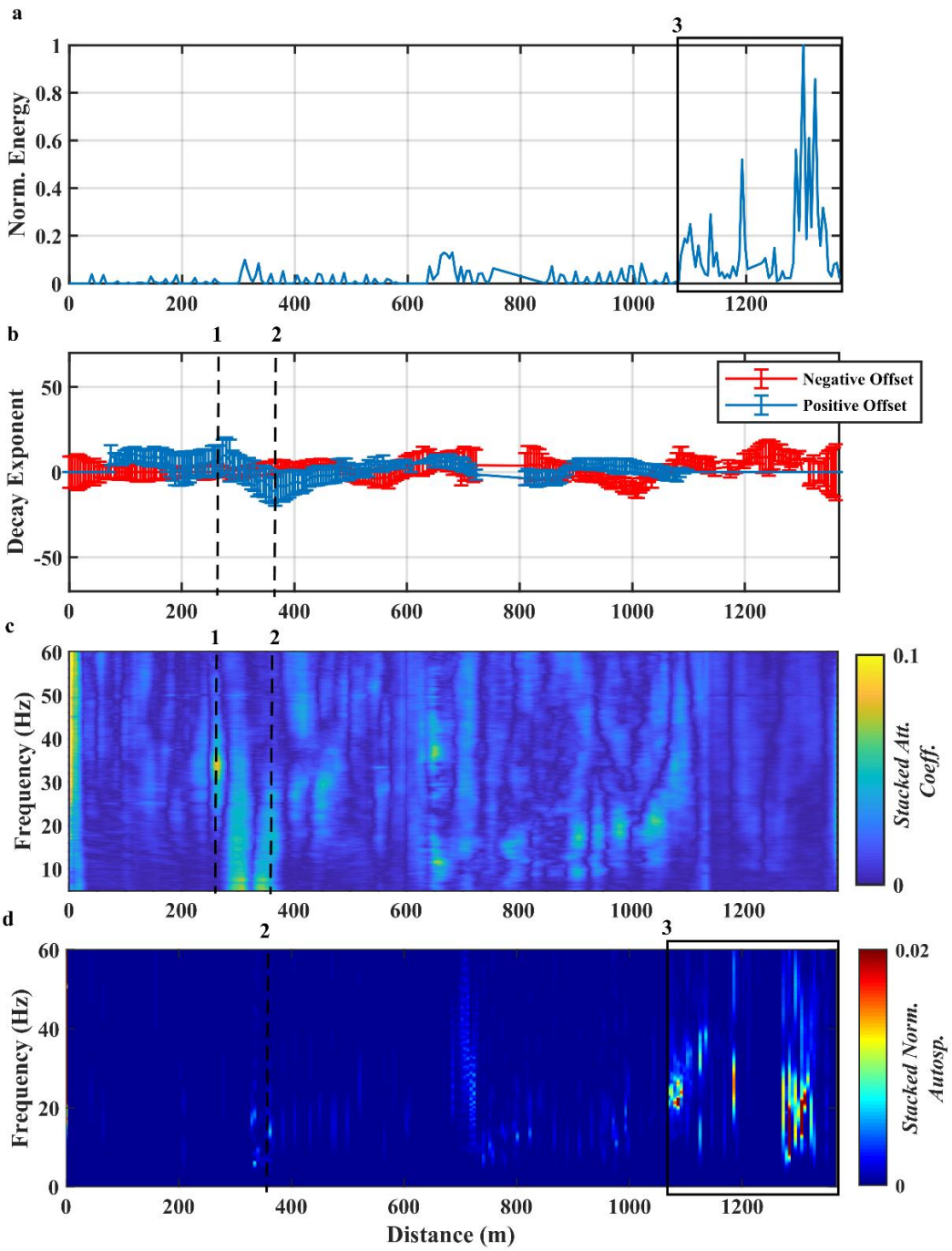

Figure 4.13: Same as Figure 4.2, computed along line SM1. The estimated positions of the sharp lateral variations are labelled as "1"- "3".

The selected processing parameters for the multichannel analysis are summarized in Table 4.5. An example of the multichannel DC extraction can be seen in Figure 4.14a, where we present the $f-v$ spectrum of the window located at distance 250 m and the spectral maxima (black dots) corresponding to the picked DC. In total, 23 multichannel DCs were extracted along the line and are plotted in

Figure 4.14b where, despite the significant level of noise, a clear dispersive trend can be identified at high phase velocities, in agreement with the expected hard-rock environment of the site. The result of the clustering algorithm applied to the DCs, is the dendrogram of Figure 4.14c, that shows two major clusters, which we interpret as two separate zones of uniform characteristics. The first cluster, which will be onward referred to as "Zone 1" (green in Figures 4.14b and 4.14c), extends from 0 m to 750 m (Figure 3.10) and contains 13 DCs. The second one, named as "Zone 2" (red in Figures 4.14b and 4.14c), extends from 850 m to 1360 m (Figure 3.10) and contains 10 DCs. Between the two zones, no DCs were picked due to the gap of the receiver line (Figure 3.10).

Table 4.5: *Windowing parameters for the DC extraction of line SM1.*

Processing parameter	Value
Window size	100 m
Step	50 m
Minimum offset	10 m
Maximum offset	580 m

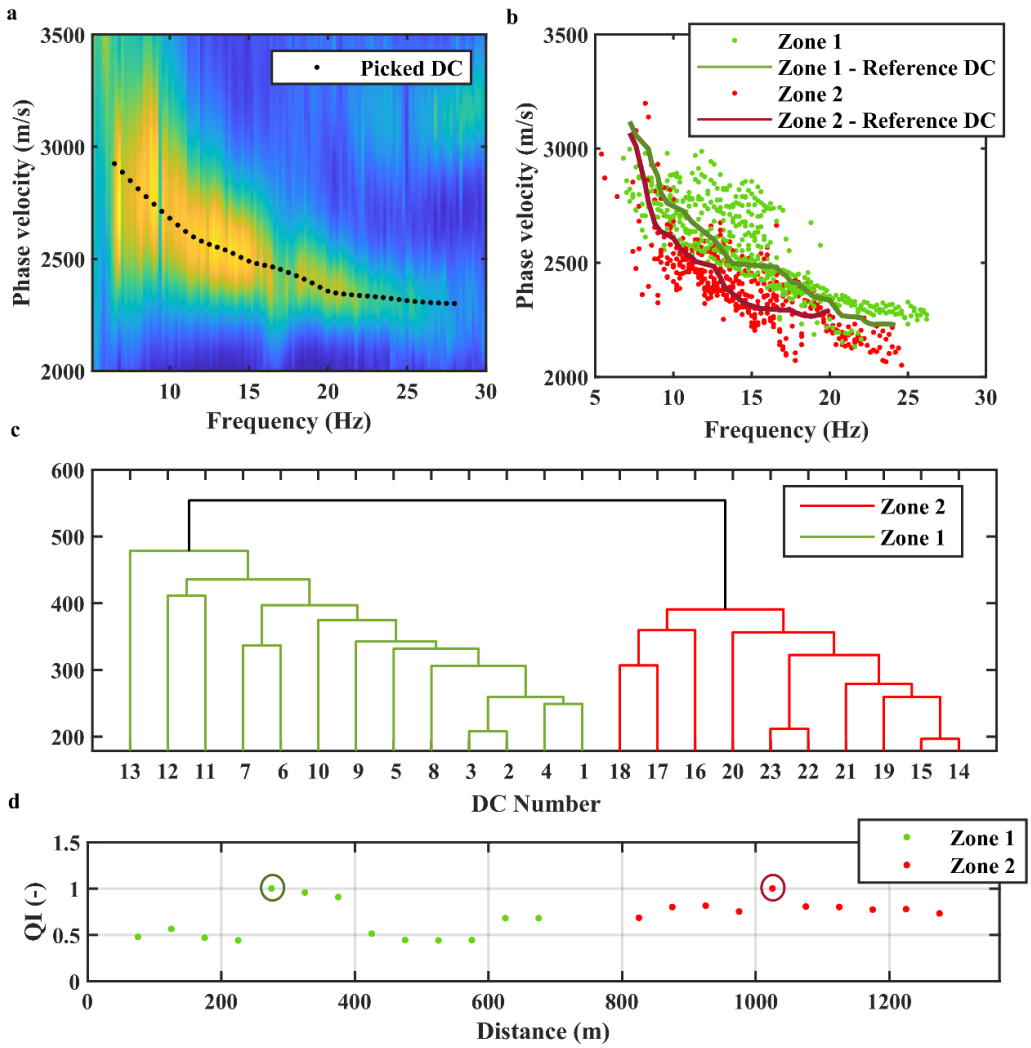

Figure 4.14: a) example $f-v$ spectrum and its corresponding picked DC (black) b) Multichannel DCs (dots) and estimated reference DCs (lines) c) Clustering result and d) *QI* of the DCs of each zone. The circles indicate the DCs with the highest *QI*. In all panels, green and red represent the two main clusters, corresponding to Zone 1 and Zone 2.

In Figure 4.14b, it can be observed that the DCs of the two clusters carry different characteristics, with presence of higher phase velocities in the curves of Zone 1, with respect to Zone 2. The *QI* of the DCs, computed separately for each cluster according to eq. 4.8, is plotted in Figure 4.14d at the corresponding DC position. The positions of highest-*QI* DCs, which were chosen as reference for Zone 1 (250 m) and Zone 2 (1050 m), are highlighted in Figure 4.14d, by the red and green circles, respectively. The reference DCs are plotted as green (Zone 1) and red (Zone 2) lines in Figure 4.14b.

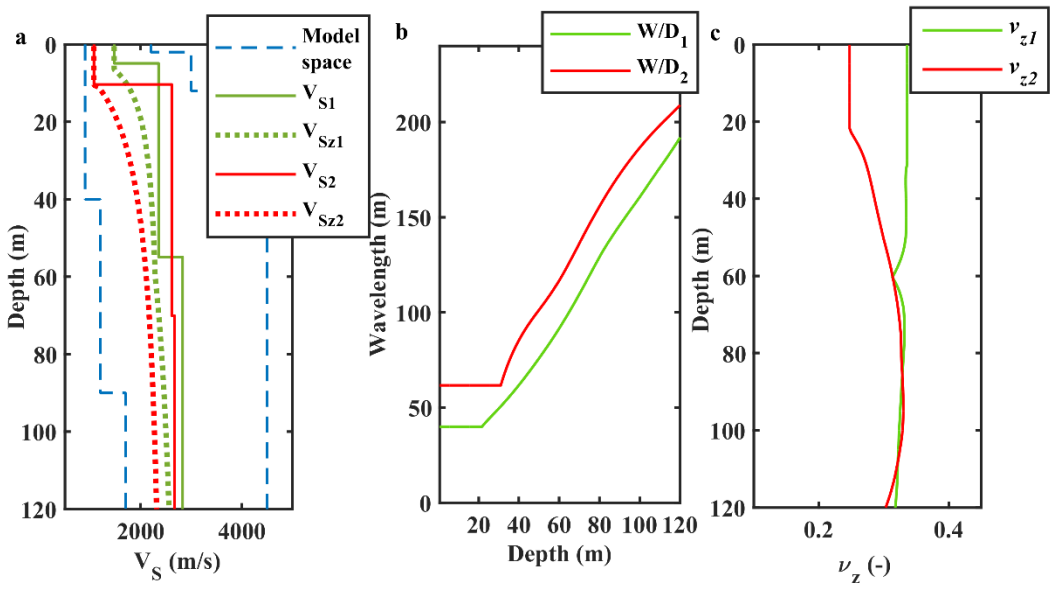

Figure 4.15: a) Model-space boundaries for the Monte Carlo inversion (blue dashed) and estimated reference V_S (solid lines) and reference V_{Sz} (dots). Plot of the estimated b) W/D relationship and c) ν_z. In all panels, green stands for Zone 1 and red for Zone 2.

For the Monte Carlo inversion of each reference DC, one million 4-layered (3 layers plus halfspace) V_S profiles were randomly generated from the model space outlined in blue dashed in Figure 4.15a. The value of ρ was fixed at 2500 kg/m^3 for the shallow layers and 2800 kg/m^3 for the halfspace, while ν was randomly sampled between 0.1 and 0.4, to be wider than the expected values on the site (Malehmir et al., 2017). Figure 4.15a shows, for Zone 1 and Zone 2, the inverted reference V_{S_1} and V_{S_2} models (solid green and solid red, respectively) and their corresponding V_{Sz_1} and V_{Sz_2} (green and red dots, respectively), computed using eq. 4.9. Figure 4.15b shows, in the same color scale, their estimated W/D$_1$ and W/D$_2$ and Figure 4.15c, the corresponding ν_{z1} and ν_{z2}.

The transformation of the DCs into V_{Sz} models, using the corresponding W/D relationship for each cluster, provided the pseudo-2D V_{Sz} model plotted in Figure 4.16a. The corresponding V_{Pz} model is plotted in Figure 4.16b, and the V_P static shift, computed for different values of (floating) datum depth between 40 m and 120 m, is plotted in Figure 4.16c.

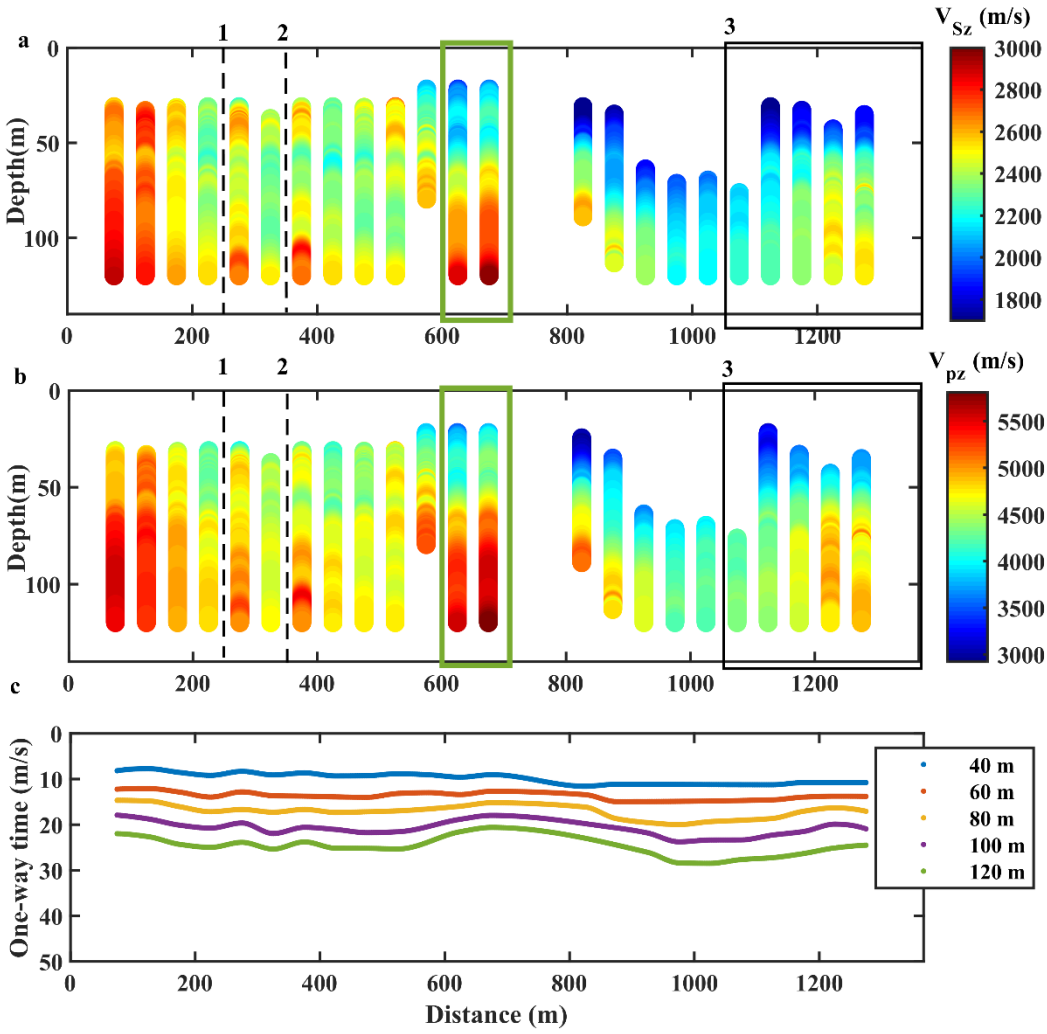

Figure 4.16: Pseudo-2D a) V_{Sz} and b) V_{Pz} model. The thickness of the 1D models is illustrative. c) Estimated P-wave one-way traveltime (static shift). The dashed lines and black box in (a) and (b), indicate the estimated positions of the sharp lateral variations shown also in Figure 4.13. The green box shows a high-velocity zone, indicated also as a green box in Figure 4.17.

4.4.2 Discussion of the results

The SW direct statics estimation method has led to the retrieval of the V_P static corrections for the seismic line SM1 of the Siilinjärvi mining site. The sharp-lateral variation detection methods identified the location of subsurface anomalies, which could be associated to the known lithological variations in the area.

The energy anomalies, denoted as “1” and “2” in Figures 4.13b and 4.13c, present strong localization, and therefore, they are probably related to subsurface targets of narrow lateral extent. A comparison of these locations with the geological

map of the area, zoomed around line SM1 (Figure 4.17), shows that they correspond to the intrusions of the tonalite within the (mineralized) carbonatite-glimmerite body. The larger-scale anomaly, highlighted by the black box in Figures 4.13a and 4.13d, is located eastern to the contact of the carbonatite-glimmerite with the fenite bedrock (Figure 4.17). Considering that the maximum frequency affected by the black-box anomaly in the Autospectrum plot (Figure 4.13d) increases from 35 Hz to 60 Hz towards the east, the anomaly could be indicative of a rise of the bedrock.

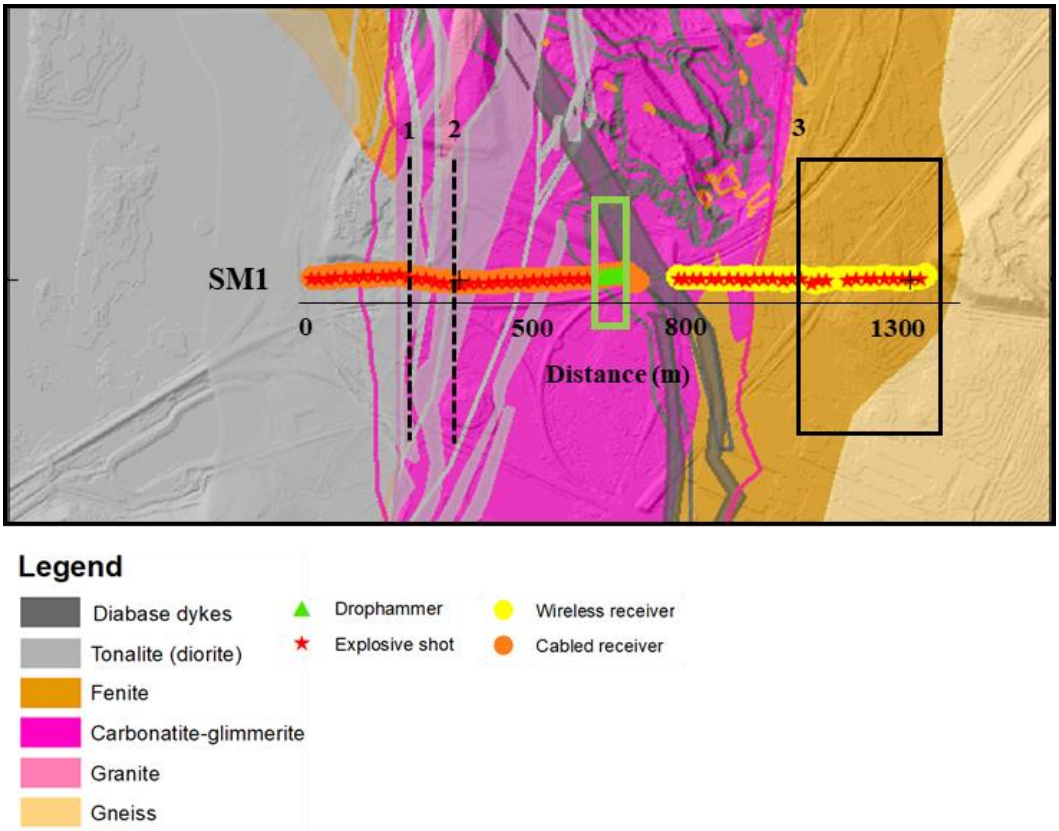

Figure 4.17: Geological map of the Siilinjärvi mining area (provided by Yara), zoomed around line SM1, with an elevation model 2008-2019, 2 m x 2 m © National Land Survey of Finland. The dashed lines and the black boxes, indicate the estimated positions of the sharp lateral variations of Figure 4.13. The green box highlights a high-velocity area, also indicated as a green box in Figure 4.16.

Similar conclusions can be reached by observing the time-average velocity models of Figures 4.16a and 4.16b. Although no DCs were picked at the exact locations of the targets denoted by the dashed lines ("1" and "2" in Figures 4.13b,c and 4.16a,b), higher velocities appear at shallow depths in their proximity, probably

related to the intrusions of the tonalite. The time-average velocity models confirm the rising of the fenite bedrock in the area of the black box (Figures 4.13a,d and 4.16a,b), since the velocities appear to increase in the eastern side of the black box in both the V_{Sz} and the V_{Pz} models (Figure 4.16a and 4.16b).

Overall, the V_{Sz} and V_{Pz} values were higher in Zone 1, probably due to the tonalite intrusion (Figure 4.17). Moreover, the green box in Figures 4.16a and 4.16b, denotes an area (between 600 m and 950 m), where the velocities appear higher than in the surrounding models. These are probably related to the large-scale diabase dyke which intersects the line at the same position and is highlighted also by a green box in Figure 4.17.

Therefore, it can be concluded that the resulting time-average velocity models are in agreement with the geological information on the site, increasing the reliability of our statics estimate.

4.5 Conclusion

In this chapter, a method for the estimation of the V_P static corrections, based on multichannel SW processing, has been presented. Being based mainly on simple data transforms, the method provides the statics in a computationally efficient manner, faster than the conventional BW-based approaches, which require first-break picking, and to most SW methods, which involve excessive inversion stages. The workflow has been successfully applied to the seismic datasets from the iron-oxide mining site of Ludvika in Sweden and from the apatite mine of Siilinjärvi. The estimated velocity models were in agreement with the known geology and the retrieved V_P statics presented negligible difference with respect to statics computed through P-wave tomography. The quality of the resulting stacked section showed that the workflow can be considered as a valid alternative to estimate the statics.

Chapter 5

Optimized automatic two-station SW processing

5.1 Introduction

In this Chapter we present a novel, optimized, two-station processing scheme. For our method, the processing parameter selection is optimized with a novel, data-driven approach, which requires only minimal operator intervention, and the rest of the steps are completely automatic. We describe the fundamental stages and their mathematical background, and show the application of the method to a simple 2D synthetic model and to the more challenging 3D active-seismic dataset from the mining site of Ludvika in Sweden, described in Section 3.4.

5.2 Method overview

An overview of the method is given in the flowchart of Figure 5.1. As a first step, the receiver pairs and shots (blue in Figure 5.1), to be used for the extraction of the DCs, are selected. The receiver-pair and shot combinations which are collinear are found. From these, the shots outside the near- and far-field region are identified and selected, using a novel data-driven method which estimates the near- and far-offsets as a function of wavelength. The selected shots, receivers and

acceptable wavelength ranges are provided as input parameters to the DC picking and cleaning process (red in Figure 5.1).

The DC extraction from each of the selected receiver pairs and shots is based on the computation of the cross-correlation matrix between the corresponding traces. The individual matrices corresponding to the same receiver pair are stacked, and a DC is automatically picked by tracking the maxima at each frequency, on both the individual-shot and the stacked matrices. To ensure that the correct maxima are picked, the velocities of a reference DC are used as a guide.

Based on the individual-shot DCs, the standard deviation of the phase velocities is computed, to be used as the experimental uncertainty during the inversion of the stacked DC. An automatic cleaning is applied on the stacked DCs, to ensure that only picked maxima which are related to SW fundamental mode are kept.

Finally, an outlier detection (green in Figure 5.1) compares the stacked DCs among each other, to remove curves with unrealistic phase velocities, resulting from possible errors in the previous steps or due to low data quality.

Once the final set of stacked DCs has been retrieved, a portion of them is randomly selected and compared with DCs picked manually for the same receiver pairs, by means of an automatic *QC* (yellow in Figure 5.1). The *QC* allows to identify whether the quality of the picking is satisfactory.

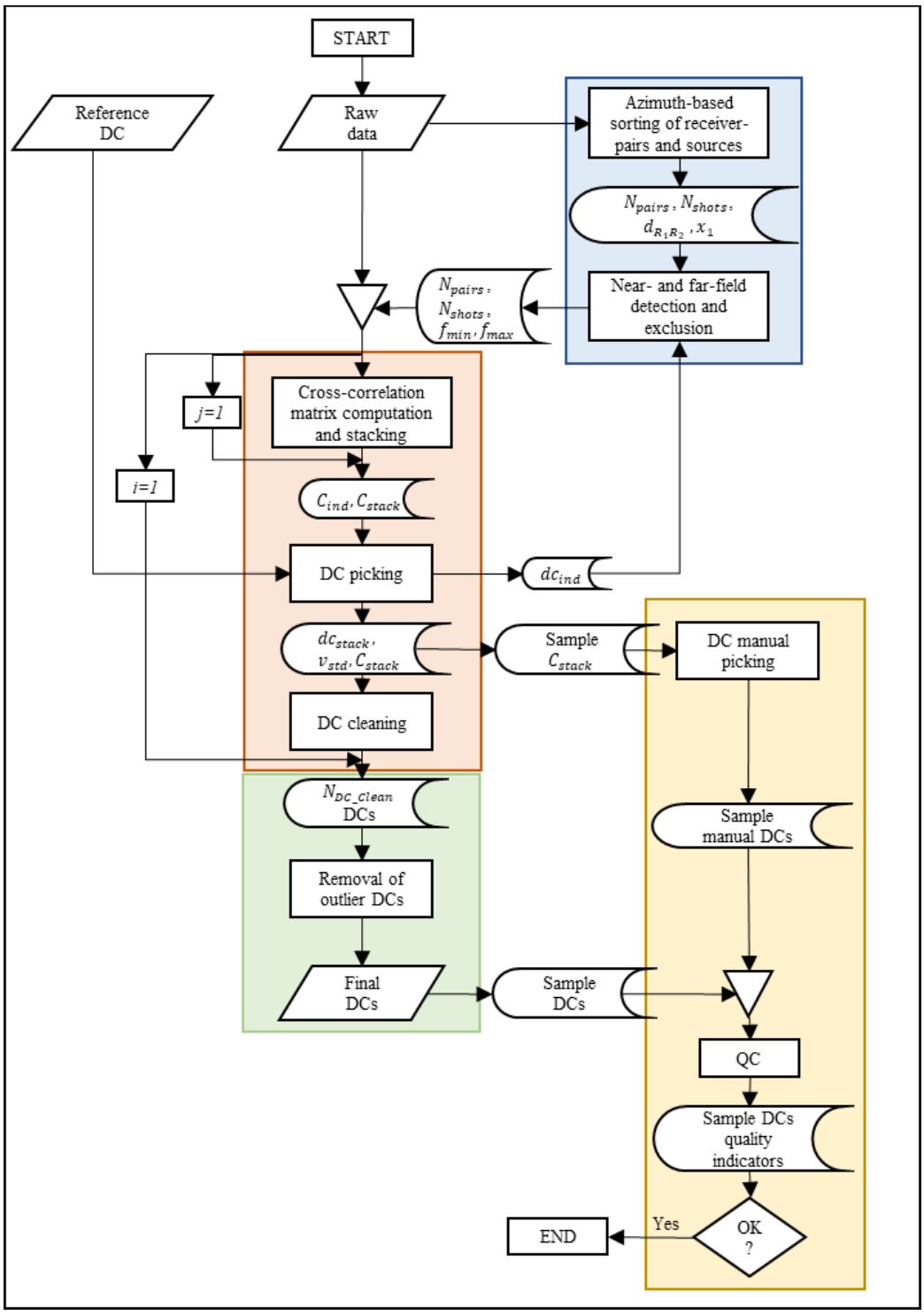

Figure 5.1: Flow-chart representation of the proposed method

5.3 Synthetic model description

The proposed method will be demonstrated using the synthetic 2D model that we plot in Figure 5.2. The model, consists of three layers (Table 5.1) and is split at 60 m distance into two laterally-homogeneous areas ("Zone 1" and "Zone 2" in

Figure 5.2). The simulated dataset consists of 101 receivers, spaced at 1 m, and 25 shots, spaced at 5 m (black dots and red circles in Figure 5.2, respectively). The simulated record length was equal to 2 s and the sampling interval was equal to 1 ms.

Table 5.1: *Synthetic model parameters.*

	Layer 1	**Layer 2**	**Layer 3**
h (m)	2	Zone 1: 8 Zone 2: 3	Zone 1: 7 Zone 2: 12
$\rho \left(Kg/m^3\right)$	2000	2100	2200
$V_S \ (m/s)$	90	140	200
$V_P \ (m/s)$	180	240	350

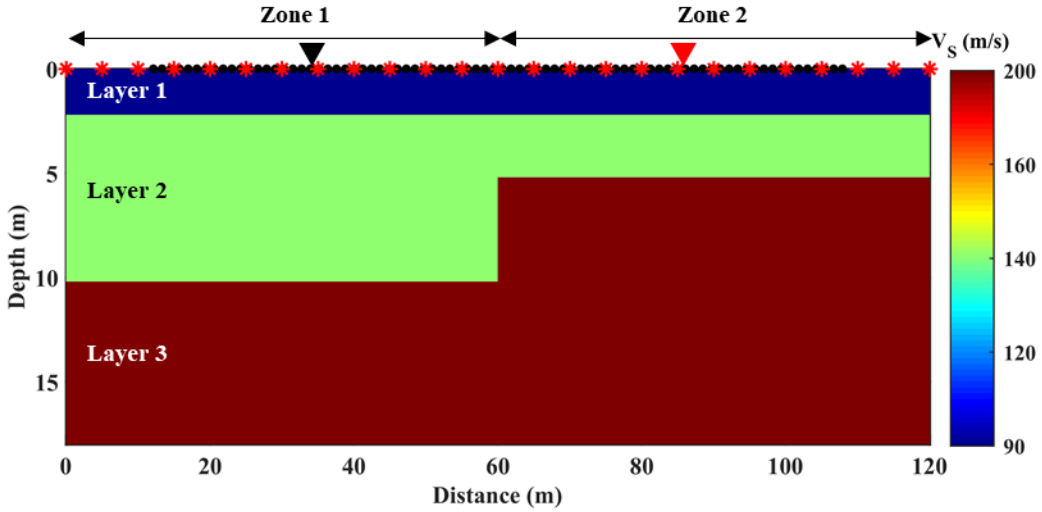

Figure 5.2: Synthetic model. The colors indicate V_S, given by the color bar. As dots and asterisks, the simulated receivers and shots, respectively.

5.4 Selection of the receiver pairs, shots and wavelength ranges

In this stage, the receiver pairs, shots and wavelength ranges for which DCs can be reliably extracted, are found.

5.4.1. Azimuth-based sorting of shots and receivers

From the entire set of seismic gathers, we identify pairs of traces which have recorded – at least one – common in-line shot. Collinearity is of great importance since, as discussed in Section 2.3.4, extraction of DCs corresponding to SW which propagate in an off-line direction, leads to erroneous phase-velocity measurements. In 3D datasets, co-linearity is ensured by selecting the appropriate source-receiver combinations, based on their azimuth angle, θ. In 2D seismic datasets, all the receivers are in-line with the sources, and therefore co-linearity is not of question. However, θ is again measured, to ensure that the shot is not located between the two receivers.

Description of the method

The proposed technique is summarized in the pseudocode of Table 5.2. Let $\mathbf{R}_x$ and $\mathbf{R}_y$ be two vectors, containing the x- and y- coordinates of the receivers, respectively. As R_i we denote the i-th receiver of the dataset, located at $(x_i, y_i) = (\mathbf{R}_x(i), \mathbf{R}_y(i))$. Correspondingly, the k-th shot, S_k, is located at $(x_k, y_k) = (\mathbf{S}_x(k), \mathbf{S}_y(k))$.

First, the azimuth (θ_{ijk}), between each of the possible receiver pairs (R_iR_j) and each of the available shots (S_k) of the dataset is computed, according to:

$$\theta_{ijk} = \cos^{-1}\left(\frac{x_i - x_k \quad y_i - y_k \; + \; x_j - x_k \quad y_j - y_k}{\sqrt{x_i - x_k}^{\,2} + \; y_i - y_k}^{\,2} \sqrt{x_j - x_k}^{\,2} + \; y_j - y_k}^{\,2} \right) \quad (5.1).$$

The same computation is performed for all the S_k shots and the same R_iR_j pair, and in the end, only the S_k for which $\theta_{ijk} = 0^o$ (e.g., Figure 5.3a), are considered suitable for the specific R_iR_j pair. In 2D datasets, this ensures that $\theta_{ijk} \neq 180^o$ (e.g., Figure 5.3b).

Running this check for all possible receiver pairs, a total of N_{pairs} receiver pairs and their corresponding in-line shots, the number of which ($N_S^{R_1R_2}$) will be different for each pair depending on the acquisition geometry, is identified.

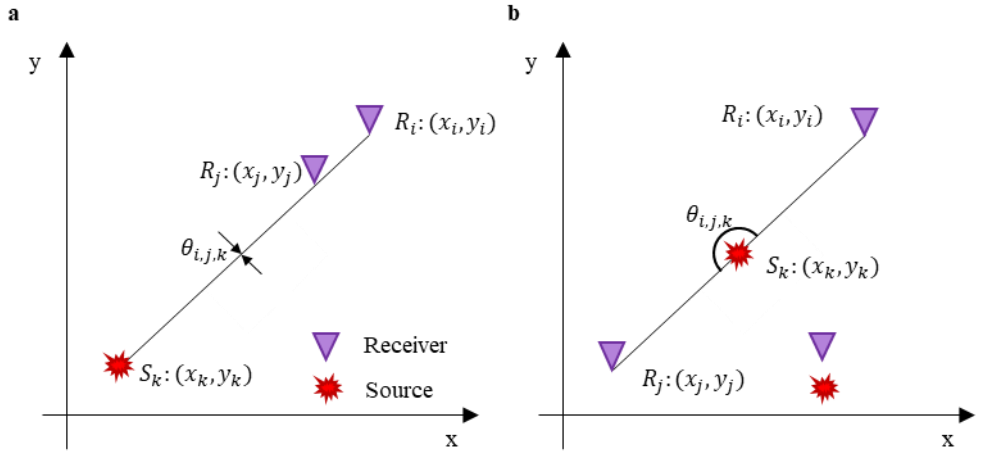

Figure 5.3: Azimuth computation (θ_{ijk}) between two random receivers R_i and R_j and a shot S_k. In (a) the angle is $\theta_{ijk} = 0^o$. In (b) the angle $\theta_{ijk} = 180^o$.

Table 5.2: *Azimuth-based sorting of receiver-pairs and shots pseudocode.*

Algorithm: Azimuth-based sorting of receiver-pairs and sources

Input: x- and y- coordinates of the *Nr* receivers, R_x and R_x. x- and y- coordinates of the *Ns* shots, S_x and S_y.

Output: Set of N_{pairs}, receiver pairs. N_{pairs} sets of N_S^{R1R2} shots in-line with each pair

---

```
1   for i from 1 to Nr-1
2   for j from i+1 to Nr
3   for k from 1 to N_S^R1R2
% Compute the azimuth between the i,j,k triplet
4     do θ = compute_azimuth (R_xi, R_yi, R_xji, R_xj, R_xk, R_xk)
% Check collinearity
5       if |θ| = 0  % Slight azimuth tolerance may be permitted, depending on the dataset characteristics
% If colinear save the receiver pair and the shot
6         save i and j to N_pairs
7         save k to N_S^R1R2
8       end
9   end
10 end
11 end
```

5.4.2 Detection and exclusion of near- and far-field effects

The $N_S^{R_1R_2}$ shots found in-line with each of the N_{pairs} receiver pairs are located at various offsets (x_1) (e.g., Figure 5.4). From these, only a limited portion can be reliably used for the DC extraction, and only for limited wavelength ranges $(\lambda_{\min}, \lambda_{\max})$. In particular, as discussed in Section 2.2.3, only shots which are outside the near- and far-field region of the two traces can be used for the DC estimation, to avoid biasing the theoretical assumptions of SW analysis, which would lead to wrong phase velocity measurements. Here, we propose a method to detect these regions as functions of the path length $d_{R_1R_2}$ and measured wavelength, which both influence the near- and far-field offset values (see Section 2.2.3 for details).

For our method it is necessary to pick the DCs from all the $N_S^{R_1R_2}$ shots in-line with all the N_{pairs} pairs, and for a broad wavelength band (workflow stages in red in Figure 5.1). Once the near- and far-field regions have been detected, the picking is performed again only for the acceptable $N_S^{R_1R_2}$ shots and wavelength ranges. This second round of picking provides the DCs that will be further inverted whereas the first round is only used to optimize the processing parameters.

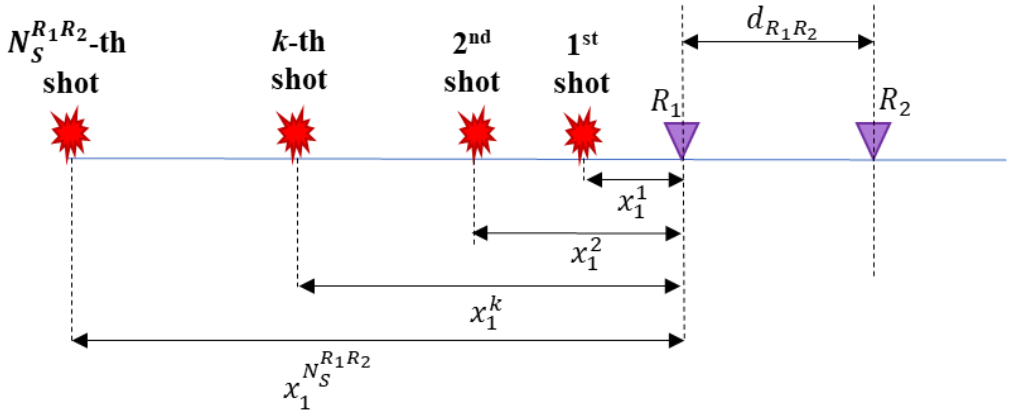

Figure 5.4: Scheme depicting a set of $N_S^{R_1R_2}$ shots, corresponding to an R_1R_2 receiver pair.

Description of the method

The proposed method is summarized in the pseudocode of Table 5.3. Each DC, corresponding to a receiver pair R_1R_2 and a shot $k \in N_S^{R_1R_2}$ (Figure 5.4), is described as a set of:

- A phase-velocity vector, $\mathbf{v}_k^{R_1R_2}$
- A wavelength vector, $\boldsymbol{\lambda}_k^{R_1R_2}$
- The path length $d_{R_1R_2}$
- The source offset, x_1^k

For each R_1R_2 **pair**, using the DCs of the $k \in N_S^{R_1R_2}$ individual shots, we compute the mean phase velocity ($\bar{\mathbf{v}}^{R_1R_2}$) at each i wavelength as:

$$\bar{\mathbf{v}}^{R_1R_2}(i) = \frac{\sum_{k}^{N_S^{R_1R_2}} \mathbf{v}_k^{R_1R_2}(i)}{N_S^{R_1R_2}} \tag{5.2},$$

where $\mathbf{v}_k^{R_1R_2}(i)$ is the phase velocity at a wavelength $i \in \lambda_k^{R_1R_2}$. **The key idea** of our method is that the DCs corresponding to the same receiver pair should be identical, independently from the source location. If any of the DCs presents inconsistent phase velocities at a specific wavelength range, its corresponding offset probably lies within the near/far-field regions (e.g., according to O'Neill (2003), Bodet et al., (2009), Foti et al. (2018), near-field is associated with phase-velocity underestimation). To detect them, we compute a misfit:

$$\mathbf{m}^{R_1R_2}(k,i) = \frac{\| \mathbf{v}_k^{R_1R_2}(i) - \bar{\mathbf{v}}^{R_1R_2}(i) \|}{\bar{\mathbf{v}}^{R_1R_2}(i)} \tag{5.3},$$

which shows the distance of each individual DC from the mean $\bar{\mathbf{v}}^{R_1R_2}$, at each wavelength. Since the k-th shot is located at a distinct offset x_1^k from the receiver pair, we associate misfit $\mathbf{m}^{R_1R_2}(k,i)$, to the corresponding value of x_1^k.

We compute eq. 5.3 **for all the** R_1R_2 **pairs**, and compute a matrix of the normalized global misfit from all the DCs of the dataset as

$$\mathbf{M}(x_1^k, i) = \frac{\sum_{R_1R_2} \sum_{k}^{N_s^{R_1R_2}} \mathbf{m}^{R_1R_2}(k,i)}{\sum_{R_1R_2} \sum_{k}} \tag{5.4}$$

Plotting $\mathbf{M}$ versus wavelength and offset, allows to identify, at each offset, the wavelength range $(\lambda_{\min}, \lambda_{\max})$ for which the misfit is low, and which is, therefore, most likely unaffected by near- and far-field effects. The low-misfit zones are manually picked on a user interface, creating a "mask" of acceptable offset vs $(\lambda_{\min}, \lambda_{\max})$.

To account also for the dependence of the near- and far-field from $d_{R_1R_2}$, we classify the receiver pairs into groups depending on their path lengths $d_{R_1R_2}$ and compute the misfit $\mathbf{M}$ separately for each group. A "mask" corresponding to each group is picked separately.

The shots at offsets outside the "mask" are disregarded from the $N_S^{R_1R_2}$ selection. For the accepted shots, the corresponding acceptable $(\lambda_{\min}, \lambda_{\max})$ ranges are transformed into ranges of frequency, i.e., $(f_{\min}, f_{\max})$, and used in the DC computation. To transform the wavelengths into frequencies, we use the average of all the $\bar{\mathbf{v}}^{R_1R_2}$ computed according to eq. 5.2 for all the receiver pairs.

Table 5.3: *Detection and exclusion of near- and far-field effects pseudocode.*

Algorithm: Detection and exclusion of near- and far-field effects
Input: Set of $N_{selected\_pairs}$ sets of N_S^{R1R2} DCs (v_{dc}, λ_{dc}, x_1, d_{R1R2}), in a limited range of d_{R1R2}
Output: "Mask" of acceptable N_S^{R1R2} vs frequency, for each receiver pair

---

```
1  for i from 1 to N_selected_pairs
2    for j from 1 to N_S^R1R2
3      Read v_dcj , λ_dcj, x_1, d_R1R2
% Compute mean phase velocity of each individual DC
4      do v_m,i = compute_mean_DC (v_dc,j)
% Compute misfit of each individual DC wrt mean phase velocity
5      do mi,j = compute_misfit (v_m,i)
6    end
7 end
% Compute the global misfit, for all the selected pairs and all the offsets
8 do M = sum_misfit_of all_pairs_and_same_offset (m)
% Plot the global misfit and select a "mask" enclosing the low-misfit zones
9 do plot M
9 do mask=select_low_misfit_zones_on_the_plot (M)
```

Examples

As an example, we show in Figure 5.5, the misfit $\mathbf{M}$ computed from all the DCs of the Ludvika 2019 dataset (see Section 3). The values of $\mathbf{M}$ in panels (a)-(d), have been computed from DCs with $d_{R_1R_2}$ between 0 m – 100 m , 100 m – 200 m , 200 m – 300 m and 400 m – 450 m, respectively.

In all panels, the colorscale indicates the misfit, and the straight lines correspond to the most commonly used empirical relationships between x_1 and λ (see Table 2.1), for the determination of the near- and far-field regions. The red dashed lines define the low-misfit areas and have been picked as the offset vs $(\lambda_{\min}, \lambda_{\max})$ "masks". After this step, the cross-correlation matrices will be computed for each pair, only considering the shots in the offset and wavelength range defined by the mask. For instance, for two receivers at distance 80 m from each other, we will use only the shots at offset between 20 m and 560 m (Figure 5.5a). For the shot at 500 m offset, only wavelengths between $\lambda_{\min} = 77$ m and $\lambda_{\max} = 110$ m will be considered in the DC computation. Therefore, the finally retrieved DCs will contain data points which are, most likely, unaffected by near- and far-field effects.

It can be noticed that our estimation of acceptable offset ranges is different than the one of the empirical rules. To validate our method, we performed the entire processing workflow using both approaches, and our data-driven method provided a higher-quality dispersion image. Further discussion on this comparison can be found at the end of this chapter (Section 5.11).

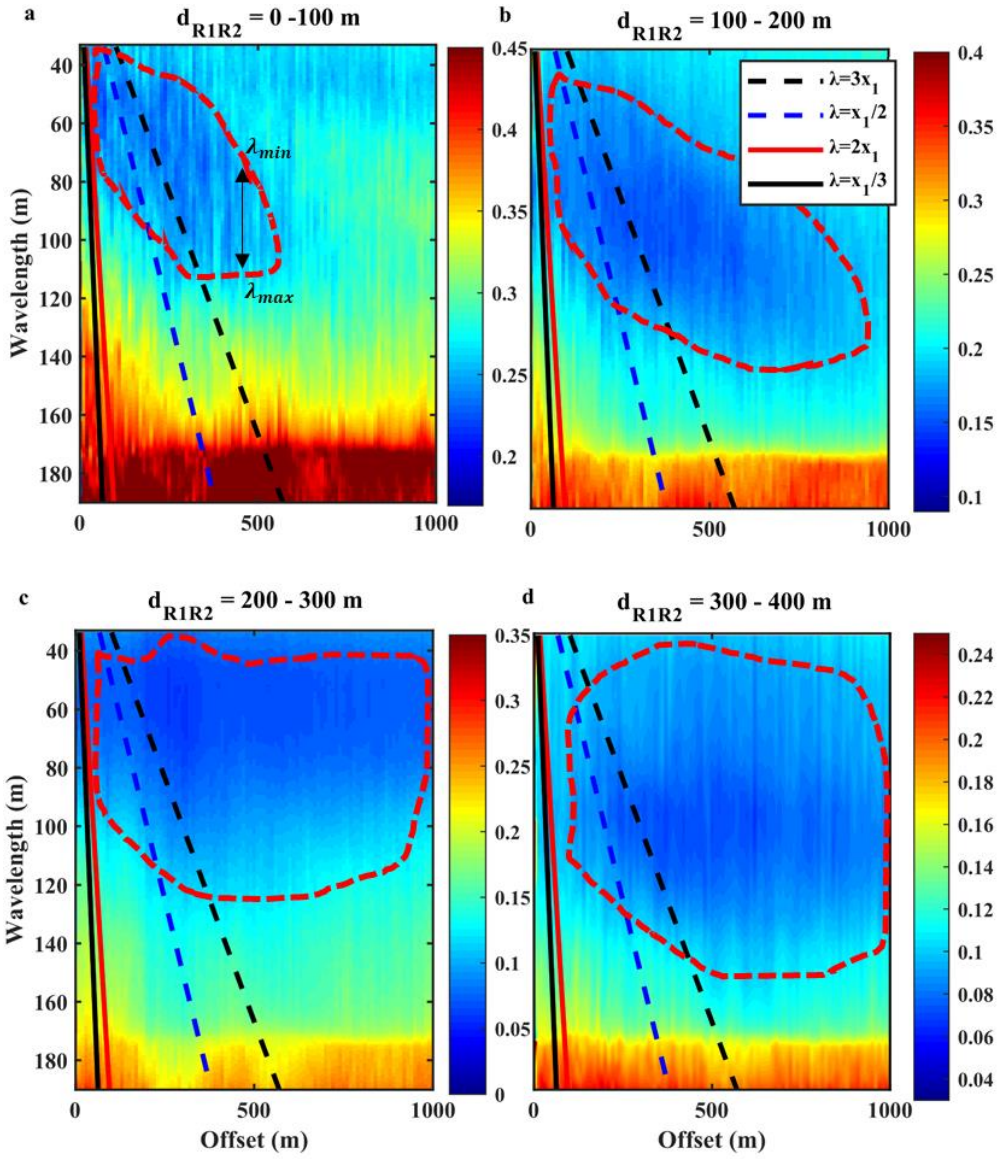

Figure 5.5. In all panels, the colorscale indicates the misfit $\mathbf{M}$ (eq. 5.4). The straight lines correspond to the most common empirical definitions of the near- and far-field (Table 2.1). In red dashed, our estimation of the near- and far-field limits.

5.5 Cross-correlation matrix computation and stacking

This stage is based on the two-station method, as originally formulated by Bloch & Hales (1968). The theoretical background of the method is described in detail in Section 2.3.2. Here, we provide the basic mathematical definitions necessary for the implementation of the method in the discrete (in terms of both time and space) domain of data processing.

In summary, a pair of traces is analysed into monochromatic components, using a frequency-domain narrow band-pass filtering, as originally proposed by Dziewonski & Hales (1972). The analysed traces are then cross-correlated, frequency by frequency, to retrieve the cross-correlation matrix. In the end, the matrices corresponding to the same receiver pair and different shots are stacked, and the same operation is performed for all the receiver pairs and shots, selected in the previous stage.

5.5.1 Description of the method

The method is summarized in the pseudo-code of Table 5.4. Inputs are the traces $\mathbf{u}_r^k$ recorded by a receiver pair R_r ($r \in \{1,2\}$), for all its selected k shots ($k \in \left(1, N_S^{R_1R_2}\right)$). The path length corresponding to the receiver pair, d_{R1R2}, is also known.

Each trace $\mathbf{u}_r^k$ is a discrete finite signal $\mathbf{u}_r^k[n]$, $n \in (1, N_T)$. Its length (N_T) depends on the sampling parameters and equals $N_T = T/SR$, where T is the record duration and SR is the temporal sampling rate. The sampling parameters will be onwards assumed constant and the trace will be simply denoted as $\mathbf{u}_r^k$.

We define the domain for which the cross-correlation matrix will be computed, i.e.:

- A phase-velocity vector $\mathbf{v_C}$, containing s_V velocities between $(v_{\min}, v_{\max})$:

$$\mathbf{v_C}(j) = V_{\min} + j \cdot \delta V \tag{5.5},$$

where

$$\delta_V = \frac{V_{\max} - V_{\min}}{s_V} \tag{5.6}.$$

- A frequency vector $\mathbf{f}_\mathbf{C}$, containing s_f frequencies between $(f_{\min}, f_{\max})$:

$$\mathbf{f}_\mathbf{C}(i) = f_{\min} + i \cdot \delta_f \tag{5.7},$$

where

$$\delta_f = \frac{f_{\max} - f_{\min}}{s_f} \tag{5.8}.$$

The values of $f_{\min}$ and $f_{\max}$ are those selected as in Section 5.4.2. The values of $v_{\min}$ and $v_{\max}$ are input by the user, based on the expected phase velocities in the recorded data.

The two $\mathbf{u}_r^{\,k}$ traces are analysed into monochromatic ($\forall f_i \in (f_{\min}, f_{\max})$) components $\mathbf{u}_r^{f_i,k}$, using the technique of Dziewonski & Hales (1972). Specifically, the traces are transformed in frequency domain using the Discrete Fourier Transform (DFT):

$$\mathbf{U}_r^{\,k} = \mathcal{F}\left(\mathbf{u}_r^{\,k}\right) \tag{5.9},$$

where $\mathcal{F}$ denotes the DFT operator. A band-pass filter is applied $\forall f_i \in (f_{\min}, f_{\max})$ on the $\mathbf{U}_r^{\,k}$ spectra, to isolate their individual frequency responses: each of the $\mathbf{U}_r^{\,k}$ spectra is multiplied by a narrow window, which, following Dziewonski & Hales (1972), was chosen to be a Gaussian function $\mathbf{G}^{f_i}$ centred at f_i:

$$\mathbf{G}^{f_i} = e^{-\frac{1}{2}\left(\frac{\mathbf{f}_\mathbf{C} - f_i}{\sigma}\right)^2} \tag{5.10},$$

where σ is the standard deviation of the Gaussian function. The filtered spectra can be therefore expressed as:

$$\mathbf{U}_r^{f_i,k} = \mathbf{G}^{f_i} \circ \mathbf{U}_r^{k} \tag{5.11},$$

where ∘ denotes the Hadamard element-wise multiplication. The filtered spectra are converted back to time domain applying the inverse Fourier transform:

$$\mathbf{u}_r^{f_i,k} = \mathcal{F}^{-1}\left(\mathbf{U}_r^{f_i,k}\right) \tag{5.12},$$

where $\mathcal{F}^{-1}$ is the inverse DFT.

Following the classical definition of the cross-correlation function between two discrete signals $A[n]$ and $B[n]$:

$$(A \otimes B)[m] = \sum_{n=-\infty}^{\infty} A[n]B[n+m] \tag{5.13},$$

the cross-correlation between $\mathbf{u}_1^{f_i,k}$ and $\mathbf{u}_2^{f_i,k}$ is performed, over a time-lag vector $\mathbf{t}_L$, which is computed based on the velocity range $(v_{\min}, v_{\max})$ and the path length d_{R1R2}. Specifically, we compute the time range:

$$(t_{min}, t_{max}) = \left(\frac{d_{R1R2}}{v_{max}}, \frac{d_{R1R2}}{v_{min}}\right) \tag{5.14},$$

and we discretize it, using the temporal SR of the signal, into time steps as:

$$(N_{min}, N_{max}) = \left(\frac{t_{\min}}{SR}, \frac{t_{\min}}{SR}\right) \tag{5.15}.$$

The time-lag vector $\mathbf{t}_L$ is then computed as:

$$\mathbf{t}_L(n) = \left(N_{\min}, N_{\min}+1, \cdots, N_{\max}\right) \tag{5.16}.$$

The cross-correlation results $\forall f_i \in \left(f_{\min}, f_{\max}\right)$ form the cross-correlation matrix:

$$\mathbf{C}^k(i,n) = \left(\mathbf{u}_{1,f_i}{}^k\right) \otimes \left(\mathbf{u}_{2,f_i}{}^k\right)\left[\mathbf{t}_L(n)\right] \tag{5.17}.$$

It is the matrix of the cross-correlation of all the $f_i \in f_{\min}, f_{\max}$ components of the signal $\mathbf{u}_{1,f_i}{}^k$ and of the signal $\mathbf{u}_{2,f_i}{}^k$ shifted by the elements n

of $\mathbf{t}_L$. To transform the matrix from a function of time into a function of phase velocity, we compute:

$$\mathbf{v}_{\mathbf{C}}^{orig}(n) = d_{R1R2} \circ \mathbf{t}_L(n)^{-1} \tag{5.18}$$

Since the velocities in $\mathbf{v}_{\mathbf{C}}^{orig}$ have a one-to-one correspondence to the time lags $\mathbf{t}_L$, the elements n of the matrix $\mathbf{C}^k(i,n)$, are related to a specific value of velocity $\mathbf{v}_{\mathbf{C}}^{orig}(n)$. To convert the matrix into the chosen velocity discretization, $\mathbf{v}_{\mathbf{C}}(j)$, following Yao et al. (2006), we perform a 1D spline interpolation of its values with respect to the velocities. The final matrix is of the form $\mathbf{C}^k = \mathbf{C}^k(i,j)$.

The same process is repeated for all the selected shots, i.e., $\forall k \in \left(1, N_S^{R_1R_2}\right)$, leading to the estimation of $N_S^{R_1R_2}$ matrices $\mathbf{C}^k$ for the same R_1R_2 pair.

Considering that the cross-correlation is a representation of the similarity of the two signals, the computed matrices will present a maximum when the dominant events of the two traces become in-phase, i.e. at the travel-time (or equivalently the velocity) of the dominant propagating waveform between R_1R_2 (with a 2π ambiguity, resulting from the periodicity of the transformed signal as described in detail in Section 2.3.2).

Assuming that the highest energy levels are carried by the SW fundamental mode on both traces, the maximum of the cross-correlation is expected to represent the phase velocity at each frequency. Therefore, the cross-correlation matrix is the dispersion image that will be used in the following stage to pick the DC.

Since high levels of random noise could reduce the relative weight of the SW event in the cross-correlation, we take advantage of the repetitive (k) measurements over the same R_1R_2 pair, contained in the $N_S^{R_1R_2}$ shot gathers, to improve the S/N. We sum the individual matrices $\mathbf{C}^k$, normalizing for the source-offset, and retrieve a stacked cross-correlation matrix for the receiver pair ($\mathbf{C}^{stack}$):

$$\mathbf{C}^{stack} = \sum_k \frac{1}{x_1^k} \mathbf{C}^k \tag{5.19}$$

Table 5.4: *Cross-correlation matrix computation and stacking pseudocode.*

Algorithm: Cross-correlation matrix computation and stacking

Input: Inter-receiver distance (d_{R1R2}), number of shots selected from the "butterfly" method (k)

Output: Set of k individual cross correlation matrices (C_{ind}), Stacked cross-correlation matrix (C_{stack})

---

for k **from** 1 **to** N_{shot}
  read $trace1_k(t)$ $trace2_k(t)$
  read f_{min}, f_{max}, v_{min}, v_{max}
% Transform the traces in the frequency domain
  do [$trace1_{FT}(f)$, $trace2_{FT}(f)$] = fft ($trace1_k(t)$, $trace2_k(t)$)
  for f_i **from** f_{min} **to** f_{max}
% Apply Gaussian window
    [$trace1_{FT}^{fi}(f)$, $trace2_{FT}^{fi}(f)$] = GaussianWindow ($trace1_{FT}(f)$, $trace2_{FT}(f)$, f_i)
% Transform the filtered traces in time domain
    [$trace1^{fi}(t)$, $trace2^{fi}(t)$] = ifft ($trace1_{FT}^{fi}(f)$, $trace2_{FT}^{fi}(f_i)$)
% Compute *the individual cross-correlation matrix*
      for t **from** 1 **to** $tlags$
        $xcorr\_t(f_i,t)$ = xcorr ($trace1^{fi}(t)$, $trace2^{fi}(t)$)
      end
  end
% Convert the matrix from a function of frequency and time to a function of frequency and phase velocity
  $C_{ind}(f,v,k)$ = spline ($^{t_{lags}}/_{d_{R1R2}}$, $xcorr\_t(f,t)$, $[v_{min},v_{max}]$)
end
% Compute the stacked *cross-correlation matrix*
do C_{stack} = sum ($C_{ind}(f,v)$)

5.5.2 Examples

In Figure 5.6, we demonstrate the method, using, as an example, two traces (Trace 1 and Trace 2, in Figure 5.6a), from the synthetic dataset presented in Section 5.3. The traces represent the records of two receivers at distance $d_{R_1R_2} = 10$ m from each other and a shot located at distance $x_1 = 4$ m from the first receiver. In Figure 5.6b we show, using the same colours as in Figure 5.6a, the corresponding filtered traces, after applying a Gaussian filter around 20 Hz. We computed the cross-correlation of the filtered traces for the velocity interval between 50 m/s – 400 m/s, and therefore, for the time interval between 0.025 s – 0.2 s. The resulting cross-correlated trace is shown in Figure 5.6c.

Performing the cross-correlation of the traces filtered around all frequencies between 10 Hz and 60 Hz (with a step of 0.5 Hz), resulted in the individual-shot cross-correlation matrix plotted in Figure 5.6d. Finally, in Figure 5.6e, we show the cross-correlation matrix in the frequency – phase velocity domain, resulting from

the spline interpolation of the matrix of Figure 5.6d. We note that for this synthetic model, stacking of different individual-shot matrices did not modify the result due to the absence of noise in the traces.

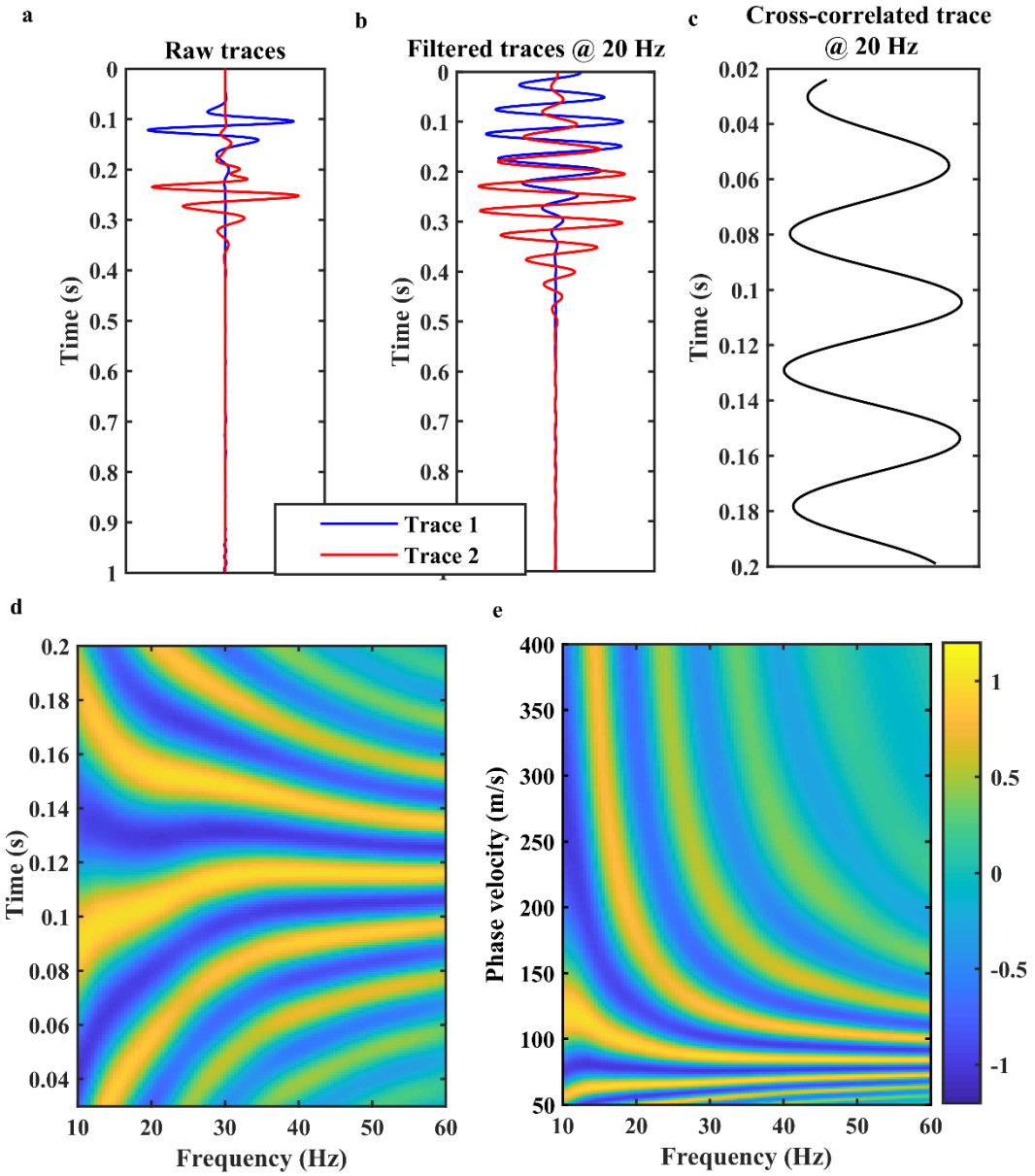

Figure 5.6: a) Two synthetic traces. b) The same traces after frequency band-pass filtering around 20 Hz. c) Cross-correlation of the traces in panel (b). Cross correlation matrix as a function of d) frequency and time and, e) frequency and phase velocity.

In Figure 5.7 we demonstrate the effect of stacking different individual-shot matrices, using an example belonging to the 3D dataset of Ludvika. In Figure 5.7a, we show the cross-correlation matrix computed for a pair of receivers, at distance

of $d_{R_1R_2} = 522\,\text{m}$ from each other, considering a shot at distance $x_1 = 100\,\text{m}$ from the first receiver. The matrix presents maxima which follow a clear dispersive trend -characteristic of SW- in the lowest frequency band (approximately 10 Hz – 40 Hz), while above 40 Hz, the dispersive trend is interrupted, probably due to the dominance of high-frequency noise. In Figures 5.7b – 5.7d, we show the matrix corresponding to the same receiver pair, but gradually stacking 2, 5 and 9 individual-shot matrices, corresponding to shot-offsets between 100 m – 190 m. It can be observed that the dispersive pattern in the low-frequency portion of the matrix becomes clearer and more energetic.

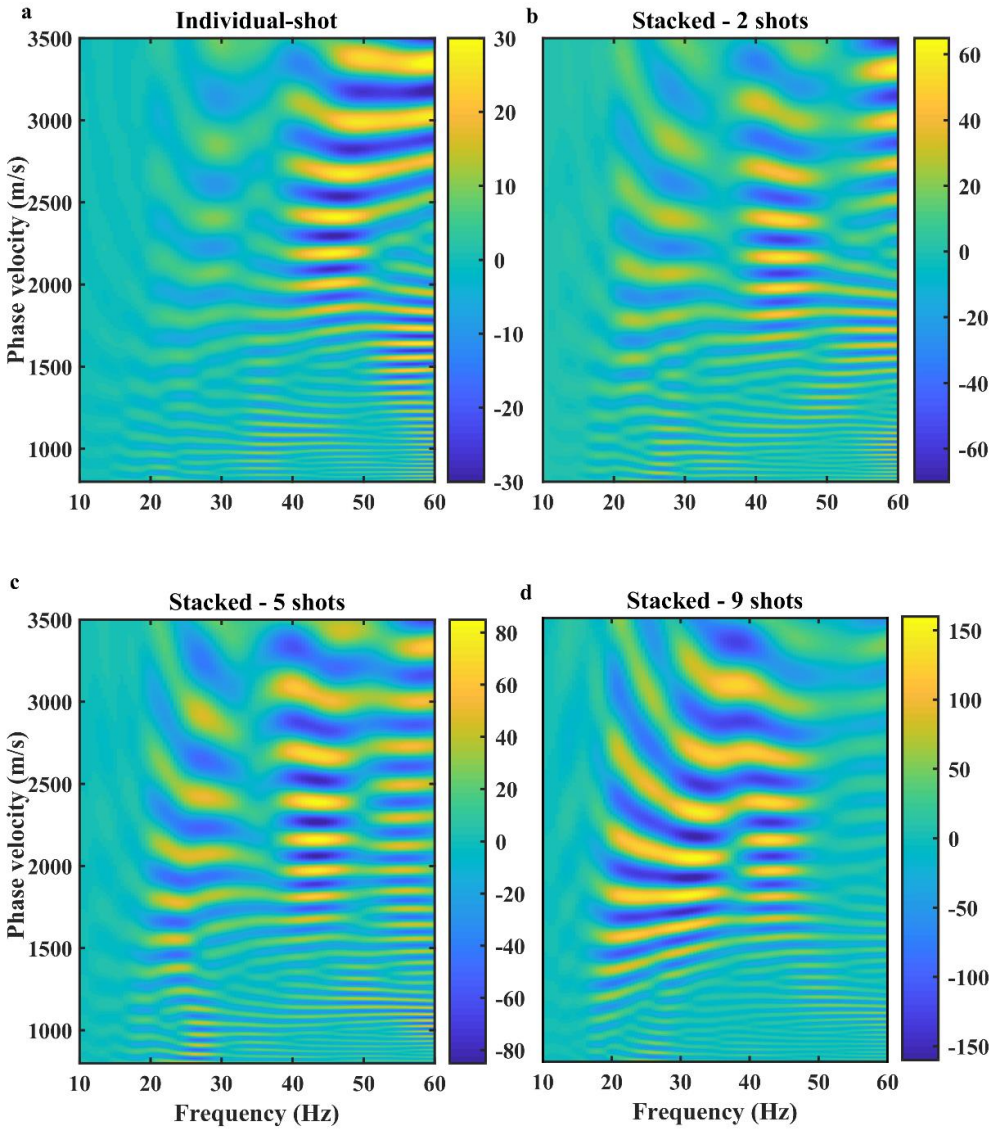

Figure 5.7: a) Individual-shot matrix and stacked matrix after summation of b) 2, c) 5 and d) 9 individual-shot matrices, corresponding to different shots and the same receiver couple.

5.6 DC Picking

Here, a DC is picked on both the individual and the stacked cross-correlation matrices $\mathbf{C}^k$ and $\mathbf{C}^{stack}$. The process is identical for both $\mathbf{C}^k$ and $\mathbf{C}^{stack}$ and, thus, we will onward generalize the description of the proposed technique, omitting the indices and referring to the input of the method as the cross-correlation matrix $\mathbf{C}$.

The **key idea** of the method is that the phase velocities of SW will correspond to **maxima on the matrix** (since we assume that SW are the most energetic events of the original traces), which follow a **smooth dispersive trend** along the different frequencies (since the DC is an inherently smooth function between the phase velocity and frequency).

However, at each frequency, the matrix presents maxima at several velocities (2π ambiguity), and to decide which ones to pick, we compare them with an *a priori* reference on the expected phase-velocity ranges. Throughout the thesis, we always use as reference, a multichannel DC located near to the receiver pair, which can be obtained using the workflow presented in Chapter 4.

A problem which arises is that the reference DC might be narrow-banded with respect to the matrix $\mathbf{C}$. On the other hand, we would like to pick the DC for the entire frequency band for which useful SW signal exists. To do so, we pick a maximum on the cross-correlation matrix, at a frequency where reference information exists, and we use it as a starting point (a "*seed*"), to pick the entire curve, following a *smooth trend*.

Since, however, starting from only one point carries high degree of uncertainty, e.g., because the reference DC might not correspond to the correct $\mathbf{C}$ maxima in the entire frequency band of the matrix, we will consider the picked curve only as a *candidate* DC. We will pick several candidate curves, starting from every frequency where the reference velocities are known, i.e., *from every possible seed* and, in the end, we will select the candidate that is closest to the reference DC at all frequencies.

In the following, we describe the technique, with reference to the pseudocode of Table 5.5 and the flowchart of Figure 5.8.

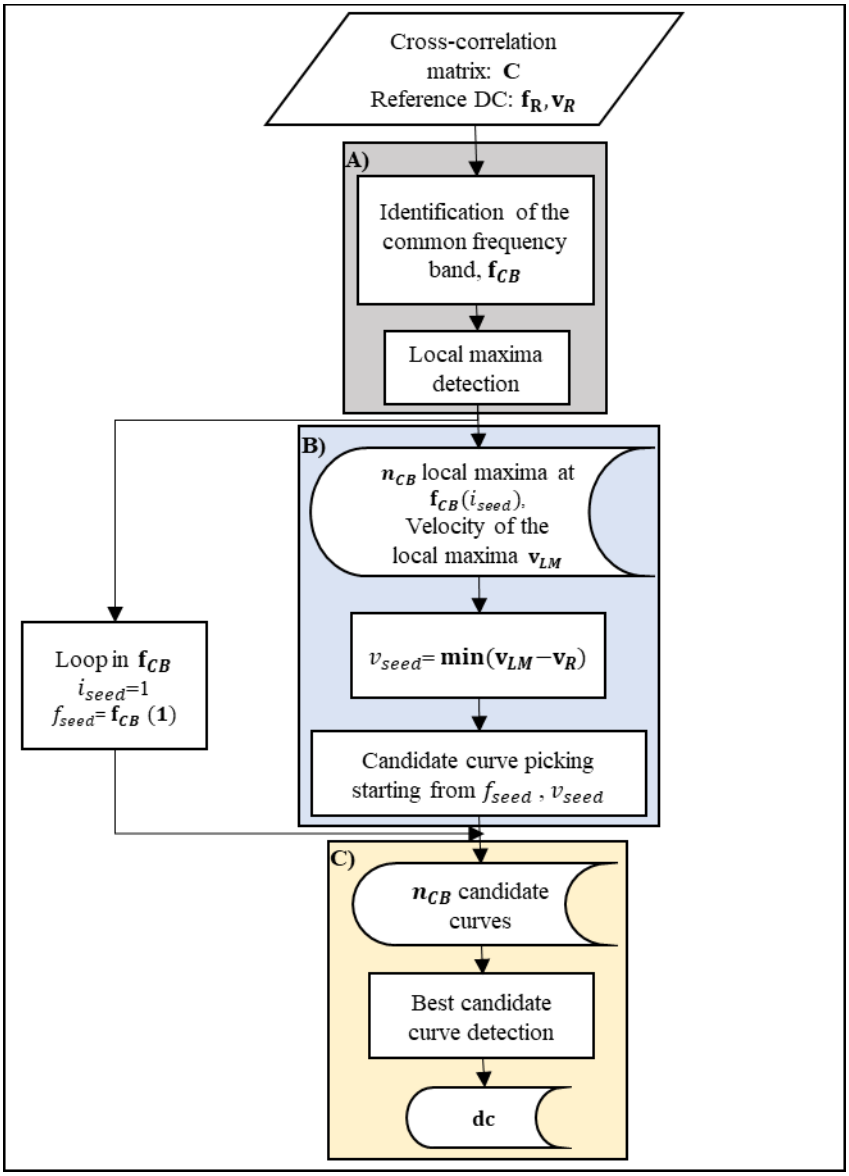

Figure 5.8: Flow-chart representation of the proposed DC picking method.

5.6.1 Description of the method

Input to the method are the cross-correlation matrix $\mathbf{C}$ ($\mathbf{C}^k$ or $\mathbf{C}^{stack}$) and the vectors which define its frequency and phase velocity coordinates: $\mathbf{f_C} = \left(f_{\min} \cdots f_{\max}\right)^{\mathrm{T}}$ and $\mathbf{v_C} = \left(v_{\min} \cdots v_{\max}\right)^{\mathrm{T}}$, respectively. The reference DC is input as a vector $\mathbf{f}_R = \left(f_{r1} \cdots f_{rdp_R}\right)^{\mathrm{T}}$, containing its frequency values, and a vector $\mathbf{v}_R = \left(v_{r1} \cdots v_{rdp_R}\right)^{\mathrm{T}}$ containing its phase velocity, where dp_R is the number of data points of the reference DC. We denote as $\mathbf{f}_{CB}$ a vector containing the n_{CB} elements

which are common in $\mathbf{f}_C$ and $\mathbf{f}_R$ (i.e., the common frequency band between the cross-correlation matrix and the reference DC).

A. *Local maxima detection*

For each frequency within the common frequency band, i.e., for each $f_{seed} \in \mathbf{f}_{CB}$ where $f_{seed} = \mathbf{f}_C(i_{seed})$, we find the corresponding local maxima of $\mathbf{C}$, by searching for elements j such that:

$$\mathbf{C}(i_{seed}, j) > \mathbf{C}(i_{seed}, j \pm 1),\ \forall\ j = \{1,..s_v\} \qquad (5.20),$$

i.e., for the elements of $\mathbf{C}(i_{seed}, j)$ with a cross-correlation amplitude larger than their neighbouring (in the velocity direction) ones. We refer to the vector containing all the $\mathbf{v}_C(j)$ satisfying eq. 5.20 as $\mathbf{v}_{LM}$.

B. *"Seed" point selection*

The value of $f_{seed} = \mathbf{f}_C(i_{seed})$ is the frequency of the "seed" point. To find its velocity, $v_{seed} = \mathbf{v}_C(j_{seed})$, we identify the element of $\mathbf{v}_{LM}$ nearest to the reference DC. If v_{ref}^{seed} is the phase velocity of the reference DC at frequency f_{seed}, i.e.:

$$v_{ref}^{seed} = \mathbf{v}_R(\mathbf{f}_R = f_{seed}) \qquad (5.21),$$

then the "seed" velocity, v_{seed}, is:

$$v_{seed} = \mathbf{v}_{LM}(k)\ \ni\ \left|\mathbf{v}_{LM}(k) - v_{ref}^{seed}\right| \le \left|\mathbf{v}_{LM}(i) - v_{ref}^{seed}\right|, \forall i \in \mathbf{v}_{LM} \quad (5.22).$$

Combining f_{seed} and v_{seed}, a "seed" point, $P(f_{seed}, v_{seed}) = \{\mathbf{f}_C(i_{seed}), \mathbf{v}_C(j_{seed})\}$ is defined.

C. *Candidate curve picking*

The "seed" point, $P(f_{seed}, v_{seed})$, is the first point of the candidate curve. Therefore, the velocity of the candidate curve, $\mathbf{v}_{cand}$, at a frequency f_{seed} is:

$$\mathbf{v}_{cand}\left(i_{seed}\right) = v_{seed} \tag{5.23}$$

To update $\mathbf{v}_{cand}$ for all the frequencies between f_{seed} and $f_{\max}$, a counter jj is initialized to zero and then, $\forall ii \in \left(1, \frac{f_{\max} - f_{seed}}{\delta f}\right)$, jj is incrementally updated, until $\mathbf{C}\left(i_{seed} + ii, j_{seed} + jj\right)$ becomes a local maximum, according to eq. 5.20. The value of $\mathbf{v}_{cand}$ is then updated as:

$$\begin{gathered} \mathbf{v}_{cand}\left(i_{seed} + ii\right) = \mathbf{v}_{\mathbf{C}}(j_{seed} + jj) \\ \text{or} \\ \mathbf{v}_{cand}\left(i_{seed} + ii\right) = \mathbf{v}_{\mathbf{C}}(j_{seed} - jj) \end{gathered} \tag{5.24}$$

depending on the $\pm$ direction where the first local maximum was encountered.

This process is schematized in Figure 5.9. The blue squares are points of an assumed cross-correlation matrix and the numbers on the squares indicate the cross-correlation amplitude at each point. The red square with the blue circle in Figure 5.9a is the "seed" point, found as the local maximum (having a cross-correlation amplitude of 43) of the matrix, nearest to the velocity of the reference DC (green square) at frequency f_{seed}. In the first iteration along frequency (so for $ii = 1$), a search is performed to check if v_{seed} ($jj = 0$) is a local maximum. In this case it is not, since it does not have an amplitude higher than its neighbouring (in the velocity direction) points. Therefore, a second check is performed for the cross-correlation amplitude at $\mathbf{v}_{\mathbf{C}}\left(j_{seed} \pm 1\right)$. In this case, $\mathbf{v}_{\mathbf{C}}\left(j_{seed} - 1\right)$ presented a local maximum (amplitude of 44), and therefore it was picked as the point of the candidate curve at $\mathbf{f}_{\mathbf{C}}\left(i_{seed} + 1\right)$ (it became red in Figure 5.9b). In the next iteration, so for $ii = 2$, the same check is performed, i.e., we check which of the components of the matrix along the column of $\mathbf{f}_{\mathbf{C}}\left(i_{seed} + 2\right)$ is the one that is a local maximum, nearest to $\mathbf{v}_{\mathbf{C}}\left(j_{seed} - 1\right)$ and so on, until a point has been picked for all the frequencies between f_{seed} and $f_{\max}$ (Figure 5.9c).

The same process is repeated "backwards" in the interval $\left(f_{\min}, f_{seed}\right)$: starting from $P\left(f_{seed}, v_{seed}\right)$ and reducing i_{seed} by $ii \in \left(1, \frac{f_{seed} - f_{\min}}{\delta f}\right)$, the nearest to v_{seed}

local maxima of $\mathbf{C}(i_{seed}-ii, j_{seed}\pm jj)$ are identified and their $\mathbf{v}_\mathbf{C}$ coordinates update the vector $\mathbf{v}_{cand}$. When this process is finalized for all the frequencies, the complete candidate curve $(\mathbf{f}_\mathbf{C}, \mathbf{v}_{cand})$ has been retrieved, starting from a single $P(f_{seed}, v_{seed})$ point.

In the end, the process is repeated $\forall f_{seed} \in \mathbf{f}_{CB}$, i.e., starting from every "seed" inside the common frequency band, to pick a set of n_{CB} candidate curves.

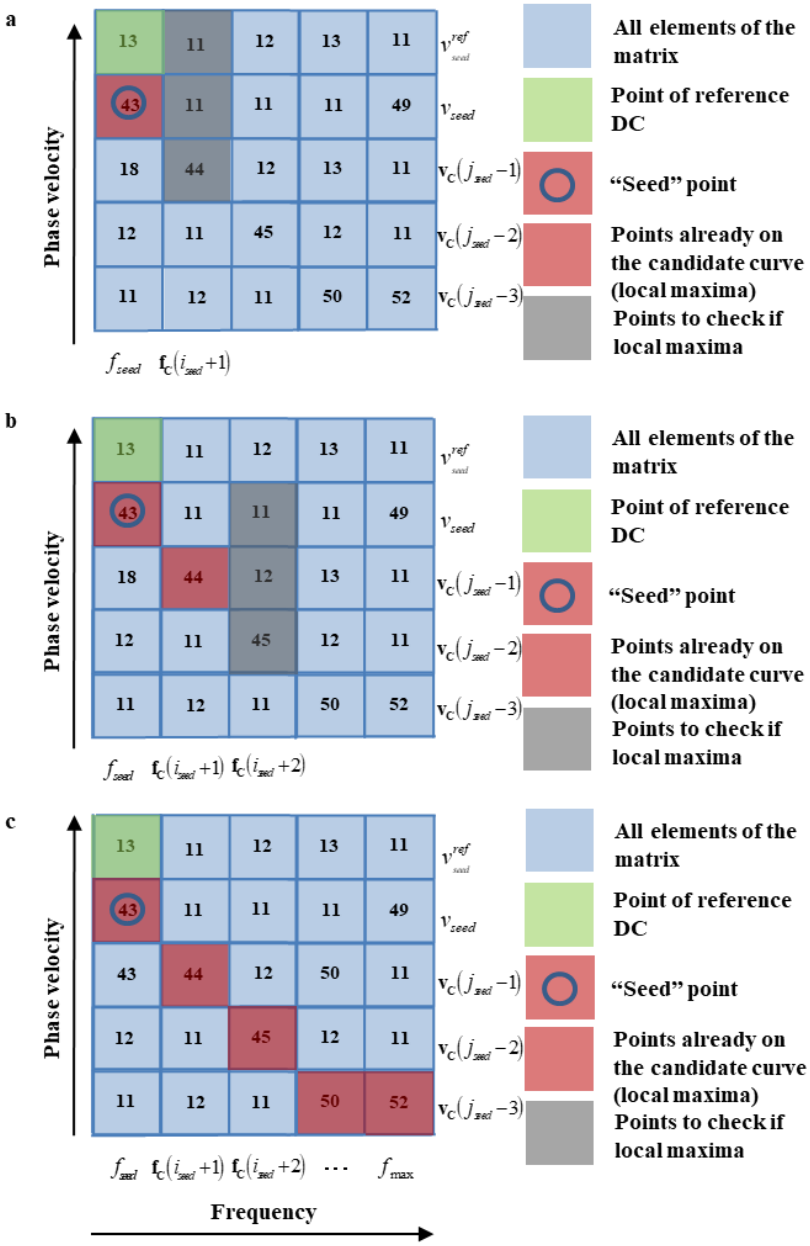

Figure 5.9: Picking of a candidate curve. In all panels, in green, the reference DC and in red with a blue circle, the seed point; in grey, the points to be checked as local maxima and in red, the points identified as local maxima.

D. *Best candidate curve detection*

The n_{CB} candidate curves, picked from all the seeds, are compared with the reference DC in their entire common $\mathbf{f}_{CB}$, to identify the best candidate, i.e. the candidate curve which is nearest to the reference and is, therefore, most likely representative of the actual SW dispersion. For each q candidate DC, we compute the l_1 norm distance of its velocity $\mathbf{v}_{cand}^{q}(i)$ from $\mathbf{v}_R(i)$ within the common frequency band:

$$d_q = \sum_{i=1}^{n_{CB}} \left| \mathbf{v}_{cand}^{q}(i) - \mathbf{v}_R(i) \right|, \; i \in (1, n_{CB}) \tag{5.25}.$$

The velocity of the best candidate is the one that minimizes 5.25, i.e.:

$$\mathbf{v}_{cand}^{q^{best}} : \; q^{best} = \arg\min_{q}(d_q) \tag{5.26}.$$

The picked DC from the cross-correlation matrix $\mathbf{C}$ is:

$$\mathbf{dc} = \left\{ \mathbf{f}_{\mathbf{C}}, \mathbf{v}_{cand}^{q^{best}} \right\} \tag{5.27}.$$

For the same receiver pair, DCs are picked on all of its computed individual $\mathbf{C}^k$ and on the stacked $\mathbf{C}^{stack}$, but only the DC from $\mathbf{C}^{stack}$ (stacked DC) will be used in the inversion, since it is considered more reliable. The purpose of picking the DCs also from the $\mathbf{C}^k$ (individual DCs), is that they can provide a measure of the experimental uncertainty, to be used as a weight in the inversion of the stacked DC. In particular, we compute as the experimental uncertainty, the standard deviation of the phase velocities of the individual DCs. The following DC cleaning steps, will be applied only on the stacked DC.

Table 5.5: *DC picking pseudocode.*

Algorithm: DC Picking

Input: Stacked or individual cross-correlation matrix (C), Velocity (v_c) and frequency (f_C) domain of the cross-correlation matrix, velocity (v_R) and frequency (f_R) of the reference DC

Output: Picked DC (DC)

---

read C, f_C, v_C
read f_R, v_R
% Find the common band between cross-correlation matrix and reference DC
do f_{CB} = find_common_band (f_C, f_R)
% Start searching from the first element of the common frequency band
for f_{seed} **from** 1 **to** f_{CB}
% to find the seed velocities at each f_{seed}
  do v_{seed} = Find_local_maxima (C(:,f_{seed}))
% Start picking the maxima at all the other frequencies of the cross-correlation matrix
    for f_{ci} **from** *1* **to** f_R
% looking for the local maxima nearest to the seed
      do v_{cand} = Find_nearest_local_maxima (C(:,f_{ci}))
      $t_{b=}$ t_{b+1}
    end
% You have created one candidate curve Now find the candidate curve for the next seed
  end
% Now find the L_1 norm distance of all the candidate curves from the reference DC
do $d(i)$ = computeL1_norm ($v^i_{cand}(f_{CB})$, v_R (f_{CB}))
% Now find the best candidate
do v_{BEST} = find_v$_{cand}$_with_min_d(i) (d, v_{cand})
% Create the DC
do DC = [f_C v_{BEST}]
end

5.6.2 Examples

As example, in Figure 5.10 we show the DC picking on the stacked cross-correlation matrix of Figure 5.7d.

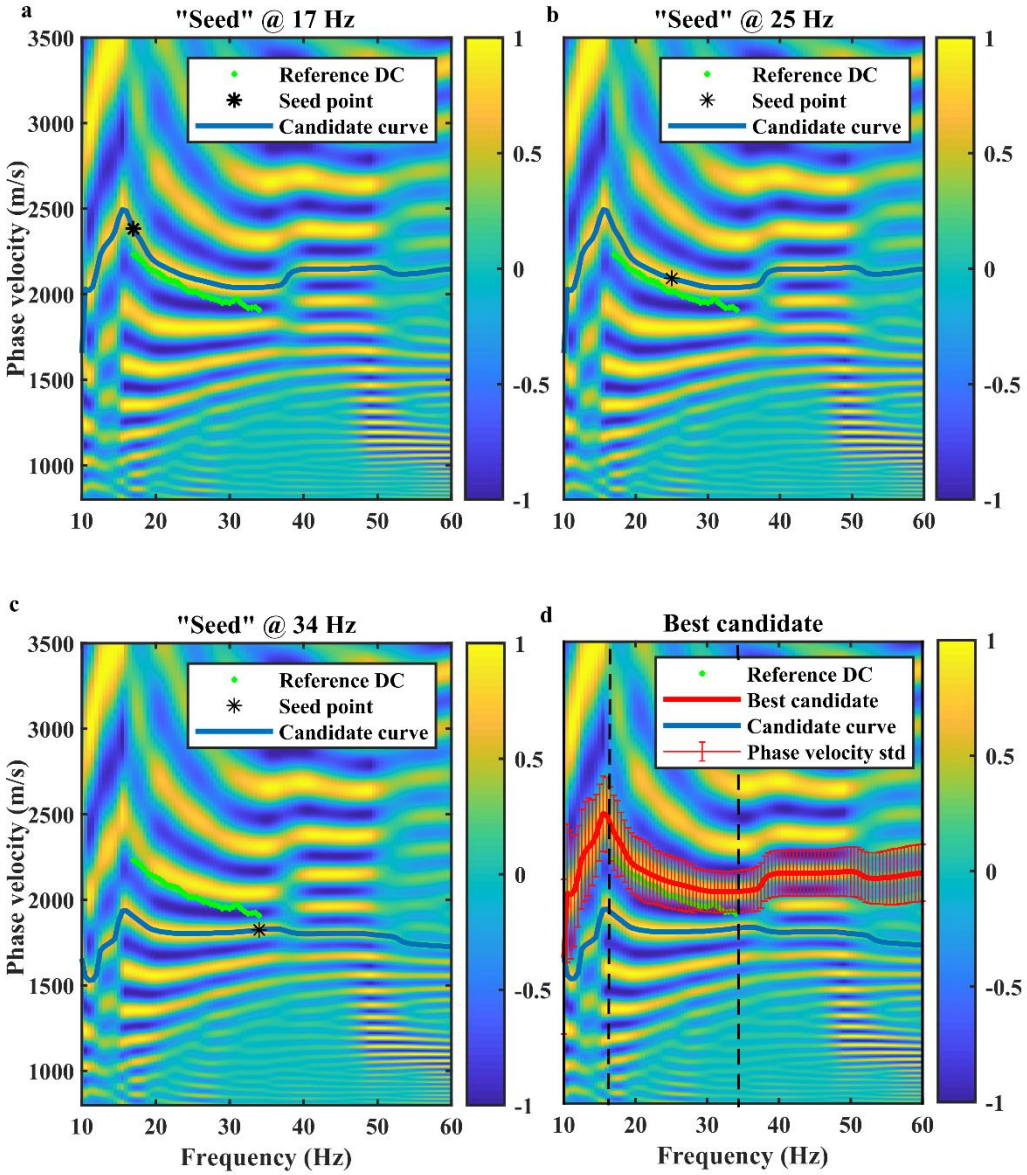

Figure 5.10: Picking the DC on the stacked cross-correlation matrix of Figure 5.7d. In green, the reference DC and in blue, the picked candidate curve. In (a)-(c), the stars are the "seed" points. In (d), in black, the limits of the common frequency band between candidate and reference DC. In red, the best candidate.

In Figure 5.10a, the reference DC (green) is superimposed on the matrix. The common frequency band between the reference DC and the matrix is between 17 Hz and 34 Hz. The first "seed" point, found as the local maximum of the matrix, nearest to the reference DC at 17 Hz, is plotted as an asterisk in Figure 5.10a, while the picked candidate curve is shown in blue. In the same manner, all the frequencies between 17 Hz and 34 Hz were used as "seed" frequencies and different candidate curves were obtained. Corresponding to most of the "seed" frequencies, the same

candidate curve was obtained, e.g., for the "seed" at 25 Hz, shown in Figure 5.10b the candidate DC (blue line) is the same as the one of Figure 5.10a. Nevertheless, the "seeds" obtained for frequencies >32.5 Hz, provided a candidate curve at lower velocities, as for instance the "seed" at 34 Hz (asterisk in Figure 5.10c), which provided the candidate shown in blue in Figure 5.10c. When all candidates were retrieved, their distance from the reference DC was computed, according to eq. 5.25, for their common frequency band (17 Hz – 34 Hz, black dashed in Figure 5.10d). The best candidate, which minimized the distance from the reference, was the one shown in red in Figure 5.10d, and it was saved as the picked DC for the specific matrix. The error bars indicate the phase-velocity standard deviation, computed from the DCs picked on the individual-shot cross-correlation matrices (not shown in Figure 5.10) and saved, to be used as the experimental uncertainty during the inversion.

For our synthetic example, the best candidate, picked on the cross-correlation matrix of Figure 5.10e, is shown in Figure 5.11 in red while, in green, we show the reference DC. It is apparent that in this case, the picked DC is almost identical to the reference DC, and therefore, even a single "seed" point would be sufficient to pick the correct maxima on the matrix.

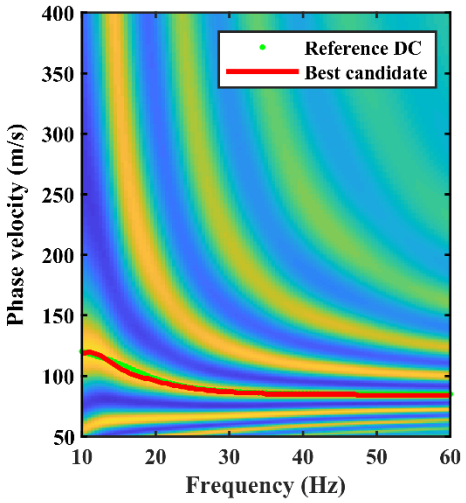

Figure 5.11: In red, the DC picked from the synthetic cross-correlation matrix, shown also in Figure 5.9e. In green, the reference DC.

5.7 DC Cleaning

The method described in the previous stage resulted in a DC which was picked as a set of local maxima of the stacked cross-correlation matrix along its entire frequency band.

Nevertheless, so far there has been no guarantee that the picked maxima are indeed representative of SW dispersion. The cross-correlation presents a maximum at the time-lag when the entire recorded waveform, or at least its most energetic component, becomes in-phase. If the recorded traces were dominated by SW in the entire frequency band, the picked curve is expected to present a smooth and dispersive pattern, corresponding to uniform (along frequency) and always high cross-correlation amplitudes (as for instance the curve shown in red in Figure 5.11).

If the recorded traces were not dominated by SW, the cross-correlation would only indicate the time when two, spurious for our purpose, events became in-phase. If SW were dominant only within a specific frequency band, then only an "effective" portion of the picked curve would be related to SW, while the rest of it would again be spurious. In both cases, the cross-correlation amplitudes at the DC coordinates would not be uniform (always high) and the picked curve would not be smooth and dispersive in the entire frequency band: at each frequency, a different event of different amplitude and velocity would dominate the cross-correlation. Such a behaviour can be observed, for instance, in the curve shown in red in Figure 5.10d.

The method proposed here, establishes the frequency band for which the picked curve is representative of SW dispersion. The **main idea** of our method is to search for bands where the cross-correlation amplitudes drop and the smoothness of the curve presents "breaks", signifying a transition to a non-SW related event. In our global workflow, the method is applied only on the stacked DC, since this will be the final outcome to be inverted. Therefore, to simplify the description, we onward refer to the stacked DC and the stacked cross-correlation matrix, respectively, as DC and $\mathbf{C}$.

5.7.1 Description of the method

The proposed method is summarized in the pseudocode of Table 5.6. Input to the method is the stacked cross-correlation matrix $\mathbf{C}$ and the picked DC, which corresponds to a discrete set coordinates of $\mathbf{C}$. It contains n_{dp} data points and is structured as

- A vector of frequencies: $\mathbf{f}_{DC} = \left(f_1 = f_{\min} \cdots f_{n_{dp}} = f_{\max} \right)^{\mathrm{T}}$
- A vector of phase velocities: $\mathbf{v}_{DC} = \left(v_1 \cdots v_{n_{dp}} \right)^{\mathrm{T}}$

The vector containing the cross-correlation amplitudes at the coordinates of the DC is denoted as $\mathbf{cc}$:

$$\mathbf{cc}(i) = \mathbf{C}(i, j), \text{ where } \mathbf{v}_{\mathbf{C}}(j) = \mathbf{v}_{DC}(i) \tag{5.28}$$

Our method, in essence, detects the $\mathbf{f}_{DC}(i)$ frequencies where the value of $\mathbf{cc}(i)$ presents a significant drop and at the same time, the value of $\mathbf{v}_{DC}(i)$ suddenly changes. To detect them, we make a quantitative analysis of the trends of $\mathbf{cc}$ and $\mathbf{v}_{DC}$ with respect to $\mathbf{f}_{DC}$. The adopted approach can be easily described, neglecting the discrete nature of our problem, and assuming that $\mathbf{cc}$ and $\mathbf{v}_{DC}$ are functions over a continuous space f, i.e.,

$$\begin{gathered} V_{DC}(f) : (f_{\min}, f_{\max}) \to R \\ \text{and} \\ CC(f) : (f_{\min}, f_{\max}) \to R \end{gathered} \tag{5.29}$$

We perform a search for frequencies f_b, for which $CC(f_b)$ is a *local minimum* and the rate of change of V_{DC} over f, i.e. its derivative $\frac{dV_{DC}}{df}$, presents *local extrema*. We therefore impose that:

Condition 1:

$$\left.\frac{dCC}{df}\right|_{f_b} = 0 \quad \text{and} \quad \left.\frac{d^2CC}{df^2}\right|_{f_b} > 0 \tag{5.30},$$

and that

Condition 2:

$$\left.\frac{d^2V_{DC}}{df^2}\right|_{f_b} = 0 \tag{5.31}.$$

When both conditions are fulfilled, this signifies a *breaking point*, i.e. a frequency f_b where a new event becomes dominant.

This process splits the $\left(f_{\min}, f_{\max}\right)$ band into distinct intervals. In particular, if we assume that a number of n_b breaking points, i.e., $f_b = \left\{f_{b_1} \cdots f_{b_{n_b}}\right\}$, satisfy eq. 5.30 and eq. 5.31, and by setting as $f_{n_{b_0}} = f_{\min}$ and as $f_{n_{b_{n_b+1}}} = f_{\max}$ (so that the first interval begins from $f_{\min}$ and the last ends to $f_{\max}$), the produced intervals can be defined as:

$$\mathbf{f}_{int}\left(l\right) = \left(f_{b_{l-1}}, f_{b_l}\right),\ l \le n_b + 1 \tag{5.32}.$$

Their union is the entire $\left(f_{\min}, f_{\max}\right)$:

$$\left(f_{\min}, f_{\max}\right) = \bigcup_{l \in (0 \cdots n_b+1)} \mathbf{f}_{int}\left(l\right) \tag{5.33}.$$

To select which of the $\mathbf{f}_{int}$ subsets corresponds to the DC, we make the assumption that in the traces, the energetically dominant event in the broadest frequency band, is the SW. We therefore anticipate that the part of the cross-correlation matrix associated with SW, presents, with respect to all the other parts, the highest CC for the broadest frequency band. Under this assumption, we perform a search for the *broadest band* for which the CC amplitude is *maximized*.

This can be easily achieved in a continuous space, by computing the area below the curve (the integral), of CC with respect to f, that we denote as A^l_{CC}, separately for each $\mathbf{f}_{int}$, and select the interval with the maximum A^l_{CC} value. We therefore seek $l_{\max}$:

Condition 3: $$l_{\max} = \arg\max_l A^l_{CC} = \arg\max_l \int_{f_{b_l}}^{f_{b_{l+1}}} CC(f)df \; l \in \{0, \cdots, n_{b+1}\} \quad (5.34).$$

The phase velocity of the "cleaned" DC is then the restriction of the function $V_{DC}(f)$ in $\left(f_{l_{\max}}, f_{l_{\max}+1}\right)$ and its frequency is $\mathbf{f}_{int}\left(l_{\max}\right)$.

For our discrete implementation, the DC is the set $\mathbf{f}_{DC}(i), \mathbf{v}_{DC}(i)$. Therefore, to check whether a point of the DC is a local minimum (and therefore satisfies **Condition 1**) it is preferable, instead of using an unstable numerical differentiation scheme, to check for points i which satisfy:

$$\mathbf{cc}(i) < \mathbf{cc}(i \pm 1) \quad (5.35),$$

i.e., which have a value lower than their neighbours. To check whether the rate of change of the phase velocity presents peaks (**Condition 2**), we approximate the derivative of $\mathbf{v}_{DC}$ as:

$$\mathbf{v}^d_{DC} = \frac{\mathbf{v}_{DC}(i+1) - \mathbf{v}_{DC}(i)}{\delta f} \quad (5.36),$$

and look for its local extrema by checking:

$$\begin{gathered} \mathbf{v}^d_{DC}(i) < \mathbf{v}^d_{DC}(i+1) \wedge \mathbf{v}^d_{DC}(i) < \mathbf{v}^d_{DC}(i-1) \\ \vee \\ \mathbf{v}^d_{DC}(i) > \mathbf{v}^d_{DC}(i+1) \wedge \mathbf{v}^d_{DC}(i) > \mathbf{v}^d_{DC}(i-1) \end{gathered} \quad (5.37).$$

The $\mathbf{f}_{DC}(i), \mathbf{v}_{DC}(i)$ points which satisfy eq. 5.35 and eq. 5.37, are the coordinates where $\mathbf{cc}$ presents a local minimum and, at the same time, presents a "break": the breaking points $\mathbf{bp}$. If n_{bp} breaking points exist, the frequency vector $\mathbf{f}_{DC}$ is split into $n_{bp}+1$ intervals $\mathbf{f}_{int}(l)$, within which, the cross-correlation

amplitude **cc** and the phase velocity $\mathbf{v}_{DC}$ vary smoothly. We approximate the integral A^{l}_{CC} as:

$$\mathbf{A}_{cc}(l) = \sum_{\mathbf{bp}(l)\le i<\mathbf{bp}(l+1)} \mathbf{cc}(i), l < n_{bp} \quad (5.38),$$

and retrieve its maximum value (**Condition 3**):

$$\mathbf{A}_{cc}^{\max} = \mathbf{A}_{cc}(l_{\max}) \ \ni \ \mathbf{A}_{cc}(l_{\max}) > \mathbf{A}_{cc}(l), \forall l \neq l_{\max} \quad (5.39).$$

Finally, the frequency band of the cleaned DC is

$$\mathbf{f}_{cleaned} = \mathbf{f}_{\text{int}}(l_{\max}) = \mathbf{f}_{DC}\left[\mathbf{bp}(l_{\max}), \mathbf{bp}(l_{\max})+1, \cdots, \mathbf{bp}(l_{\max}+1)\right]^{\mathbf{T}} \quad (5.40),$$

i.e. the part of $\mathbf{f}_{DC}$ that starts from the breaking point $\mathbf{bp}(l_{max})$ up to the next breaking point $\mathbf{bp}(l_{max}+1)$. The phase velocity of the cleaned DC equals

$$\mathbf{v}_{cleaned} = \mathbf{v}_{DC}\left[\mathbf{bp}(l_{\max}), \mathbf{bp}(l_{\max})+1, \cdots, \mathbf{bp}(l_{\max}+1)\right]^{\mathbf{T}} \quad (5.41).$$

The picking and cleaning processes are repeated for the picked DCs of all the N_{pairs} selected receiver pairs, leading to the estimation of a N_{DC_clean} cleaned DCs.

Table 5.6: *DC Cleaning pseudocode.*

Algorithm: DC Cleaning

Input: Stacked cross-correlation matrix C, Phase Velocity (v_{DC}) and frequency (f_{DC}) of the picked DC

Output: Picked DC (DC)

---

1 **read** C, f_{DC}, v_{DC}

% Compute the value of C at f_{DC} and v_{DC}

2 **do** $cc = C(v_{DC}, f_{DC})$

% Find the local minima of cc

3 **do** *lm=find_local_minima(cc)*

% Compute the derivative of v_{DC}

4 **do** v_{DC}^{d} = der(v_{DC})

% Find the local extrema of v_{DC}^{d} at the local minima of cc

5 **do** *bp*=find_local_minima/maxima*(cc(lm))*

% Find the intervals of the frequency band between the bp points

6 **do** *Int= break_f_{DC}_into_intervals*

% Find the integral of cc inside the intervals

7 **do** *Area=cc*Int*

% And find its maximum

8 **do** *clean_f_{DC}=find*(max(*Area*))

% Compute the phase velocity corresponding to *clean_f_{DC}*

9 **do** *clean_v_{DC}= v_{DC}(clean_f_{DC})*

5.7.2 Examples

In Figure 5.12, we demonstrate the cleaning of the DC of Figure 5.10d. In Figure 5.12a, we plot the cross-correlation amplitude (CC) corresponding to the DC, as a function of frequency. The triangles are the local minima of CC, which were in total 4. Their corresponding frequencies are checked for local extrema on $\frac{dV_{DC}}{df}$ (plotted in Figure 5.12b). In total, three local extrema are identified at frequencies corresponding to local minima and are plotted as black triangles in Figure 5.12b. Therefore, the black triangles are the *breaking points* bp that split the frequency band of the DC into four intervals ($f_{int,1} - f_{int,4}$), for which we separately compute the corresponding area below the plot (integral) of CC with respect to the frequency, A_{CC}.

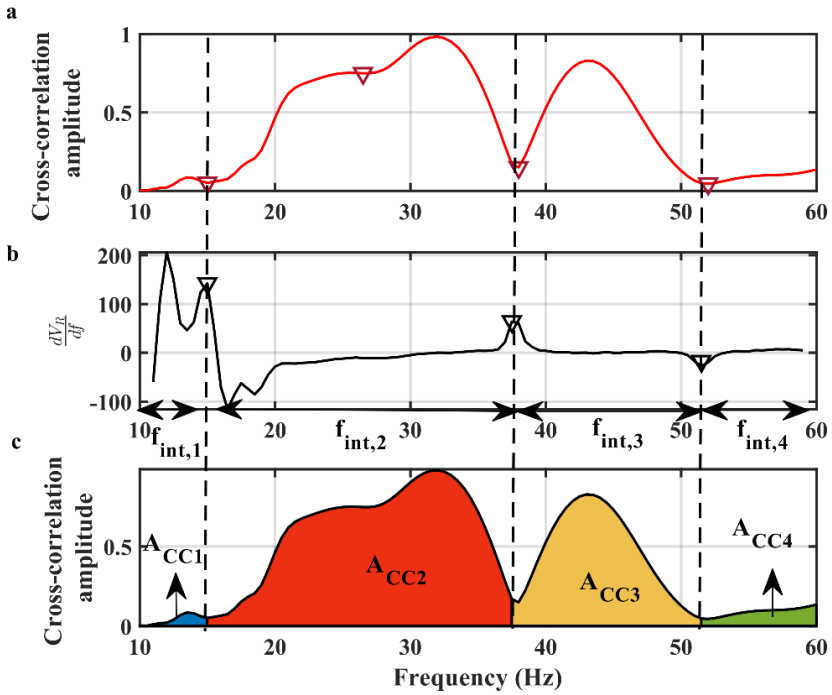

Figure 5.12: Plot of a) the (normalized) cross-correlation amplitude and b) the derivative of the phase velocity of the DC. The red triangles are the local minima of (a), and the black triangles are also local extrema of (b). c) Same as (a), color-coding the area below the curve between $f_{int,1} - f_{int,4}$.

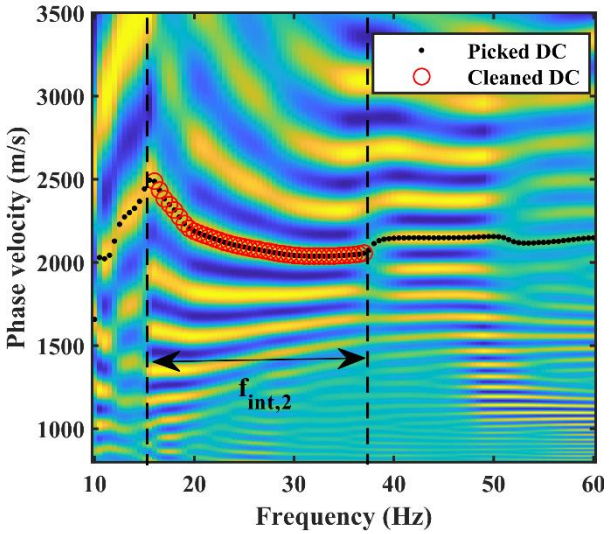

Figure 5.13. Same as in Figure 5.10d. In red, the portion of the DC which was kept after the DC cleaning.

In Figure 5.12c, we plot again the CC, color-coding the areas A_{CC} ($A_{CC,1} - A_{CC,4}$, respectively). The interval with the largest area (coloured in red), is

$f_{int,2}$, corresponding to a frequency band of 15 Hz – 37.5 Hz. Therefore, the only portion of the DC that is considered reliable and kept is the one within $f_{int,2}$ (red circles in Figure 5.13), and rest of the curve is disregarded.

5.8 Removal of outlier DCs

With the cleaning process described in Section 5.7, each DC were cleaned from low-amplitude and discontinuous frequency bands, and therefore all the DCs have a smooth trend and correspond to high cross-correlation values. Nevertheless, the cleaning did not take care of the following issue: it is possible that the achieved smooth trend of the DCs falls on wrong velocities, e.g., because several maxima of a cross-correlation matrix were very close to the reference DC and the wrong maxima were picked.

Assuming that such problems are exceptions, we deal with these DCs as outliers and detect them, based on their phase velocity, among all the other DCs. The **key idea** is that the phase velocity at a given frequency of a set of curves, whose paths scan the same subsurface zone (such as the paths shown as lines in Figure 5.14, which overlap in the area highlighted in grey and denoted as "A"), should be internally consistent (Zahedi, 2020). DC data points which belong to wrong maxima will have a significantly different velocity with respect to all the other DCs in the same zone, allowing their detection.

However, a set of DCs which scan the same confined portion might have different velocities, not due to mistakes in the DC picking, but because their paths are different and might be crossing subsurface portions which are laterally heterogeneous. For instance, the paths in Figure 5.14, overlap inside the zone denoted as "A" but each one of them scans different areas, which might have different properties. To ensure that the information on the lateral variability of the subsurface properties is preserved, we reject a DC only if it is detected as an outlier in most of the locations along its path.

To do so, we compare the phase velocities of the DCs, using their position (given by the coordinates of the corresponding path) and wavelength. We therefore consider our domain as a 3D ($x-y-\lambda$) volume and discretize it into voxels. In each voxel, we evaluate the distribution of the phase velocities of all the included DC points and detect the ones which are outliers using a median-based analysis. To

characterise the entire DC as an outlier and remove it from the dataset, we check if its data points have been flagged as outliers in more than half the voxels to which it belongs.

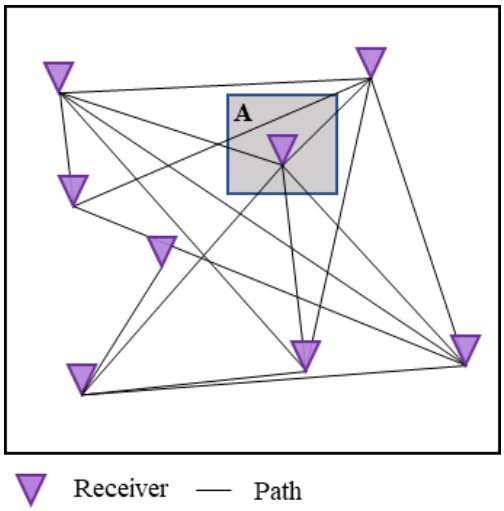

Figure 5.14: Illustration of paths (lines) between different receivers (triangles).

5.8.1. Method description

We describe the method with reference to the pseudocode of Table 5.7. The input of this method is the dataset of the N_{DC_clean} cleaned DCs, output from the cleaning stage of the workflow. Each k DC, corresponding to a different R_1R_2 receiver pair, contains a different number of data points, $n_{dp,k}$, and is structured as:

- A vector of frequencies $\mathbf{f}_k = \left(f_1 \cdots f_{n_{dp,k}}\right)^{\mathrm{T}}$,
- A vector of phase velocities $\mathbf{v}_k = \left(v_1 \cdots v_{n_{dp,k}}\right)^{\mathrm{T}}$.

A vector $\mathbf{p}_k = \left(x_{k1}, y_{k1}, x_{k2}, y_{k2}\right)^{\mathrm{T}}$, contains the $x-y$ coordinates of the corresponding receivers R_{k1} and R_{k2}, respectively. The DC wavelengths λ are computed as:

$$\boldsymbol{\lambda}_k = \mathbf{v}_k \circ \mathbf{f}_k^{-1} \tag{5.42}.$$

Given these inputs, in the following, the k-th DC ($\mathbf{DC_k}$) of the dataset will be referred to as the tuple:

$$(\boldsymbol{\lambda}_k, \mathbf{v}_k, \mathbf{p}_k, k) \quad (5.43).$$

Moreover, we will refer to each point of the DC individually as a *data point*. As the i-th data point of the k-th DC (i,k), we will refer to the tuple:

$$(\lambda_{i,k}, \mathrm{v}_{i,k}, \mathbf{p}_k, k) \quad (5.44),$$

where $i \in \{1...n_{dp,k}\}$.

3D space parameterization

The minimum value of the x-coordinates of the entire set of N_{DC_clean} DCs is denoted as $x_{\min}$ and the maximum as $x_{\max}$, and, respectively, for the y-coordinates as $y_{\min}$ and $y_{\max}$. The minimum wavelength of all the DCs is denoted as $\lambda_{\min}$ and the maximum $\lambda_{\max}$. We consider the 3D $(x-y-\lambda)$ space which encloses the spatial and wavelength coordinates of all the DCs, and has the following dimensions (Figure 5.15):

$$(x_{\min}, x_{\max}) \times (y_{\min}, y_{\max}) \times (\lambda_{\min}, \lambda_{\max}) \quad (5.45).$$

We perform a discretization of the 3D space as following:

- The $x-y$ dimension is uniformly discretized on a user-defined $N \times M$ grid. Therefore, the x-axis is split into N parts with size $\frac{x_{\max} - x_{\min}}{N}$, and the y-axis into M parts with size $\frac{y_{\max} - y_{\min}}{M}$.
- The discretization on the λ-axis corresponds to the L unique wavelength values contained in all the DCs, i.e., in all the $\boldsymbol{\lambda}_k, k \in (1, N_{DC\_clean})$ vectors, rounded to a common decimal.

Therefore, the λ discretization is such that each data point of the dataset can be associated to only one λ grid, but it can be associated to several $x-y$ grids, depending on the length and location of the corresponding path. We note that the suitability of the chosen N and M values is not critical at this stage and it will be

verified in a later stage of the process. Therefore, a reasonable "guess" is sufficient to begin with.

With these limits and discretization, our 3D space, onward referred to as *voxel space*, can be described as:

$$\mathbf{V} = \overbrace{(x_{\min}, x_{\max})}^{\text{in } N \text{ parts}} \times \overbrace{(y_{\min}, y_{\max})}^{\text{in } M \text{ parts}} \times \overbrace{(\lambda_{\min}, \lambda_{\max})}^{\text{in } L \text{ parts}} \tag{5.46}$$

Each (n,m,l) element of $\mathbf{V}$ is a *voxel* with dimensions:

$$(x_n, x_{n+1}) \times (y_m, y_{m+1}) \times (\lambda_l, \lambda_{l+1}) \tag{5.47}$$

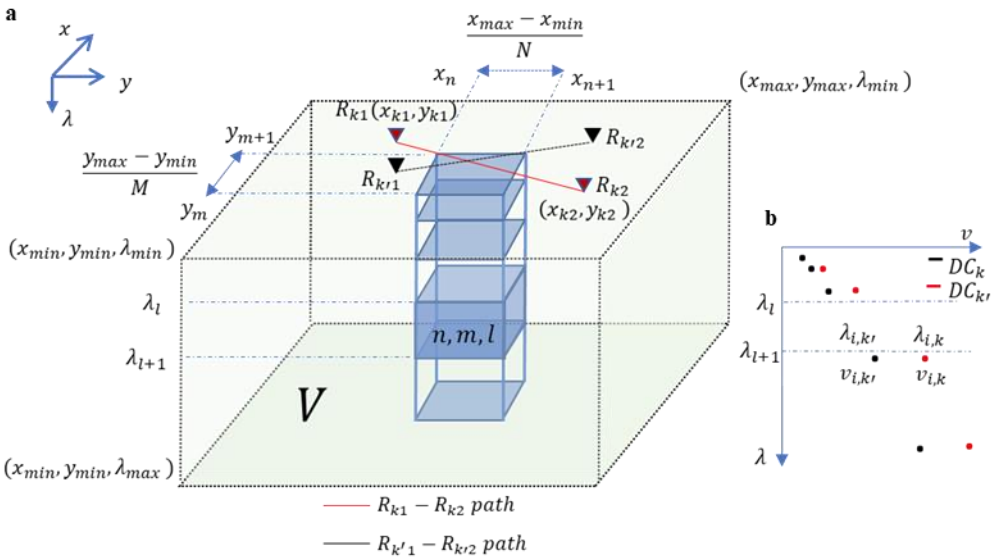

Figure 5.15: a) Scheme of the created 3D voxel workspace and its discretization. b) Two different DCs. Their paths are shown in the same colour in (a).

Allocation of data points to voxels

Once the voxel space has been constructed, the phase velocity of each data point is ascribed to voxels, depending on their $x-y-\lambda$ correspondence. Specifically, **one** specific i-th **data point** of the k-th DC is considered to correspond to **one** (n,m,l) **voxel**, if the following conditions are met:

- **Condition 1:** The path connecting the $\mathbf{p}_k$ coordinates crosses the $(x_n, x_{n+1}) \times (y_m, y_{m+1})$ area and,

- **Condition 2:** $\lambda_l < \lambda_{i,k} \leq \lambda_{l+1}$.

The two conditions might be fulfilled by data points belonging to different DCs, crossing the same $(x_n, x_{n+1}) \times (y_m, y_{m+1})$ area and having the same λ_i. For instance, the data points A and B in Figure 5.15b, have the same wavelength but belong to DC_k and $DC_{k'}$, respectively. The two curves correspond to two different paths (shown with the same colorscale in Figure 5.15a), which cross the same (n,m,l) voxel. Using **all the** (i,k) **data points** that correspond to the **same** (n,m,l) **voxel**, i.e., all the data points for which **Conditions 1** and **2** hold true, we build a vector $\mathbf{d}_{n,m,l}$, which contains their corresponding $v_{i,k}$ values:

$$\mathbf{d}_{n,m,l} = \left(v_{i,k} \cdots\right)^{\mathrm{T}} \tag{5.48}.$$

Detection of outlier data points

The distribution of values in $\mathbf{d}_{n,m,l}$ is used in a statistical analysis, to check for outlier velocities in the voxel. We use as a metric the centrality of the distribution, i.e. its median (μ). We follow the standard median-based outlier detection, according to which, the measured distribution is split into quartiles. The median estimator is the second quartile, $\mu_{1/2}$, while the distance between the lower quartile $\mu_{1/4}$ and the upper quartile $\mu_{3/4}$ is the inter-quartile distance. We flag a data point as an outlier in a voxel if (**Condition 3**):

$$\begin{aligned} v_{i,k} &> \mu_{3/4}(\mathbf{d}_{n,m,l}) + 1.5 \cdot \left(\mu_{3/4}(\mathbf{d}_{n,m,l}) - \mu_{1/4}(\mathbf{d}_{n,m,l})\right) \\ &\vee \\ v_{i,k} &< \mu_{1/4}(\mathbf{d}_{n,m,l}) - 1.5 \cdot \left(\mu_{3/4}(\mathbf{d}_{n,m,l}) - \mu_{1/4}(\mathbf{d}_{n,m,l})\right) \end{aligned} \tag{5,49},$$

i.e., if its velocity is larger than the upper quantile by more than 1.5 times the inter-quantile distance, or, if it is lower than the lower quantile by more than 1.5 the inter-quantile distance.

Detection and removal of outlier DCs

We characterize a DC as an outlier based on how "often" its data points have been flagged as outliers in the voxel space. Specifically, we define a function

$$\mathbf{P}\left[(n,m,l),\mathbf{DC_k}\right]=\begin{cases}1 & \mathbf{DC_k}\text{ has data points in }(n,m,l)\text{ voxel}\\ 0 & \text{otherwise}\end{cases} \quad (5.50),$$

which takes the value 1 if **Conditions 1** and **2** are true for any component of $\mathbf{DC_k}$. Additionally, we define a function

$$\mathbf{O}\left[(n,m,l),\mathbf{DC_k}\right]=\begin{cases}1 & \mathbf{DC_k}\text{ has an outlier in }(n,m,l)\text{ voxel}\\ 0 & \text{otherwise}\end{cases} \quad (5.51),$$

which takes the value 1 if **Conditions 1** and **2** are true for any component of $\mathbf{DC_k}$ and if any of the components was flagged as an outlier, according to **Condition 3**. We then compute:

$$e_{\mathbf{DC_k}}=\frac{\sum_{n=1}^{N}\sum_{m=1}^{M}\sum_{l=1}^{L}\mathbf{O}\left[(n,m,l),\mathbf{DC_k}\right]}{\sum_{n=1}^{N}\sum_{m=1}^{M}\sum_{l=1}^{L}\mathbf{P}\left[(n,m,l),\mathbf{DC_k}\right]} \quad (5.52)$$

and if $e_{\mathbf{DC_k}}\geq\frac{1}{2}$, i.e., if the data points of $\mathbf{DC_k}$ were flagged as outliers in more than half the voxels, $\mathbf{DC_k}$ is considered an outlier and removed from the dataset.

Table 5.7: *Removal of outlier DCs pseudocode.*

Algorithm: Removal of outlier DCs
Input: N_{dc_clean} picked and clean DCs (including their velocity v_{dc}, wavelength, λ_{dc}, coordinates p_{dc} (x,y)(i)
Output: Outlier DCs

```
% Compute the voxel space
1  do V = [min_of_all_x max_of_all_x],[min_of_all_y max_of_all_y],[min_of_all_λ
max_of_all_λ]
% Split it in voxels
2  do all_voxels = V/(N,M,N_L)
% Check in all the voxels
3  for voxel from 1 to all_voxels
% And all the DCs
4    for dc_k from 1 to N_dc_clean
5      read v_DC,k, λ_DC,k, p_DC,k
% Check if the i-th component of the DC belongs to the voxel
6       if dc_k(i) =belongs_to(voxel)
% Create a vector with all the velocities in the voxel
7         do d(voxel) = [d(voxel), v_DC,k(i)]
% and flag that the DC k has a data point that belongs to a voxel
8         do P(k,i)=1
9       end
10    end
11 end
% Detect outlier velocities at each voxel with the median criterion
12  for voxel from 1 to all_voxels
13    for dc_k from 1 to N_dc_clean
14       if dc_k(i) =outlier_in(d(voxel))
% Flag that the DC k has a data point that is outlier in a voxel
15         do O(k,i)=1
16       end
17    end
18 end
19 if O(k)/P(k)
20    do dc_k=outlier
21 end
```

5.8.2 Examples

In the following, we demonstrate the outlier-detection method, using three synthetic examples. In the first case, the phase velocity distribution of the DCs is uniform and no outlier DCs exist. The second case presents the results when an outlier DC is introduced, and the third case shows the results when the subsurface properties change abruptly (strong phase velocity variability exists), but no outlier DCs are introduced.

Case 1: No outlier data points, no outlier DCs

In Figure 5.16a, we show a set of synthetic DCs computed, using the forward modelling described in Socco et al. (2014), for 121 1D layered synthetic velocity models, the properties of which are presented in Table 5.8. The location of the models was assumed at the positions indicated by the green asterisks in Figure 5.16b, and for the modelling we assumed the receiver geometry shown as black triangles, and the intra-receiver paths shown as lines.

Table 5.8: *Properties of the synthetic 1D models.*

	Cases 1 and 2	**Case 3**
Number of layers	6	6
Layer V_S	375 - 600 m/s ± 1%	375 - 600 m/s ± 1% and 550 - 800 m/s ± 1% for x = 0 – 40 m and y=10 – 40 m
Layer ν	0.2 m/s	0.2 m/s
Layer ρ	1 m	1 m
Layer h	4 m + halfspace	4 m + halfspace

The colour-scale in Figure 5.16b, indicates the phase velocity of the DCs at a wavelength of 3 m, while the black lines show the dimensions of the voxel discretization in the $x-y$ plane. The complete voxel-space is shown in Figure 5.16c, where the colours represent the median phase velocities, computed at each voxel (same colorscale as in Figure 5.16b).

In Figure 5.16d, we show the resulting boxplots computed according to eq. 5.49 for the voxels at $\lambda = 3\,\mathrm{m}$ (Figure 5.16b). The median phase velocity is shown as a red line and the length of the boxes corresponds to the intra-quantile distance. No phase velocities were measured outside the boundaries set in eq. 5.49, and therefore no outliers were detected. The result (not shown) was the same for all the voxels of Figure 5.16c.

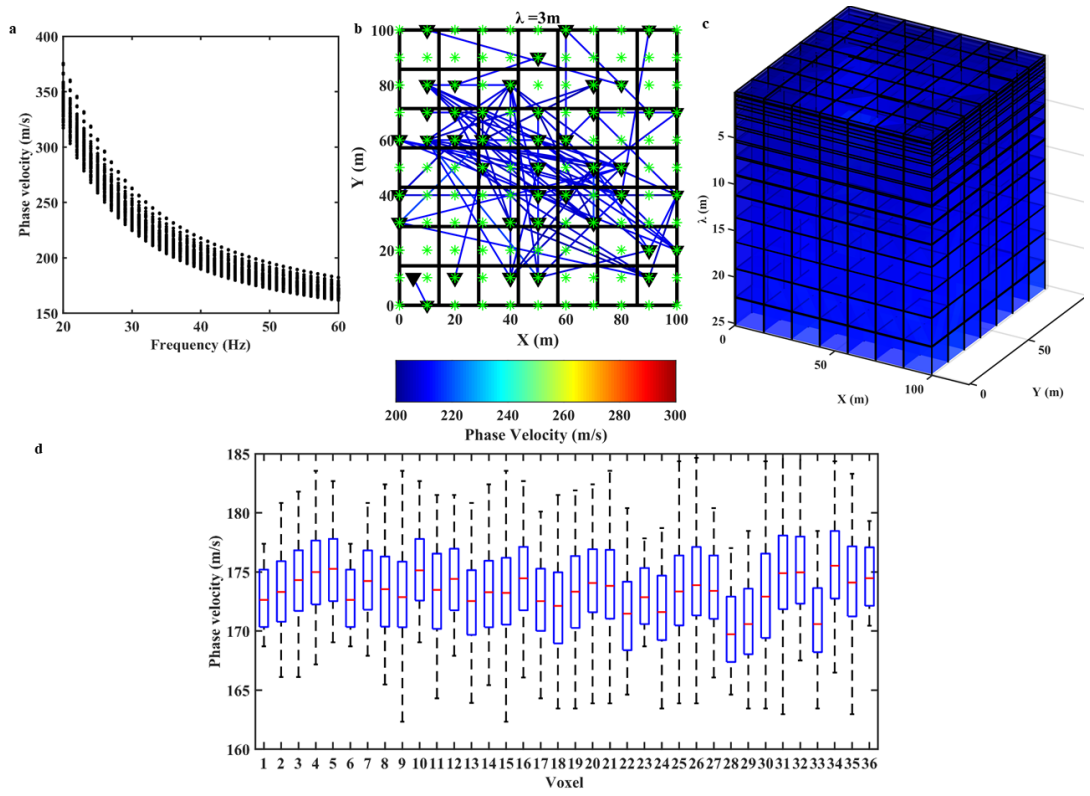

Figure 5.16: Case 1- a) Synthetic DCs. b) Slice of the voxel space at $\lambda = 3\,\mathrm{m}$. In green, the position of the synthetic 1-D models and, as black triangles, the positions of the receivers. c) Voxel space. d) Boxplot of the detection of outlier data points.

Case 2: Outlier data points, one outlier DC

In Figure 5.17a, we show the same DCs as in Figure 5.16a but, for testing, we included the "dummy" DC shown in red in Figures 5.17a and 5.17b, where we present the slice of the voxel space at $\lambda = 3\,\mathrm{m}$.

The boxplot of Figure 5.17c, shows the result of the outlier-data point detection for all the voxels at $\lambda = 3\,\mathrm{m}$. The red crosses show the phase velocities, which in six voxels (denoted by the red crosses in Figure 5.17c), were detected as outliers according to eq. 5.49. They all belong to the "dummy" DC. The result was the same for the voxels at all λ (not shown here), and therefore, according to eq. 5.52 $e_{\mathbf{DC_k}} = 1$ and the "dummy" DC was detected as an outlier.

Case 3: Outlier data points, no outlier DCs

In Figure 5.18a we show the DCs corresponding to 121 synthetic 1D models, for which we used the same geometry as in Figure 5.16b, but imposed lateral V_S variability among them. Specifically, most of the models had the same properties

as in Figure 5.16b, but for the models in within the red box of Figure 5.18b, we used higher V_S values, in the ranges shown in Table 5.8. As a result, the DCs which crossed the red-box region, presented higher phase velocities than the rest of the DCs, as clearly indicated in the slice at $\lambda = 3\,\mathrm{m}$ (Figure 5.18b). We note that in this case, the red DC (used as a "dummy" DC in the previous example), resulted from the forward modelling and was therefore "true" and corresponding to the local properties of the red box.

Therefore, in this case, the red DC was flagged as an outlier (red crosses circled in dark red in Figure 5.18c), only in one voxel (red cross in Figure 5.18b). Considering that it passed through 4 voxels (green crosses in Figure 5.18b), the value of $e_{\mathrm{DC_k}}$ was equal to 0.25, and therefore the DC was not considered as an outlier.

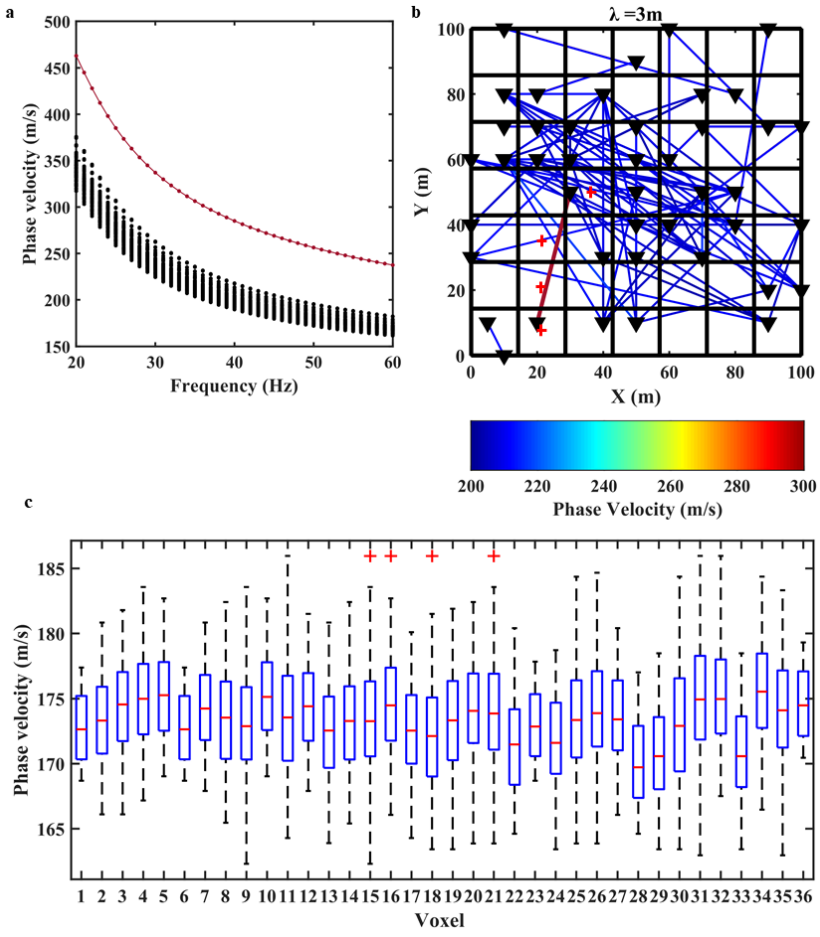

Figure 5.17: Case 2- a) Synthetic DCs. In red, the "dummy" DC. b) Same as in Figure 5.16(b). In red, the voxels corresponding to the "dummy" DC. c) Same as in Figure 5.16 (d).

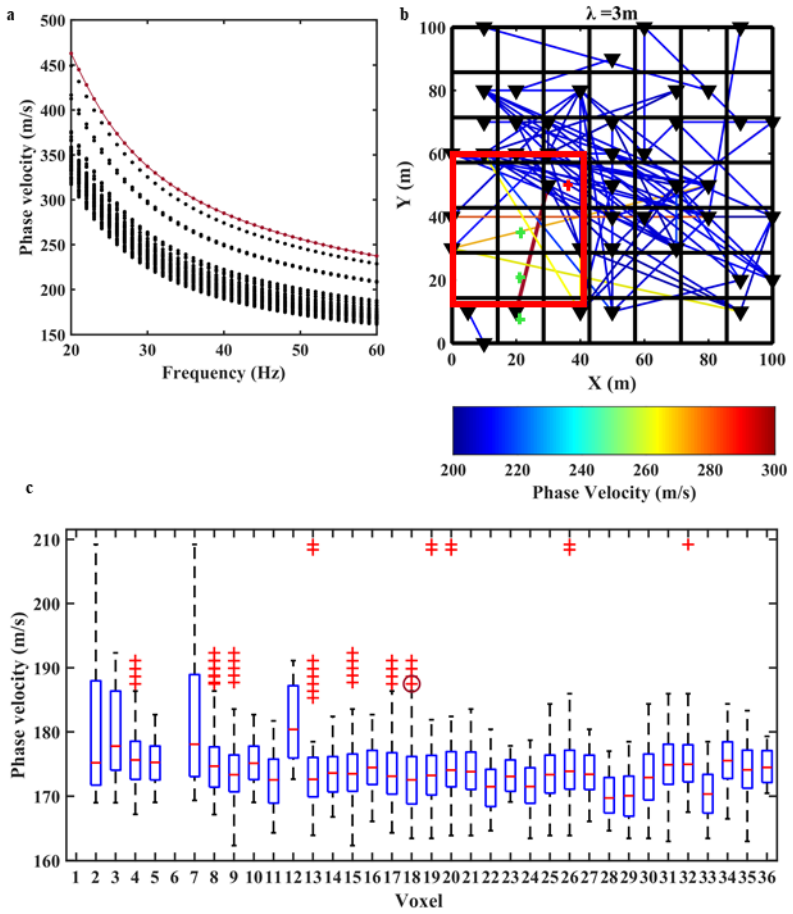

Figure 5.18: Case 3- Same as in Figure 5.17. In (b), the box shows the high-velocity zone, the crosses show the "dummy" DC path and the red cross, the voxel in which the "dummy" DC was detected as an outlier.

Discretization suitability check

Since our outlier detection was based on the median estimator, an important consideration is whether the applied discretization of the 3D space, and the resulting distribution of the velocities in $\mathbf{d}_{n,m,l}$, were suitable for a reliable statistical result.

In particular, even though the median is a powerful outlier detector, "the value of the median depends on only one or two central inputs" (Beliakov et al., 2011) and therefore it is almost insensitive to a concentration of outlier values that could signify a bimodal distribution.

For example, in Figure 5.19a, the values of "A" clearly cluster around the number 5. The median in this case properly predicts the central value 5, suggesting that the number 15 is an outlier. For "B" and "C", the distribution becomes bimodal,

i.e. the values concenter around 5 and around 15. In these cases, the values around 15 should not be thrown away as outliers. Instead, the spatial discretization should change so that the two groups do not lie within the same voxel.

To check if the distribution of the velocities within $\mathbf{d}_{n,m,l}$ is adequate for a statistically reliable estimation, we perform the following test. Supposing an ideal population $\mathbf{d}_{n,m,l}$, of which the distribution is adequate for a representative median estimation and that $\mathbf{d}_{n,m,l}$ is only a sample of $\mathbf{d}_{n,m,l}$. The median of the actual $\mathbf{d}_{n,m,l}$ equals $\mu(\mathbf{d}_{n,m,l})$ while an approximation of the median of $\mathbf{d}_{n,m,l}$ can be found using the Hodges–Lehmann estimator on $\mathbf{d}_{n,m,l}$, i.e., $\mu(\mathbf{d}_{n,m,l}) \approx \mathcal{H}(\mathbf{d}_{n,m,l})$. Their distance indicates how far our distribution is from a statistically-reliable population.

In the example of Figure 5.19a, the distance between μ and $\mathcal{H}$ increases drastically from "A" to "C", suggesting that the distribution of "C" is not reliably represented by the median.

In practice, we retrieve $\mathbf{d}_{n,m,l}$ starting from different N and M values, while the discretization in λ, which is determined by the data, remains fixed. Each time we compute, separately for each voxel, a "median-estimation error" ε, as:

$$\varepsilon_{n,m,l} = \frac{\left|\mu(\mathbf{d}_{n,m,l}) - \mathcal{H}(\mathbf{d}_{n,m,l})\right|}{\mu(\mathbf{d}_{n,m,l})} \tag{5.53}.$$

We then compute the summation of $\varepsilon_{n,m,l}$ of all the voxels:

$$E_V = \sum_{N\times M\times L} \varepsilon_{n,m,l} \tag{5.54},$$

and the N and M which E_V is minimized, are selected as the discretization of the outlier detection.

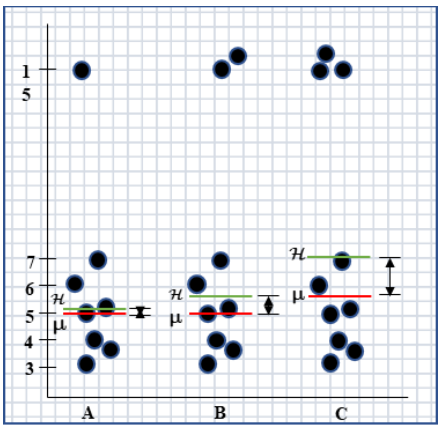

Figure 5.19: Examples of distributions and their computed median μ and theoretical median $\mathcal{H}$.

5.9 QC of the picked DCs

The methods proposed in the previous sections are implemented in a tool that can virtually carry out automatic DC picking in a fully data-driven way. Nevertheless, the performances of this automatic process may be strongly dependent on the quality of the dataset. Hence, it is important to be able to assess the quality of the automatic picking results. This can be done by using a sub-set of DCs which are also picked manually, as benchmark, to validate the automatic picking results for the whole dataset. Manual picking is based on human observation, which can avoid possible pitfalls, such as following the wrong maxima on the cross-correlation matrix or insufficient cleaning of the picked curve. Thus, the manually picked DCs are considered as a benchmark for our method.

For the comparison, we apply the automatic DC quality-control (QC) approach, presented in detail in Chalabiyev (2020). The method evaluates how similar an automatically picked DC is to a DC picked manually for the same receiver couple, by comparing the correspondence of their frequency bands and their phase velocity difference.

5.9.1 Description of the method

We denote as DC^{auto} and DC^{man}, the a DC picked automatically (with our workflow) and manually, for the same R_1R_2 receiver pair. The automatically picked DC contains $n_{dp,auto}$ data points and is structured as:

- A vector of frequencies $\mathbf{f}_{auto} = \left(f_1 \cdots f_{n_{dp,auto}} \right)^{\mathrm{T}}$,
- A vector of phase velocities $\mathbf{v}_{auto} = \left(v_1 \cdots v_{n_{dp,auto}} \right)^{\mathrm{T}}$.

The respective vectors of the manually picked DC are:

- $\mathbf{f}_{man} = \left(f_1 \cdots f_{n_{dp,man}} \right)^{\mathrm{T}}$,
- $\mathbf{v}_{man} = \left(v_1 \cdots v_{n_{dp,man}} \right)^{\mathrm{T}}$.

First, we evaluate the number of data points of the automatically picked DC which lie in the same frequency band as the manually picked one. The number of data points at frequencies which exist in the manually picked DC but are absent (discarded) from the automatically picked one, is denoted as $n_{dp,disg}$, while the number of points (frequencies) which exist in the automatically picked DC but not in the manually picked one is denoted as $n_{dp,extra}$.

The number of data points in the common frequency band is then:

$$n_{dp,auto}^{common} = n_{dp,auto} - n_{dp,extra} \tag{5.55}$$

We use as a metric to evaluate the portion of the automatically picked DC that lies within the common frequency band, the following effectiveness ratio:

$$A_{effec} = \frac{n_{dp,auto}^{common}}{n_{dp,auto}} \cdot 100\% \tag{5.56}$$

An effectiveness of 100% means that the entire automatically picked DC lies within the common frequency band, while an effectiveness of 0 % means that there are no common frequency bands between the two curves.

To compare the DCs in terms of phase velocity, we assume that the manually picked velocities correspond to the correct cross-correlation maxima. If the automatically picked curve corresponds to the correct maxima as well, it should have equal phase velocities with the manually picked DC. If the phase velocities are different, it means that the automatically picked DC corresponds to wrong maxima.

We denote as $n_{cv} \leq n_{dp,auto}^{common}$ the number of data points within the common frequency band and for which the velocities of automatically picked DC are equal to the velocities of the manually picked DC. Thus, for any such point we will have that:

$$\mathbf{v}_{auto}(i_{auto}) = \mathbf{v}_{man}(i_{man}) \tag{5.57}.$$

The similarity of the automatically picked DC to the manually picked one can be then evaluated with the following index:

$$\mathrm{S}_{ind} = \frac{n_{cv}}{n_{dp,man}} \tag{5.58}.$$

An index of 1 means that the two DCs are identical, having the same frequency band and equal velocities. An index of 0 means either that there is no common frequency band between the two curves, or that there is no data point with equal velocity inside the common frequency band.

The effectiveness ratio (eq. 5.56) is examined together with the similarity index (eq. 5.58), to describe how well the two curves match. This evaluation is performed only for a sample of DCs, before the actual processing of the entire dataset, to indicate the expected effectiveness of our method.

5.10 Case study 1: Synthetic model

We describe the application of our method to the synthetic dataset presented in Section 5.3. With the workflow presented in Chapter 4, we extracted two reference multichannel DCs, using separately all the receivers located in each zone. The reference DCs are plotted in Figure 5.20a as black, corresponding to “Zone 1” and red, corresponding to “Zone 2”, dots. Their position (the midpoint of each zone) is indicated as triangles of the corresponding colour in Figure 5.2.

For the extraction of the DCs with our two-station workflow, the decision of the input processing parameters (receiver pairs and shots to be used and frequency band for the cross-correlation matrix computation) was not critical, since near- and far-field effects were not introduced in the model. To ensure that a large number of DCs would be picked, we used all the pairs of receivers with path length between

1 m and 45 m (in total 4214). For each pair, a DC was picked on the stacked cross-correlation matrix, computed by summing the individual matrices of all the shots.

For each DC, we used the appropriate reference DC, depending on whether the receivers were located within “Zone 1” or “Zone 2”. For the pairs of which the path crossed both zones, we used the reference DC which was nearest to the pair, although this choice was not critical, since the phase velocities of the two reference curves were similar, and, in the frequency band 20 Hz – 60 Hz, identical.

The DCs picked from the 4214 pairs are plotted in Figure 5.20b. All the DCs show smooth velocity transitions, and no unrealistic “breaks” are present. Therefore, the DCs did not undergo the cleaning and outlier removal stages of the workflow. In Figure 5.20c, we plot, in different colours, the achieved DC coverage, measured as the number of curves crossing each location at each wavelength. Due to the large number of DCs, the coverage was dense and in most positions along the line, higher than 200 (the coverage of 200 is indicated by the black dashed lines in Figure 5.20c) down to a wavelength of approximately 35 m.

In Table 5.9, we present a breakdown of the runtimes of the computations of the different processing stages, on a single-core commercial laptop. In total, from raw data to the whole set of DCs, the data processing lasted approximately 39 minutes.

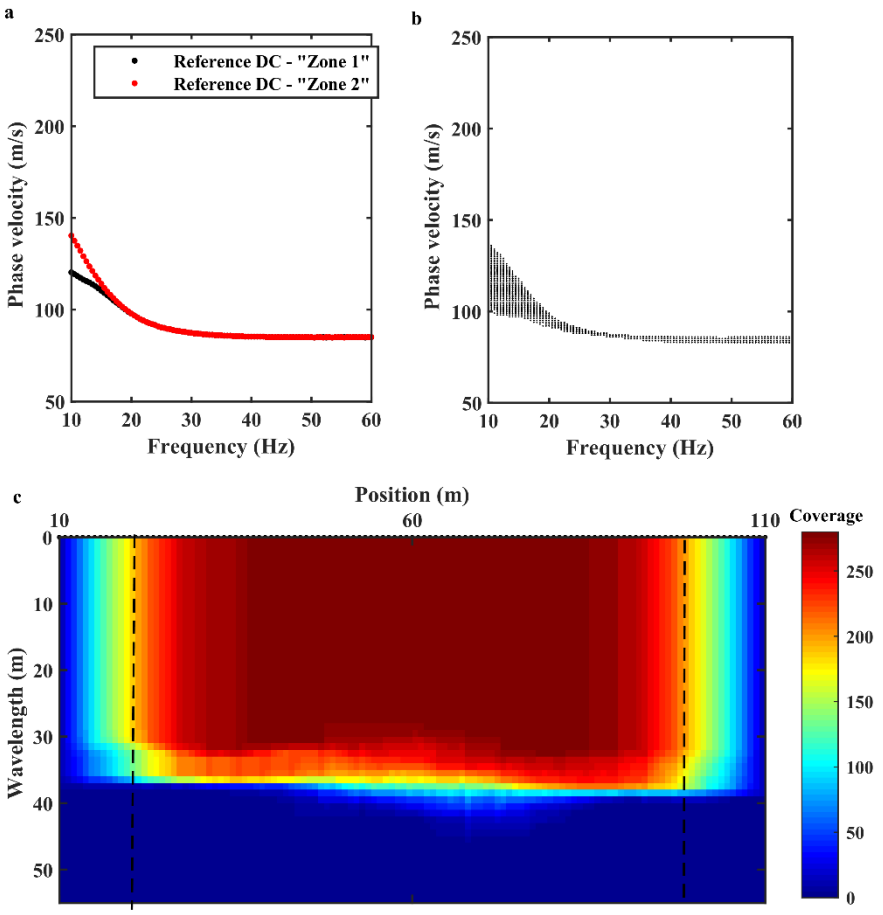

Figure 5.20: a) Reference multichannel DCs. b) DCs resulting from our workflow. c) Plot of the DC coverage. The dashed lines correspond to a coverage of 200.

Table 5.9: *Breakdown of the processing workflow runtimes.*

Workflow stage	Automation level	Runtime
Cross-correlation matrix computation and stacking	Automatic	482.83 s
DC picking	Automatic	1853.12 s
		Total: 2357.58 s

5.11 Case study 2: 3D dataset from the Ludvika mining site, Sweden (2019)

Here, we present the results of the proposed two-station DC extraction method on the 3D dataset acquired in 2019 in the Ludvika mining site in Sweden. The purpose of this application was to extract a set of DCs, covering the entire

investigation area, to be used as input to the model estimation and statics computation method based on SW tomography, presented in the following chapter.

Input to the workflow was the raw dataset in SEG-Y format, provided by "Smart Exploration". The file, having a total size of 5.5 Gb, was split into separate shot gathers in MATLAB format, to be compatible with the routines corresponding to the stages of the workflow. All the computations were performed by a 10-core workstation.

5.11.1 Workflow application and results

Before extracting the DCs with the proposed two-station method, a set of multichannel reference DCs were extracted from the dataset, to obtain an initial estimation of the phase velocity distribution in the area.

For the multichannel DC extraction, the method presented in Chapter 4 was applied. Using the parameters summarized in Table 5.10, the DCs (in total 40) shown in Figure 5.21a were picked, while the locations associated to the curves are shown as dots in Figure 5.21b.

Table 5.10: *Windowing parameters for the reference DC extraction from the Ludvika 2019 dataset.*

Processing parameter	Value
Window size	100 m
Step	50 m
Minimum offset	10 m
Maximum offset	580 m

The DC clustering revealed four clusters, shown in different colors in Figure 5.21. Within each cluster, the DCs presented smooth transitions of the phase velocity and, based on the location of the curves of each cluster, we identified the following uniform zones in the investigated area: a) a zone in the north-western side of the area ("Zone A", red in Figure 5.21), where the phase velocities were in the range of 1700 m/s and 2700 m/s, in agreement with the existing lithological information (Maries et al. 2017); b) a narrow zone of relatively lower phase velocities (in the range of 1700 m/s – 2000 m/s), referred to as "Zone B" and shown in green in Figure 5.21; c) a zone ("Zone C") of significantly lower velocities (<500

m/s, blue in Figure 5.21) in the north-eastern end of the area, where old mine-tailings are known to exist. The tailings appear as shallow, unconsolidated overburden materials, which probably cause such low phase velocities; d) a zone ("Zone D") extending from the center and reaching to the south-eastern end of the area. This zone shows a concentration of high phase velocities (mostly > 2700 m/s, purple in Figure 5.21), suggesting the presence of a shallow bedrock.

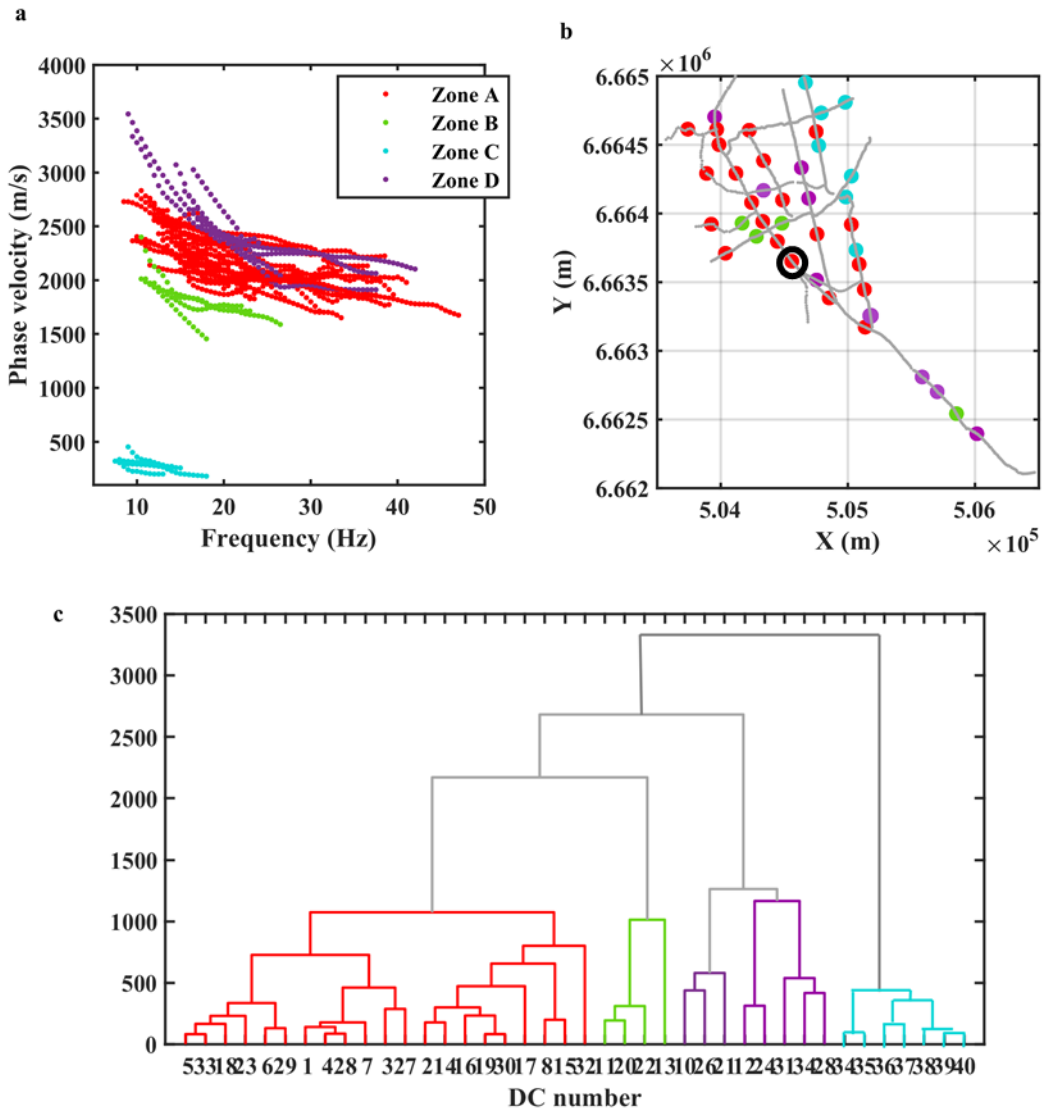

Figure 5.21: a) Multichannel DCs picked from the Ludvika 2019 3D dataset. b) Position and, c) clustering of the multichannel DCs. The colors correspond to the four clusters estimated for the site. Circled in (b), the position of the DC plotted in red in Figure 5.30.

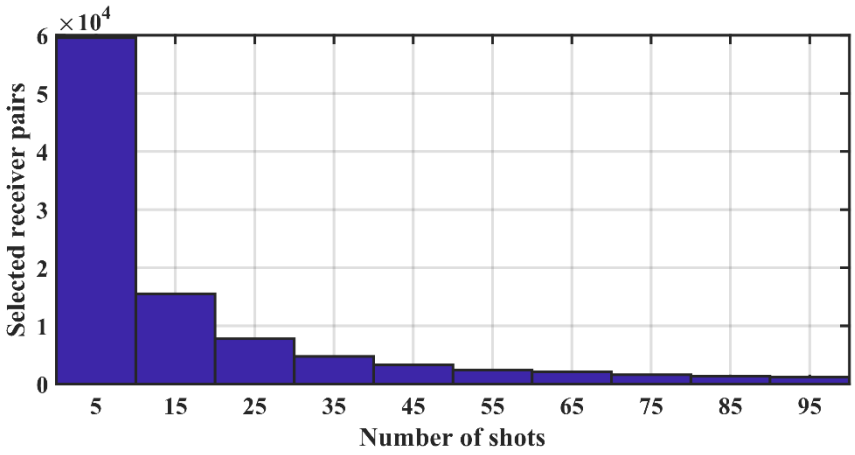

Figure 5.22: Distribution of the number of in-line shots corresponding to each of the receiver pairs selected for processing.

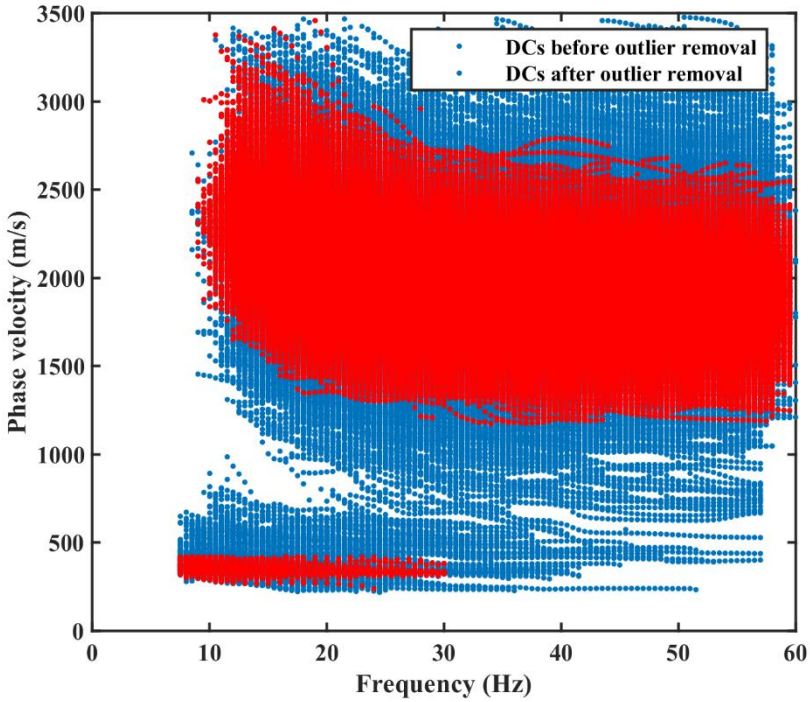

Figure 5.23: DCs picked with the proposed method before (blue) and after (red) the outlier-removal method application.

For the extraction of the DCs with our workflow, we first detected the pairs of receivers, colinear with at least one common shot position which were found to be 1584456 in total. With the method described in Section 5.4.2, several of the shot positions were found to be in the near- and far-field regions of their corresponding receiver pairs and were rejected with the application of the "masks" plotted in dashed red in Figure 5.5. As a result, the number of receiver pairs was also reduced,

since several of them did not have any in-line shot in the accepted offset ranges. The number of remaining pairs, selected for processing, was 105576. The number of shots accepted for each pair varied according to the distribution presented in Figure 5.22.

The cross-correlation matrix computation, DC picking and DC cleaning stages of the proposed workflow were applied to the selected receiver pairs. For each one of them, we chose as reference for the DC picking, the nearest to it multichannel curve, from the set of DCs shown in Figure 5.21a.

The resulting picked and cleaned DCs can be seen in blue in Figure 5.23, where it can be observed that, even though a large number of receiver pairs was processed, the number of retrieved DCs was significantly lower (in total 22336). This was due to the fact that several low-quality DCs were rejected during the DC cleaning,

In particular, in several cases, the input traces were highly corrupted by noise and the DC picking produced maxima at phase velocities similar to the ones of the reference curves, but which did not present the smooth and dispersive pattern expected from SW (e.g., Figure 5.24a). In these cases, the picked curves presented frequent “breaks” along their frequency band, resulting in multiple local minima of their cross-correlation amplitude (Figure 5.24b) and several local peaks of their phase velocity gradient (Figure 5.24c). Applying the criteria described in Section 5.7.1, the portions of the curves that were kept after cleaning (arrow in Figure 5.24d and red in Figure 5.24a) were limited to very short frequency ranges.

Considering that a great number of cross-correlation matrices produced high-quality, broadband curves (e.g., Figure 5.25), we applied a posterior rejection of curves with low number of data points (less than 10, corresponding to a frequency band of 5 Hz).

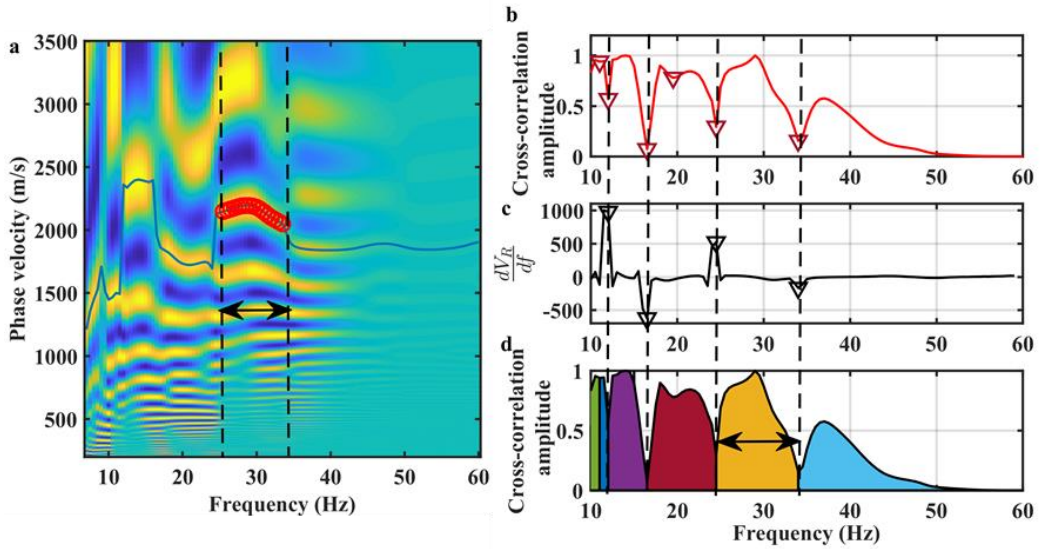

Figure 5.24: a) Example cross-correlation matrix. In blue, the picked maxima and in red, the DC after cleaning. b) Cross-correlation amplitude. c) Phase velocity gradient. d) In color, the cross-correlation amplitude integral. As red triangles, the local minima of (b) and as black triangles, the local peaks of (c). The arrow shows the frequency band that was accepted.

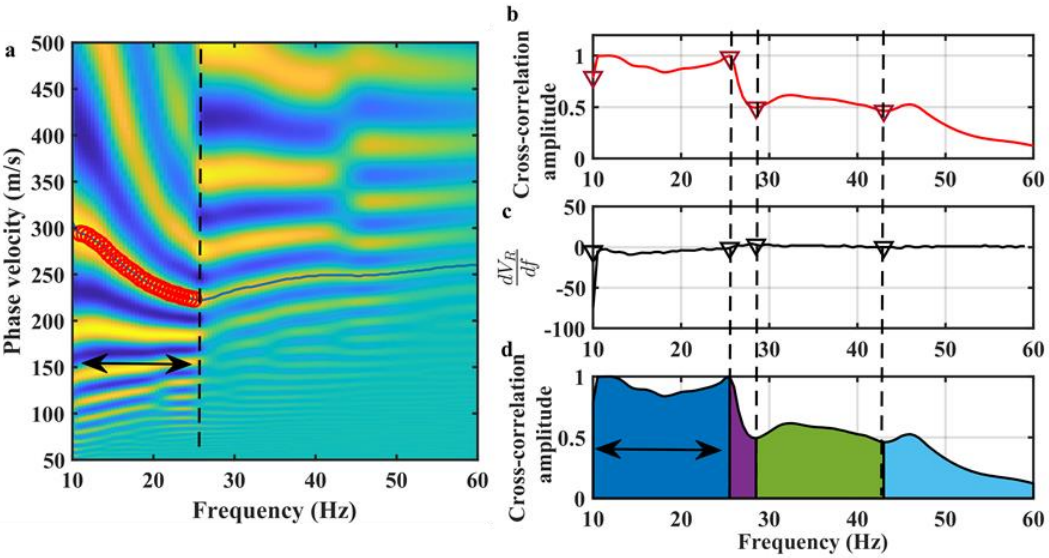

Figure 5.25. Same as Figure 5.24, but for a high-quality cross-correlation matrix.

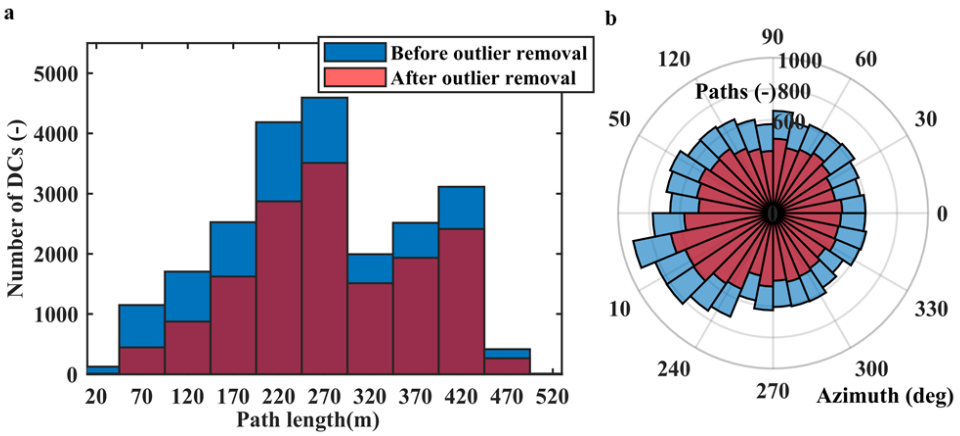

Figure 5.26: a) Path-length and b) azimuth distribution of the picked DCs before (blue) and after (red) the outlier removal.

The remaining DCs (blue in Figure 5.23), presented similar phase velocities to the ones of the multichannel DCs of Figure 5.21a, and although two-station curves are not expected to cluster, a group of DCs clearly presented the low velocities of "Zone C" (Figure 5.21), related to the mine-tailings (the example of Figure 5.25 refers to one of these low-velocity DCs).

The path-length and azimuth distributions of the DCs (blue in Figures 5.26a. and 5.26b, respectively) were wide, while a dense spatial DC coverage was achieved over the entire investigation area, at all available wavelengths (down to 350 m). This can be depicted in the coverage maps of Figure 5.27, where we plot as black dots the positions of the sources and receivers, and as colored lines, the intra-receiver paths corresponding to each DC. The different panels depict the coverage at different wavelength ranges ((a) to (f): 2 m – 20 m, 22 m – 40 m, 42 m – 80 m, 82 m -140 m, 142 m – 200 m and 202 m – 350 m). The different colors indicate the mean phase velocity of the data points of the DCs that belong to the wavelength range of each panel, and is specified in the colorbar.

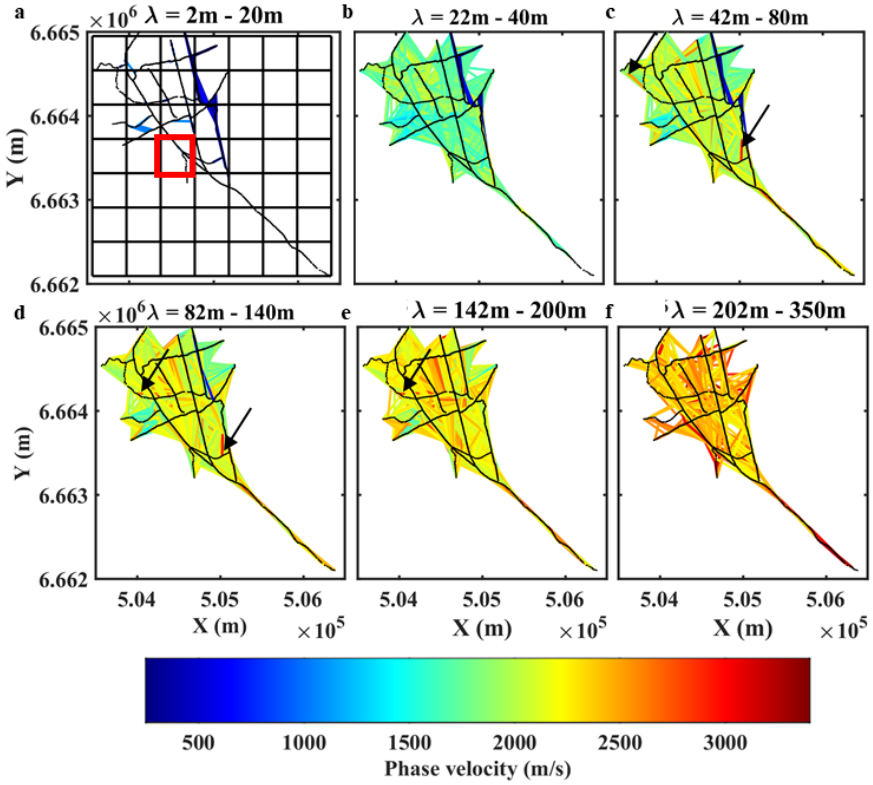

Figure 5.27. Spatial coverage of the DCs (blue in Figure 5.23) at different wavelength ranges. The lines are the intra-receiver paths and their color is the phase velocity, described in the colorbar. The arrows highlight outlying velocities. In (a), the grid is a "slice" of the voxel space. In red, the grid point corresponding to the position in circle in Figure 5.20b.

The coverage maps show that certain paths presented velocities which were abnormal, with respect to the overall trends in their corresponding location and wavelength. As an example, the arrows in Figure 5.27 point to some of these paths, which were clearly outlier DCs, resulting from the picking of wrong maxima of the cross-correlation matrix.

To detect and eliminate them from the DC set, the outlier removal, described in Section 5.8, was applied. The $x-y$ dimensions of the discretization of the voxel space that was chosen for the application of the method, are indicated by the grid in Figure 5.27a. In Figure 5.28a, we plot, in the same wavelength range, the paths of the DCs that were detected as outliers. In the rest of the panels of Figure 5.28, we plot coverage of the detected outlier DCs in the remaining wavelength intervals. The arrows in Figure 5.28 depict the same outliers shown in Figure 5.27.

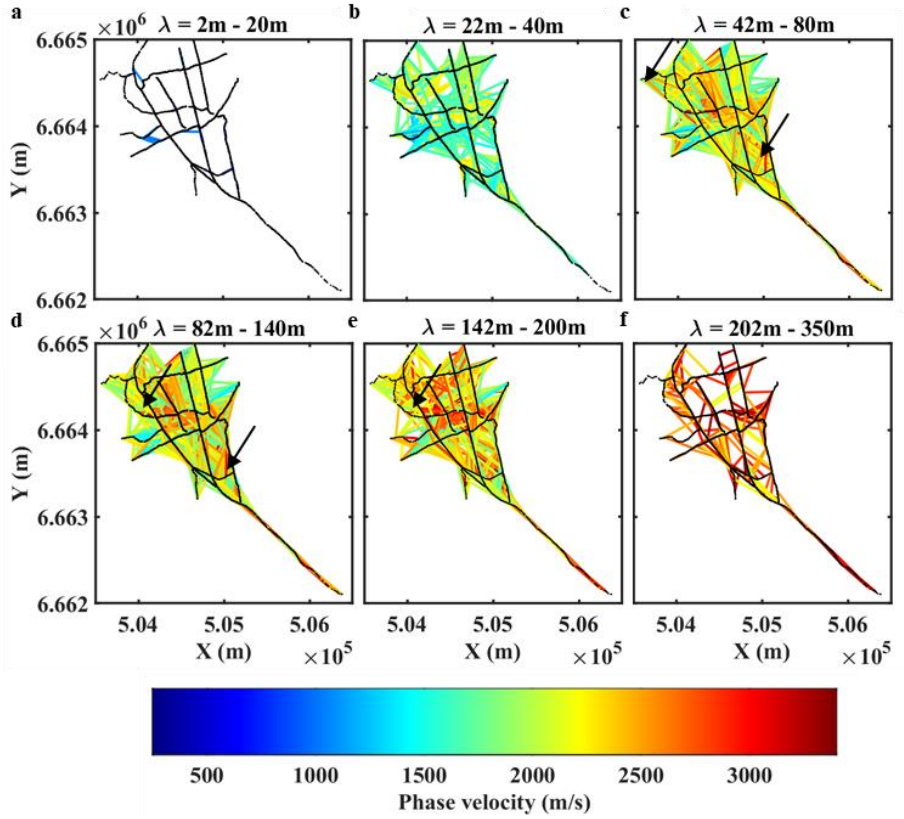

Figure 5.28. Same as Figure 5.27, but corresponding to the DCs found as outliers.

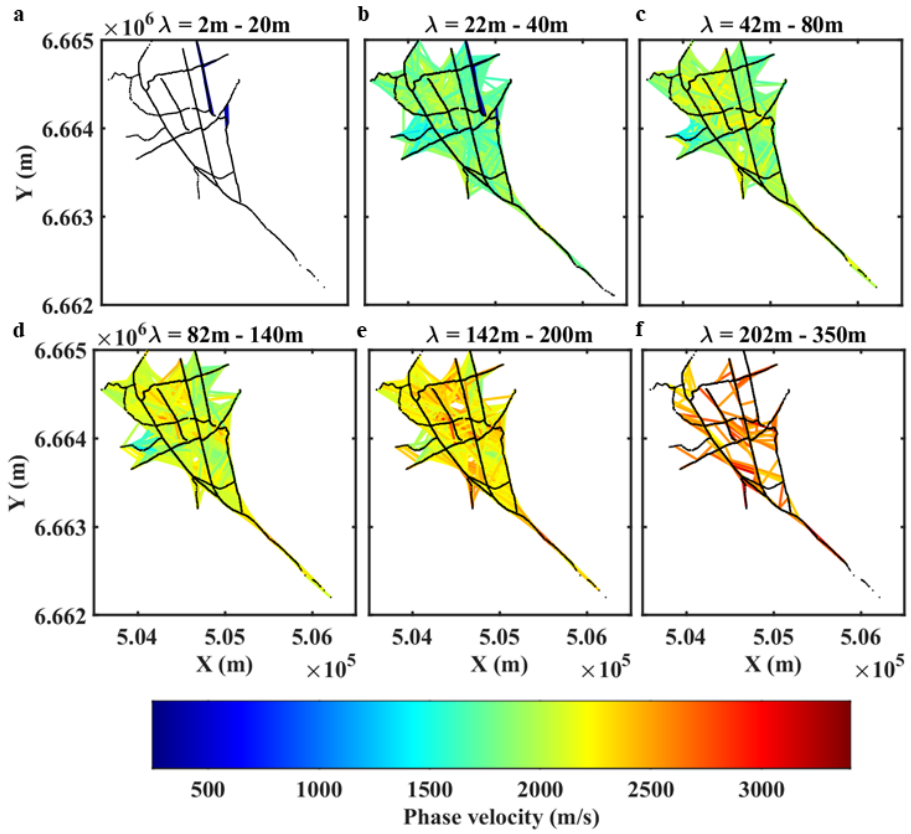

Figure 5.29. Same as Figure 5.27, but corresponding to the DCs that remained after cleaning the outliers of Figure 5.28.

The total number of the DCs which remained after the outlier removal was equal to 15188. The DCs are plotted in red in Figure 5.23, while their path-length and azimuth distributions are shown, again in red, in the histograms of Figures 5.26a. and 5.26b, respectively. Their corresponding spatial coverage maps are given in the panels of Figure 5.29. It can be observed that, even though, a considerable amount of DCs were disregarded, the coverage remained dense over the entire investigation area.

In addition, the outlier phase velocities were removed, and at the same time, smooth phase velocity variability in the lateral direction was maintained. A comparison of the coverage maps with the velocities (Figure 5.21a) and the location (Figure 5.21b) of the different clusters of multichannel DCs, shows overall agreement of the phase velocity distribution along the area, although information on the local phase velocities cannot be directly retrieved from Figure 5.29. This is because many of the paths refer to long distances, and their corresponding velocities might be affected by the local subsurface properties of different environments.

For a more meaningful comparison between the multichannel DCs and the two-station DCs, we computed the mean phase velocity, at each wavelength, of all the two-station DCs falling within the grid highlighted in red in Figure 5.27a, excluding the curves having paths longer than 200 m. The resulting “mean DC” is plotted in black in Figure 5.30 and it is compared with a multichannel DC (red in Figure 5.30) located in the same grid. The curve belongs to “Cluster 1” and its exact location is highlighted by the black circle in Figure 5.21b

It can be observed that the two DCs show similar phase velocities at each wavelength, with a maximum difference (at a wavelength of 150 m) of 287 m/s (approximately 12% of the two-station DC phase velocity). Considering that the computation of the multichannel DCs is stable, due to the use of several traces, these DCs can be considered as a benchmark for our method. The good fitting of the two curves in Figure 5.30 proves the robustness of our result.

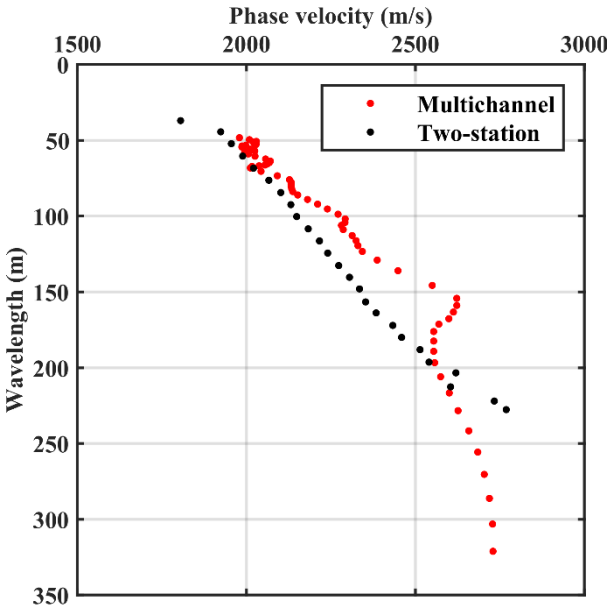

Figure 5.30. In red, the multichannel DC located in the red grid in Figure 5.27a (also shown as a black circle in Figure 5.20b); in black, the mean phase velocity of all the two-station DCs in the same grid.

To evaluate the effectiveness of the proposed method, with respect to the possible outcome of a manual DC picking, we applied the *QC* method described in Section 5.9. We compared a set of DCs (red in Figure 5.31) picked manually by an experienced operator from 100 randomly selected trace couples of the dataset, with the DCs picked by our automatic method (black in Figure 5.31) from the same trace couples. Both approaches rejected the same 13 cross-correlation matrices due to low quality, and therefore only 87 DCs were picked by both.

A visual inspection of Figure 5.31 reveals that the two sets of curves present similar frequency bands and phase velocities. This is confirmed by the values of the effectiveness ratio (eq. 5.56) and similarity index (eq. 5.58), which are plotted in Figures 5.31a and 5.31b, respectively. In Figure 5.32a, it can be observed that 86% of the automatically picked DCs presented an effectiveness ratio of more than 90 %. This means that more than 86 % of the curves contained more than 90 % of common frequency components with the manually picked ones. The plot of the similarity index (Figure 5.32b) shows that more than 57 % of the automatically picked DCs had a similarity index, with respect to the manually picked ones, of more than 0.9, while only 10 % of the curves showed similarity indexes less than 0.7. This proves that, not only the automatically picked curves contained data points at the correct frequencies, but also that most of the data points presented correct phase velocities.

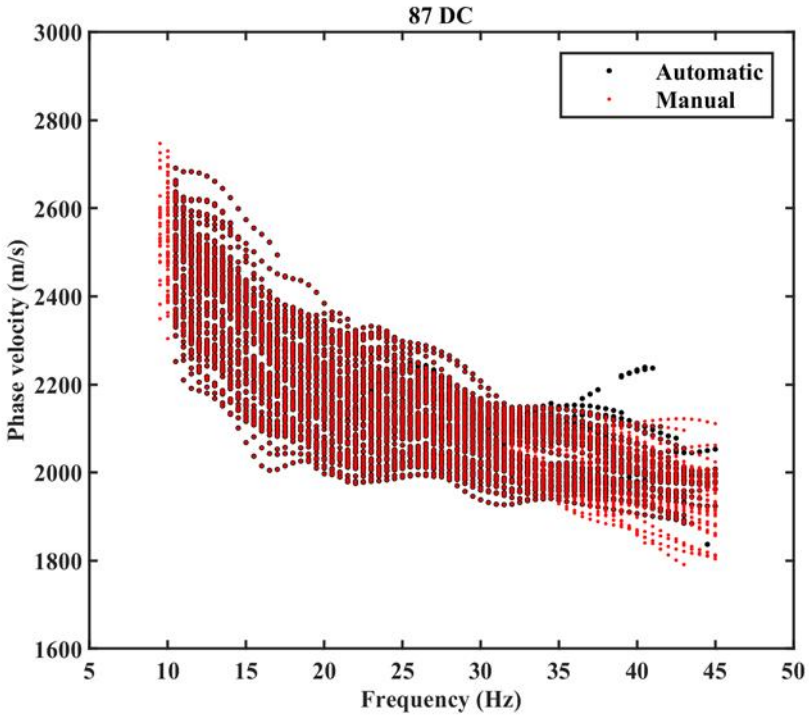

Figure 5.31. DCs picked manually (red) and automatically (black) for the same random selection of receiver couples.

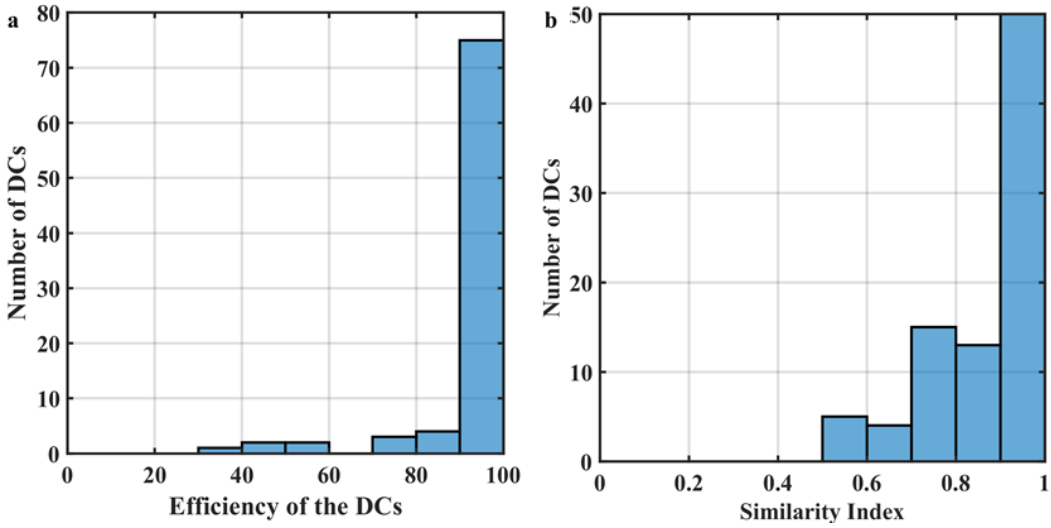

Figure 5.32. a) Effectiveness and b) Similarity index.

At the same time, the automatic approach presented the advantage of lower processing-time requirements, with respect to the manual picking. Specifically, for the computation of the curves, the automatic method ran for 768.70 s while the manual picking required the constant occupation of an operator for 2134.5 s, using the same 10-core workstation. Therefore, for this small experiment, our method was

faster by approximately three times, with respect to the manual approach. Such a gain in time is particularly important if we consider the size of the entire dataset.

In Table 5.11 we present the runtimes of the different stages of our method on the entire dataset of Ludvika. In total, the processing of the 1584456 receiver pairs lasted 128 min, without considering the first run of the cross-correlation matrix computation and stacking and DC picking stages, which were performed initially, for all possible shot positions, to allow the computations of the first stage (selection of the receiver pairs, shots and wavelength ranges). This initial run was longer (25.05 h), since it involved a high number of computations, but it was completely automatic and therefore did not require the occupation of an operator.

Table 5.11: *Breakdown of the processing workflow runtimes on the Ludvika 2019 dataset.*

Workflow stage	Automation level	Runtime
Selection of the receiver pairs, shots and wavelength ranges	Automatic, apart from a manual drawing of the "masks" on a user interface	5.2 min +25.05 h for the initial run of the DC extraction for all possible pairs and offsets
Cross-correlation matrix computation and stacking	Automatic	20.72 min
DC Picking	Automatic	79.53 min
DC Cleaning	Automatic	5.8 min
Removal of outlier DCs	Automatic	14.67 min
QC of the picked DCs	Automatic	2.1 min
		Total: 128 min + 25.05 h

Regarding the time gain with respect to the manual picking, it should be noted that for the manual DC picking of this small-scale experiment, we did not perform any investigation on the optimal source-receiver offset values, and we adopted the same values used for the automatic picking (falling within the limits set by the red dashed lines in all the panels of Figure 5.4). Usually, though, the optimal source-receiver offset range is decided upon tests on sample data, using values in the ranges of the empirical rules presented in Table 2.1. This procedure requires several trial

and error DC pickings, until the operator decides which parameters are fairly appropriate, based on experience. Such an approach, apart from its high demands in time and expertise, also encompasses the risk of selecting suboptimal parameters, jeopardizing the quality and of the final result.

As an example, we show in Figure 5.33a, a stacked cross-correlation matrix, computed for a pair of receivers at distance 70 m from each other, according to one of the criteria of Table 2.1. In particular, we estimated an individual-shot matrix for each one of the shots which obeyed $\frac{x_1}{3} \leq \lambda \leq 3x_1$, i.e., in the range between the black dashed and continuous lines in Figure 5.4a. These matrices were stacked, producing the matrix shown in in Figure 5.33a. It can be observed that the quality of this matrix is poor, and no dispersion can be detected. On the other hand, computing and stacking the individual-shot matrices for the offsets and wavelengths inside the "mask" (red dashed line in Figure 5.4a), resulted in the stacked matrix shown in Figure 5.33b. The matrix, although corresponding to a narrower frequency band, is of higher quality, presenting maxima with a clear dispersive pattern, indicative of SW.

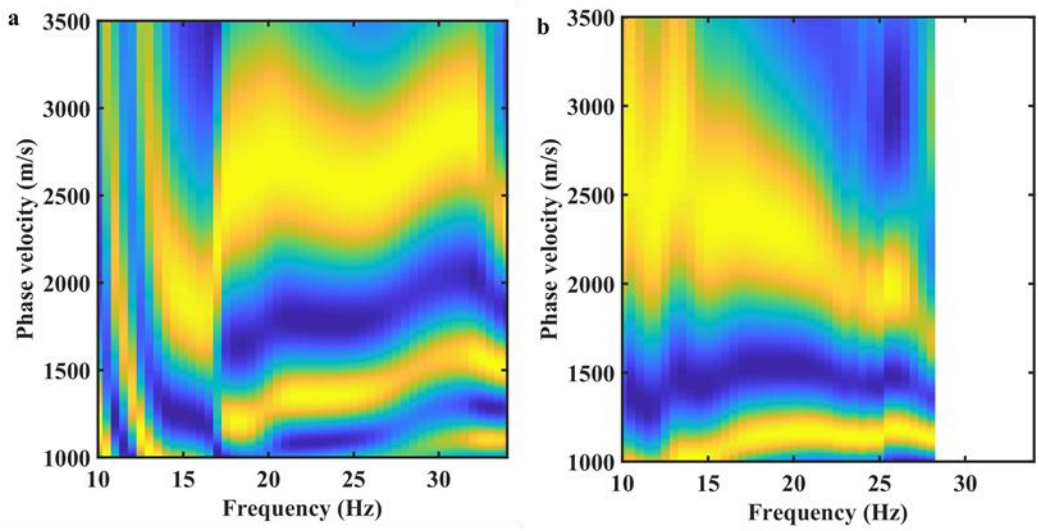

Figure 5.33: Stacked cross-correlation matrix, computed considering a) the offsets and wavelengths between the black lines in Figure 5.4a and, b) the offsets within the red dashed line in Figure 5.4a.

5.12 Discussion

In our proposed method, we firstly detect the receiver pairs which are colinear with a common shot, by imposing that the receiver-pair and shot azimuth is equal to zero, i.e., that $\theta_{ijk} = 0^{o}$. We note that this limit might reduce dramatically the number of accepted receiver pairs and shots, since a precise alignment of the acquisition equipment is improbable. In practice, a slight azimuth tolerance might be necessary, as for instance proposed by Diaz-Segura (2020) or Foti et al. (2018). In our datasets, due to the abundance of sources and receivers, we imposed a 1^{o} limit (Figure 5.3b), to obtain as accurate results as possible.

In Section 5.5, the selected receiver pairs are used for the computation of the cross-correlation matrix, along the frequency range defined by the method of Section 5.4.2, and a velocity range ($\mathbf{v_C}$), defined by the user. In general, wide velocity ranges can be selected, to ensure no information loss, since a "cleaning" of the unwanted ranges is performed automatically in a later stage (Section 5.7). Nevertheless, the computation of the matrix in a wide $\mathbf{v_C}$ space requires more computations and therefore, the available computational resources should be accounted for the selection.

In Section 5.6, the DC picking is facilitated by means of a multichannel DC, which serves as an *a priori* reference on the local phase velocities in the investigated area. The choice of a multichannel DC as reference is justified by the fact that its computation involves a large number of traces, making the DC stable and of high S/N, and it does not involve the possibility of cycle-skipping, which makes its picking reliable (see for details Sections 2.3.1 and 2.3.5). It is a common solution (e.g., Sadeghisorkhani et al., 2018; Kästle et al., 2016), adopted also in more time-demanding manual picking techniques. Our automatic approach involves several cross-checks ensuring that, even if the reference phase velocities are not appropriate in the entire frequency band of the matrix, the picking is driven by the longest frequency band for which the reference velocities are trustworthy. In this sense, it is of equivalent reliability with most of the existing two-station SW processing methods. Nevertheless, any *a priori* knowledge on the expected local phase velocities at the position of the concerning receiver pair (e.g., through forward

modeling using the velocity information from drillholes or logs) would also be appropriate.

The proposed optimized two-station method has been here applied to extract DCs of the fundamental mode of Rayleigh waves, since based on tests and from our multichannel analysis (see Chapter 4), higher SW modes were not present in any of the processed datasets. If present, higher modes might cause erroneous phase velocities in the frequency bands where they are dominant and the DC might present "jumps" from one mode to another. In this case, they would be automatically recognized and rejected since the automatic cleaning is designed to reject DC branches that are associated to jumps. Nevertheless, the effect of energetic higher modes can also be present without jumps, e.g., because there is a smooth passage of the energy from one mode to the next one. Therefore, it is recommended to apply an appropriate data pre-processing to isolate the modes prior to the DC picking. For instance, the method of Dziewonski & Hales (1972), which filters the fundamental-mode data based on the SW group velocity or the method of Khosro Anjom et al. (2021), which isolates the modes based on reference mode-velocities, can be applied.

Moreover, the method can be directly applied to process any other types of SW (e.g., Love waves, Scholte waves, Lamb waves, other guided waves) and the picking can be adopted also to multichannel processing.

Finally, although here they are applied as parts of the presented workflow, the near- and far-field detection method (Section 5.4.2) and the outlier-removal method (Section 5.8) could be used as standalone tools, to optimize any DC picking approach.

5.13 Conclusion

We presented a novel two-station method, which allows the extraction of a large number of DCs, in a reliable, fast and automatic manner. The method was tested on a relatively simple 2D synthetic dataset, efficiently achieving a high DC coverage. Applied to the more challenging and large-scale dataset of Ludvika (2019), the method provided DCs of similar quality to the ones retrieved with a manual DC picking, through an automatic and fast process. Therefore, the method can be considered convenient for industrial applications and large-scale datasets.

Chapter 6

SW tomography for mineral exploration – SW tomostatics estimation method

6.1 Introduction

We propose a method to estimate high-resolution long-wavelength V_P statics (*SW tomostatics*), which combines SW tomography, a technique which allows the retrieval of high-resolution V_S models, with the Wavelength-Depth (W/D) method, which allows to estimate ν.

We test the method on a synthetic 2D dataset (Section 5.8), to benchmark its effectiveness on laterally heterogeneous sites. We apply it to the 2D and 3D seismic datasets from the iron-oxide mining site of Ludvika in Sweden (Section 3.2) and to line SM1 from the active-seismic dataset from the Siilinjärvi apatite (phosphate) mining site in Finland (Section 3.3.3). For both sites, the retrieved SW tomostatics are applied on the 2D stacked sections and are compared with BW statics.

6.2 Method

Details on the fundamentals and common approaches to SW tomography can be found in Section 2.4. In Figure 6.1, we outline the SW tomostatics estimation method. It consists of:

- the set of multichannel processes (labelled as "A" in Figure 6.1) of the W/D method, which lead to the estimation of the reference apparent Poisson's ratio (ν_z), characterizing different uniform subsurface zones, and,
- the succession of steps that leads to the estimation of the tomographic V_S model (labelled as "B"-"F" in Figure 6.1).

The two results (ν_z and V_S model) are combined to provide the time-average V_P (V_{Pz}) model, from which the statics are computed.

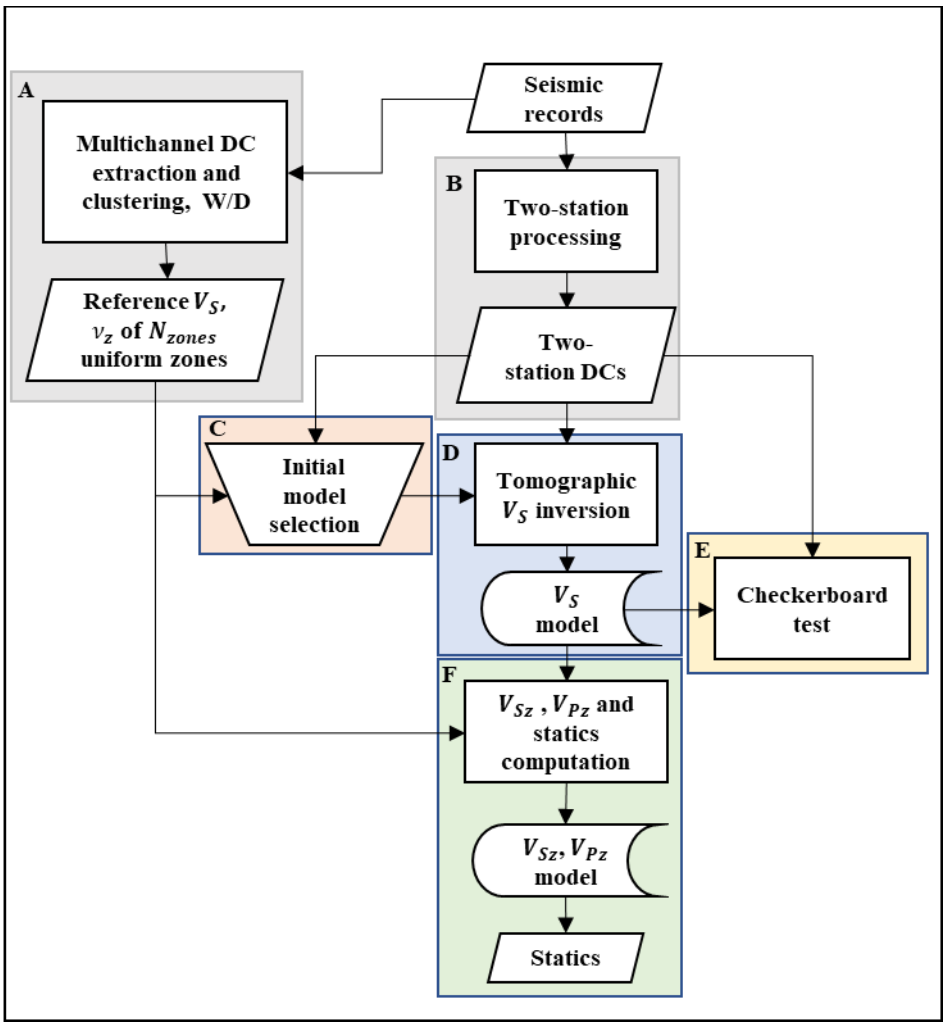

Figure 6.1: Scheme of the proposed SW tomostatics estimation method.

A. Estimation of the reference ν_z

The first part of the workflow is the same as stages "C" – "E" of the SW direct statics estimation method, described in detail in Section 4.2. In summary, an automatic processing is applied on the data to extract a set of multichannel DCs from spatial windows of receivers. The DCs are clustered, and each cluster is assumed to correspond to a uniform subsurface zone. The highest-quality DCs of each cluster are found, according to the method of Karimpour et al. (2018). They are considered reference, and are inverted to provide the reference V_S, W/D relationship (Socco et al. 2017) and ν_z of each cluster (uniform zone).

B. Two-station DC extraction

The method to extract the DCs between different pairs of receivers, to be used as input to SW tomography (step "D"), is described in Sections 5.4-5.5. The

automation tool described in Sections 5.4-5.8, can be applied to perform the DC extraction in an efficient way.

C. Initial model selection

The initial model for the inversion is constructed as a regular grid of K 1D profiles (m_k), over the area covered by the receivers. Therefore, it is a pseudo-2D or pseudo-3D model, depending on the distribution of the grid points.

Each 1D profile is defined by its layer h, V_S, ν and ρ. Although the inversion presents low sensitivity to the value of ν, to obtain as accurate results as possible, we use the ν_z estimated in step "A", after transforming it into interval ν, with the method described in Khosro Anjom et al. (2019). The initial V_S is also the one retrieved in step "A" and the initial ρ is chosen based on *a priori* information on the lithology of the site.

The model-grid dimensions (distance between the K grid points and number and thickness of the layers) are set based on *a priori* information on the geology of the area and on the reference models estimated in "A", to allow the expected lateral and vertical velocity variations to be mapped. Nonetheless, since the achievable lateral and vertical resolution is bounded by the bandwidth and the spatial coverage of the data and their sensitivity to the different model parameters (Garofalo, 2016), the model dimensions are set with the following data-driven approach. Trial inversion runs are performed, using different grid dimensions, and the grid that minimizes the final inversion misfit is selected.

D. Tomographic V_S inversion

For the tomographic inversion, we use the method developed by Boiero (2009). It is a damped weighted least-squares inversion algorithm, which estimates V_S directly from the DCs, avoiding the phase-velocity map building stage of the common SW tomography methods used in global seismology (see Section 2.4).

In particular, the forward modelling is built by computing the accumulated phase along the path $l_{R_1R_2}$ between the two receivers, corresponding to each DC, at each angular frequency ω, as:

$$\omega t_{R_1R_2}(\omega) = \omega \int_{R_1}^{R_2} p(l,\omega)\, dl \qquad (6.1),$$

where $p(l,\omega)$ is the slowness, at each location along $l_{R_1R_2}$.

The corresponding traveltime $t_{R_1R_2}(\omega)$ is then computed as:

$$t_{R_1R_2}(\omega) = \int_{R_1}^{R_2} p(l,\omega)\, dl = \sum_{i=1}^{I} p_i\left(l_{R_1R_2},\omega\right) dl_i \qquad (6.2),$$

i.e., as the integral (summation) of the slowness of each propagating phase between each segment of the path, dl_i, where $Idl_i = l_{R_1R_2}$. To find the local slowness at each point i along $l_{R_1R_2}$, bilinear interpolation of the slowness corresponding to its four surrounding grid points is performed:

$$p_i\left(l_{R_1R_2},\omega\right) = \sum_{k=1}^{K} f_{ik}\, p_k(\omega) \qquad (6.3),$$

where f_{ik} is the bilinear interpolation coefficient, which takes non-zero values only for the four grid points surrounding point i, and p_k is computed by the Haskell (1953) and Thomson (1950) forward modelling for the m_k model parameters. Finally, the phase slowness along $l_{R_1R_2}$ is computed as:

$$p_{R_1R_2}(\omega) = \frac{\sum_{i=1}^{I} p_i\left(l_{R_1R_2},\omega\right) dl_i}{l_{R_1R_2}} = \frac{\sum_{i=1}^{I}\sum_{k=1}^{K} f_{ik}\, p_k(\omega)\, dl_i}{l_{R_1R_2}} \qquad (6.4),$$

i.e., as the average of the local slownesses along $l_{R_1R_2}$.

The inversion is performed by minimizing the misfit function Q:

$$Q = \left[\left(\mathbf{d}_{obs} - d(\mathbf{m})\right)^T \mathbf{C}_{obs}^{-1}\left(\mathbf{d}_{obs} - d(\mathbf{m})\right)\right] + \left[\left(-\mathbf{R}_p\mathbf{m}\right)^T \mathbf{C}_{Rp}^{-1}\left(-\mathbf{R}_p\mathbf{m}\right)\right] \qquad (6.5),$$

where $\mathbf{d}_{obs}$ is the vector of the observed slowness (reciprocal of the DCs), $d(\mathbf{m})$ is the vector of the theoretical DCs computed based on the model parameters ($\mathbf{m}$)

and $\mathbf{C}_{obs}$ is the covariance matrix of the experimental uncertainties, used as a weight for each data point.

The inversion code uses a regularization, built as a set of horizontal and vertical constraints $\mathbf{R}_p$ which relate the model parameters between corresponding layers of neighboring models. Their strength (i.e., the maximum allowed property variation) is chosen according to *a priori* information on the expected velocity variability of the site and is defined by the covariance matrix $\mathbf{C}_{Rp}$ (Auken & Christiansen, 2004). If no *a priori* information is available, Boiero (2009) recommends to perform trial inversions with increasing constraints, and choose the highest constraint that does not increase the final misfit, due to oversmoothing.

The model at the n-th iteration can be described as:

$$m_{n+1} = m_n + \left(\begin{array}{l} \left[\mathbf{G}^T \mathbf{C}_{obs}^{-1} \mathbf{G} + \mathbf{R}_p^T \mathbf{C}_{Rp}^{-1} \mathbf{R}_p + \lambda_d \mathbf{I} \right]^{-1} \\ \times \left[\mathbf{G}^T \mathbf{C}_{obs}^{-1} \left(\mathbf{d}_{obs} - d\left(\mathbf{m}_n \right) \right) + \mathbf{R}_p^T \mathbf{C}_{Rp}^{-1} \left(-\mathbf{R}_p \mathbf{m}_n \right) \right] \end{array} \right) \quad (6.6),$$

where the Jacobian $\mathbf{G}$ is the sensitivity matrix that contains the partial derivatives of $d(\mathbf{m})$ with respect to the model parameters, and λ_d is the Marquardt damping parameter (Marquardt 1963), used to stabilize the solution.

To evaluate the final result, the following RMS error is computed

$$RMS\ error = \sqrt{\sum_i \frac{\left(\mathbf{v}_{obs}(i) - \mathbf{v}_{syn}(i) \right)^2}{e(i)^2}} \quad (6.7),$$

where $\mathbf{v}_{obs}$ and $\mathbf{v}_{syn}$ stand for the phase velocity of each experimental and corresponding synthetic DC, respectively, e is the experimental uncertainty and the summation is over all frequencies i.

E. Checkerboard test

Once the final V_S model has been estimated, its resolution is evaluated by means of a checkerboard test. Velocity perturbations, in the form of positively and negatively perturbed blocks, are applied on the inverted model. Synthetic DCs are generated for the perturbed model, using the forward modelling described in step "D" and considering the receiver pairs of the experimental DCs. The synthetic DCs

are inverted with SW tomography. If the velocity perturbations are accurately reconstructed by the inversion, the resolution is inferred by the size of the perturbation blocks. Since the resolution is not known *a priori*, different checkerboard tests are performed, using different block sizes, until the smallest possible dimensions for which the inverted result is accurate, are found.

F. V_{Sz}, V_{Pz} and statics computation

The inverted V_S model is converted into V_{Sz}, according to:

$$V_{Sz} = \frac{\sum_n h_i}{\sum_n \frac{h_i}{V_{Si}}} \tag{6.8},$$

where h_i and V_{Si} are the thickness and V_S of the i-th layer down to a depth $z = \sum_n h_i$. The V_{Pz} model is then computed, separately for each of the uniform zones, as:

$$V_{Pz} = V_{Sz}\sqrt{\frac{2\nu_z - 2}{2\nu_z - 1}} \tag{6.9},$$

where ν_z is the reference apparent Poisson's ratio, estimated through the W/D method for each zone. Finally, the static shift t_{z_d} is computed at a (floating) datum z_d as:

$$t_{z_d} = \frac{z_d}{V_{Pz=z_d}} \tag{6.10}.$$

6.3 Case study 1: Synthetic model

We present the application of the SW tomostatics estimation method to the synthetic dataset presented in Section 5.8.

The two reference multichannel DCs (Figure 5.20a), were used for the W/D method (step "A") and were inverted to retrieve the reference V_S models of the two zones (Figure 6.2a). In Figure 6.2b, we show the V_{Sz} models computed from the

models of Figure 6.2a, according to eq. 6.8. The V_{Sz} models were combined with the reference DCs (Figure 6.2b), to retrieve the W/D relationship of each zone, (Figure 6.2c). According to the process described in stage "E" of Section 4.2, the reference ν_z of each zone was estimated (Figure 6.2d).

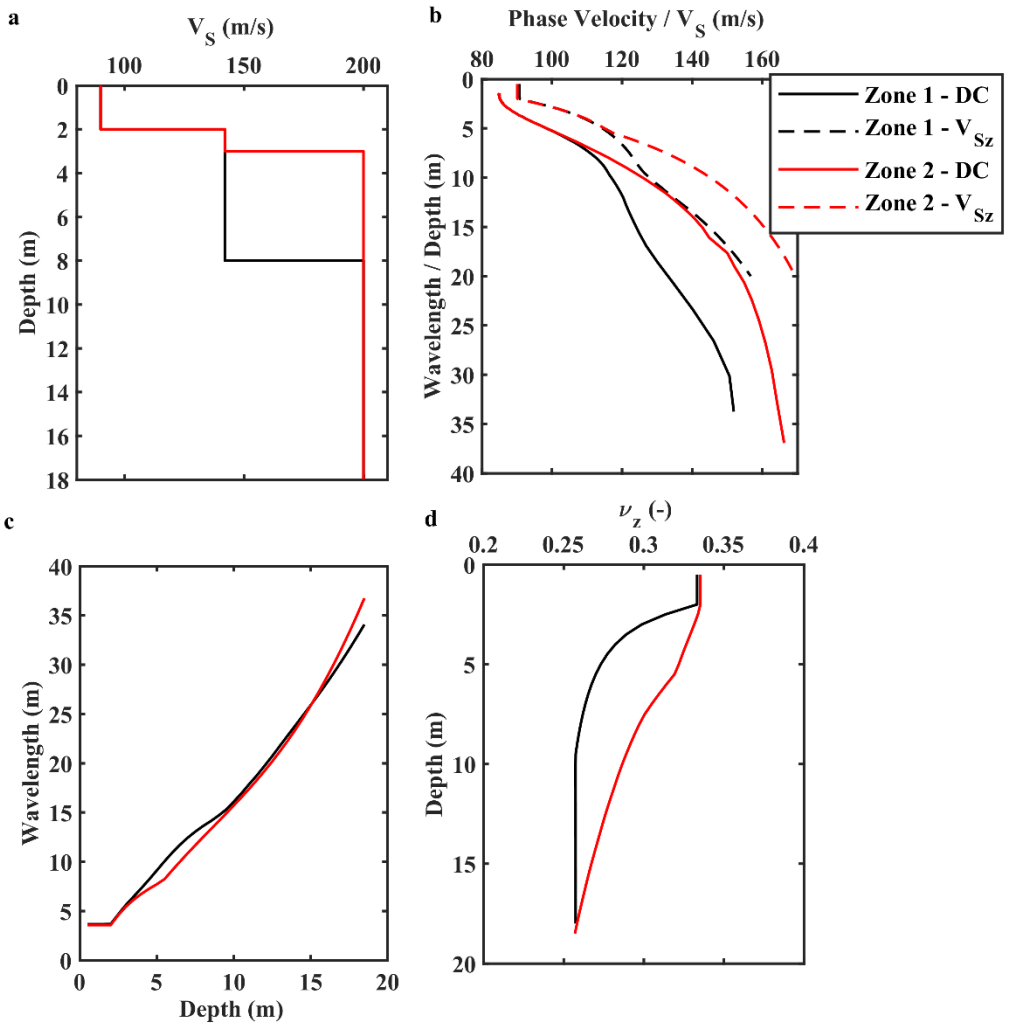

Figure 6.2: a) Inverted reference V_S models from the synthetic dataset. Reference b) V_{Sz} (solid) and DC (dashed), c) W/D, and d) ν_z. In all panels, black corresponds to "Zone 1" and red, to "Zone 2".

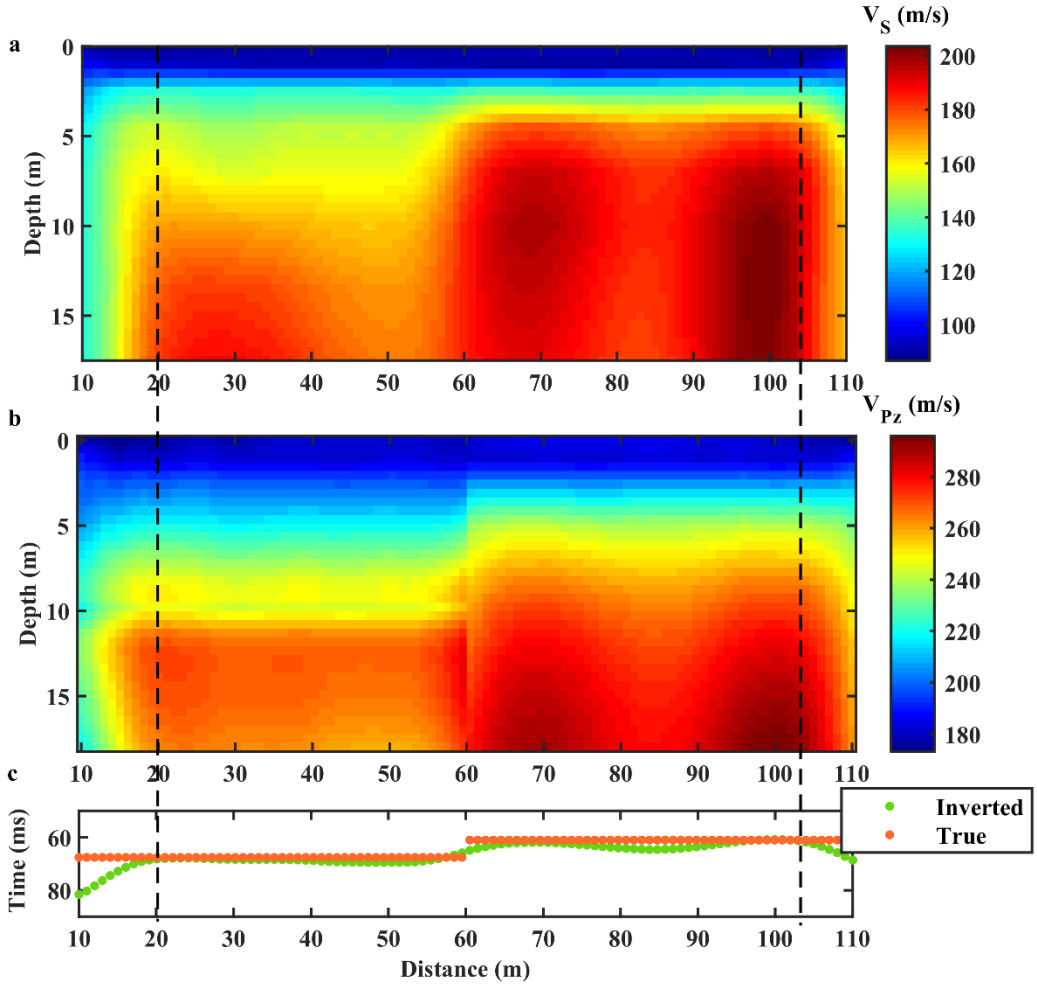

Figure 6.3: a) V_S and, b) V_{Pz} model c) Static shift at 18 m, estimated from the model in (b) (green) and from the true model (orange). In black, the low-coverage zones.

The pseudo-2D V_S model estimated by the tomographic inversion of the two-station DCs is shown in Figure 6.3a. The result shows great similarity to the true model (Figure 5.2), apart from the sides of the model, where the DC spatial coverage was very low (black in Figure 5.2c and in Figure 6.3). The estimated V_{Pz} model is shown in Figure 6.3b, while the static shift, calculated at the largest investigation depth (18 m) according to eq. 6.10, is compared to the true values in Figure 6.3c. The comparison shows that, apart from the low-coverage areas, the estimated static-shift values are similar to the true ones, with a maximum difference of 6 %, at the position of the discontinuity.

This synthetic example shows that SW tomography, coupled with the W/D method, leads to an accurate estimation of the P-wave statics, even at laterally variable sites.

6.4 Case study 2: Ludvika mining site, Sweden

Here, we apply the SW tomostatics estimation method on the portion of the seismic line of the Ludvika 2016 dataset and on the Ludvika 2019 dataset (see section 3.2 for details).

6.4.1 2D seismic dataset (2016)

Reference ν_z

For this dataset, only one reference DC was estimated (Figure 4.5a) and was used for the computation of the reference V_S and ν_z models (Figures 4.8a and 4.9b, respectively).

Two-station DC extraction

In Figure 6.4a, we show an example of the two-station DC picking, in this case performed semi-automatically. The DC (black in Figure 6.4a) was picked on the cross-correlation matrix, as the maxima nearest to the reference DC (green in Figure 6.4a).

In total, 109 DCs were picked (Figure 6.4b) and the retrieved phase velocities were in the range of 1500 m/s – 3000 m/s, which is reasonable for the area of Ludvika. The DCs presented a wide wavelength and spatial coverage and significant overlap, as shown in the spatial coverage plot of Figure 6.4c, where the colorscale indicates the number of DCs crossing each location along the line at each wavelength. The red lines show the locations and wavelengths for which the coverage was found higher than zero. Most of the line was covered by, at least, one DC in the wavelength range of 18 m – 140 m, although denser coverage was achieved for wavelengths between 20 m – 120 m.

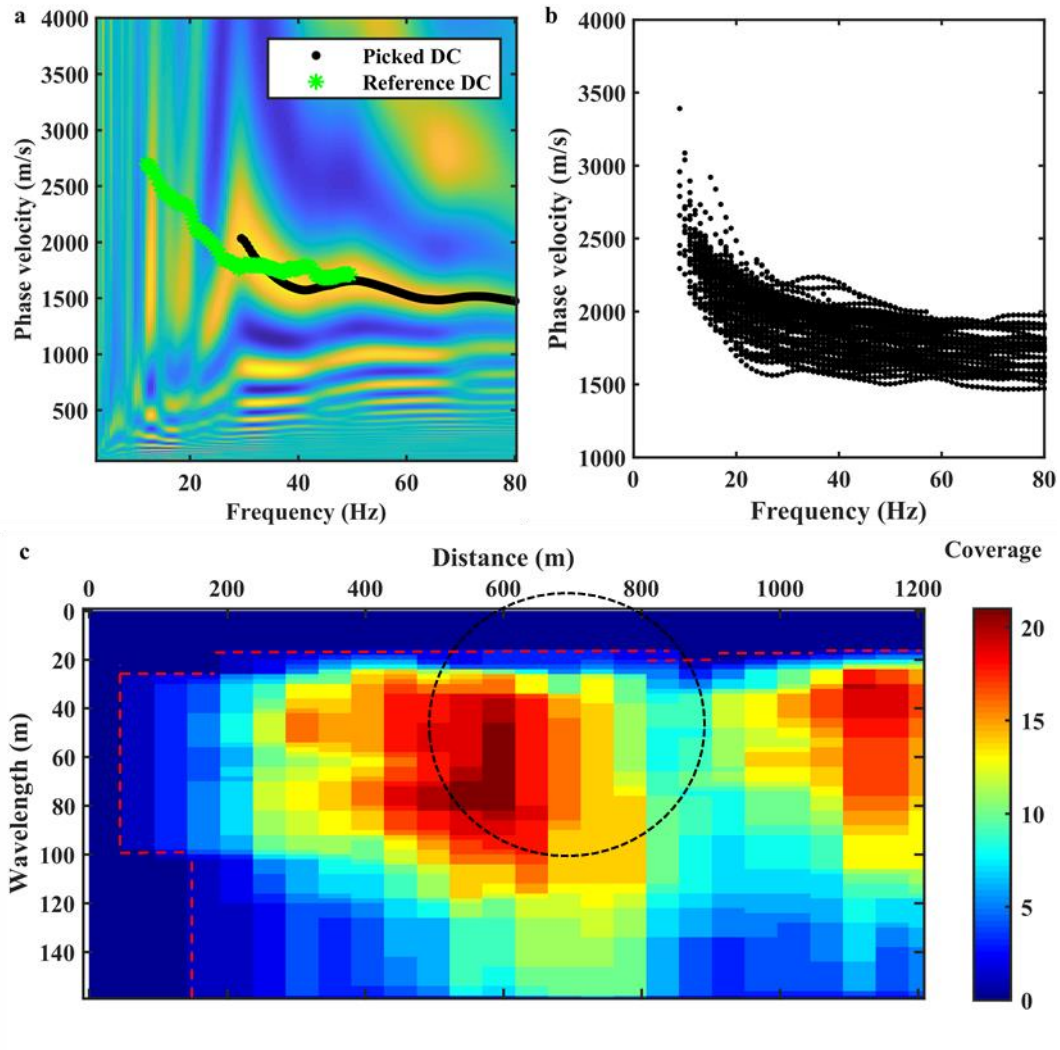

Figure 6.4: Two-station DC extraction on the Ludvika 2016 dataset. a) Example stacked cross-correlation matrix, computed for a pair of traces at distance 70 m from each other and using 13 shots. Black corresponds to the picked DC and green to the reference DC. b) All the picked DCs. c) DC coverage along the line. In red, the zero-coverage limit. The circle indicates that the location of a velocity anomaly.

Initial model selection

The initial model is described in Table 6.1. It consisted of 60 1D models, the dimensions of which were decided upon testing. The initial V_S was set based on the reference V_S model (Figure 4.8a), ρ was chosen based on the available *a priori* information and ν was set according to the reference ν_z (Figure 4.9b). After tests using different velocity constraints, a lateral constraint of 100 m/s was chosen for the inversion.

Table 6.1: *Properties of the initial model used for the Ludvika 2016 dataset.*

`	V_S (m/s)	ρ (kg/m^3)	ν (-)	h (m)
1-3	3250	2000	0.3	5
4-6	3250	2000	0.3	8
7-9	3250	2000	0.3	13
Halfspace	4000	2800	0.3	-

Tomographic inversion

The inverted pseudo-2D V_S model, resulting after nine iterations, is shown in Figure 6.5, while in Figure 6.6a, we show the error between the experimental DCs and the synthetic curves corresponding to the final inverted model, computed according to eq. 6.7.

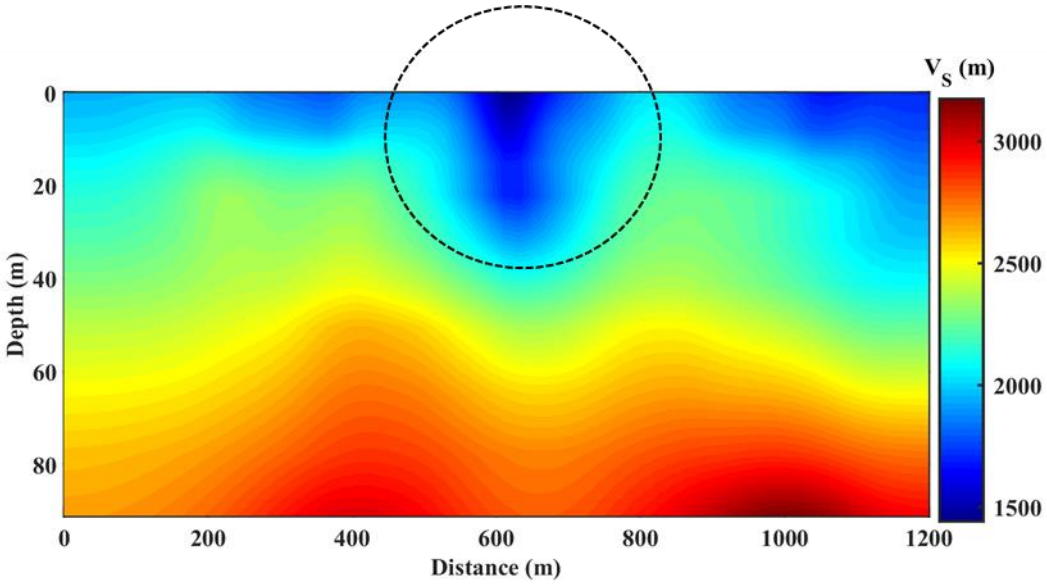

Figure 6.5: Pseudo-2D V_S model. The circle indicates a strong velocity anomaly.

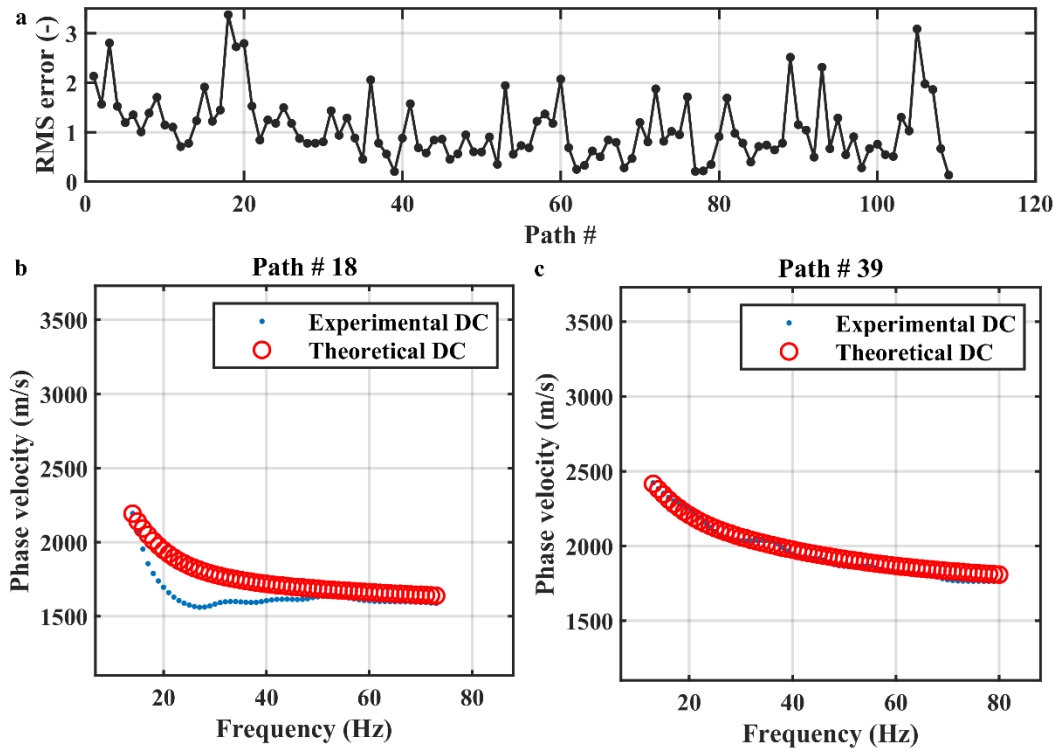

Figure 6.6: a) RMS error between the experimental DCs and the theoretical DCs corresponding to the final inverted model. b) The worst- (path # 18) and c) the best- (path # 39) DC fitting.

In Figure 6.6b, we plot the experimental DC of the worst-fitting path (# 19, with an RMS error of 3.37), compared with the corresponding theoretical DC. Even though the theoretical DC is overestimated, its trend is in general compatible with the experimental one, and nearly identical to it in the highest frequency band. For comparison, we also provide the curves corresponding to the best-fitting path (# 39, with an RMS error of 0.2) in Figure 6.6c.

The inverted model presents high V_S values (1500 m/s – 3200 m/s), which are reasonable according to the available downhole-logging information (Maries et al., 2017). In particular, the model presents an increase of V_S with depth, reaching to approximately 3000 m/s - 3200 m/s at the bedrock, the depth of which appears to vary along the line.

Several low-velocity anomalies were estimated at shallow depths, the most striking of which is the one located in the central portion of the model, marked by the circle in Figure 6.5. According to the DC coverage plot of Figure 6.4c, this zone (marked also by a circle in Figure 6.4c) was densely covered by data, and therefore

the presence of this shallow V_S anomaly can be considered reliable, given the input data.

Checkerboard test

For the checkerboard test, V_S perturbations of 8 % were applied in the form of square blocks on the inverted model. After testing different perturbation-block dimensions, the smallest block sizes that could be recovered are the ones shown in Figure 6.7a.

For the inversion of the generated synthetic DCs no property constraints were applied, to allow the recovery of the velocity perturbations. In Figure 6.7b, we plot the V_S perturbation estimated after the inversion, which shows great similarity to original one (Figure 6.7a), indicating the achieved resolution.

Since all the velocity anomalies of the inverted model of Figure 6.5 are of greater size than the estimated resolution at each depth, their estimated size can be considered reliable.

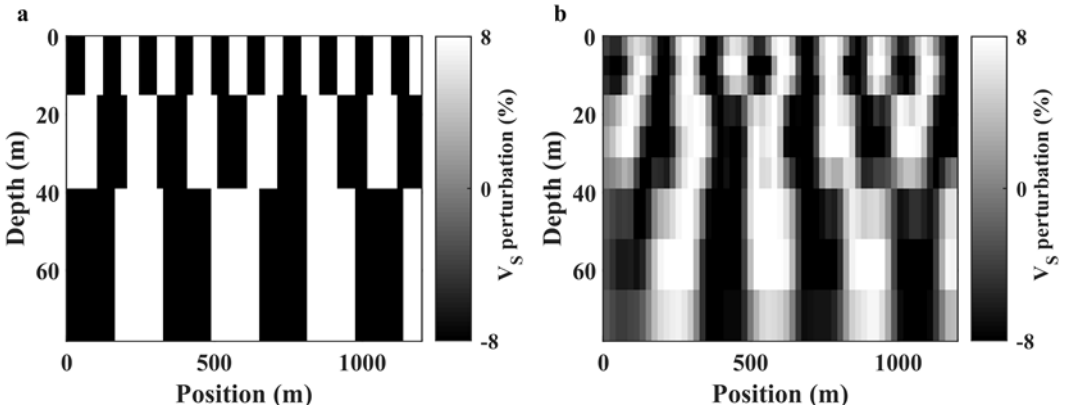

Figure 6.7: a) "True" and (b) inverted perturbation (%) applied to the V_S model of Figure 6.5 for the checkerboard test.

V_{Sz}, V_{Pz} and statics computation

The tomographic V_S model was converted into pseudo-2D V_{Sz} (Figure 6.8a), and into pseudo-2D V_{Pz} (Figure 6.8b). The SW tomostatics, at different floating datum depths within the investigation depth of the tomographic model are plotted in Figure 6.9a.

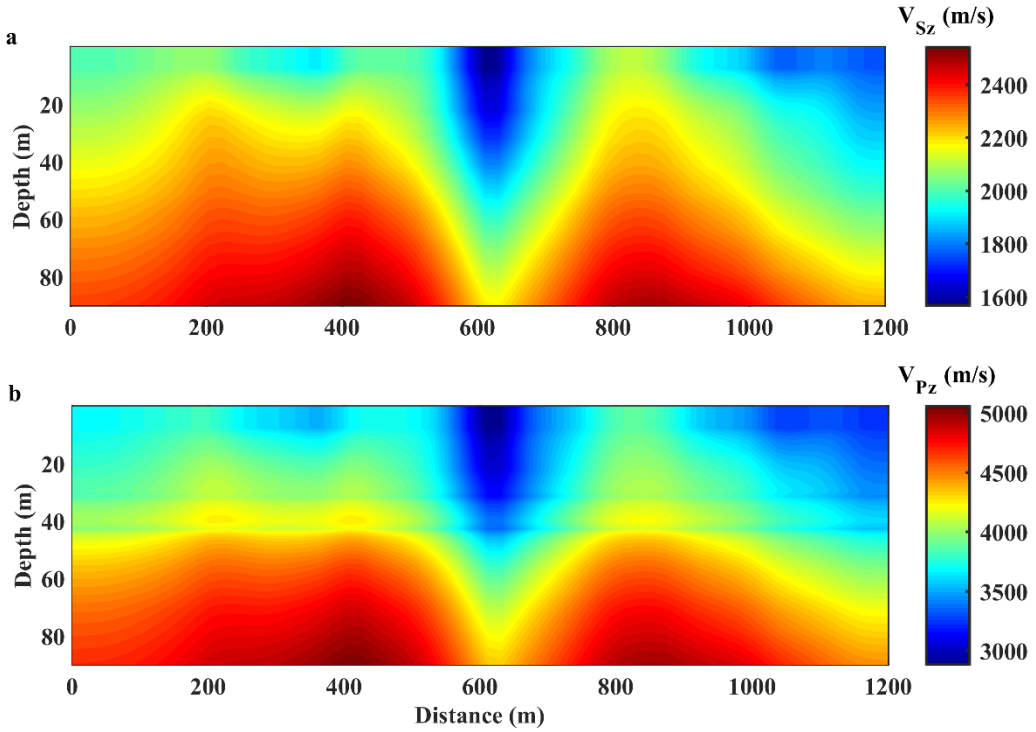

Figure 6.8: Pseudo-2D a) V_{Sz} and b) V_{Pz} model.

The statics at the datum depths of 40 m and 50 m, which are already below the estimated depth to bedrock, are shown in green in Figures 6.9b and 6.9c, respectively. They are compared to the BW tomostatics (black), retrieved at the corresponding depths from the tomographic V_P model of Bräunig et al. (2020), and to our estimated (red) SW direct statics (Figure 4.11).

For the same depths, in Figures 6.9d and 6.9e, we present the distribution of the one-way traveltime difference (Δt) between the SW tomostatics and the BW tomostatics. In both cases, more than 80 % of the static values have differences within ± 1 ms, which is equal to the SR and is, hence, considered negligible.

In Figure 6.10, we compare the stacked section before any statics (Figure 6.10a) and after the BW tomostatics of Bräunig et al. (2020) (Figure 6.10b), the SW direct statics (Figure 6.10c, shown also in Figure 4.12c) and the SW tomostatics (Figure 6.10d). Details on the retrieval stacked sections can be found in Brodic et al. (2020). The SW tomostatics solution (Figure 6.10d) led to a seismic section of similar quality to the one obtained using BW tomography, with a significant improvement in the observed coherency and continuity of the reflector (red arrows in all panels of Figure 6.10), compared to the results without any statics. Moreover, compared

to the section resulting from the SW direct statics (Figure 6.10c), the SW tomostatics provided a slight improvement in the quality of the reflector.

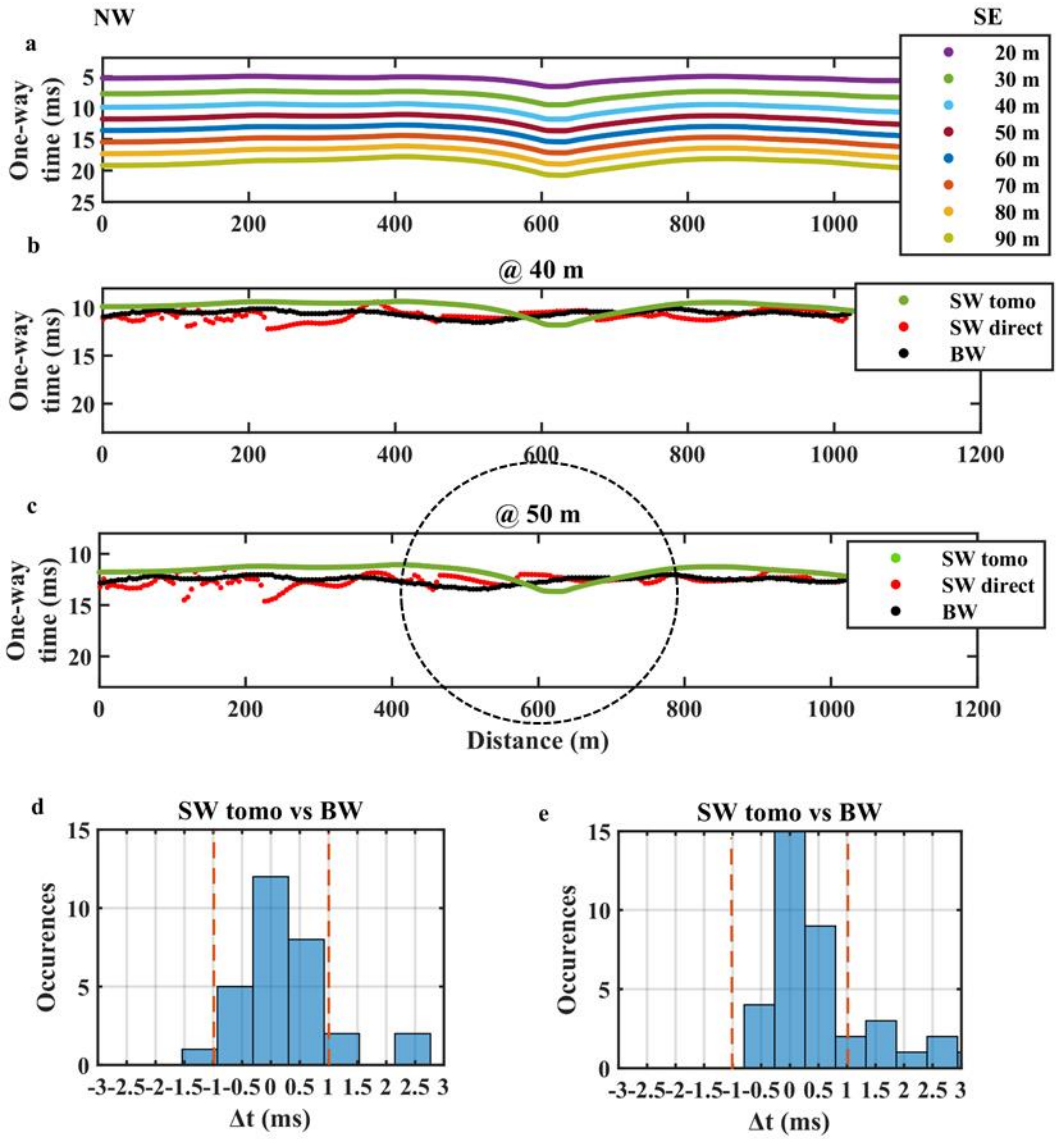

Figure 6.9: Static shift at a) various depths and, a datum of b) 40 m and c) 50 m. In (b) and (c), in green, the SW tomostatics, in red, the SW direct statics (Section 4.3) and in black, the BW tomostatics (Bräunig et al., 2020). Distribution of the one-way time difference (Δt) between the SW tomostatics and BW tomostatics at d) 40 m and e) 50 m. In orange in (d) and (e), the SR of ± 1 ms.

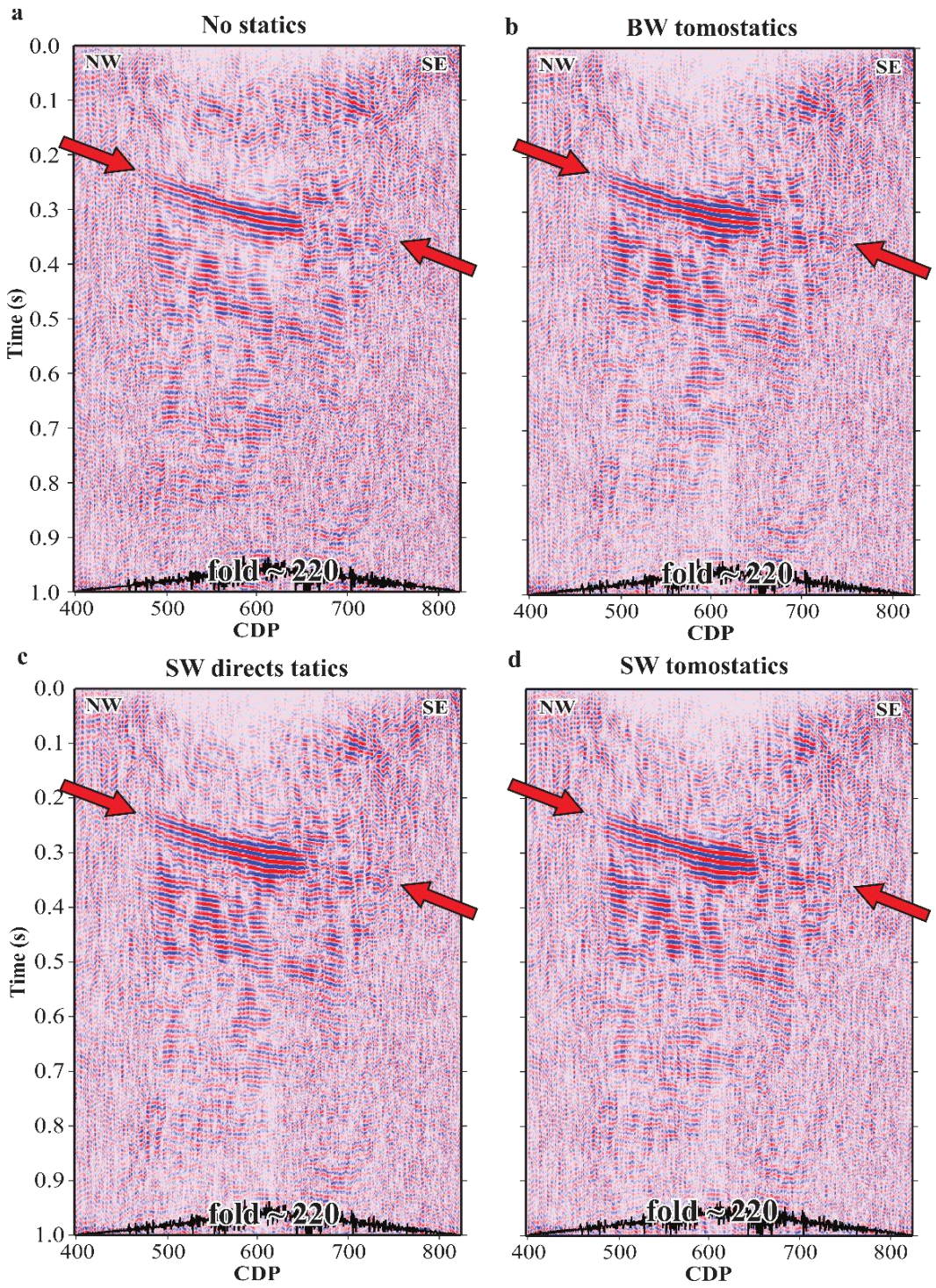

Figure 6.10: Brute stack a) before any statics and after b) BW tomostatics, c) SW direct statics and d) SW tomostatics. The main reflectors are highlighted by the arrows.

6.4.2 3D seismic dataset (2019)

Multichannel DC extraction and reference ν_z estimation

In Figure 6.11a, the four reference DCs estimated in Section 5.11 are plotted as dashed lines of the same color as their corresponding cluster. The W/D process, applied on the reference DCs, is demonstrated in Figure 6.11. For estimating the reference V_S, the Monte Carlo inversion of the reference DCs was carried out generating 10^6 random models within the V_S and h space that we show in grey in Figure 6.11b. For each layer, ν was randomly sampled in the range between 0.1 and 0.45, and ρ was set constant at 2 kg/m^3.

In Figures 6.11a and 6.11b, we plot as solid lines the best-fitting synthetic DCs and their corresponding V_S models, respectively. The lowest-misfit V_S models (dashed in Figure 6.11b) were used together with their corresponding DCs (dashed in Figure 6.11a) to retrieve the W/D of each cluster, plotted in Figure 6.11c. In Figure 6.11d, we present the reference ν_z (dashed) and ν (solid) of each cluster. It can be observed that in all clusters, the value of ν was found nearly constant at 0.35 at depths shallower than 60 m, in agreement with the ν_z values retrieved from the 2016 dataset (the geometry of which corresponds to the one of Cluster 1).

At larger depths, Cluster 2 does not present significant ν and V_S variation, indicating that its related lithology remains constant with depth. For Clusters 1 and 3, the value of V_S increases and the value of ν decreases and attains values which are reasonable for the stiffer formations expected at the site. For example, for the deepest layer of Cluster 1 (having V_S=3050 m/s), which was found to be the dominant cluster in the entire area, the value of ν equals 0.17. This $V_S - \nu$ combination, provides a V_P / V_S of approximately 1.6 which, according to Maries et al. (2017), could be attributed to a low-velocity granite.

Regarding Cluster 4, as shown in Figure 5.17b, its DCs are located in an area where it is known that the tailings of the old mine have been deposited as overburden materials. The presence of this layer is probably responsible for the extremely low V_S values (< 500 m/s), estimated for the cluster, and explains the different estimated ν.

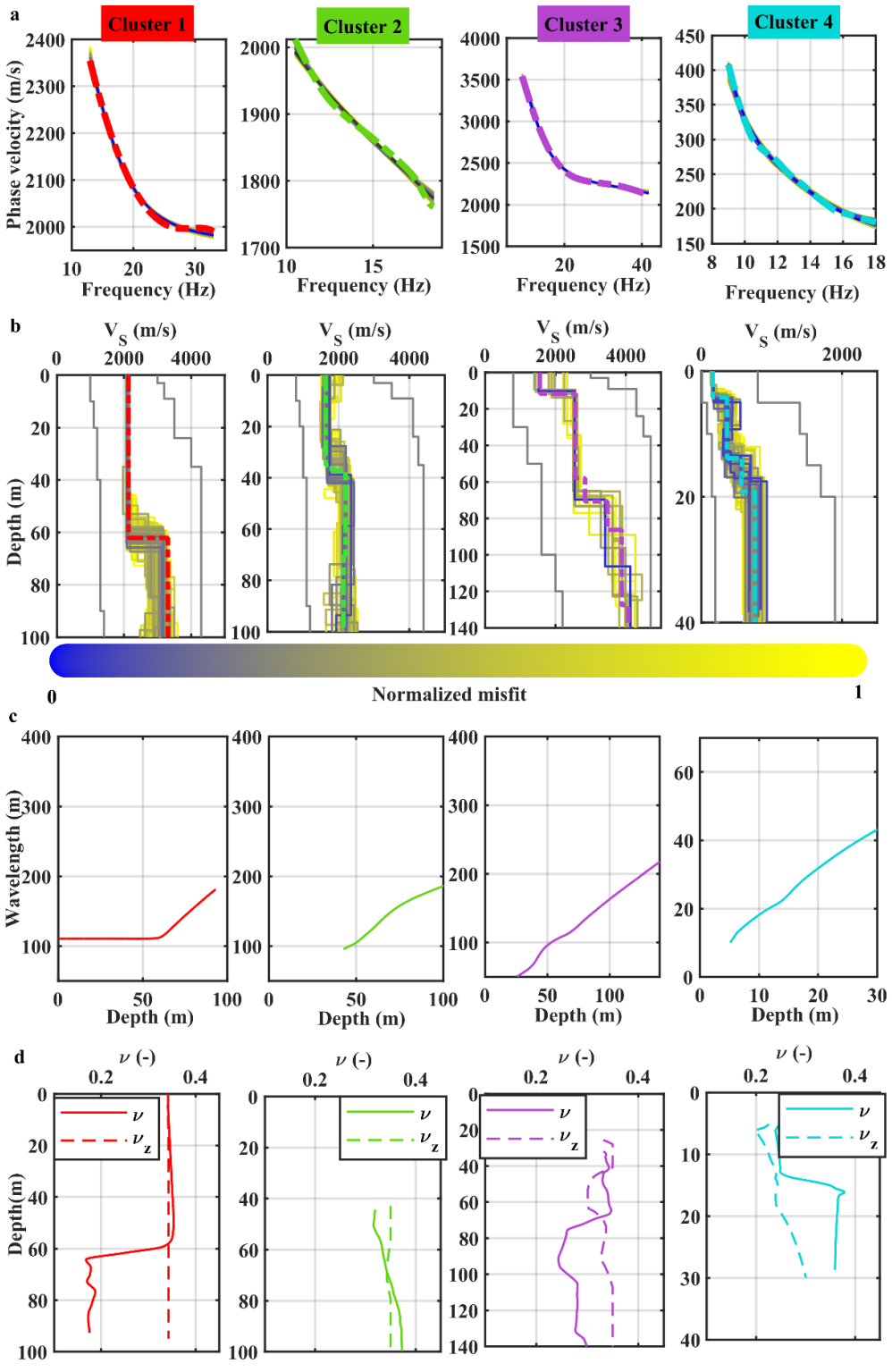

Figure 6.11: In all panels, red corresponds to Cluster 1, green to Cluster 2, purple to Cluster 3 and cyan to Cluster 4. Corresponding to each cluster: a) Reference (experimental) DC (dashed) and synthetic (solid) DCs, corresponding to the best-fitting models of the Monte Carlo inversion, shown in the same colorscale in (b). c) W/D and d) reference ν_z (dashed) and ν (solid), of each cluster.

Two-station DCs

The two-station processing applied to the raw data, is described in Section 5.9. From the extracted 15888 DCs, we used for the inversion only 5860, due to restrictions in the available computer memory. The selection of the DCs to be used was random, to maintain the original wide azimuth and path-length distribution. The new, downsized, set of DCs is plotted in Figure 6.12a. The plots of the corresponding path-length and azimuth distribution of the DCs are given in Figures 6.12b and 6.12c, respectively. It can be observed that, even reduced in number, the DCs still presented wide ranges of azimuths and path lengths.

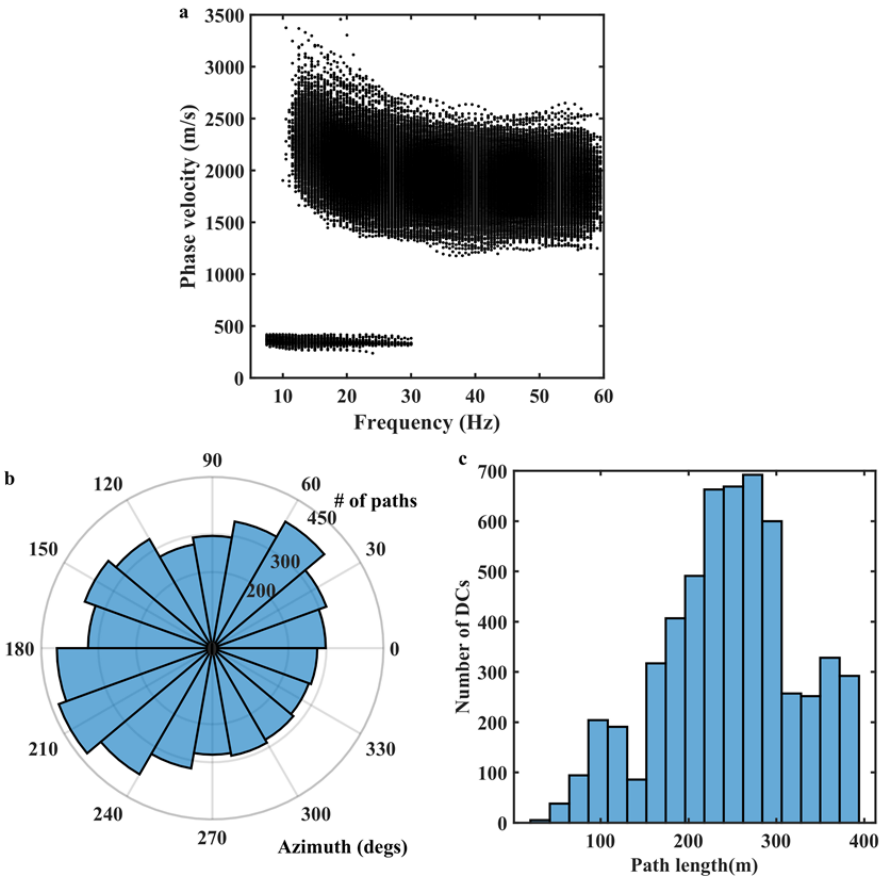

Figure 6.12: a) Downsized (number of 5860) set of DCs used in the tomographic inversion. b) Azimuth and c) path-length distribution of the DCs in (a).

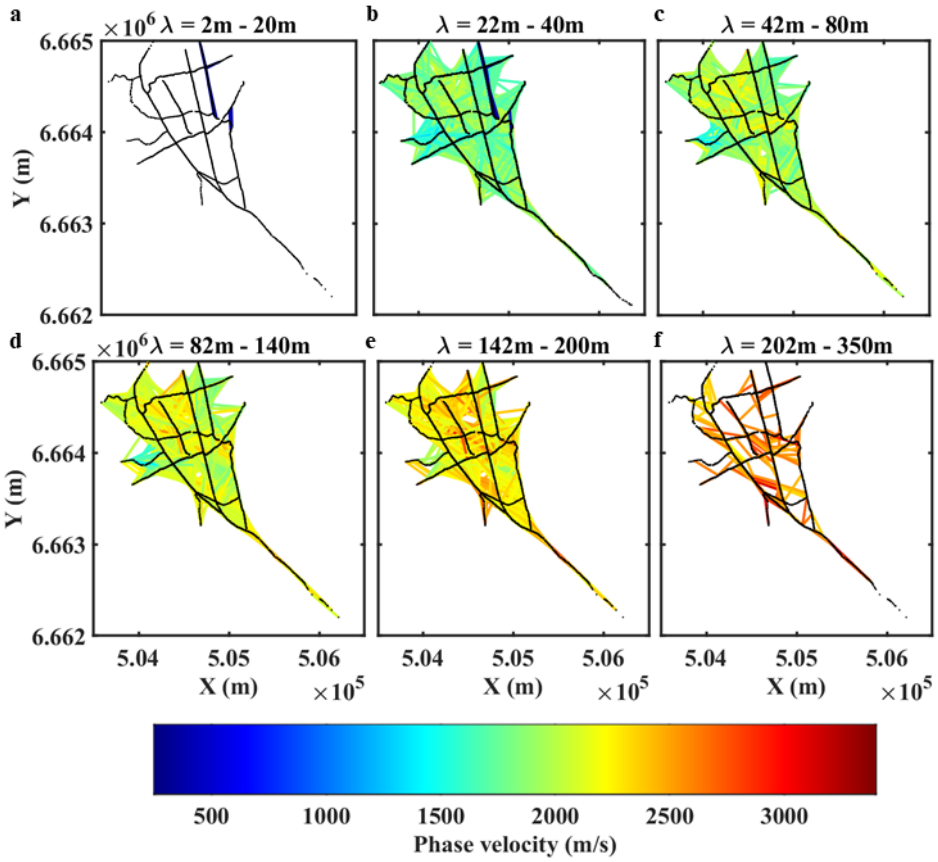

Figure 6.13 Spatial coverage of the DCs of Figure 6.12(a) at a wavelength range of a) 2 m – 20 m, b) 22 m – 40 m, c) 42 m – 80 m, d) 82 m – 140 m, e) 142 m – 200 m and f) 202 m – 350 m. The colorscale indicates the average phase velocity of the DC at each wavelength range and is specified in the colorbar.

In the different panels of Figure 6.13, we plot the spatial coverage of the DCs (the lines correspond to the intra-receiver path of each DC), for the same wavelength intervals as in Figure 5.29, where we plot the coverage of the original DC set. It can be observed that also the new set of DCs presents adequate spatial coverage at all wavelengths, apart from the longest-wavelength interval (202 m - 350 m, in Figure 6.13f), where the coverage is low, due to the originally lower number of long-wavelength data points.

Initial model selection

The initial model for the inversion was gridded as 390 uniformly spaced 1D profiles, the positions of which are shown as black dots in Figure 6.14. the properties of the layers are given in Table 6.2.

To define the initial V_S and ν, we compared the position of each profile with the position of each reference DC (Figure 5.21b), to relate each profile to a cluster. The cluster to which each profile was found to belong is given by the color of each dot in Figure 6.14, where the color-coding of the clusters is given in the colorbar. Depending on the cluster, we chose for each profile and each layer (depending on the layer depth), the appropriate reference V_S (dashed in Figure 6.11b) and ν (solid in Figure 6.11d).

For the inversion regularization, we imposed a lateral constraint of 100 m/s between the models. The constraints were interrupted at the limits of cluster 4 (cyan in Figure 6.14), where the tailings of the old mine exist, and the low phase velocities (< 500 m/s) were measured. Imposing a strong constraint would not allow to retrieve such a velocity contrast during the inversion.

Table 6.2: *Properties of the initial model used for the Ludvika 2019 dataset.*

			Cluster 1		**Cluster 2**		**Cluster 3**		**Cluster 4**	
Layer	h	ρ	V_S	ν	V_S	ν	V_S	ν	V_S	ν
	(m)	(kg/m^3)	(m/s)	(-)	(m/s)	(-)	(m/s)	(-)	(m/s)	(-)
1-2	20	2000	2100	0.34	1610	0.31	1550	0.34	390	0.24
3-4	30	2000	2100	0.34	1610	0.31	2560	0.34	760	0.37
5	40	2000	3000	0.18	2200	0.35	3500	0.33	3000	0.18
Half -space	-	4000	4000	0.18	4000	0.18	4000	0.18	4000	0.18

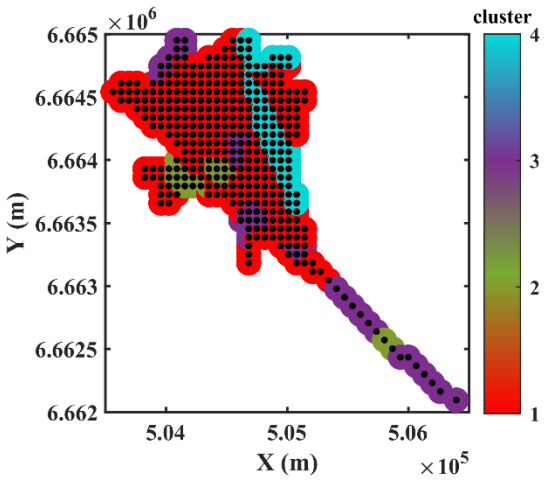

Figure 6.14: Position of the 1D profiles of the initial model. The different colors correspond to the different clusters (specified in the colorbar).

Tomographic inversion

In Figure 6.15 we present slices of the final tomographic model at different depths. In Figure 6.16, we show the misfit computed for different wavelength ranges and for each DC path, as the absolute difference (%) between the experimental and the theoretical DCs, resulting from the inversion. All of the curves present a misfit lower than 25 %, while more than 83 % of the data points present a misfit lower than 10 %.

It can be observed that the inverted model presents increasing V_S with depth, in agreement with the geological information in the area (Maries et al., 2017). Lateral velocity variability can be detected down to a depth of 140 m, where the velocity becomes nearly constant. This could be attributed to the low coverage at great wavelengths (Figure 6.13f), although the high values of velocity indicate bedrock formations, where variability is expected to be limited. As anticipated from the low velocities of the DCs corresponding to Cluster 4, the north-eastern zone of the model (indicated by the purple arrow) presents, down to a depth of 20 m, significantly lower V_S (< 500 m/s), probably related to the tailings dam. In addition, two high-velocity zones in the central and in the south-western portion of the model appear consistent at a wide depth range (20 m – 70 m), while, at all depths, a strong low-velocity anomaly (indicated by the circle in Figure 6.15) is evident. Its velocity and position suggest that it is the same low-velocity anomaly detected by the 2D SW tomography on the 2016 dataset, shown also as circle in Figure 6.5.

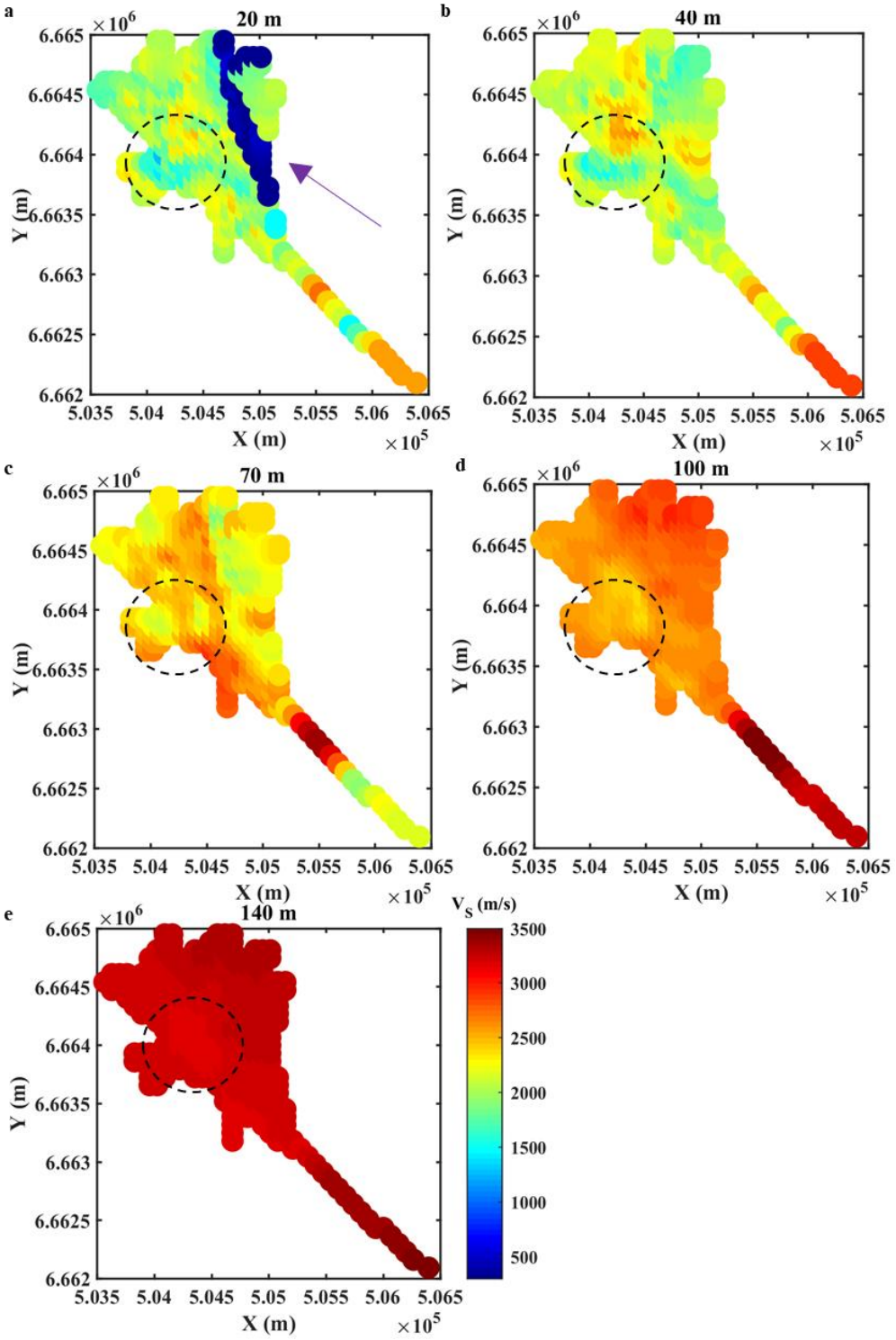

Figure 6.15: Inverted V_S model of the Ludvika site, at a) 20 m, b) 40 m, c) 70 m, d) 100 m, and e) 140 m. The arrow points to a region with extremely low velocity, and the circle indicates an anomaly, shown also as a circle in Figure 6.5.

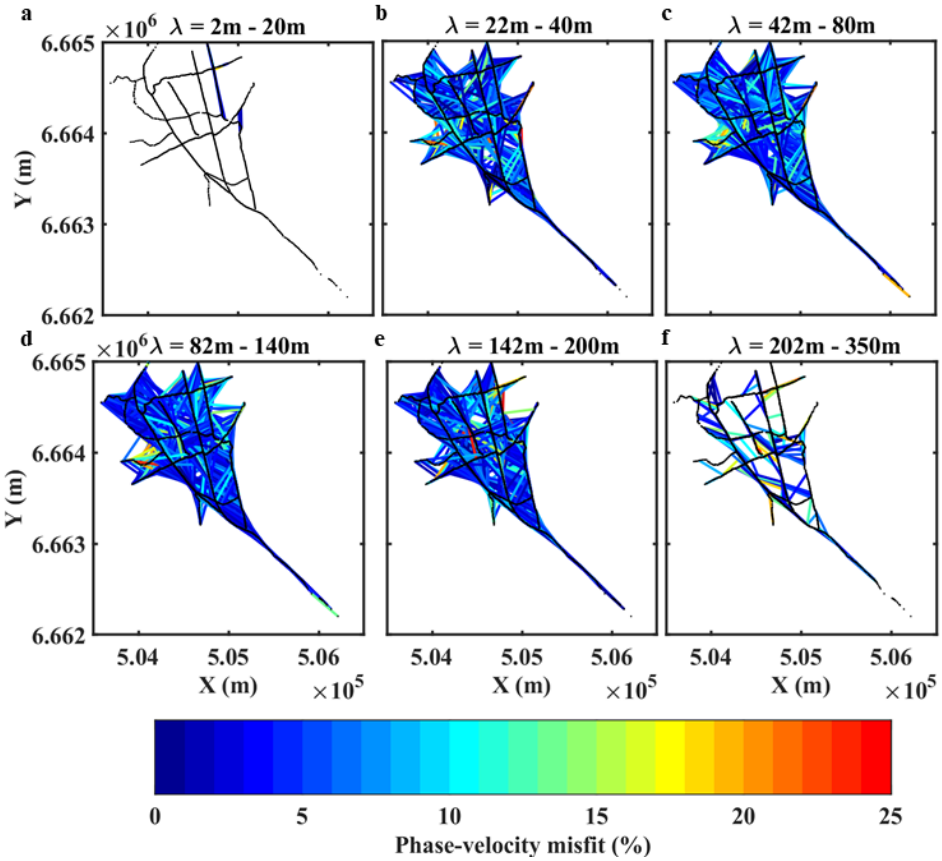

Figure 6.16: Spatial distribution of the DC misfit at a wavelength range of a) 2 m – 20 m, b) 22 m – 40 m, c) 42 m – 80 m, d) 82 m – 140 m, e) 142 m – 200 m and f) 202 m – 350 m.

Checkerboard test

In Figure 6.17a, we present the negative and positive velocity perturbations of 8 %, which were applied on the model of Figure 6.15, to create the checkerboard model. In Figure 6.17b, we show the velocity perturbations, retrieved by the inversion of the synthetic DCs, generated for the checkerboard model. It can be observed that most of the velocity perturbations at depths 20 m – 100 m were recovered by the inversion. An exception was the positive velocity perturbation at 100 m depth (inside the box in Figure 6.17), which was not accurately reconstructed. Moreover, in the deepest portion of the model (depth of 140 m), only the perturbations in the southern portion could be recovered, due to the low spatial DC coverage at the north-eastern side of the area at the longest wavelengths (Figure 6.13f). Nevertheless, no significant lateral variations were detected in this depth range in our inverted V_S model (Figure 6.15e), and therefore the lack of lateral

resolution in this limited area, was not considered critical. As a result, we conclude that all the detected velocity anomalies of our estimated V_S model (Figure 6.15) are within the resolution limits.

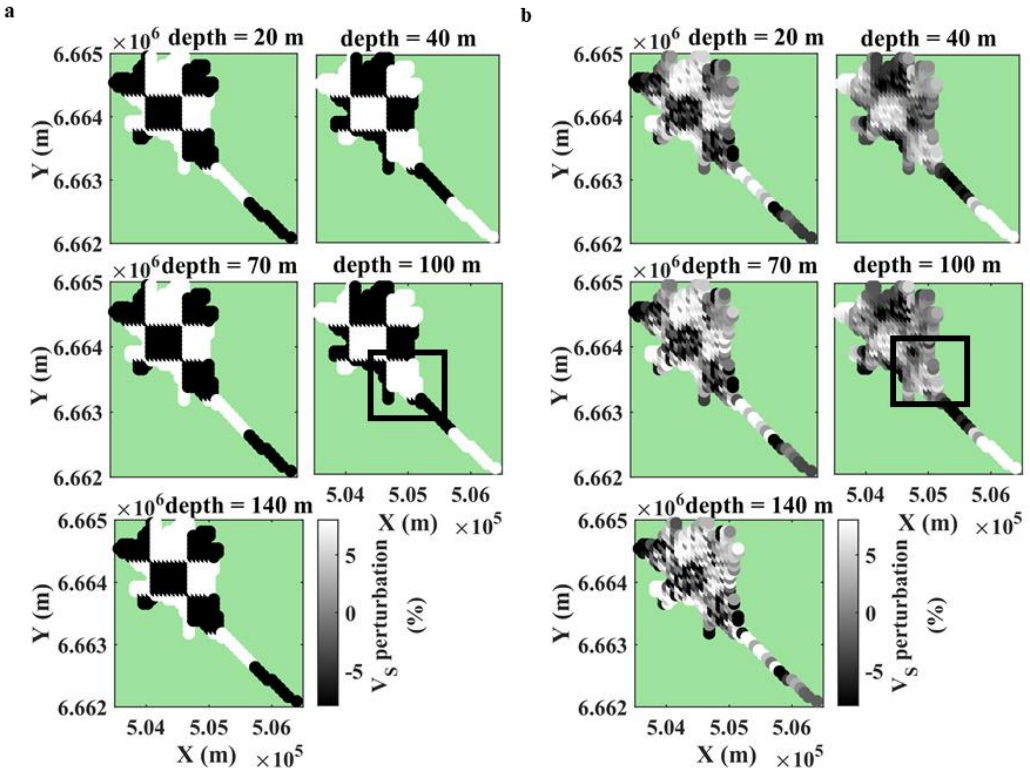

Figure 6.17: Velocity perturbations a) of the checkerboard model and, b) from the inversion of the checkerboard synthetic DCs. The box indicates a velocity perturbation which could not be accurately recovered.

V_{Sz}, V_{Pz} and statics computation

To estimate the statics, the V_S model of Figure 6.15 was converted into V_{Sz}, according to eq. 6.8. To convert it into V_{Pz}, we used, depending on the cluster allocated to each model (Figure 6.14), the appropriate ν_z from the ones presented in Figure 6.11d. V_{Pz} was then computed according to eq. 6.9 and was used for the computation of the static shift, according to eq. 6.10. Although the statics could be computed for the entire investigation depth of the model (down to 140 m), for comparison with the statics computed from the 2016 data (Figures 6.9a and 6.9b), we present in Figures 6.18a and 6.18b, the static shift computed at a (floating) datum of 40 m and 50 m, respectively.

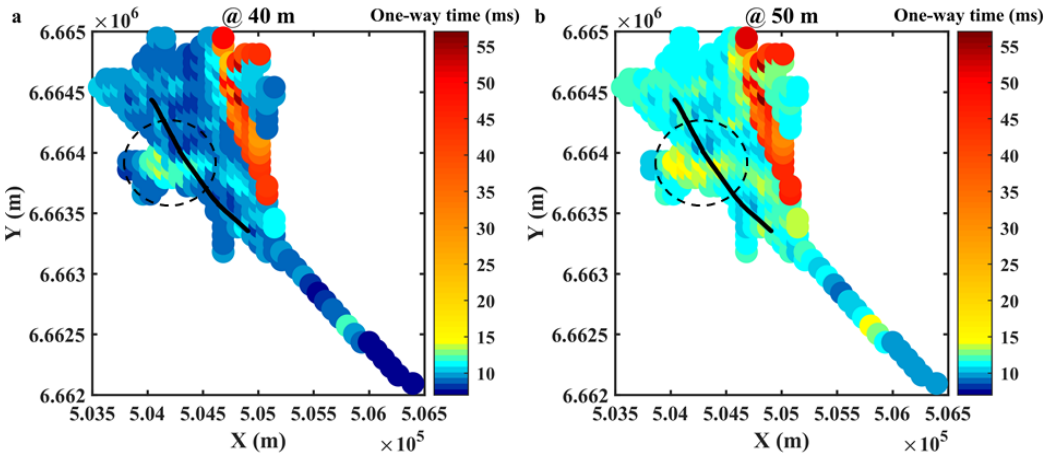

Figure 6.18: Static shift at a) 40 m and b) 50 m. The colors indicate the one-way time, given in the colorbars. The line corresponds to the processed portion of the 2016 dataset and the circle indicates a strong velocity anomaly (also in the circle in Figure 6.5).

V_P model estimation

Although not necessary for the computation of the statics, for which the input is the time-average velocity model, the information that was retrieved through our workflow allowed to estimate also a (layered) V_P model of the shallow subsurface. This model can be valuable in different stages of the seismic processing workflow, such as for the refinement of the shallow portion of the velocity model used for migration.

To estimate V_P, we applied eq. 6.9 (omitting the subscript z which denotes the time-average quantities), the tomographic V_S model of Figure 6.15 and reference ν profiles (solid lines in Figure 6.11d). Since the depths of the layers of the ν profiles did not coincide with the ones of the layers of the tomographic model, for each cluster we associated the proper ν not according to depth, but based on the value of V_S of each layer. In particular, in Figure 6.19 we show as dots, the V_S and ν of each layer of the clusters of Figure 6.11b and 6.11d, respectively. The color-coding represents the cluster number. Based on these combinations, we chose, depending on the cluster related to each profile of the tomographic model (Figure 6.15) and the V_S of each of its layers, the appropriate ν. The estimated V_P model is shown, at different depths, in Figure 6.20.

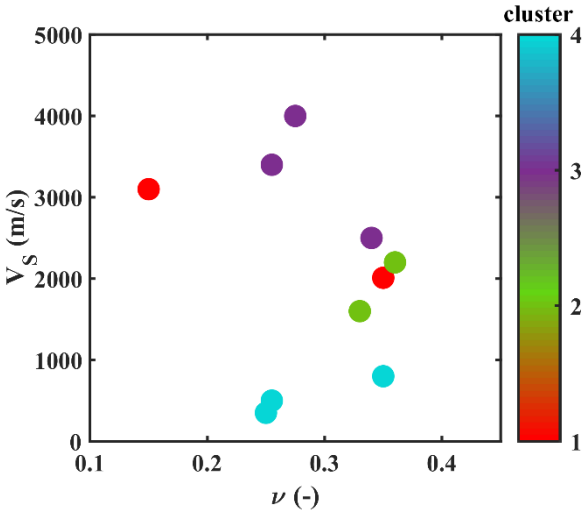

Figure 6.19: Combinations of V_S and ν of each layer of the reference models shown in Figures 6.11b and 6.11d, respectively.

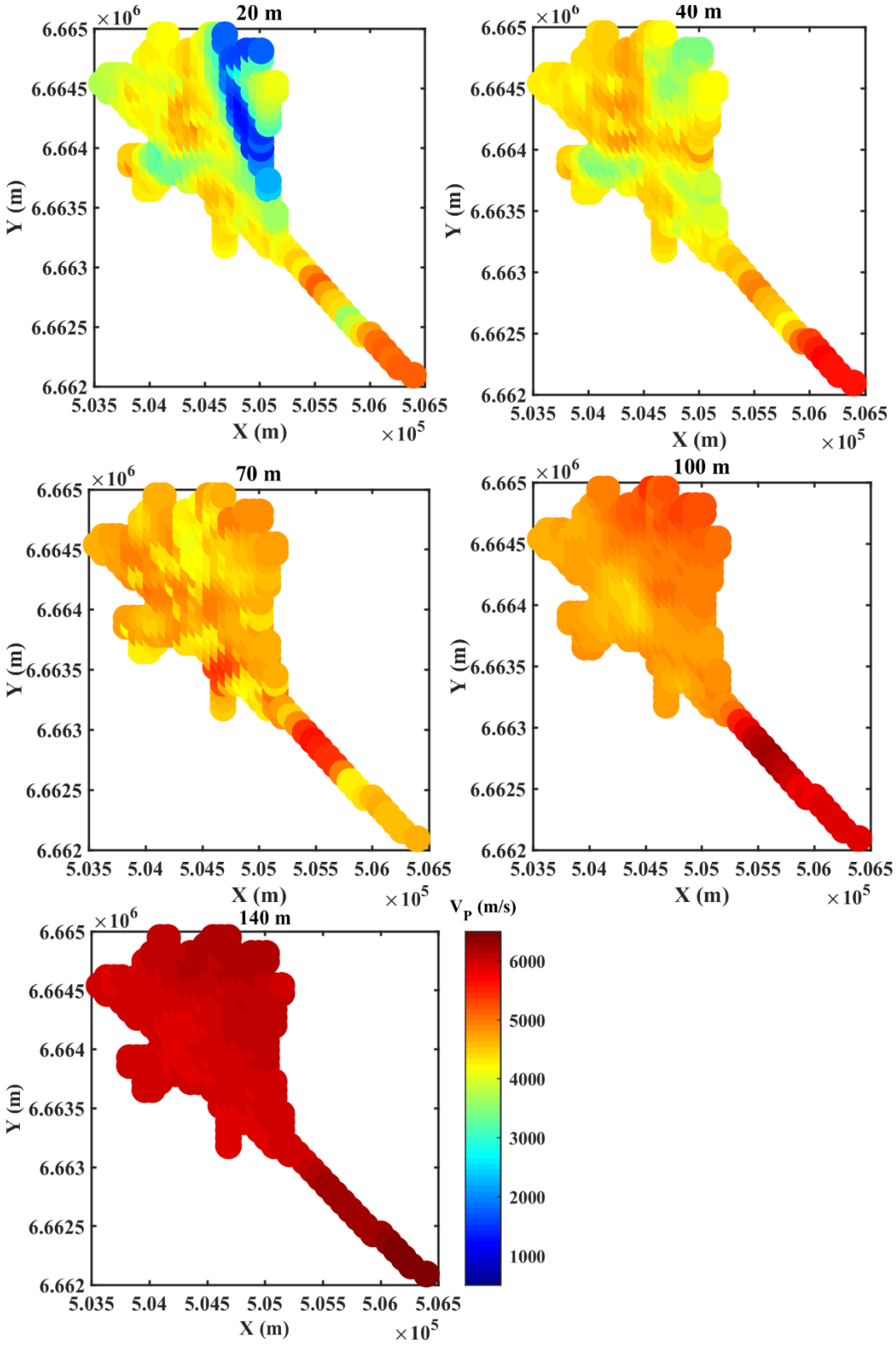

Figure 6.20: Estimated V_P from the Ludvika 2019 site at a) 20 m, b) 40 m, c) 70 m, d) 100 m, and e) 140 m.

6.4.3 Discussion

We have applied the SW tomostatics estimation workflow on the 2016 (2D) and 2019 (3D) seismic datasets from the Ludvika mining site, Sweden. In both cases, the workflow provided reliable models and statics, at a wide depth range, down to 85 m (in the 2D case) and 140 m (in the 3D case).

The comparison of the statics estimated for the 2016 dataset (green in Figures 6.10b and 6.10c), with the conventional BW tomostatics (black in Figures 6.10b and 6.10c), which we consider as a benchmark, has shown that our estimate was accurate and led to a stacked section of similar quality with the one resulting from the BW tomostatics (Figure 6.11). In both cases, the improvement of the continuity of the reflector (red arrows in all panels of Figure 6.11), with respect to the no-statics case, was apparent. Therefore, we conclude that our method can be used as an alternative to the standard BW-based methods, when retrieving the BW first-breaks is not possible or highly time-consuming (e.g., due to high levels of noise in the data).

With respect to the quality of the stacked image achieved by the SW direct statics (Figures 4.10c and 6.10d), which are based on multichannel SW processing, the one achieved by the SW tomostatics was slightly improved. Thus, with respect to the SW direct statics, the SW tomostatics can be considered as a higher resolution method to retrieve the static corrections.

Regarding the computational-time requirements, though, the SW direct statics method is, inarguably, a lower-cost alternative, since for the analysed portion of the Ludvika 2016 dataset, the computation of the direct statics from the raw data, required only 175 min (Table 4.4), using a single-core commercial laptop. Using the same computational equipment, the SW tomostatics estimation required approximately 11.4 hours (Table 6.3). We note though, that the only operation which required extensive operator involvement was the picking of the DCs, which in this case was performed semi-automatically.

For the 3D dataset from 2019, the automatic two-station processing method, presented in Chapter 5, allowed a large number of DCs to be picked, without the involvement of an operator. This led to a dense DC spatial coverage at all locations, increasing the reliability of the inverted model (Figure 6.15). Additionally, the checkerboard test (Figure 6.17) showed that the achieved lateral resolution was

adequate with respect to the size of the estimated velocity anomalies, increasing the confidence of the final result.

Table 6.3: *Breakdown of the time requirements of the SW tomostatics estimation for the processed portion of the Ludvika 2016 dataset.*

Workflow stage	Automation level	Time
A. Estimation of the reference ν_z	Automatic, apart from the processing parameter selection	173 min
B. Two-station DC extraction	Semi-automatic in this case (automatic option available, see Chapter 5)	90 min
C. Initial model selection	Automatic	Included three trials of the tomographic inversion (accounted for below)
D. Tomographic inversion	Automatic	3x100 min
E. Checkerboard test (performed three times to identify the optimal parameters)		
• Building of the checkerboard model, forward modelling	Automatic	20 min
• Checkerboard model tomographic inversion	Automatic	100 min
F. V_{Sz}, V_{Pz} and statics estimation	Automatic	2 min
		Total: ~11.4 h

The investigation depth of the 3D model was greater (140 m) with respect to the 2D model estimated from the 2016 data (85 m). This was due to the fact that the receivers of the 2019 acquisition covered a larger area, leading to longer available intra-receiver paths and, therefore, longer DC wavelengths (at maximum 350 m with respect to the maximum wavelength of 140 m in the DCs from the 2016 dataset).

The multichannel analysis on the 2019 dataset led to the estimation of values of ν, which are in agreement with the one estimated from the 2016 dataset, in the common locations and depths of the two profiles (bottom left panel of Figure 6.11d

for the 2019 dataset and Figure 4.9b for the 2016 dataset). In Figure 6.21, we compare the 3D statics estimated from the 2019 dataset (Figure 6.18) with all the static solutions estimated from the 2016 dataset (Figures 6.9a and 6.9b). Since the 2016 geometry covered only a portion of the one of 2019 (their overlap is the black line shown in Figure 6.18), we limit our comparison along the common line. In Figures 6.21a and 6.21b we show in purple, the one-way P-wave traveltime (static shift) estimated from the 3D model along the line, at a datum of 40 m and 50 m, respectively.

All the static solutions are similar and, compared to the SW tomostatics of the 2016 dataset, the ones of 2019 are nearly identical, depicting clearly the large time-shifts (dashed circle in Figure 6.21b), caused by the low-velocity anomaly which was detected in both tomographic models (black circle in Figure 6.5 and in Figure 6.15).

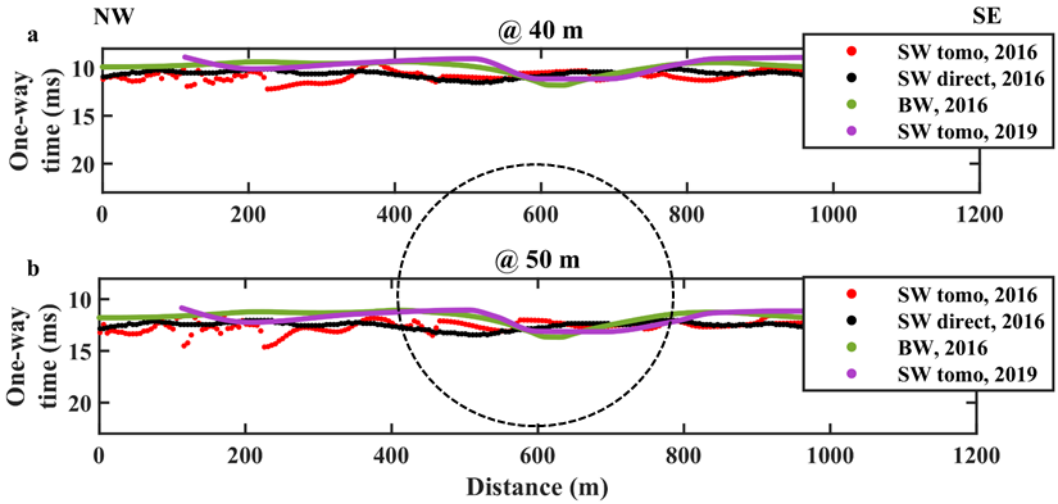

Figure 6.21: Static shift at a) 40 m and b) 50. In purple, the SW tomostatics computed from the 2019 3D dataset along the line shown in black in Figure 6.15. In green, the SW tomostatics, in red, the SW direct statics and in black, the BW tomostatics (Bräunig et al., 2020), all computed from the 2016 2D dataset.

Since the two datasets and their processing were independent, we are highly confident about the reliability of this low-velocity anomaly, although no prior information on its origin exists. In Figures 6.22a and 6.22b, we plot again the estimated 3D V_S and V_P models, after interpolating for better visualization. The low-velocity anomaly is indicated by the blue arrow. It can be observed that it presents a lateral extension of approximately 400 m and appears consistent

throughout the entire investigation depth. A possible explanation for this anomaly could be the local fracturing of the shallow rock.

One of the most striking features of the models, is the shallow (down to 20 m depth) low-velocity (V_S < 500 m/s) layer, in the north-eastern zone, where the tailings dam of the old mine is located. In the same zone, the refraction-static solution of (Malehmir et al., 2021), reproduced in Figure 6.23b, also presented extremely low V_P (approximately 700 m/s – 1000 m/s), although a direct comparison of the two velocity models is not straightforward, since they refer to different depths. However, this velocity match serves as a benchmark of our ν estimation.

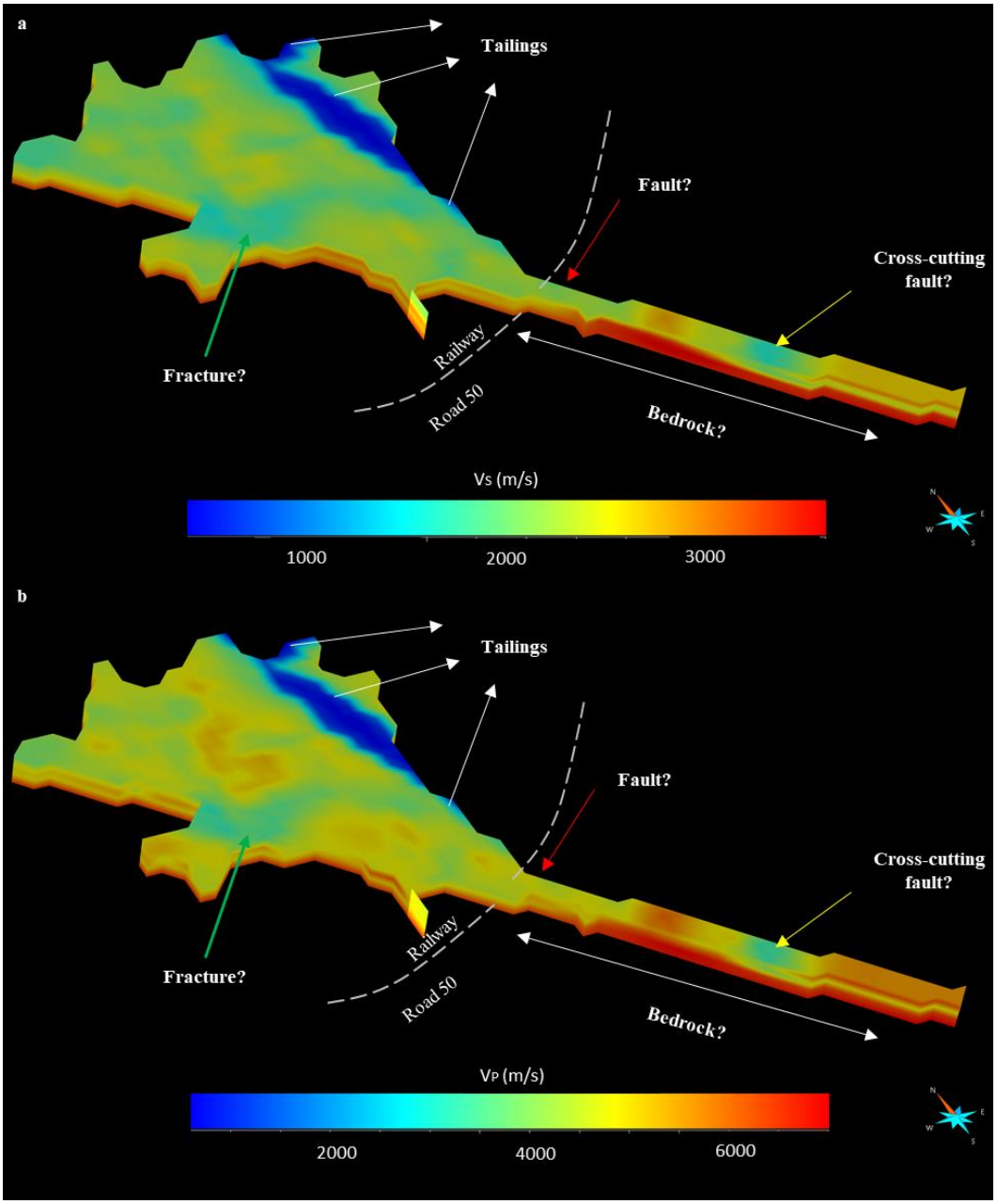

Figure 6.22: a) V_S and b) V_P model retrieved from the Ludvika 2019 dataset.

In the position where the model intersects the railway and road (red arrow in Figure 6.22), a narrow low-velocity zone is evident in the entire investigation depth. The area south to this zone, presents particularly high velocities at all depths, reaching a maximum V_S of 3500 m/s and V_P of 6000 m/s. In the same area, Malehmir et al. (2021) have detected a sudden increase of the bedrock V_P (Figure 6.23c), reaching similar values to our V_P estimate. According to Malehmir et al. (2021), this velocity jump could be explained by the presence of a normal fault in

the vicinity of the railway intersection, which has caused the rise of the bedrock (Figure 6.23d), and therefore the higher velocities. Our estimated local low-velocity anomaly at the intersection of the models with the railway (red arrow in Figure 6.22), could indicate the surface-location of this fault.

Further south to the railroad, a second narrow low-velocity zone is evident in Figure 6.22 (yellow arrow). The works of Bräunig et al. (2020) and Markovic et al. (2020) have shown that the southern portion of the mineralization is cross-cut, at a depth of approximately 1200 m, by a fault. The cross-cutting fault is assumed to extend at shallow depths towards the southern portion of the model, and our estimated low-velocity anomaly indicates the predicted position of its shallow expression.

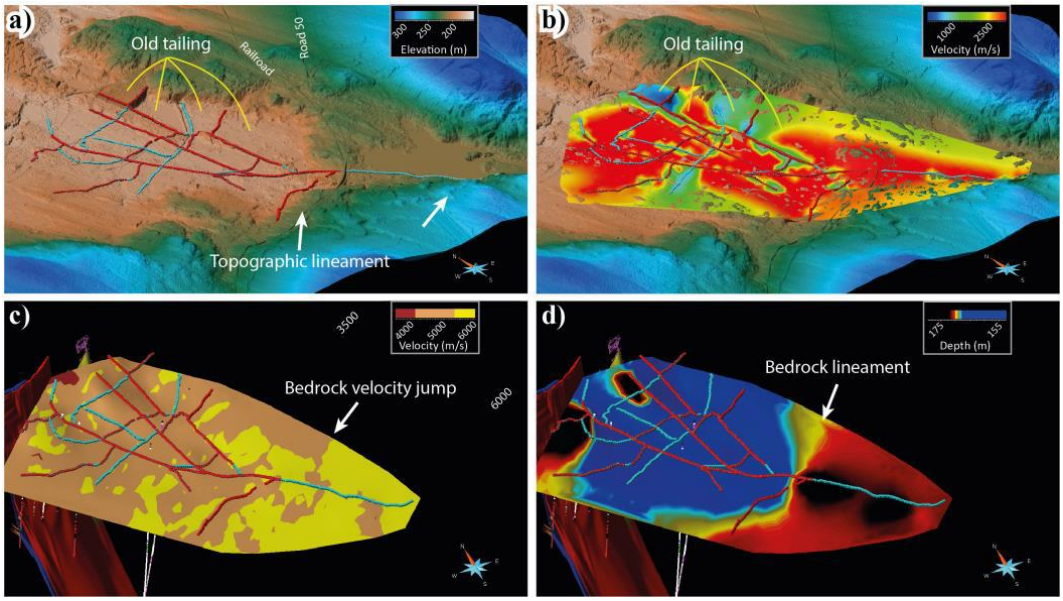

Figure 6.23: Reproduced from to Malehmir et al. (2021), a) LiDAR elevation map, b) shallow-V_P model, retrieved from 3D refraction static solution, c) bedrock V_P and d) bedrock depth.

6.5 Case study 3: Line SM1, Siilinjärvi mining site, Finland

We apply the SW tomostatics method to line SM1 (Figure 3.10) from the active-seismic dataset acquired in 2018 in the Siilinjärvi mining area in Finland (Section 3.3).

Estimation of the reference ν_z

Description of the extraction of the multichannel DCs and of the estimation of the reference V_S, ν_z and ν profiles for the two (Zone 1 and Zone 2) identified clusters can be found in Section 4.4.

Two-station DC extraction

The two-station processing parameters are presented in Table 6.4. For the DC picking, the reference multichannel DCs (solid in Figure 4.14b) were used as indicators of the local phase velocity in each zone. In Figure 6.24a, we show, as an example, the stacked cross-correlation matrix computed for two receivers located in Zone 2 (located at 880 m and 1240 m).

Table 6.4: *Processing parameters of the two-station method in Line SM1.*

Processing parameter	Value
Minimum receiver separation	50 m
Maximum receiver separation	600 m
Minimum offset	50 m
Maximum offset	580 m

In total, we extracted 274 DCs, which are plotted in the frequency - phase velocity domain in Figure 6.24b, and in the wavelength – phase velocity domain Figure 6.24c. The frequency band of the curves extends from 8 Hz to approximately 50 Hz, and the DCs present high phase velocities, in agreement with the geological information on the site (Malehmir et al., 2017). The wavelengths (Figure 6.24c) vary from a minimum value of 28.5 m to a maximum of 615 m, even though, according to the histogram of Figure 6.24d, nearly 91% of the wavelength measurements are limited in the range between 30 m - 160 m, where the wavelength distribution is wide (Figure 6.24e). In Figure 6.25, we indicate the DC spatial coverage which, in the wavelength range of 30 m – 160 m, is larger than zero along the entire line (the dashed line shows the boundaries of the non-zero coverage region).

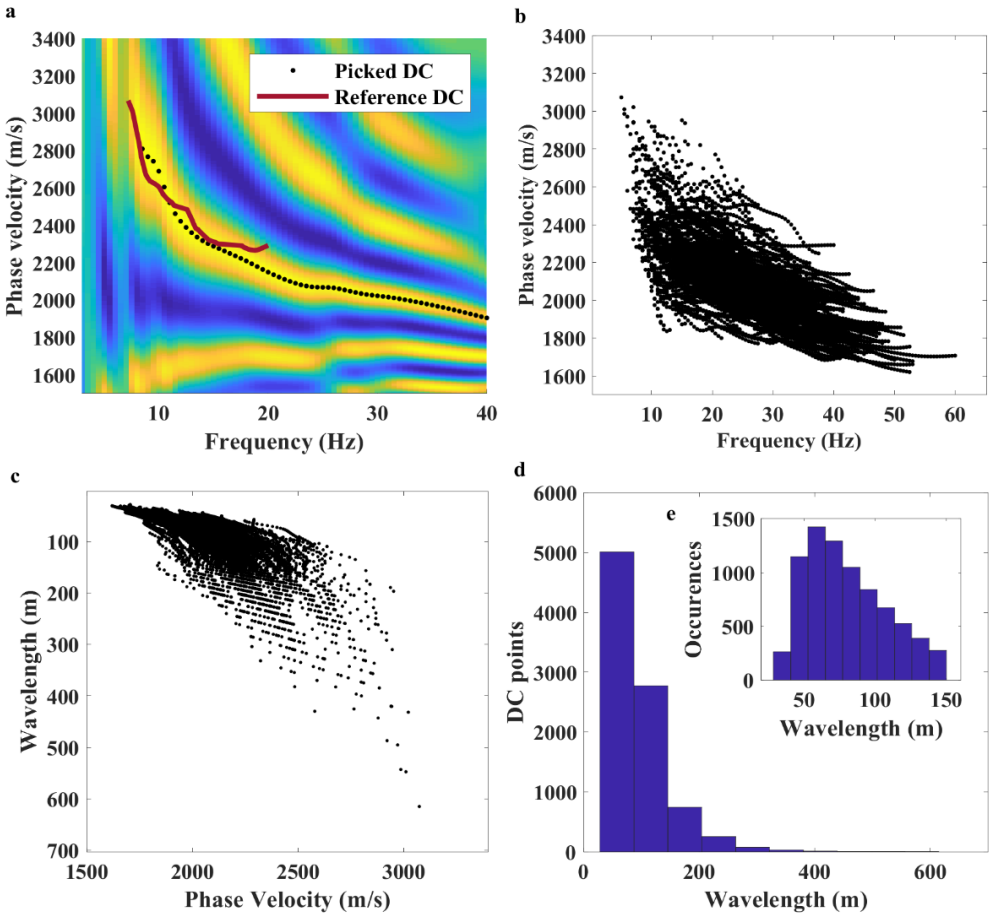

Figure 6.24: a) Example cross-correlation matrix. Extracted path-average DCs in (b) frequency – phase velocity and, (c) phase velocity – wavelength domain. d) Distribution of wavelengths between 28.5 m and 615 m, with (e) an inset showing enlarged view of distances between 30 m and 160 m.

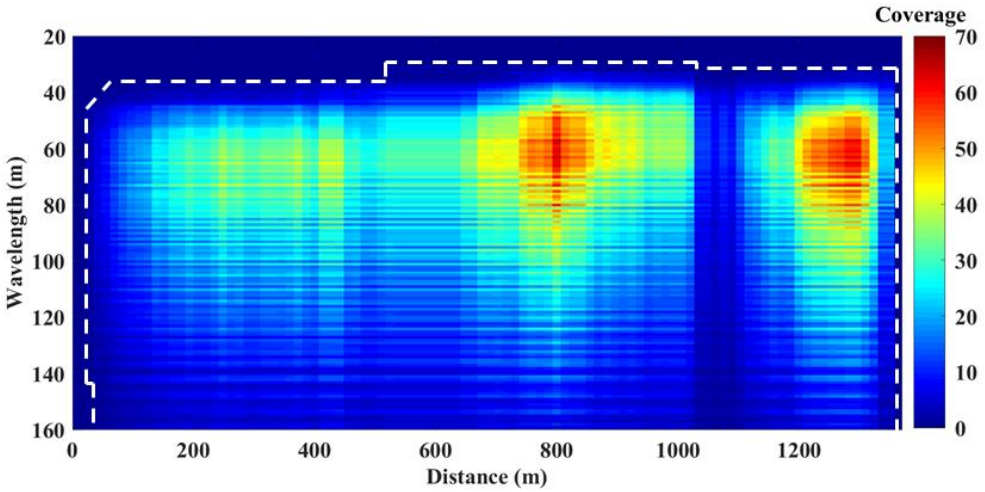

Figure 6.25: Plot of DC coverage as a function of wavelength along the line. The color scale represents the coverage and the dashed lines show the limits of non-zero coverage.

Initial model selection

The initial model is described in Table 6.5. The grid was set as 100, evenly spaced 1D velocity models, with a maximum depth of 80 m, which is deeper than the known bedrock depth (Da Col et al., 2020) and was therefore considered adequate for the static shift computation. The initial V_S and ν were set, depending on the position of the 1D models with respect to Zone 1 and Zone 2, according to the reference V_S (solid in Figure 4.15a), and ν (dashed in Figure 4.15) models. The density was selected following Malehmir et al. (2017). The inversion regularization was set by imposing lateral V_S constraints of 150 m/s, which were interrupted at the transition between the two uniform zones (at 800 m).

Table 6.5: *Properties of the initial model used for the line SM1 SW tomography.*

`	**Initial model - Zone 1**				**Initial model - Zone 2**			
Layer	V_S (m/s)	ρ (kg/m^3)	ν (-)	h (m)	V_S (m/s)	ρ (kg/m^3)	ν (-)	h (m)
1	2354	2500	0.25	20	2613	2500	0.332	20
2-3	2354	2500	0.34	10	2613	2500	0.3135	10
4-7	2830	2500	0.327	10	2608	2500	0.2936	10
Halfspace	3300	2800	0.351	-	3300	2800	0.2977	-

Tomographic inversion, V_{Sz} , V_{Pz} and statics estimation

The inversion result, after 10 iterations, is the pseudo-2D V_S model shown in Figure 6.26a. The estimated V_S ranges between 1650 m/s and 3000 m/s, which are in agreement with the known geology of the site (Malehmir et al., 2017). The model presents strong lateral heterogeneity, with presence of high velocities at shallow depths, in the area between 500 m and 900 m. The overburden layer presents several vertical high-velocity anomalies between 0 m – 40 m depth, and its thickness increases abruptly in the area corresponding to Zone 2. The V_S model was transformed into V_{Sz} by applying eq. 6.8, and to V_{Pz}, using eq. 6.9 and the corresponding ν_{z1} and ν_{z2} (Figure 4.15c), depending on the position along the line. In Figure 6.26b we plot the one-way time (static shift), computed according to eq. 6.10 for different (floating) datum depths within the model investigation thickness.

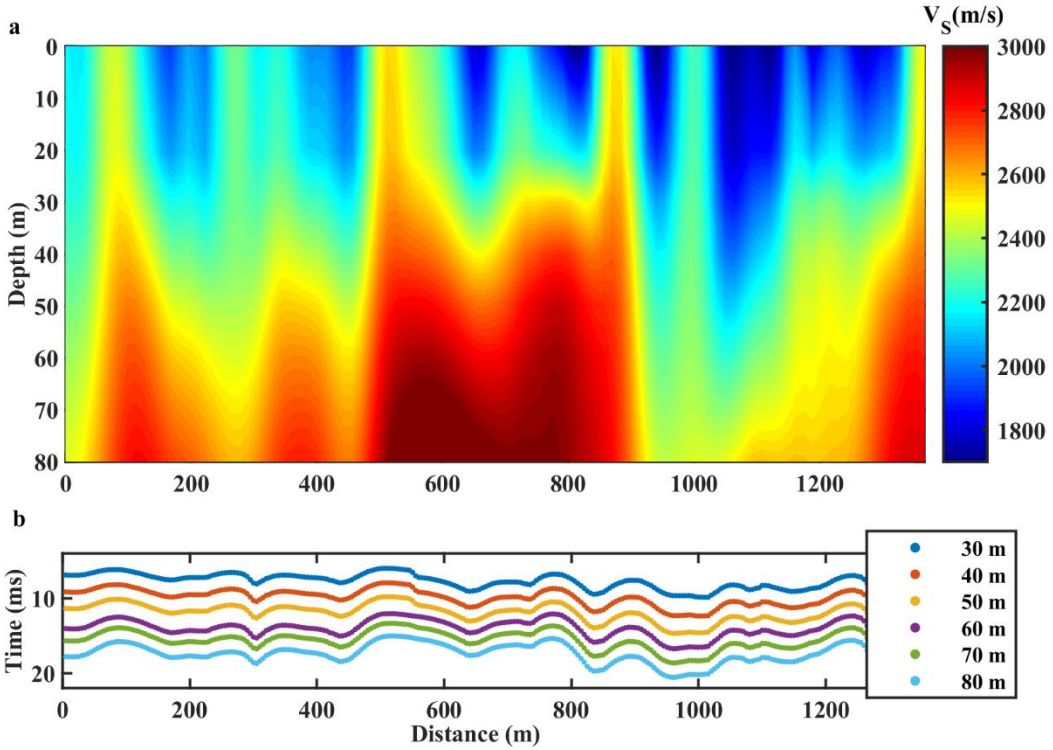

Figure 6.26: a) Tomographic V_S model. b) Static shift for different datum depths, indicated by the different colors.

Checkerboard test

The checkerboard test is presented in Figure 6.27. The model was created by applying a V_S perturbation of ±8% (according to the pattern shown in Figure 6.27a) to the retrieved model (Figure 6.26a).

The inversion of the synthetic DCs corresponding to the checkerboard model, provided the V_S perturbation shown in Figure 6.27b. Comparing the inverted perturbation model(Figure 6.27b) with the "true" one (Figure 6.27a), we observe that most of the velocity blocks were accurately reconstructed for the entire investigation depth, apart from the ones inside the square in Figure 6.27b. We can, therefore, conclude that our resolution equals, at least, the perturbation-block size for the entire model, excluding the ones in the area of the square (Figure 6.27b). Comparing these results with the retrieved V_S model (Figure 6.26a), we conclude that all detected velocity variations are within the resolution limits, implying the reliability of our estimation.

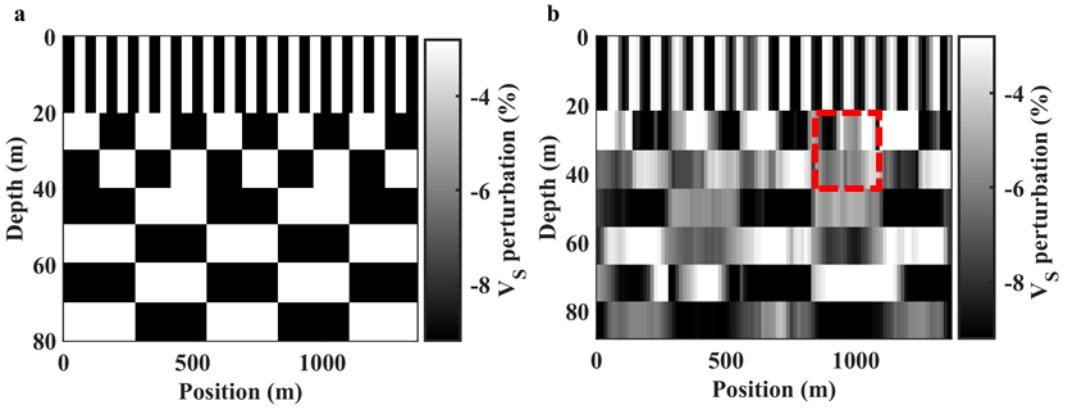

Figure 6.27: a) "True" and b) inverted checkerboard perturbation. The square in panel (b) depicts a zone where the perturbation blocks were not accurately reconstructed.

To interpret the estimated tomographic V_S model of Figure 6.26a, we superimpose it to a geological model, built by Yara Suomi Oy prior to the seismic survey based on surface-geology and drillhole information, shown in Figure 6.28. It can be observed that the two models are in good agreement, providing similar structural information. The low velocities of our V_S estimate correspond to the appearances of the carbonatitic rocks (light purple in Figure 6.28), the V_S of which are known to range between 2000 m/s and 2500 m/s. The high-velocity anomalies of the tomographic model, given by the blue arrows in Figure 6.28, match the intrusions of the higher-velocity tonalite-diorite (grey) in the carbonatite complex, reinforcing the reliability of the geological model. The high-velocity zone which appears at shallow depths in the tomographic model in the area indicated by the green box, can be associated to a larger-scale high-velocity, horizontally oriented, folded diabase dyke that is not captured by the geological model shown in Figure 6.28. This result fortifies the indications of Kauti et al. (2019), who have shown, based on production drilling data, that a large-scale horizontal diabase dyke can be expected at this depth in the southern part of the pit, in the immediate vicinity of SM1.

The low-V_S anomaly (white box), which appears on the tomographic model above the interpreted diabase intrusion (green box), is probably related to the railway and road (Figure 3.10) that crosses the seismic line at this position. Finally, the black arrow indicates a higher-velocity anomaly within the low-velocity

carbonatite area, which cannot be interpreted by the geological model. It could be indicative of yet another, smaller-scale diabase dyke, and/or the low-velocity anomalies around it could be related to large shear zones that run at the eastern contact to the carbonatite complex.

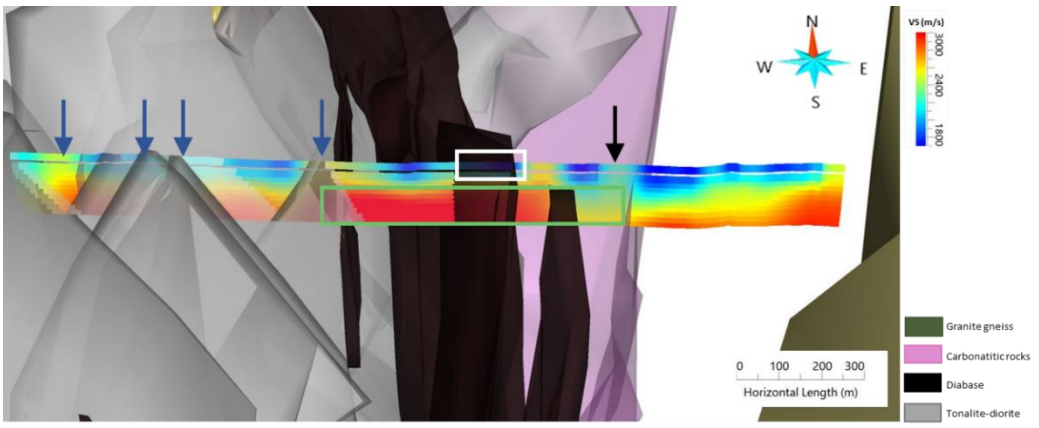

Figure 6.28: Superposition of the estimated tomographic V_S model (Figure 6.26) to the geological model of the area, provided by Yara Suomi Oy.

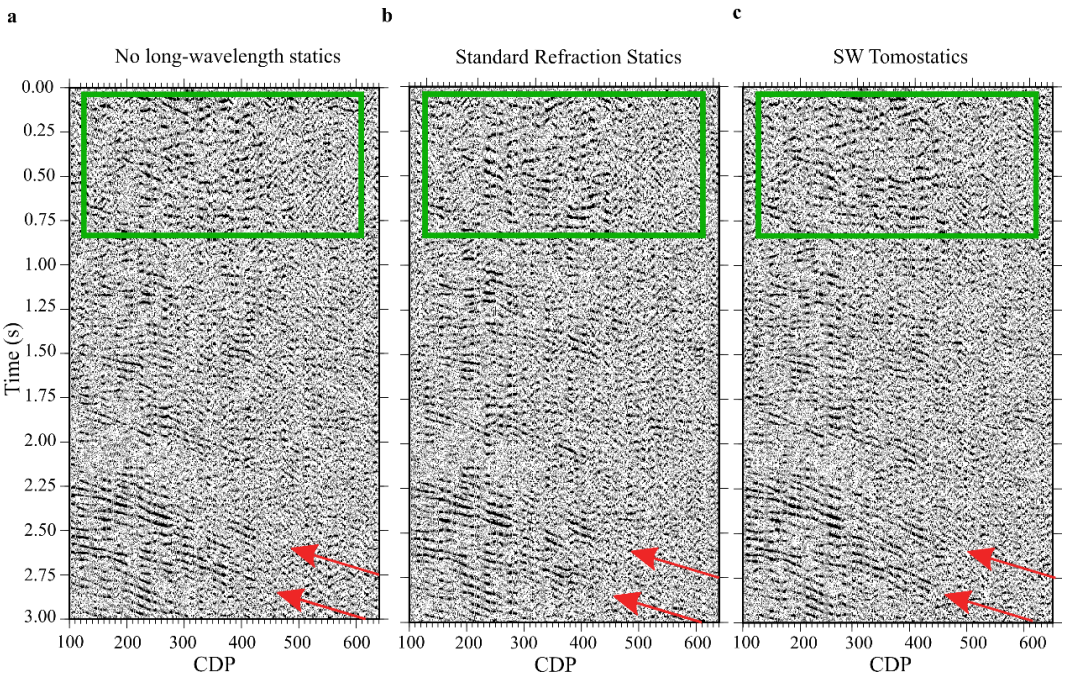

Figure 6.29: Stacked seismic sections a) without long-wavelength statics, b) after standard refraction statics and c) after SW-tomostatics.

The estimated SW tomostatics have been used both for the long-wavelength statics and for further redatuming. The datum depth was chosen as 70 m, to ensure that the entire overburden thickness is accounted for. In Figure 6.29a, we report the

stacked section without long-wavelength statics and in Figure 6.29b the section after applying refraction-tomography statics, computed based on a 3-layered velocity model. In Figure 6.29c, the stacked section after applying SW tomostatics is presented. All the results include the residual statics, resulting after two rounds of velocity analysis (the details of the overall prestack processing workflow have been described in Laakso, 2019). Comparison reveals that the SW tomostatics improved the consistency of both shallow and deep reflections with respect to the section without the long-wavelength statics and provided similar results with the standard refraction-based static solution.

The most significant improvement can be observed with respect to the deep reflectors, indicated in Figure 6.29 by the red arrows. These, in Figure 6.29c become longer and more coherent compared to the no-statics case (Figure 6.29a), and similar to the case of refraction-tomography statics (Figure 6.29b). Of great interest are the shallow reflections (down to 1000 m depth), since they refer to the currently mineable depths and are related to the intrusions of diabase and tonalite-diorite into the carbonatite ore body. Here, the effect of the SW tomostatics is again beneficial. Most of the shallow reflections (within the green boxes in all panels of Figure 6.29) appear more coherent in the section after the SW-tomostatics correction with respect to the no long-wavelength statics section and of similar quality compared to the section after the refraction-tomography statics.

6.6 Conclusion

We have shown that the SW tomostatics method is an effective approach to estimate the V_P statics. It combines SW tomography, which provides a high-resolution V_S model, with the W/D method, which can efficiently estimate ν, using only the SW content of exploration seismic data.

Application of the method to the presented mineral-exploration datasets showed that it is as a valid alternative to the standard statics-estimation methods, particularly beneficial in presence of lateral heterogeneity. It led to stacked sections of, at least, equal quality to the ones resulting from the conventional BW approach, while the result was slightly improved with respect to the multichannel, lower-resolution, SW direct statics.

In terms of processing-time requirements, the W/D process is efficient since it is completely automated and most its processes are simple data transformations, requiring simple and fast computations. The applied tomographic inversion algorithm is completely automated and optimized for exploration, since it estimates directly V_S, skipping the phase-velocity map building stage of the common SW tomography schemes. The most demanding process is the extraction of the path-average DCs, input to SW tomography, which can be largely accelerated by the automation option proposed in Chapter 5.

Finally, although the case studies presented here regarded typical active-source seismic datasets, the method is applicable to passive-source data as well, requiring only an additional pre-processing stage. A fast and efficient pre-processing method of passive-source seismic data is presented in the Chapter 7.

Chapter 7

Processing of passive seismic data

7.1 Introduction

In this Chapter, we present a fully-automated passive-source data pre-processing method, to identify the portions of the data which contain useful SW information and estimate the azimuth direction of SW propagation, necessary for an accurate phase velocity measurement with the two-station processing.

We apply the method to the ambient-noise dataset from the forest area of the Siilinjärvi mining site (Section 3.3). From the detected windows, we extract the DCs and invert them, together with DCs extracted from active data (Da Col et al., 2020), to retrieve a high-resolution model in a wide depth range.

Moreover, we develop a workflow to optimize the retrieval of seismic reflections with passive seismic interferometry. Its basis is the illumination diagnosis (Vidal et al., 2014), used to isolate the time windows which contain useful BW signal and to perform the interferometry only on these windows. The method is applied on the portion of the same data recorded along lines SM2 and SM3 (Figure 2.8).

7.1.1 Overview of passive-source SW methods

Passive-seismic methods have proven to be valuable exploration tools since they can be used to investigate the subsurface without the utilization of active seismic sources. As a result, they are cost-effective and environmentally friendly. Moreover, they allow exploration in areas where the use of active sources is logistically inconvenient or restricted by safety regulations.

Compared to BW methods, typically used for resource-exploration, SW analysis is more attractive for passive investigations, since ambient seismic noise is typically dominated by SW. Moreover, the SW signal contained in ambient noise is usually of lower frequency (longer wavelength), with respect to the one produced by active sources which, in the context of SW analysis, allows deeper investigation.

For this reason ambient-noise SW tomography is widely used as the primary investigation tool for the characterization of the deep structures of the earth in regional to continental-scale applications (Ritzwoller & Levshin, 1998; Kennett & Yoshizawa, 2002; Shapiro & Campillo, 2004; Sabra et al., 2005; Yao et al., 2006; Yang et al., 2007; Lin et al., 2009; Bao et al., 2015). In the field of natural-resource evaluation, passive SW tomography is mainly used for the characterization of deep geothermal reservoirs (e.g., Lehujeur et al., 2017; Martins et al., 2020; Planès et al., 2020), while promising examples have shown its potential also in hydrocarbon (e.g., Bussat & Kugler, 2009) and mineral (e.g., Hollis et al., 2018; Lynch et al., 2019) exploration.

Apart from SW tomography, passive-source data are used also in the scheme of MASW for various applications, such as engineering investigations (Park et al., 2019) and site characterization (e.g., Rahman et al., 2016). Often, the combination of active and passive measurements is preferred, to retrieve wide wavelength coverage, increasing the investigation depth (e.g., Yoon & J. Rix, 2004; Luke et al., 2008; Comina et al., 2011).

The use of noise for the extraction of the DCs is different from the analysis of active-source data (see Chapter 2), since the location of the source with respect to the receivers is unknown. It has been shown that under the assumption of a spatially- and temporally-diffuse noise-field, the source position can be disregarded during processing since, if a long enough time window is used, off-line propagation phenomena will eventually average out (Campillo, 2006; Gouédard et al., 2008).

Nevertheless, these assumptions are rarely met entirely and usually the SW content of noise presents directivity (e.g., Roux, 2009; Le Feuvre et al., 2015).

To optimize the phase-velocity estimation, the direction of propagation of SW should be estimated prior to the DC extraction and only receivers in-line with this direction should be used for two-station processing. A common approach to estimate both the phase velocity and the direction of the energetically dominant event with multichannel processing, is is to deploy an areal receiver geometry and process the data with a beamforming technique. A commonly used method is the frequency-domain beam-forming (FDBF) of Zywicki (1999), described in detail in Section 2.3.4, but other similar tools can be found in literature (e.g., Park et al. 2004). To estimate the phase velocities with the two-station method, Roux (2009) performs beamforming on the data recorded by a network of 3C receivers to compute the SW azimuth. A rotation of the 3C data from different receiver pairs is performed towards the identified azimuth, and the rotated data are processed with seismic interferometry.

Here we present a fully-automatic pre-processing scheme suitable for the extraction of DCs from passive-source data with the two-station method. Our method detects the time windows of the entire record dominated by SW and estimates the SW propagation direction using the FDBF technique. The detected windows and their corresponding azimuths are used in the two-station processing (Chapter 5) to extract the DCs only from receiver pairs aligned with the estimated azimuth.

7.2 Pre-processing scheme for SW analysis

The **main idea** of our method is that if a SW event, originating from a specific, unknown, location, is recorded at a specific time window, it will be energetically dominant in a wide frequency band and it will present traveltimes (velocity), characteristic of SW, allowing its detection. To avoid having windows capturing more than one SW arrivals, a check is performed to ensure that a recurrent dominant azimuth is measured in a wide frequency band, while a quality-control is performed to ensure that only the highest-quality SW data are considered.

7.2.1 Description of the method

An overview of the method is given in Figure 7.1. As a first step, the raw noise record is split into short time windows, to be processed separately. Since our goal is to find the windows which carry characteristics of SW only, the length of each window should be long enough to capture possible SW arrivals to all the receivers, but short enough to isolate them from other events (additional SW arrivals or other events such as BW, coherent noise etc.). *A priori* information on the expected phase velocities in the area can be useful for the selection of the proper window size.

Each window is transformed into the $f-k$ domain with the FDBF, which computes the power-spectral density $P(f,\mathbf{k})$ of the signal, as a function of frequency and of the vector of the k_x and k_y wavenumbers, $\mathbf{k}$. The value of $P(f,\mathbf{k})$ represents the frequency and wavenumber distribution of the energy of the windowed signal. Its maxima at each frequency are located at the k_x and k_y values of the dominant event in the record.

To check whether the dominant event is a SW arrival, we pick the maxima of the $P(f,\mathbf{k})$ amplitude $A_P(f,\mathbf{k})$ at each frequency f_i, and use their corresponding k_x and k_y coordinates ($k_{x,i}^{\max}$, $k_{y,i}^{\max}$) to compute the wavenumber magnitude:

$$|k|_i = \sqrt{\left(k_{x,i}^{\max}\right)^2 + \left(k_{y,i}^{\max}\right)^2} \tag{7.1}$$

The velocity of the dominant event is then computed as

$$V_i = \frac{2\pi f}{|k|_i} \tag{7.2}$$

We compare the computed velocity with an envelope of the expected SW phase velocities in the area, a "dispersion region", frequency by frequency. If a satisfactory portion (larger than a pre-defined "cut-off" criterion) of the computed V_i values fall within the "dispersion region", the panel is considered as SW-dominated. If not, the window is considered dominated by other kinds of events and is disregarded from further processing. The used "cut-off" criterion is a compromise between the number and quality of the retrieved DCs but, given the long records

usually acquired in passive surveys, strict criteria may be applied, to accept only the highest-quality SW signal without jeopardizing the retained information.

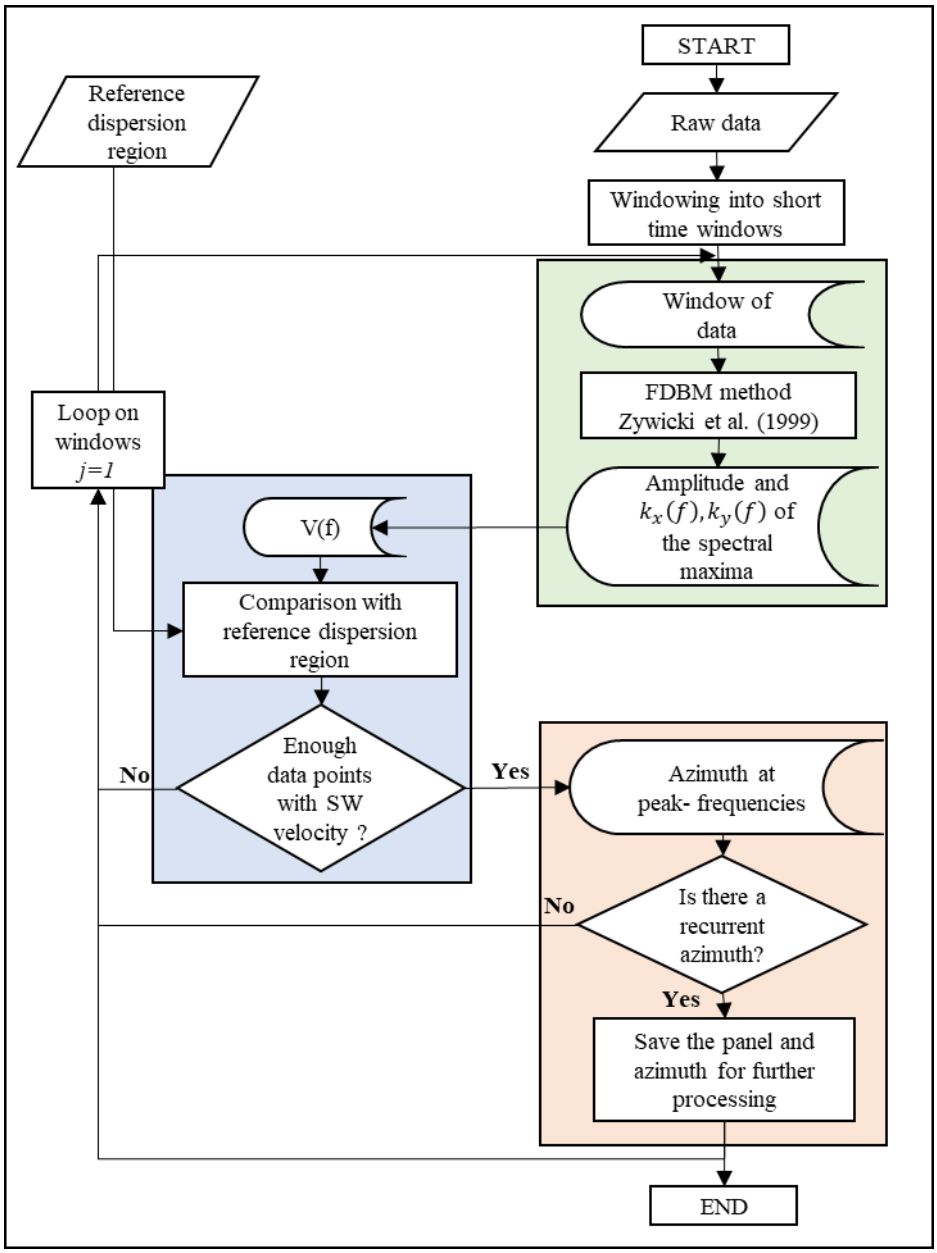

Figure 7.1: Scheme of the proposed SW pre-processing workflow of passive-seismic data.

For the SW-dominated windows, we use the $k_{x,i}^{\max}$ and $k_{y,i}^{\max}$ values to compute the direction of SW propagation. The direction is computed only at the frequencies where the signal is highly energetic, to ensure that we only measure the direction of SW and not of other events which might be dominant in a limited frequency

band. To do so, we only use the frequencies f_j at which $A_P(f,\mathbf{k})$ presents peaks and compute the corresponding azimuth as:

$$\theta_j = \tan^{-1}\left(\frac{k_{j,y}^{\max}}{k_{j,y}^{\max}}\right) \tag{7.3}.$$

Since SW arrivals, originated by different azimuths, might be dominant at different frequencies, several values of θ_j might be estimated. To assess whether the window contains a coherent SW event (coming from one direction), we evaluate the occurrences of θ_j and check whether the same θ_j has been measured, at least in half of the f_j frequencies. If not, we consider the window unsuitable for the DC estimation and disregard it from further processing. If a recurrent (in at least half the dominant frequencies) θ_j appears, the window is considered suitable, and it is saved along with its θ_j, to be used as input to the DC extraction with the two-station method (Chapter 5).

7.3. SW analysis of the passive-seismic dataset from the Siilinjärvi mining site

The passive- and active-source dataset, acquired in the forest area of the Siilinjärvi mining site, is described in Section 3.3.3. The purpose of recording both active and passive data was to retrieve SW information on a wide wavelength range, to be used with SW tomography for the estimation of a high-resolution model in a wide depth range, possibly indicating the mineralization target.

Details on the processing and of the active-source data can be found in Da Col et al. (2020). In total a number of 433 DCs were extracted, covering the entire area. The DCs presented frequencies in the range of 5.5 Hz and 49.5 Hz, corresponding to wavelengths between 32 m and 672 m. Here we present the processing applied to the passive-source data and the tomographic inversion of the combined active-passive DC set.

7.3.1. Pre-processing of the data

The 1-minute SEG-Y files of the 13-day ambient-noise record were split into 2-s windows. This window length was considered adequate, given that the minimum phase velocity estimated in the area from our active SW tomography was approximately 1650 m/s and the maximum distance between the receivers was slightly larger than 2000 m. In total 334880 windows were extracted.

The spectral computation with the FDBF method was performed in a frequency range between 2 Hz - 20 Hz, since our target was to extract SW DCs in the low-frequency bands, which were not sufficiently covered by the active-source DCs (only 8% of the active-source DC had a minimum frequency lower than 6.2 Hz). In Figure 7.2, we demonstrate the application of FDBF process on one of the 2-s windows. In Figure 7.2a, we show examples of the $f-\mathbf{k}$ spectra computed for different frequencies, plotted against k_x and k_y. The spectral maxima were picked at all frequencies and their amplitude values, $A_p(f,\mathbf{k})$, are plotted in Figure 7.2b.

The k_x and k_y coordinates of the spectral maxima were used to compute, at each frequency, the wavenumber magnitude $|k|$, according to eq. 7.1. The velocity was computed from the estimated $|k|$ at each frequency, according to eq. 7.2, and is plotted in Figure 7.2c. In the same figure, we plot in red, the "dispersion region", i.e., the range of the expected phase velocities, which was set based on the velocities of the active-source DCs. For this example, 85 % of the picked data points had a velocity within the dispersion region, and the window was considered dominated by SW.

The frequencies of the locally maximum values of the spectral amplitude (peak frequencies) were identified and are highlighted by the circles in Figure 7.2c. The azimuth was computed only at those frequencies, to ensure that only SW are examined. The azimuth computation is schematized in the panels of Figure 7.2a which correspond to the peak frequencies, i.e., the panels highlighted with the rectangles of the same color-coding as their peak frequencies in Figure 7.2c.

The histogram of Figure 7.2d depicts the occurrences of the estimated azimuths at the peak frequencies. It can be observed that the azimuth of 240^o was estimated for half (3 out of 6) the peak frequencies, and therefore the signature of the dominant

SW event was considered coherent. This azimuth was assigned to the specific time window, which was saved for further processing with the two-station method.

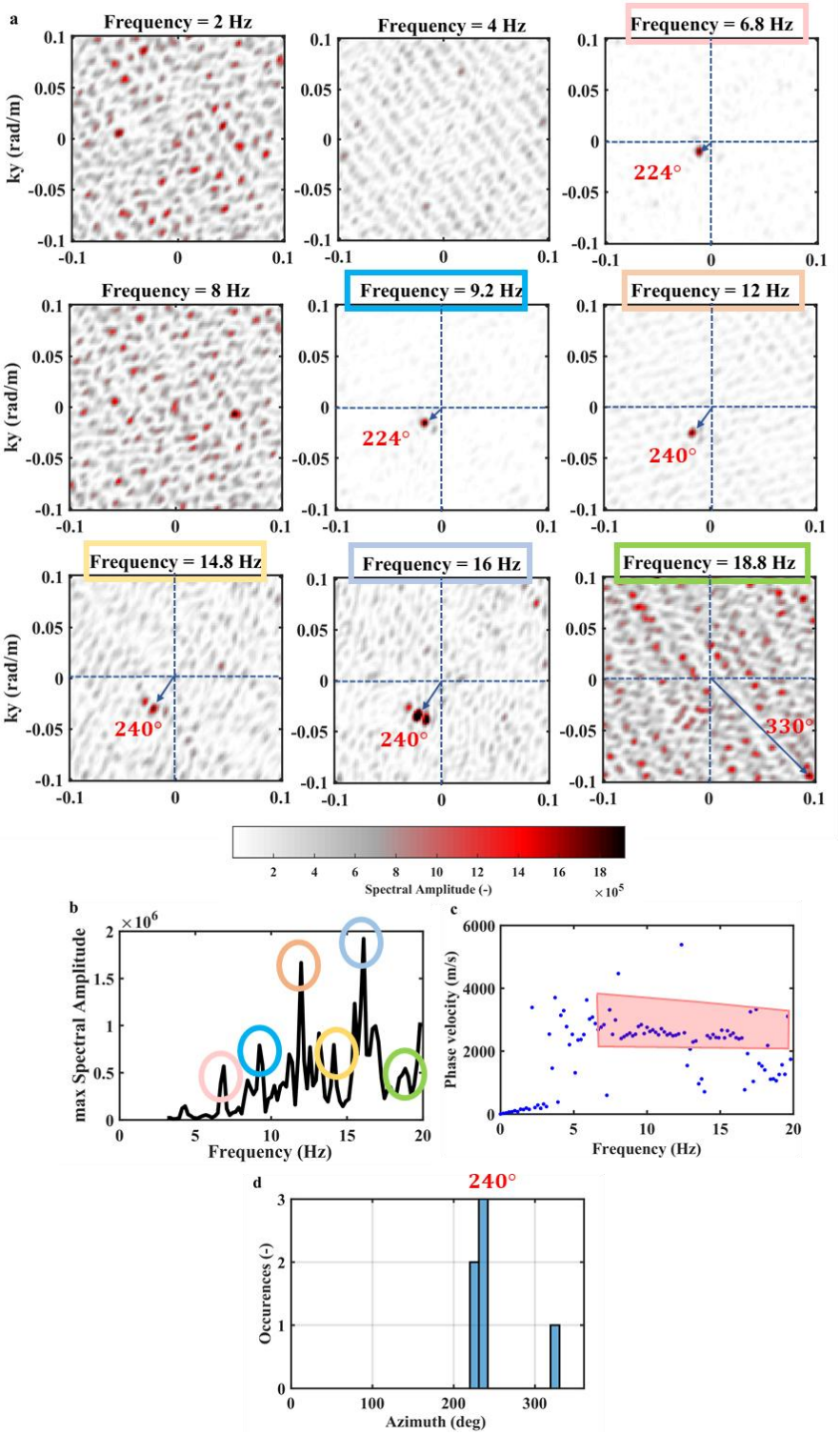

Figure 7.2: a) $f-\mathbf{k}$ spectrum computed at different frequencies. b) Amplitude $A_P(f,\mathbf{k})$ at each frequency. The circles indicate the peak values. c) Velocities at each frequency. In red, the "dispersion region". d) Distribution of the SW propagation azimuths.

The same process was repeated for all the time windows of the dataset. The results showed that 25691 windows contained dominant SW signal and the corresponding azimuth was estimated. The total number of SW occurrences compared to the number of 2-s windows of each day is shown in Figure 7.3a, while the histogram of all the azimuth directions is reported in Figure 7.3b. It was found that a cluster of 16272 events originated at an azimuth between 200° and 240° (according to the reference system shown in Figure 7.3c), while a second cluster of 6505 events was found at an azimuth of 42° - 60°.

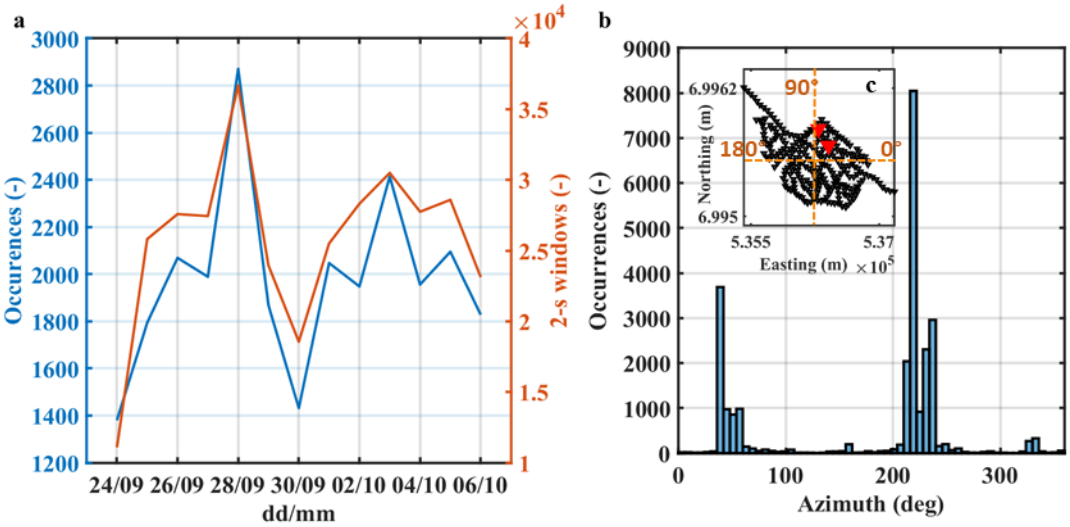

Figure 7.3: a) Analyzed 2-s windows (orange) and 2-s windows containing SW signal (blue) for each recording day. b) SW occurrences for each azimuth. c) Map of the array with indication of the azimuth reference system. In red, the receivers used in Figure 7.4.

7.3.2 Extraction of the SW DCs from the noise time-windows

For the extraction of the DCs we used the method described in Chapter 5. The only difference with respect to the active-source data processing shown in Chapter 5 was that, instead of active-shot gathers, we used as input the individual time windows which were found as SW dominated. We identified, for each time window, all the receiver pairs aligned with the dominant azimuth and performed the cross-correlation matrix computation for each one of them. For each pair, the matrices computed from all the windows were stacked, to increase the S/N and, in the end, only one DC was (semi-automatically) picked on the stacked cross-correlation matrix.

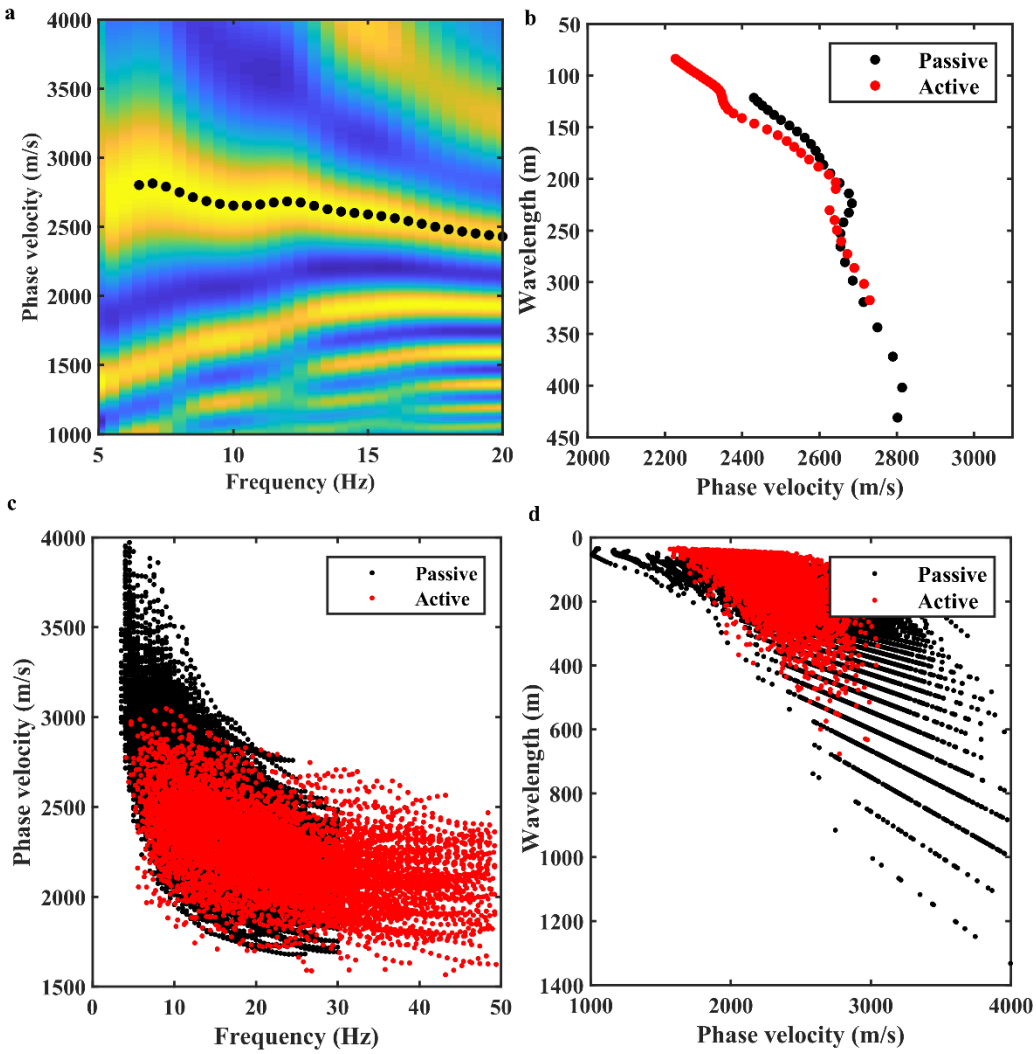

Figure 7.4: a) Example stacked cross-correlation matrix and picked DC (black). b) In black, the picked DC of (a), and in red, the active-source DC. DCs from the passive (black) and active (red) data in the c) frequency – phase velocity domain and, d) phase velocity – wavelength domain.

In Figure 7.4a, we show, as an example, the stacked cross-correlation matrix, computed for the receiver pair highlighted in red in Figure 7.3c. In Figure 7.4b, we compare the same DC in the wavelength – phase velocity domain with the DC retrieved from the active data, for the same pair. The two DCs almost overlap in the wavelength region between 110 m – 320 m, showing a continuous trend and matching phase velocities, proving that the DCs from the ambient-noise data can be considered reliable.

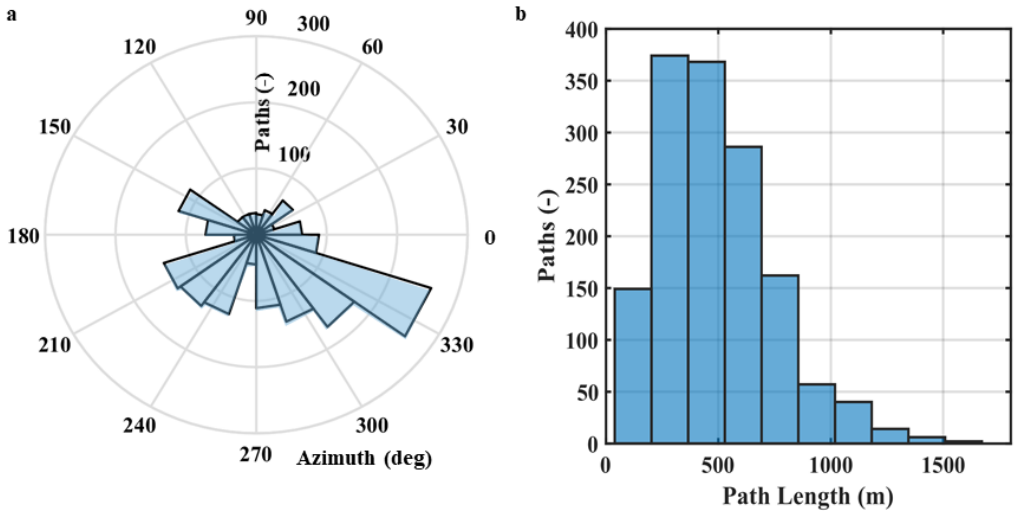

Figure 7.5: a) Azimuth and b) path-length distribution, of the DCs from the ambient-noise dataset.

In total, 1473 DCs were picked and are plotted in black in Figure 7.4c, in the frequency-phase velocity domain and in Figure 7.4d, in the phase velocity-wavelength domain. The distribution of the path azimuths of all the DCs is shown in Figure 7.5a. It can be observed that although we observed peaks in the estimated azimuths around 200°- 240° and 42° - 60° (Figure 7.3b), this did not translate to corresponding peaks in the DC azimuth coverage. Instead, the distribution of DC azimuths is rather homogeneous, apart from a peak in the 150° and 330° direction. This was due to the fact that, for the extraction of the DCs, the cross-correlation matrices, computed for the same receiver pair and different time windows, were stacked, and only one DC was extracted for each receiver pair.

Moreover, due to the random geometry of the receivers, several receiver pairs with different path lengths existed at the same azimuths and, therefore, a wide range of path lengths was included in the DC set (Figure 7.5b).

The curves from the passive-source data show similar trends with the 433 active-source DCs (red in Figures 7.4c and 7.4d), but they are characterized by longer wavelengths. In fact, the maximum wavelength of the passive-source DCs (1200 m, reached by 14 DCs) is nearly double the one of the active-source curves.

We consider the long wavelengths reliable since the passive-source DCs are consistent among each other, in their entire wavelength range. This can be observed in Figure 7.6, where we plot the spatial DC coverage at different wavelength ranges, indicated in the title of each panel. The curves present consistent lateral velocity

variability along the entire investigation area and at all wavelengths. The DC coverage is nearly full at all locations and wavelengths between 81 m and 700 m, while it remains dense also in the wavelength intervals between 61 m and 80 m and between 801 m and 1000 m. Nevertheless, the coverage at wavelengths between 40 m and 60 m was almost zero (Figure 7.6a) since our processing involved only low frequencies and the highest-frequency information was retrieved from the active-source processing. In Figures 7.7a, 7.7b and 7.7c we show the coverage achieved with the combination of active- and the passive-source DCs at wavelength ranges 40 m – 60 m, 61 m – 80 m and 81 m – 100 m. Compared to the corresponding panels of Figure 7.6 (Figure 7.6a-7.6c), the increase in the DC coverage is apparent.

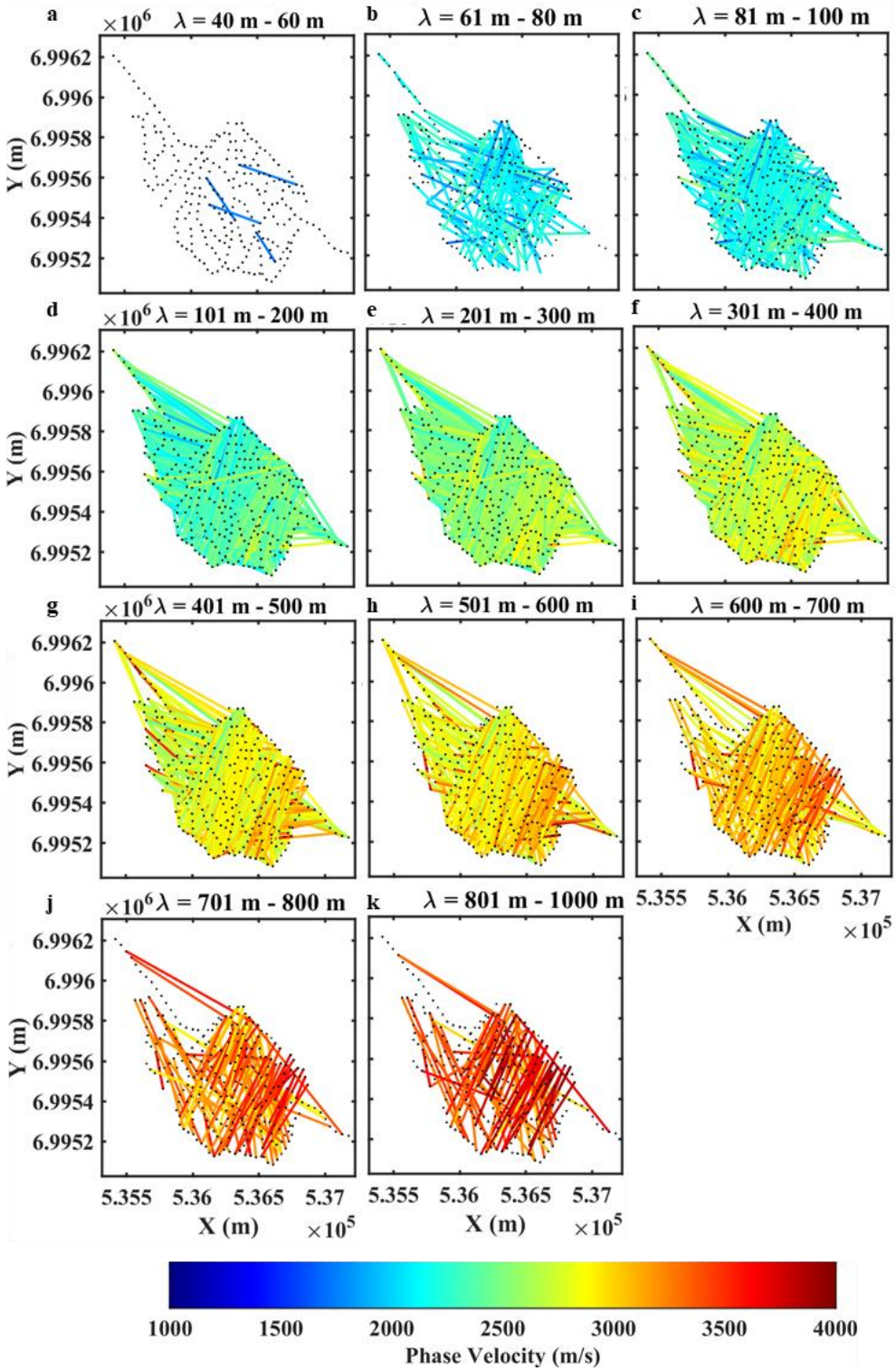

Figure 7.6: Spatial coverage maps of the passive-source DCs. The lines are the intra-receiver paths of the DCs at different wavelength ranges, indicated in the panel-titles. The colorscale indicates the average phase velocity of the DCs, given in the colorbar.

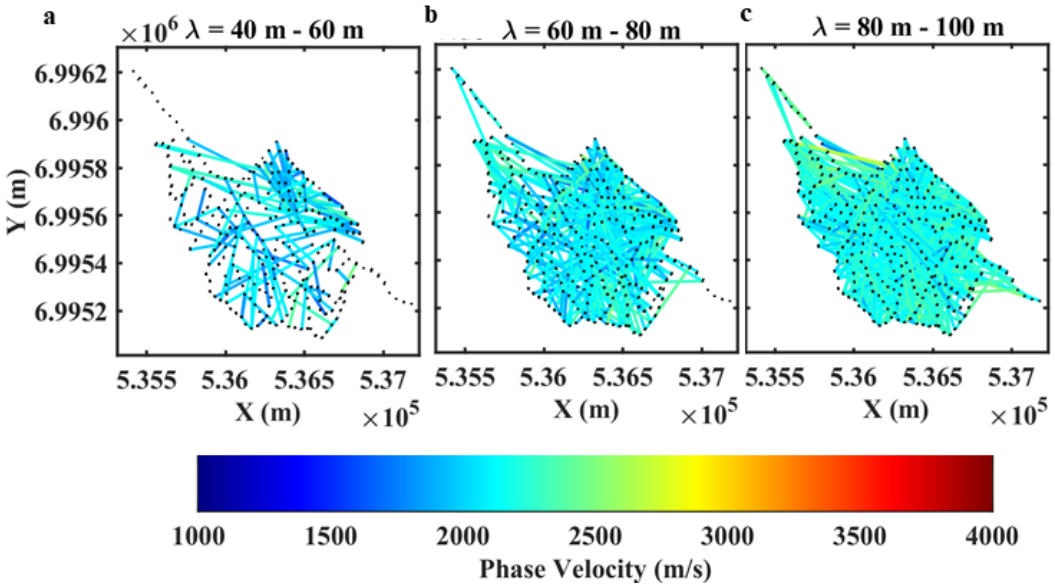

Figure 7.7: Spatial coverage maps of the combined active- and passive-source DC sets, between a) 40 m – 60 m, b) 61 m – 80 m, c) 81 m – 100 m.

7.3.3 Tomographic inversion of active- and passive-source DCs

We performed a tomographic inversion of the combined set of active- and passive-source DCs, using the method described in Chapter 6. The properties of the initial pseudo-3D model, selected for the inversion, are presented in Table 7.1. The initial V_S and ρ selection was based on the logging information presented in Malehmir et al. (2017). In particular, we used the information from well R628, which was the closest to the forest area. For the initial ν, the assumed values were in the ranges of the ones estimated by the W/D process along line SM1 (Figure 5.15), which is located northern to the forest area. According to Lanaro & Fredriksson (2005), the selected values are reasonable for the lithology of the site.

Table 7.1: *Properties of the initial model used active SW tomography in the Siilinjärvi forest area.*

	Active SW tomography initial model – Forest area			
Layer	V_S (m/s)	ρ (kg/m^3)	ν (-)	h (m)
1	2200	2700	0.27	30
2	2300	2700	0.27	60
3	2400	2700	0.27	60
4	2600	2700	0.25	60
5	2800	2700	0.25	60
6	3000	2700	0.25	60
7	3200	2700	0.25	60
Halfspace	3500	2700	0.25	-

For the spatial discretization, we assumed 420 uniformly distributed grid points, at 44 m from each other. After testing different vertical-discretization dimensions, we concluded that the best DC fitting was achieved assuming 7 layers, reaching a maximum depth of 480 m.

We used a lateral V_S constraint of 150 m/s for the first four layers and of 500 m/s for layers 5-7. These were found to be the strongest constraints which did not increase the inversion misfit.

The final V_S model, obtained after 12 iterations, is shown in Figure 7.8, as slices of V_S at different depths. The model presents a clear mapping of the low-V_S values (around 2000 m/s and 2800 m/s), which have been attributed to the carbonatite ore formation (Da Col et al., 2020). In addition, down to 240 m, the model presents several high-V_S (around 3500 m/s) anomalies, which have been attributed to the intrusions of diabase dykes in the ore body. At 240 m depth (Figure 7.8d), the shape of the high-velocity anomalies is preserved but the model is characterized by higher V_S (up to 4000 m/s). The layers between 330 m and 480 m (Figures 7.8e-g) present a greater extent of high-V_S zones (3300 m/s – 4000 m/s) and lower lateral variability.

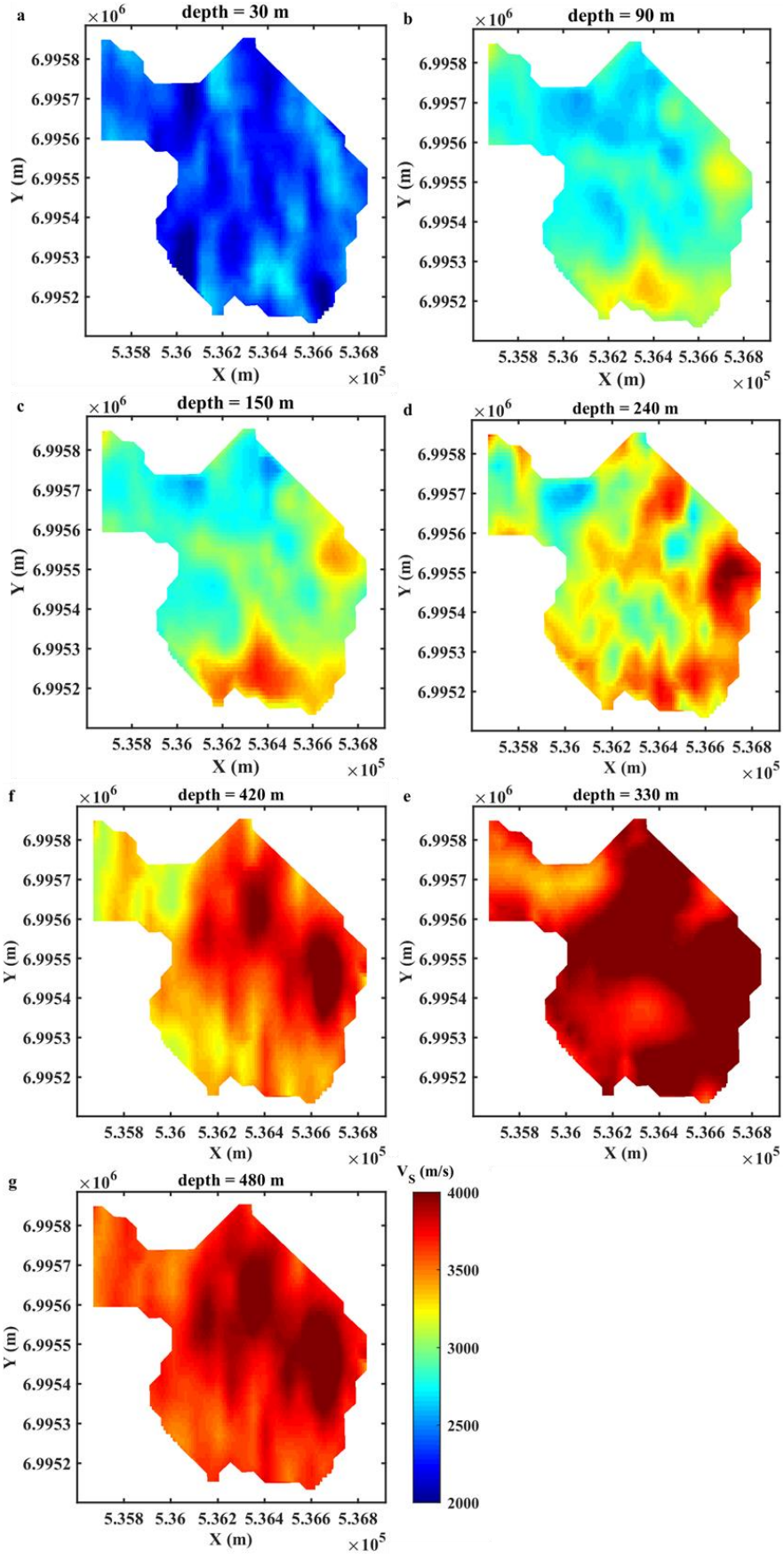

Figure 7.8: V_S model. Velocity slices at a) 30 m, b) 90 m, c) 150 m, d) 240 m, e) 330 m, f) 420 m and, g) 480 m.

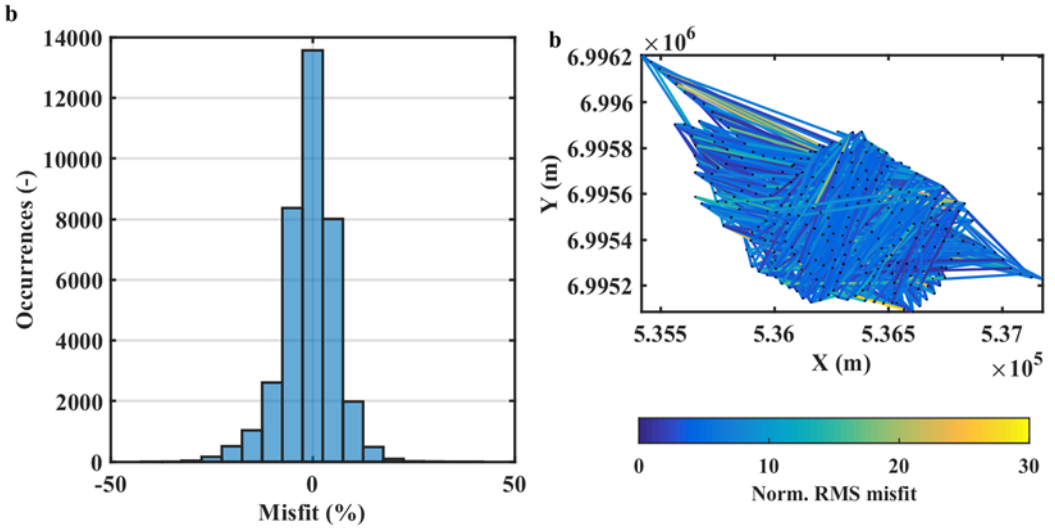

Figure 7.9: a) Percentage misfit of the theoretical DC data points with respect to their corresponding experimentally retrieved DC points. b) Map of the Normalized RMS misfit of the DCs along the analysed two-station paths.

The histogram of Figure 7.9a shows the misfit (%) between the experimental and theoretical (computed for the inverted model) DC points. In Figure 7.9b, we present the mean RMS misfit of each DC (path). It can be observed that the misfit is lower than 12.5 % for more than 75 % of the data points, and there are no zones over the area with concentration of high misfits.

The checkerboard model was created by applying a ±8% velocity perturbation on the inverted model of Figure 7.8, according to the pattern shown in Figure 7.10a. The V_S perturbations obtained after the inversion are presented in Figure 7.10b. It can be observed that the velocity perturbations at depths 30 m - 330 m were well reconstructed, apart from the south-western portion of the slice at 90 m, which we indicate with the red box in Figure 7.10. At depths 330 m – 480 m, the quality of the inverted checkerboard model reduces, especially at 330 m depth, where the perturbations in a southern portion of the model (blue in Figure 7.10) appear smoothened. Nevertheless, the dimensions of the rest of the perturbation blocks at all the other layers are clearly identified in the inverted checkerboard model.

Therefore, it can be concluded that the resolution of the experimentally-retrieved V_S model of Figure 7.8 equals, at least, the size of the perturbation blocks of Figure 7.10a, except for the zones indicated by the red and blue boxes.

Comparing the resolution with the dimensions of the velocity anomalies of the inverted model of Figure 7.8, we conclude that all of them are resolvable.

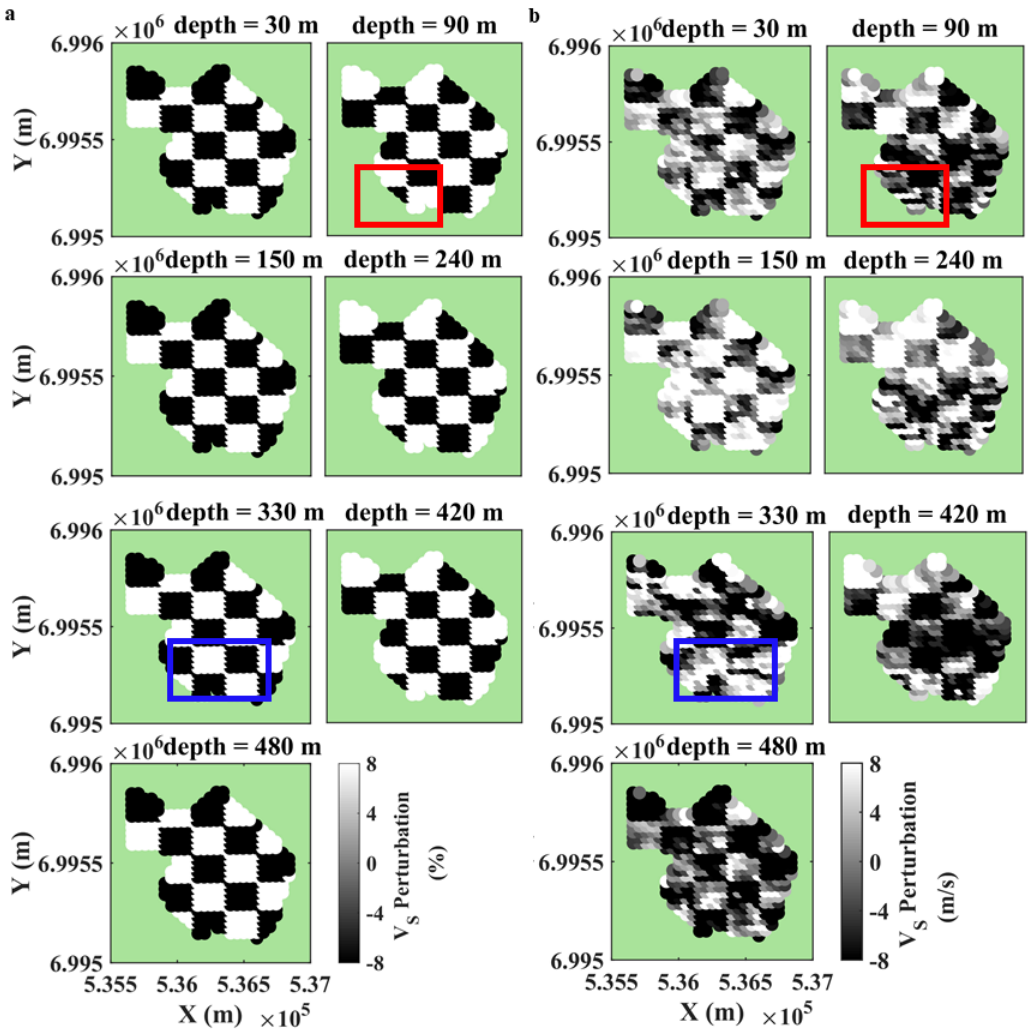

Figure 7.10: a) "True" and b) inverted checkerboard velocity perturbation. The boxes indicate velocity perturbations which could not be accurately recovered.

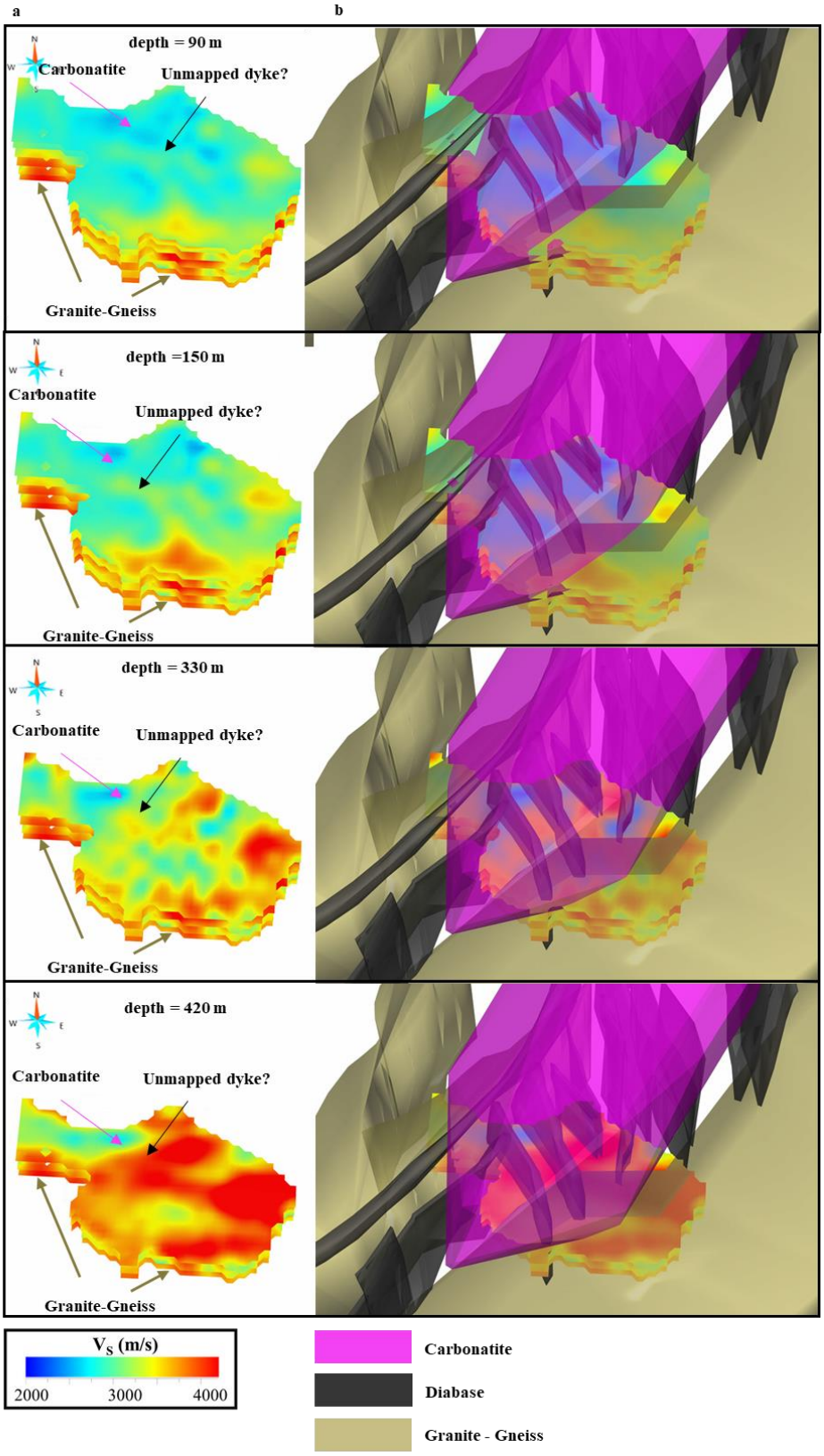

Figure 7.11: a) 3D view of portion (240 m - 420 m) of the final tomographic model. b) Comparison of the slices in (a) with the geological bodies of interest. The diabase-dyke model pre-dates the seismic survey and has been built by Yara based on surface geological and borehole data.

7.3.4 Discussion

The presented method allowed to efficiently detect and isolate the portion of the 13-day ambient-noise dataset which contained coherent SW signal and estimate its azimuth direction.

Although the azimuths estimated for the SW occurrences were distributed, most of the occurrences originated at an azimuth between 42° - 60° (Figure 7.3b). These were probably related to the factory of the mine, located towards the NE of the forest area, where the apatite concentrate is processed on site to produce phosphoric acid and fertilizers. The occurrence peaks at 200° - 240°, were probably caused by a workshop, located W-SW of the forest area, where industrial machines are produced and tested.

Nevertheless, the azimuth coverage of the DCs (Figure 7.5a) was not affected by these peaks and was fairly uniform. The DCs presented similar phase velocities with the curves estimated from the active-source data in their common frequency band (Figure 7.4a), which serves as a validation of our estimation. The passive-source DCs contained slightly lower-frequencies (at minimum 3.5 Hz) with respect to the active-DC frequencies (at minimum 5.5 Hz), which due to the high phase velocities in the area, increased significantly the measured wavelengths (approximately 1200 m in the passive-source DCs, compared to 672 m in the active-source ones).

As a result, the inverted V_S model was deeper than the one estimated from the active SW tomography (Da Col et al., 2020), and reached to a depth of almost half a km. The model presented a clear image of the shallowest portion of the mineralization, known (see Section 3.3.2) to be characterized by lower V_S compared to the granite-gneiss host-rock and to the diabase-dyke intrusions. Such low velocities were clearly mapped in our model and are indicated by the magenta arrow in Figure 7.11a, where we plot slices of the V_S model at different depths.

In the same figure, the brown arrow points to a high-V_S zone, enclosing the low-V_S carbonatite area. A comparison of our model, with the pre-existing geological model (Figure 7.11b), built by the owning company (Yara), proves that this high-V_S region correlates well with the geologic model of the granite-gneiss (brown). The diabase dykes, shown in black in the geological model, are recognized

in the V_S model as linear high-velocity anomalies, cross-cutting the low-velocity carbonatite complex. Finally, at all depths, an additional high-V_S anomaly (black arrow in Figure 7.11a) was found in the tomographic model. This anomaly could be indicative of a, so far unmapped, horizontal diabase dyke.

Following the low velocities of our V_S model, the existing geological model of the carbonatite ore body was prolonged towards the south. The new 3D model of the mineralization is presented in purple in Figure 7.11b. Its southern extension is wider and deeper than originally assumed and can be used to guide future drilling efforts and to plan the new open pit in the area.

Due to the large size of the dataset (almost 800 GB), the pre-processing computations required around 3 weeks, running in parallel on a 10-core workstation. However, the processing was automatic and did not require the work of an operator. Including only the accepted time windows the dataset was downsized to approximately 61.5 GB. The time required for the two-station processing, stacking and semi-automatic DC picking was approximately 1 week, while the tomographic inversion required approximately 6.5 hours on the same 10-core workstation.

7.4 Illumination diagnosis on the Siilinjärvi passive-seismic dataset for the retrieval of BW reflections

Seismic reflections can be extracted from passive-source data with seismic interferometry, which estimates the Green's function between pairs of receivers as if one of the receivers would be a source. Although this method has been successfully applied to ambient-noise and earthquake data for the extraction BW (e.g., Draganov et al., 2009), the typical dominance of SW in the ambient-noise records poses limitations to the retrieval of high-quality reflections. A possible solution, to enhance the retrieval of BW, and at the same time reduce the computational cost of the processing stage, is to use only the portion of the records where BW are dominant, applying the illumination diagnosis method proposed by Vidal et al. (2014). Here, we optimize and apply illumination diagnosis on the ambient-noise data recorded along lines SM2 and SM3 (details in Section 3.3) at the Siilinjärvi mining site.

7.4.1 Description of the method

The workflow is schematized in Figure 7.12. It uses as input ambient-noise data recorded along two perpendicular lines (denoted as line A and line B in Figure 7.12). This is done to ensure that a SW event, travelling in a direction perpendicular to the seismic line is not misinterpreted as a BW, due to its higher apparent velocity. The records from both lines are split in shorter time windows, the length of which is selected as a compromise between computational costs and ability to isolate individual reflections, based on the expected BW traveltimes on the site.

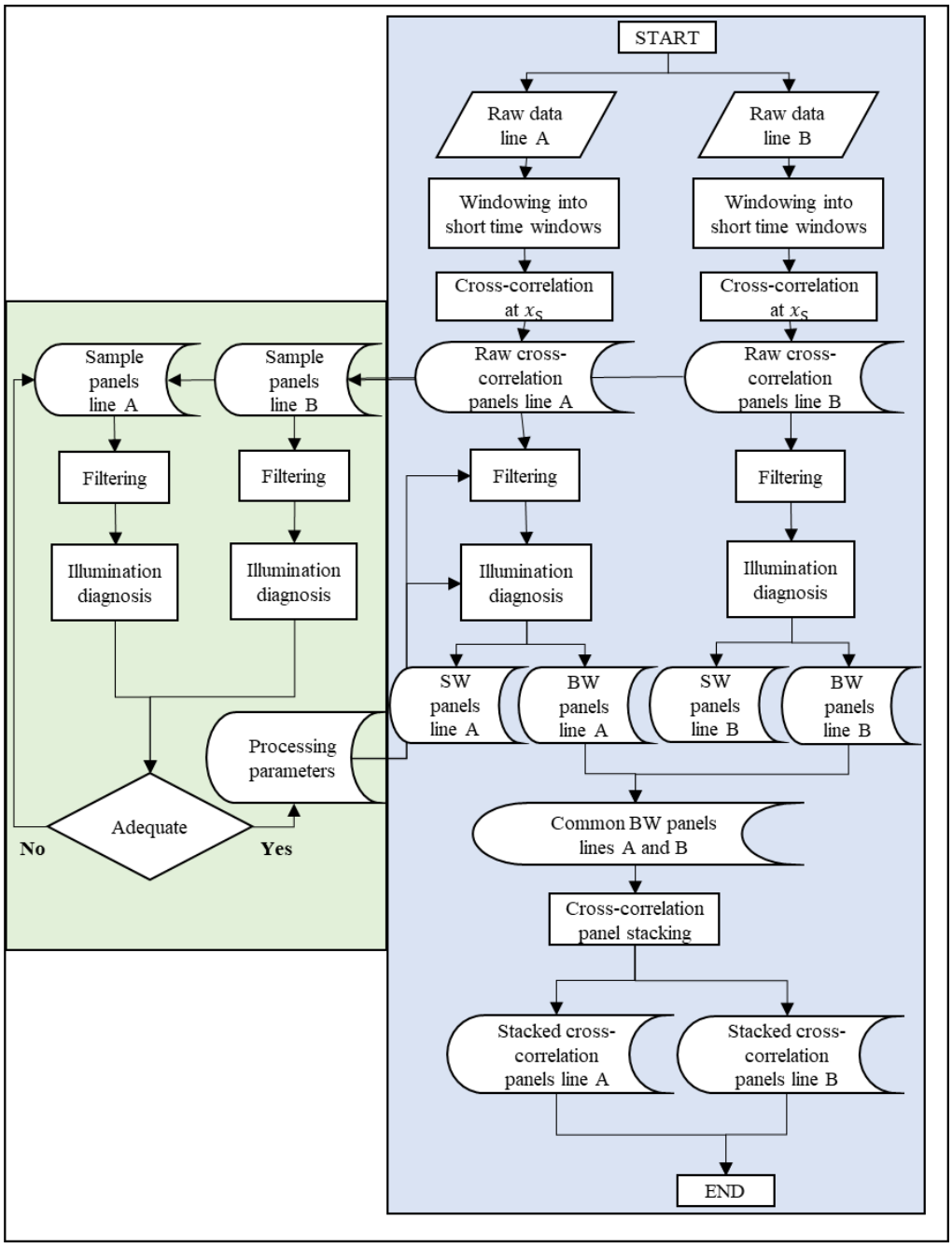

Figure 7.12: Workflow representation of the proposed method.

To select the optimal pre-processing, which will increase the possibility of detecting the reflections with the illumination diagnosis and evaluate its performance, a sample of the data for which the BW dominance is known *a priori* is used for testing (green in Figure 7.12). Once the optimal parameters have been identified, they are used to process the entire dataset (blue in Figure 7.12).

The retrieval of reflections is based on seismic interferometry, a method which allows to estimate the Green's function ($G(\mathbf{x}_A, \mathbf{x}_B, t)$) between two receivers, located at $\mathbf{x}_A$ and $\mathbf{x}_B$, as if there were a source at one of them (e.g., at $\mathbf{x}_A$). Assuming sources at positions $\mathbf{x}_s$, this is possible with the following expression of seismic interferometry with cross-correlation:

$$\Re\{G(\mathbf{x}_A, \mathbf{x}_B, t)\} * S_0(t) \approx \frac{1}{\rho c} \oint_{\partial D} u\left(\mathbf{x}_A, \mathbf{x}_S, -t\right) * u\left(\mathbf{x}_B, \mathbf{x}_S, t\right) d\mathbf{x}_S \quad (7.4),$$

where it is assumed that the sources have the same autocorrelation function $S_0(t)$, $\Re$ denotes the real part, ρ is the density and c the velocity of the medium at and inside the source boundary ∂D, $u\left(\mathbf{x}_A, \mathbf{x}_S, -t\right)$ is the (time-reversed) wavefield from a source at $\mathbf{x}_s$ observed at $\mathbf{x}_A$ and $*$ denotes convolution.

For ambient-noise sources, assuming that they have the same autocorrelation function $S_0(t)$, the Green's function can be retrieved, according to Wapenaar & Fokkema (2006), as:

$$\Re\left\{G\left(\mathbf{x}_A, \mathbf{x}_B, t\right)\right\} * S_0(t) \approx \left\langle u\left(\mathbf{x}_A, -t\right) * \left(\mathbf{x}_B, t\right)\right\rangle \quad (7.5),$$

where $u\left(\mathbf{x}_A, -t\right)$ is the (time-reversed) wavefield from the uncorrelated noise sources observed at $\mathbf{x}_A$, and $\langle \cdot \rangle$ stands for the ensemble average. The ensemble averaging in field observations can be substituted from the summation of discrete time windows, as long as the overall recording time is long. Therefore, eq. 7.5 can be substituted from

$$\Re\left\{G\left(\mathbf{x}_A, \mathbf{x}_B, t\right)\right\} * S_0(t) \approx \sum_i \left(u\left(\mathbf{x}_A, -t\right) * \left(\mathbf{x}_B, t\right)\right)_i \quad (7.6),$$

where i stands for the separate time windows.

When eq. 7.6 is applied to receivers at variable $\mathbf{x}_B$ and a constant virtual-source at $\mathbf{x}_A$, a correlated common-source panel can be retrieved:

$$C^i\left(\mathbf{x}_A,\mathbf{x}_B,t\right)=u_i\left(\mathbf{x}_A,-t\right)*u_i\left(\mathbf{x}_B,t\right) \tag{7.7}.$$

The illumination diagnosis method of Vidal et al. (2014), makes use of the fact that the events of $C^i\left(\mathbf{x}_A,\mathbf{x}_B,t\right)$ that pass through $t=0\,\mathrm{s}$ and the virtual-source position $\mathbf{x}_A$, contain the illumination characteristics of the source, i.e., all the necessary information to conclude whether a noise source emits mainly SW or BW. According to van Der Neut (2013), these events are called the virtual-source function.

The method of Vidal et al. (2014) studies the virtual-source function based on the slant-stack transform of the common virtual-source panel of eq. 7.7 at $t=0\,\mathrm{s}$ and the location of the virtual source $\mathbf{x}_A$:

$$\tilde{C}^i\left(\mathbf{x}_A,p\right)=\int C^i\left[\mathbf{x}_B,\mathbf{x}_A,p\left(\mathbf{x}_B-\mathbf{x}_A\right)\right]d\mathbf{x}_B \tag{7.8},$$

where p is the slowness. Eq. 7.8 is computed for all panels, and every time, a search is performed for the slowness $p^i_{\mathbf{x}_A}$, for which the source function takes its maximum value, i.e., the slowness of the dominant event in the panel:

$$\tilde{C}^i\left(\mathbf{x}_A,p^i_{\mathbf{x}_A}\right)=\left\|\tilde{C}^i\left(\mathbf{x}_A,p\right)\right\|_{\max} \tag{7.9}.$$

Once this has been performed for every panel, the absolute values of $\left\|p^i_{\mathbf{x}_A}\right\|$ for which eq. 7.9 was satisfied, are compared with a pre-defined limit slowness $p_{\lim}$, representing the threshold between the expected SW slowness from the one of BW. Therefore, each panel undergoes the following automatic check:

$$C^i\left(\mathbf{x}_A,\mathbf{x}_B,t\right)=\begin{cases}0 & \text{if } \dfrac{\max\left(\left\|\tilde{C}^i\left(\mathbf{x}_A,p\right)\right\|_{\|p\|\le p_{\lim}}\right)}{\max\left(\left\|\tilde{C}^i\left(\mathbf{x}_A,p\right)\right\|_{\|p\|> p_{\lim}}\right)}\le R \\ u_i\left(\mathbf{x}_A,-t\right)*u_i\left(\mathbf{x}_B,t\right) & \text{if } \dfrac{\max\left(\left\|\tilde{C}^i\left(\mathbf{x}_A,p\right)\right\|_{\|p\|\le p_{\lim}}\right)}{\max\left(\left\|\tilde{C}^i\left(\mathbf{x}_A,p\right)\right\|_{\|p\|> p_{\lim}}\right)}> R\end{cases} \quad (7.10).$$

where R is the maximum acceptable ratio between the maxima of $\tilde{C}^i\left(\mathbf{x}_A,p^i_{\mathbf{x}_A}\right)$ which are lower, and the ones which are higher than $p_{\lim}$. This means that if a noise panel has a dominant slowness $\left\|p^i_{\mathbf{x}_A}\right\|$, which is larger than $p_{\lim}$, it is automatically rejected from the retrieval of the reflection response. Moreover, a panel is rejected also if it has a $\left\|p^i_{\mathbf{x}_A}\right\|$ lower than $p_{\lim}$, but if less than R maxima of $\tilde{C}^i\left(\mathbf{x}_A,p^i_{\mathbf{x}_A}\right)$ were characterized by a slowness lower than $p_{\lim}$. This way, not only the panels dominated by SW are rejected, but also the panels which are dominated by BW but have a high content of SW energy.

In Figure 7.13, we show an example of this process to line SM3. In Figure 7.13a, we show a correlated panel, computed by cross-correlating the trace that was selected as a virtual source (located at the intersection of lines SM2 and SM3, shown as a green star in Figure 7.2) with all the other traces of the line. We indicate the position of the virtual source at $t=0$ s as a black dot, while the slope of the red line corresponds to a slowness of -5×10^{-4} s/m, used as the first trial slowness for which the slant stack at $t=0$ s was computed.

The corresponding normalized slant-stack result is shown as a dot in Figure 7.13b. In Figure 7.13c, the red lines indicate all the used trial slownesses, and their corresponding slant-stack results are shown in Figure 7.13d. The green lines in both figures indicate the limit slowness, chosen as 2.5×10^{-4} s/m, which was slightly higher than the SW velocity of the DCs extracted for the site (Figure 7.4c). The slowness of 3.77×10^{-4} s/m was found to provide the highest slant-stack result (magenta star in Figure 7.13d). It is higher than the limit slowness of SW (green lines in Figure 7.13c) and, therefore, the panel was estimated to be dominated by SW and was disregarded from seismic interferometry.

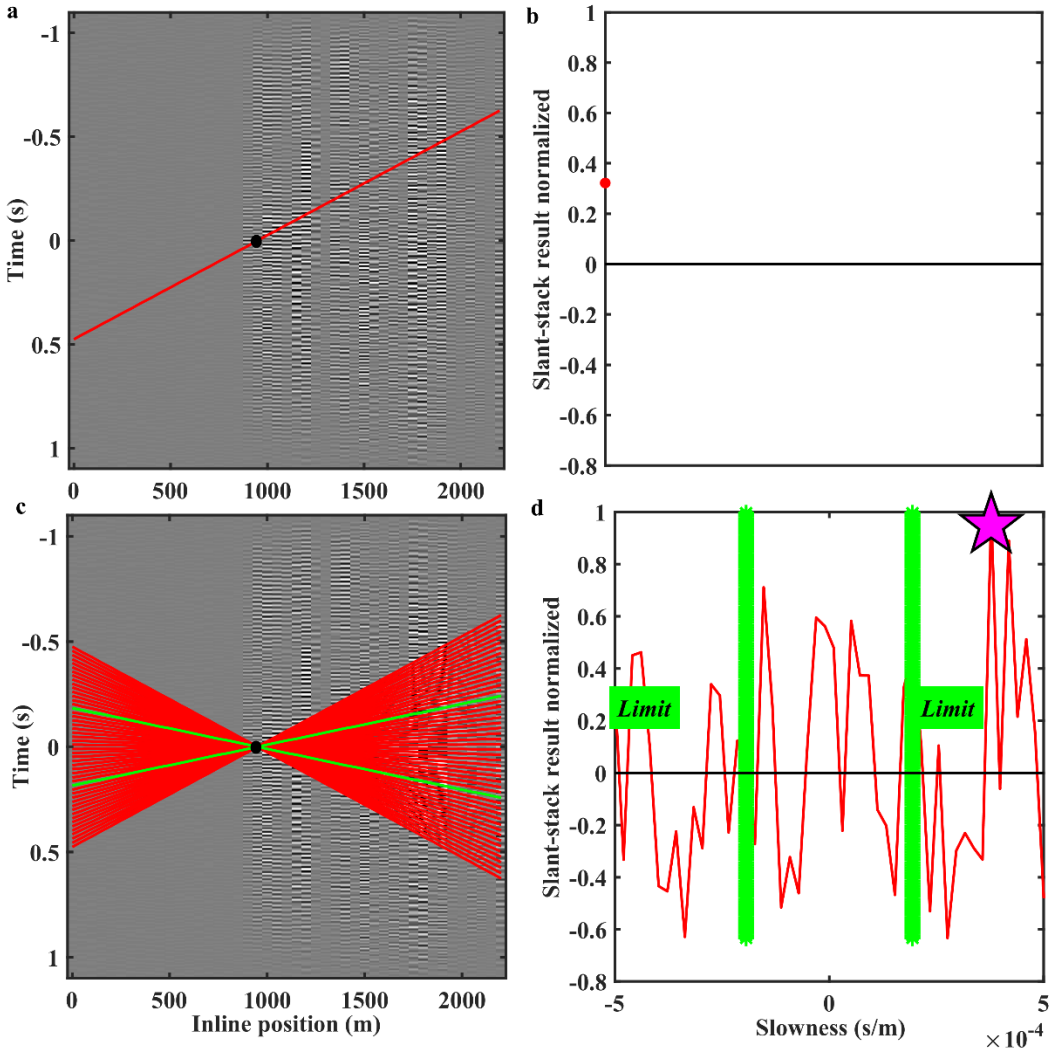

Figure 7.13: a) Example correlated panel from line SM3. As dot, the virtual-source position. The line corresponds to $p = -5\times10^{-4}$ s/m. b) Normalized slant stack, along $p = -5\times10^{-4}$ s/m and $t = 0$ s. c) and d), same as (a) and (b), but for slownesses between -5×10^{-4} and 5×10^{-4} s/m. In green, the limit of 2.5×10^{-4} s/m. In (d), the star shows the slowness of the maximum slant-stack result.

In practice, the dominant slowness is computed for all the noise panels and for both perpendicular lines and, for each line, the panels which are estimated as BW-dominated by the check of eq. 7.10, are flagged. In the end, only panels which are flagged as BW-dominated in both lines are considered for the interferometry, i.e., for the summation of eq. 7.6.

This stage is performed only for one virtual-source position (x_S in Figure 7.12), and then, the correlated panels corresponding to other virtual sources are computed and stacked, only for the time windows identified in the illumination diagnosis.

7.4.2 Application to the dataset

We analyse the data recorded by the 45 and 62 receivers, spaced at 50 m, along lines SM2 and SM3, respectively. It was decided to perform our analysis on 10s-long time-windows of the noise record, since these provided the best compromise between the retrieval of high-quality BW energy and computational cost. We computed the corresponding correlated panels, using as virtual sources the receivers located at the intersection of lines SM2 and SM3.

In Figure 7.14, we show samples of amplitude spectra, computed for 300 randomly selected panels from both lines. It can be observed that significant levels of energy at a frequency band that could be related to BW (20 Hz – 80 Hz) were detected. Nevertheless, the raw correlations clearly suffered from high-amplitude noise (for instance the amplitude spikes that appear around 52 Hz – 57 Hz).

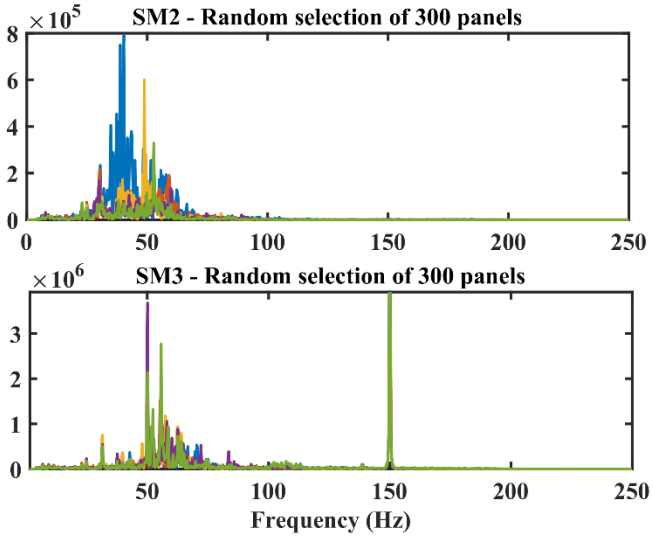

Figure 7.14: Amplitude spectra computed for 300 randomly selected 10-s noise panels of line SM2 (top) and SM3 (bottom) and stacked for all traces.

Table 7.2: *Time periods during the Siilinjärvi ambient-noise acquisition period, when military jets passed near to the acquisition area.*

Day	Take-off time	Landing time	Day	Take-off time	Landing time
24/09	09:30	10:30	27/09	09:30	10:35
24/09	11:00	12:00	27/09	10:10	11:30
24/09	14:00	15:00	27/09	12:00	13:10
25/09	09:30	10:30	27/09	14:00	15:10
25/09	11:27	12:00	01/10	12:00	13:00
25/09	11:30	12:50	01/10	13:50	14:40
25/09	12:45	13:20	01/10	14:00	15:00
25/09	14:00	15:00	02/10	09:40	10:40
25/09	14:00	15:00	02/10	10:50	At a different base
25/09	15:00	16:00	02/10	11:10	12:10
25/09	At a different base	17:00	02/10	12:20	14:20
26/09	09:30	10:30	02/10	13:20	14:00
26/09	09:30	At a different base	02/10	13:50	14:40
26/09	10:00	10:50	03/10	09:30	10:20
26/09	11:30	12:30	03/10	12:00	12:50
26/09	12:00	13:00	03/10	14:00	14:40
26/09	13:00	14:00	03/10	14:25	15:30
26/09	14:00	15:15	04/10	09:30	10:30
26/09	14:40	15:40	04/10	12:20	13:20

To design the pre-processing strategy for optimizing the retrieval of BW, we performed tests on windows which "captured" the passing of military jets, which occurred at known time periods during the acquisition and were expected to contain significant BW energy, due to the plane waves generated by the jets. In Table 7.2, we present a list of these time periods, and in Figure 7.15a and 7.15b we show, respectively, the 10-s records of line SM2 and SM3 which captured the passing of a jet on 25/09/2018 at 11:27 am (highlighted in red in Table 7.2). In both records, a high-amplitude event is clearly visible.

The corresponding raw correlations are plotted in the top panels of Figures 7.16a and 7.16b, respectively, while the bottom panels show the corresponding stacked amplitude spectra. The two panels present high levels of noise, which hinders the identification of the wave, particularly for line SM3 (Figure 7.15b). In Figures 7.16c and 7.16d, we respectively present the same correlations (top) and

their spectra (bottom), after applying a band-pass filter (20 Hz – 80 Hz) and deconvolving using a short window extracted around t=0 s from the autocorrelated virtual-source trace.

The quality of the event of interest (highlighted in blue in Figures 7.16c and 7.16d) was significantly improved, and the event can be easily recognized in both panels. Therefore, it was decided to apply the same filtering on the entire dataset, prior to the illumination diagnosis.

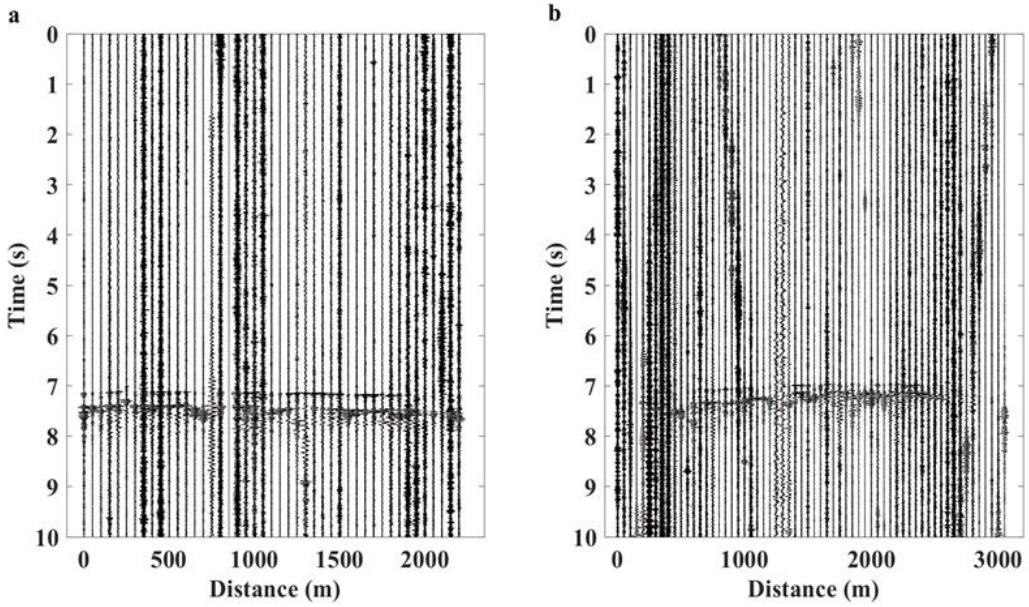

Figure 7.15: Raw noise time-window, capturing the passing of a military jet that occurred on 25/09/2018 at 11:27 am, recorded on line a) SM2 and b) SM3.

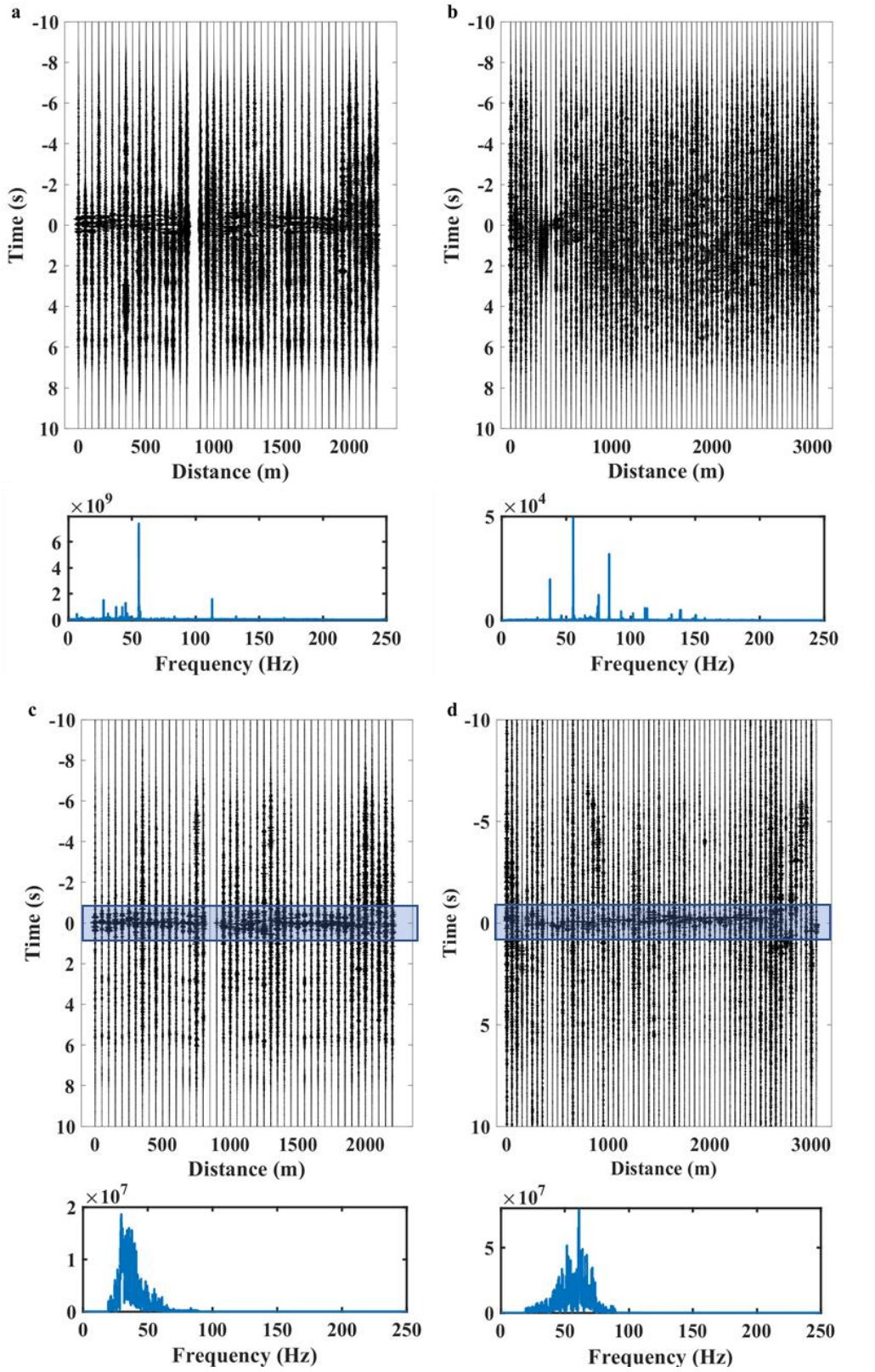

Figure 7.16: Correlated panels (top) and amplitude spectra (bottom) of line SM2 a) raw and c) filtered, and SM3 b) raw and d) filtered.

We tested the performance of the illumination diagnosis by assessing its ability to identify the panels of Figures 7.16c and 7.16d (labelled as "1" in Figures 7.17a and 7.17b, respectively) as BW-dominated and discriminate them among five additional, randomly selected 10-s panels, numbered from "2" to "6" in Figures 7.17a (line SM2) and 7.17b (line SM3). The discrimination result is given in Figures 7.17c and 7.17d, for lines SM2 and SM3, respectively. The crosses represent the slowness of the maximum-amplitude event in the $\tau - p$ spectrum for each panel, and are compared with the threshold p_{lim} (green lines in Figures 7.17c and 7.17d). Events with $p < p_{\text{lim}}$ were characterized as BW (blue in Figures 7.17c and 7.17d) and the ones with $p > p_{\text{lim}}$ were flagged as SW (magenta in Figures 7.17c and 7.17d). These results show that only the panels of interest (labelled as "1" and highlighted by the red box in Figures 7.17a and 7.17b) were identified as BW-dominated for both lines, while panel "4", identified as BW-dominated only in line SM2, was excluded from further processing, proving the efficiency of the method.

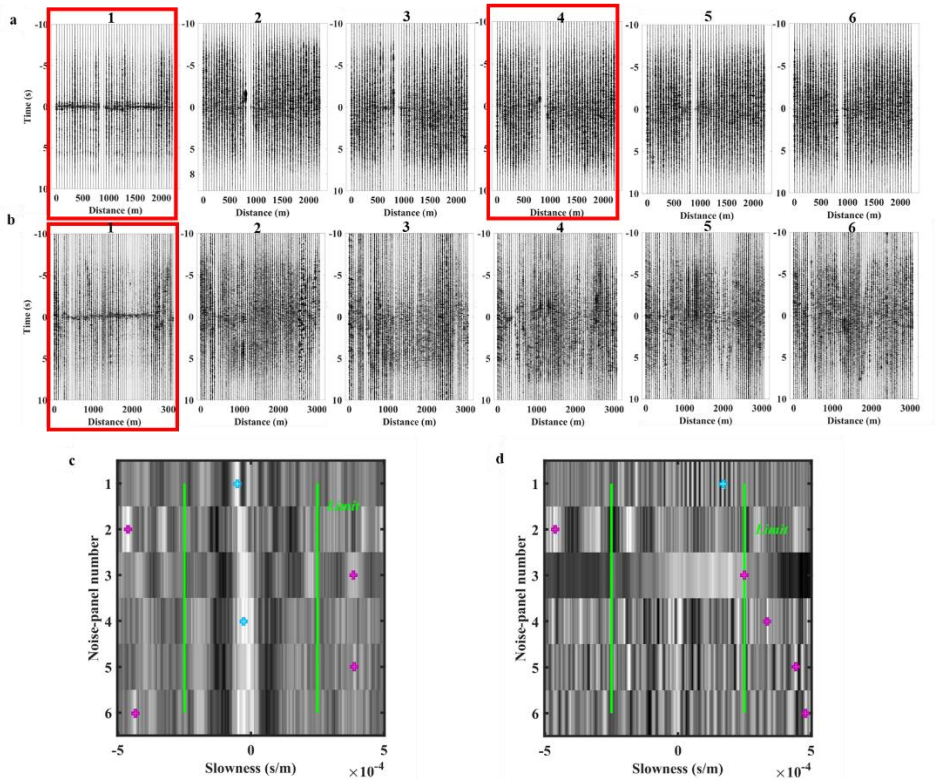

Figure 7.17: a) Test correlation panels for line a) SM2 and b) SM3. Illumination diagnosis on the panels of c) line SM2 and d) line SM3. In (c) and (d), the crosses highlight the dominant slowness. In blue, the panels dominated by BW, indicated by the red boxes in (a) and (b), and in magenta, the ones dominated by SW

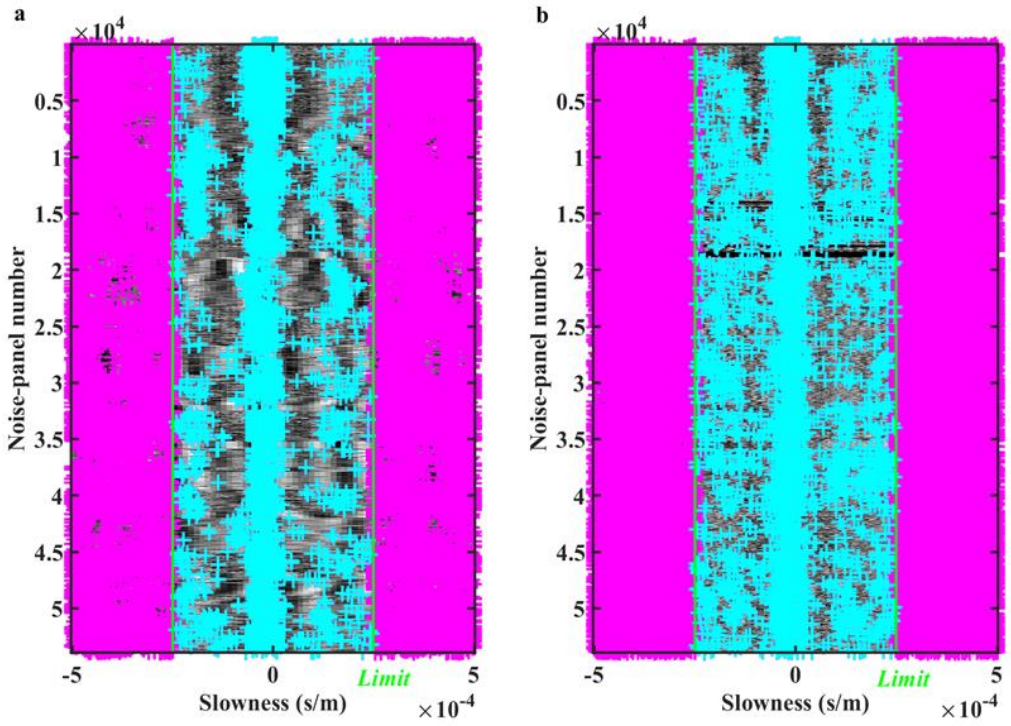

Figure 7.18: Illumination diagnosis applied to the complete 13-day record along line a) SM2 and b) SM3. Blue corresponds to BW and magenta to SW.

The results of the illumination diagnosis on all the correlated panels of the 13-day dataset are given for SM2 and SM3 in Figures 7.18a and 7.18b, respectively. We highlight, in magenta, the maxima corresponding to SW and in blue, the ones corresponding to BW. Even though more than 97 % of the maxima corresponded to SW, we were able to identify 1366 noise panels with dominant BW along both lines. These were automatically extracted and used for reflection retrieval with seismic interferometry.

In Figures 7.19a and 7.19b, we show, for line SM2 and SM3, the stacked correlated panels, which resulted after summing all the panels that were flagged as BW-dominated by the illumination diagnosis. Both panels show a consistent appearance of a reflective event at around 0.2 s (red arrow in Figures 7.19a and 7.19b), which, considering that the V_P of the site is roughly 5000 m/s (Malehmir et al., 2017), approximates the two-way-time to the expected depth of the mineralization (around 1000 m). In Figure 7.19a, the magenta arrow indicates an additional event, probably related to a deeper reflector. In Figures 7.19b and 7.19d, we present the stacked sections retrieved from the analysis of the active-source data by McKevitt (2020) for lines SM2 and SM3. The sections confirm the presence of

reflective events at the times indicated by the passive interferometry, proving the validity of our preliminary result. Interferometry will be performed using all the receivers of the lines as virtual sources and the retrieved panels will be processed further to retrieve stacked sections.

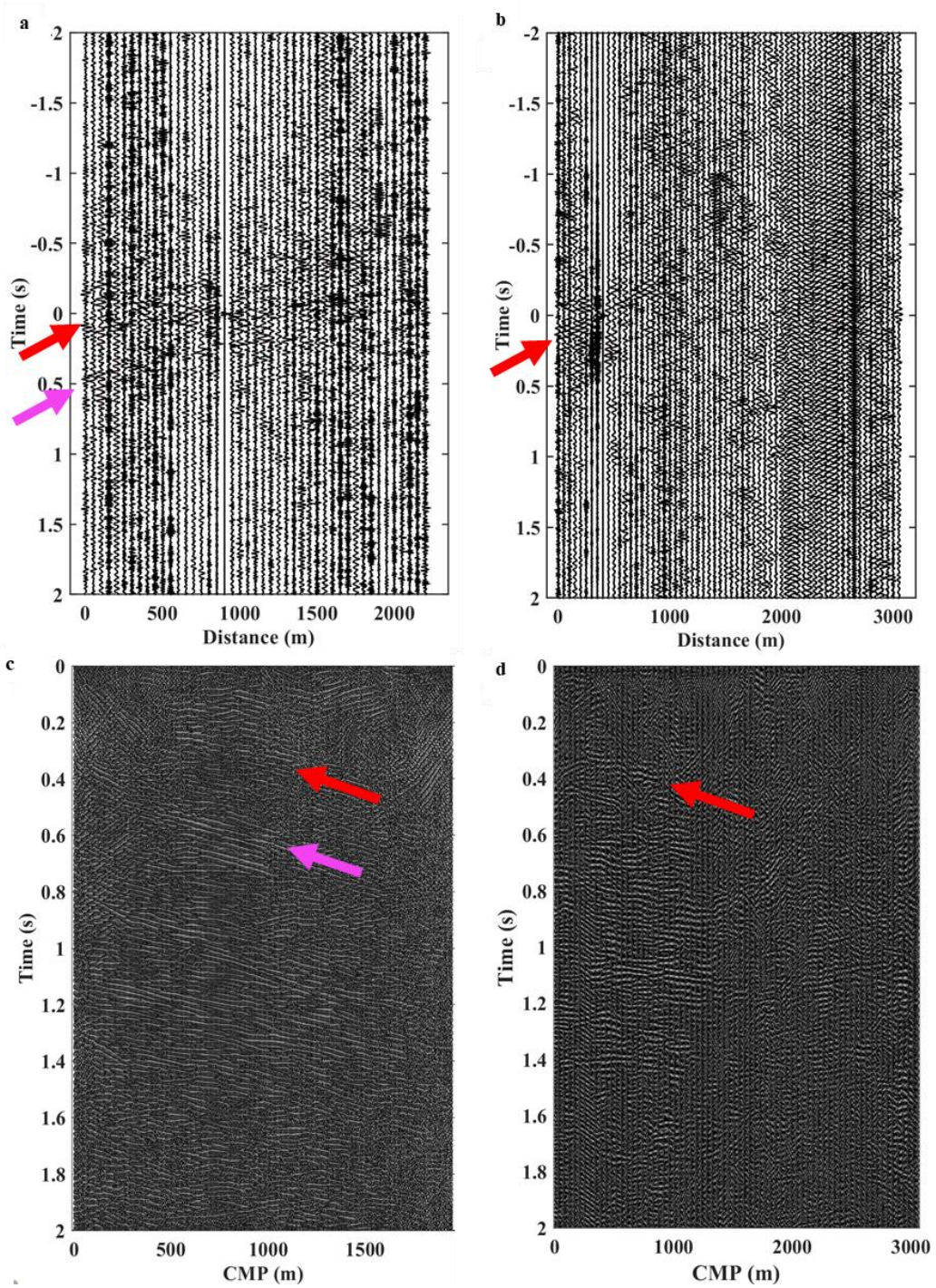

Figure 7.19: Stacked cross-correlation panel for a) SM2 (passive) and b) SM3 (passive) and (reproduced from McKevitt, 2020), c) SM2 (active) and b) SM3 (active). The arrows point to reflective events.

7.5 Conclusion

We have presented a fully automatic pre-processing workflow for the estimation of the propagation direction of SW, which is necessary for the accurate estimation of the SW DCs from ambient-noise seismic data. The successful application of the workflow on the dataset from the Siilinjärvi mining site has proven that the use of passive-seismic data with SW tomography is a promising, cost-effective and environmentally friendly tool to characterize the subsurface, overcoming the need for active seismic sources. Since longer SW wavelengths are contained in the passive data, passive SW tomography can be used as a method to map, at least the shallowest portion, of the mineralization. Combination of active- and passive-source data, allows subsurface investigation in a wide depth range.

In addition, passive-seismic interferometry is a good candidate for retrieving seismic reflections, even in the challenging environments of mineral exploration. Using time windows which contain dominant BW energy, it is possible to organize a customized pre-processing strategy and enhance the retrieval of BW from the entire noise record. Tests on noise panels and comparison with active-source stacked sections showed that the illumination diagnosis is a fast and reliable tool that can aid the retrieval of accurate BW reflections from ambient-noise data.

Chapter 8

Conclusion

8.1 Final remarks

It has been shown that SW methods are valuable tools for mineral exploration. Contributing to the sparse scientific literature on SW analysis for complex hard-rock settings, the thesis demonstrated that, not only hard-rock challenges can be tackled, but also that the results can be of great quality and significance if appropriate techniques are used. We showed that SW can be used to efficiently estimate shallow velocity models and static corrections, optimizing the imaging of the exploration targets and the planning of the mining activity. Moreover, the long wavelengths of SW, caused by the high seismic velocities of hard rock, allow to characterize portions of the mineralized bodies while, processing passive-source data, which usually contain longer wavelengths, permits even deeper investigation. Overall, the presented developments form a framework for an efficient, data-driven way of processing the recorded data, towards fast site investigations and convenient implementation of sophisticated analysis methods.

The SW direct statics-estimation method, introduced in Chapter 4, overcomes the, common in hard rock, challenge of sharp lateral variations and retrieves the statics in a fast and computationally-efficient manner. The DCs are picked with a nearly-automatic tool and, thanks to the W/D method, they are directly transformed into V_{Sz} and V_{Pz} models, without the need of inversion. The method was validated

through comparison with *a priori* information for the 2016 2D dataset from the mining site of Ludvika and line SM1 from the Siilinjärvi mining site. In both cases the achieved investigation depth (100 m for Ludvika and 120 m for Siilinjarvi) was deeper than the known bedrock, and therefore adequate for the statics computation. The lateral resolution, defined by the minimum length of the spatial window used for the DC extraction (75 m for Ludvika and 100 m for Siilinjärvi), was also satisfactory since 92 % of the estimated statics for Ludvika were found in agreement to the standard BW statics and provided at least as good stacked sections. Therefore, the method can be considered as a valid, and possibly faster, alternative to estimate the statics, particularly useful when the retrieval of reliable BW traveltimes is not possible or is highly time-consuming. It can be used as a standalone tool or as an initial near-surface characterization method, whose outcomes help optimize further analyses.

The SW tomostatics estimation method, presented in Chapter 6, integrating SW tomography with the W/D technique, is designed to estimate higher resolution V_S and V_P models and statics. Applied to the Ludvika 2016 dataset, the method estimated the statics down to a depth of 90 m, achieving lateral resolution in the range between 60 m and 162 m (depending on the depth) while, for Siilinjärvi SM1, the maximum depth was 85 m and the lateral resolution was found between 40 m - 280 m. In both cases, the resulting stacked sections were of similar quality with the ones obtained with standard BW statics, while the automatic two-station processing (Chapter 5) provided a convenient solution for picking the required DCs. Applied to the 2019 (3D) dataset from the Ludvika site, the automatic two-station processing estimated a set of more than 15000 DCs, densely covering the investigation area. Approximately 86 % of the curves were found similar by more than 90 % with DCs picked manually, which we considered as benchmark, while the automatic picking was faster by more than three times and did not require the operator.

The SW pre-processing method to efficiently utilize passive-source data, presented in Chapter 7, is fully automatic and data-driven, and therefore, it can efficiently handle the large volumes of data recorded in passive-seismic acquisitions. The method, applied to the ambient noise dataset from Siilinjärvi, achieved a wide spatial and azimuth DC coverage with longer wavelengths (nearly double) than the DCs retrieved from the active data. Combined, the two sets of

curves, provided a tomographic V_S model, the lateral resolution of which was 195 m down to 500 m depth. The model indicated the, so far unmapped, shallowest portion of the mineralization.

Finally, we showed that using parts of the noise records for which the dominance of BW energy is known *a priori*, it is possible to optimize data pre-processing and enhance BW retrieval from ambient-noise data. The pre-processing workflow allowed to apply seismic interferometry and retrieve reflections from the Siilinjärvi passive-source dataset, providing preliminary information on the mineralization depth-extension.

The methodological tools presented in the thesis, although developed to address a specific problem, the optimization of the state-of-the-art seismic mineral exploration workflows, are all directly applicable to any kind of seismic measurements, from small-scale datasets recorded for engineering purposes, to data recorded for global seismology and to hydrocarbon-exploration seismic datasets.

The automatic two-station processing and the automatic passive-source SW data pre-processing have been applied to extract DCs of the fundamental mode of Rayleigh waves, since no higher modes were found in our data. If higher modes exist, the picking code can prevent jumps among them since it automatically detects and rejectes discontinuities in the DC trends. Nonetheless, since there might be smooth energy transitions between the modes, their detection based on velocity jumps might not be sufficient. Therefore, pre-processing of the data (e.g., Dziewonski & Hales, 1972; Khosro Anjom et al., 2021) to isolate the modes prior to the two-station processing should be applied.

Two-station processing of other types of SW (e.g., Love waves, Scholte waves, Lamb waves, other guided waves) is also possible with the presented method while, with only minimal modifications, the automation tool can be applied to multichannel processing as well.

The presented near- and far-field detection method and the outlier removal technique have been here used as parts of the presented automatic two-station SW processing scheme, but can be used also as standalone tools, to optimize any DC extraction method.

To our knowledge, the thesis presents the first example of P-wave statics estimated fully from SW and the results were proven to be of high quality. This shows that, if no analog filters (including acquisition strategies) are applied during

reflection-seismic data acquisition, a great amount of information is contained in the recorded SW wavefield and, in the framework of an effective seismic exploration workflow, it should not be left unprocessed. Evidently, the acquisition can also be specifically carried out targeting SW and while in the first case the acquisition is designed to optimal reflected BW retrival and SW analysis must be adapted to acquisition layouts and parameters that may be non-optimal, in the second case the survey must be carefully designed to optimize spatial, azimuth and wavelength coverage.

The results presented in this thesis have been included in the deliverables of Smart Exploration and have helped improve the existing knowledge on the ore-deposit volumes at both presented sites, which are both of great significance within the EU. Our estimated statics and velocity models from the Ludvika mining site, which is one of the most important mineral-exploration sites in Sweden with great socio-economic relevance, have contributed to the delineation of the mineralization target and have indicated possible shallow weakness zones (shallow expressions of faults, fractured zones). This information is currently being used to assist the ore evaluation and planning of the new mining activity.

The statics, velocity models and BW reflections estimated for the apatite mining site of Siilinjärvi in Finland, showed that the mineralization probably extends further than originally assumed, and will be used to decide future development strategies. Considering that this site is the only operating mine within the EU producing phosphorus, listed as one of the critical raw materials by the EU, also this result is promising towards the secure and sustainable future supply of significant mineral resources.

8.2 Suggestions for future developments

The proposed automatic two-station processing method is, in essence, an intelligent system to identify characteristic pattern of the DC from large volumes of data. A natural evolution of this method is the implementation of a Machine Learning (ML) approach, which can possibly further increase the fidelity of the DC pattern recognition. Our method could be used as a training and testing stepping stone for ML algorithms, as well as a benchmark to establish when/if such ML methods provide measurable improvement over our approach.

The SW direct statics method, proposed in Chapter 4, allows to obtain an estimate of the time-average velocities with minimal time requirements (less than two hours in the used 2D seismic datasets). Further developments could allow the implementation of the method into a real-time tool, to be used on-site, while acquiring the data. In the long term, such approaches could evolve into a new paradigm of data acquisition, where the measurement setup is optimized real-time, to improve the data quality.

Finally, in our SW tomostatics approach (Chapter 6), the V_S model resulting from SW tomography was combined with the ν from the W/D method, to obtain a V_P model. The same value of ν was set constant in the initial model of the tomographic V_S inversion, to ensure that the V_S estimate is optimized, although ν has negligible influence. A further improvement of the SW tomostatics would be to simultaneously estimate V_S and ν, through a joint inversion of the two-station DCs and the W/D.

References

Abudeif, A. (2016). *Integration of Ultrasonic Vp and Vs into MASW inversion: Is it viable and beneficial?* SAGEEP, Denver, USA.

Adam, E., Perron, G., Arnold, G., Matthews, L., & Milkereit, B. (2000). 3-D seismic imaging for VMS deposit exploration, Matagami, Quebec. *SEG Technical Program Expanded Abstracts 2000*, 1093–1096. doi: 10.1190/1.1815576

Adebisi, A. A. (2012). *Calculating the Surface Seismic Signal from a Trapped Miner*. Graduate Theses, Dissertations, and Problem Reports. 2282. https://researchrepository.wvu.edu/etd/2282

Ahmadi, O. (2015). *Application of the Seismic Reflection Method in Mineral Exploration and Crustal Imaging: Contributions to Hardrock Seismic Imaging*. Acta Universitatis Upsaliensis.

Aki, K., & Richards, P. G. (1980). *Quantitative seismology* (2. ed., corr. print). Univ. Science Books.

Albarello, D., & Gargani, G. (2010). Providing NEHRP Soil Classification from the Direct Interpretation of Effective Rayleigh-Wave Dispersion Curves. *Bulletin of the Seismological Society of America*, *100*(6), 3284–3294. doi: 10.1785/0120100052

Albarello, Dario. (2011). The Contribution of the Ambient Vibration Prospecting in Seismic Microzoning: An example from the area damaged by the April 6, 2009 L'Aquila (Italy) earthquake. *Bollettino di Geofisica Teorica ed Applicata,* 52, 513-538. doi: 10.4430/bgta0013.

Al-Hunaidi, M. O. (1992). Difficulties with phase spectrum unwrapping in spectral analysis of surface waves nondestructive testing of pavements. *Canadian Geotechnical Journal*, *29*(3), 506–511. doi: 10.1139/t92-055

Allen, R. L., Lundstrom, I., Ripa, M., & Christofferson, H. (1996). Facies analysis of a 1.9 Ga, continental margin, back-arc, felsic caldera province with diverse Zn-Pb-Ag-(Cu-Au) sulfide and Fe oxide deposits, Bergslagen region, Sweden. *Economic Geology*, *91*(6), 979–1008. doi: 10.2113/gsecongeo.91.6.979

Anukwu, G. C., Khalil, A. E., Nawawi, M., & Younis, A. M. (2020). Delineation of shallow structures in the vicinity of Ulu Slim hot spring using seismic refraction and MASW techniques. *NRIAG Journal of Astronomy and Geophysics*, *9*(1), 7–15. doi: 10.1080/20909977.2019.1702803

Auken, E., & Christiansen, A. V. (2004). Layered and laterally constrained 2D inversion of resistivity data. *Geophysics*, *69*(3), 752–761. doi: 10.1190/1.1759461

Azapagic, A. (2004). Developing a framework for sustainable development indicators for the mining and minerals industry. *Journal of Cleaner Production*, *12*(6), 639–662. doi: 10.1016/S0959-6526(03)00075-1

Bakırcı, T., Yoshizawa, K., & Özer, M. F. (2012). Three-dimensional S-wave structure of the upper mantle beneath Turkey from surface wave tomography: 3-D upper-mantle structure beneath Turkey. *Geophysical Journal International*, *190*(2), 1058–1076. doi: 10.1111/j.1365-246X.2012.05526.x

Balestrini, F., Draganov, D., Malehmir, A., Marsden, P., & Ghose, R. (2020). Improved target illumination at Ludvika mines of Sweden through seismic-interferometric surface-wave suppression. *Geophysical Prospecting*, *68*(1), 200–213. doi: 10.1111/1365-2478.12890

Bao, X., Song, X., & Li, J. (2015). High-resolution lithospheric structure beneath Mainland China from ambient noise and earthquake surface-wave tomography. *Earth and Planetary Science Letters*, *417*, 132–141.

Beliakov, G., Sola, H., & Fernandez, J. (2011). The median and its extensions. *Fuzzy Sets and Systems,*175 (1), 36-47, doi: 10.1016/j.fss.2011.01.002.

Bergamo, P., Comina, C., Foti, S., & Maraschini, M. (2011). Seismic characterization of shallow bedrock sites with multimodal Monte Carlo inversion of surface wave data. *Soil Dynamics and Earthquake Engineering*, *31*(3), 530–534. doi: 10.1016/j.soildyn.2010.10.006

Bergamo, P., & Socco, L. V. (2014). Detection of sharp lateral discontinuities through the analysis of surface-wave propagation. *Geophysics*, *79*(4), EN77–EN90. doi: 10.1190/geo2013-0314.1

Bijwaard, H., & Spakman, W. (2000). Non-linear global *P* -wave tomography by iterated linearized inversion. *Geophysical Journal International*, *141*(1), 71–82. doi: 10.1046/j.1365-246X.2000.00053.x

Bloch, S., & Hales, A. L. (1968). New techniques for the determination of surface wave phase velocities. *Bulletin of the Seismological Society of America*, *58*(3), 1021–1034.

Bodet, L., Abraham, O., & Clorennec, D. (2009). Near-offset effects on Rayleigh-wave dispersion measurements: Physical modeling. *Journal of Applied Geophysics*, *68*(1), 95–103. doi: 10.1016/j.jappgeo.2009.02.012

Boiero, D. (2009). *Surface wave analysis for building shear wave velocity models*. Ph. D. Thesis, Politecnico di Torino.

Boiero, D., Bergamo, P., Bruno Rege, R., & Socco, L. V. (2011). Estimating surface-wave dispersion curves from 3D seismic acquisition schemes: Part 1 — 1D models. *Geophysics*, *76*(6), G85–G93. doi: 10.1190/geo2011-0124.1

Bona, A., Pevzner, R., Tertyshnikov, K., Greenwood, A., Sun, B., Yavuz, S., & Urosevic, M. (2013). Diffraction Imaging in Hard-rock Environments. *75th EAGE Conference and Exhibition incorporating SPE EUROPEC 2013*. doi: 10.3997/2214-4609.20130702

Bongajum, E., Milkereit, B., Adam, E., & Meng, Y. (2012). Seismic imaging in hardrock environments: The role of heterogeneity? *Tectonophysics*, *572–573*, 7–15. doi: 10.1016/j.tecto.2012.03.003

Boschi, L., & Ekström, G. (2002). New images of the Earth's upper mantle from measurements of surface wave phase velocity anomalies. *Journal of Geophysical Research: Solid Earth*, *107*(B4), ESE-1.

Boschi, L., Weemstra, C., Verbeke, J., Ekström, G., Zunino, A., & Giardini, D. (2013). On measuring surface wave phase velocity from station–station cross-correlation of ambient signal. *Geophysical Journal International*, *192*(1), 346–358. doi: 10.1093/gji/ggs023

Bräunig, L., Buske, S., Malehmir, A., Bäckström, E., Schön, M., & Marsden, P. (2020). Seismic depth imaging of iron-oxide deposits and their host rocks in the Ludvika mining area of central Sweden. *Geophysical Prospecting*, *68*(1), 24–43. doi: 10.1111/1365-2478.12836

Brodic, B., Papadopoulou, M., Bräunig, L., Socco, V., Draganov, D., Buske, S., & Malehmir, A. (2020). Data-Driven Weathering Layer Statics for Hardrock Imaging: Solutions Based on First-Breaks and Surface Waves. *Near Surface Geoscience 2020-26th EAGE European Meeting of Environmental and Engineering Geophysics*.

Bullen, K. E., & Bolt, B. A. (1985). *An introduction to the theory of seismology* (4th ed). Cambridge University Press.

Buske, S., Bellefleur, G., & Malehmir, A. (2015). Introduction to special issue on "hard rock seismic imaging." *Geophysical Prospecting*, *63*, 751–753.

Bussat, S., & Kugler, S. (2009). Recording noise - Estimating shear-wave velocities: Feasibility of offshore ambient-noise surface-wave tomography (answt) on a reservoir scale. *SEG Technical Program Expanded Abstracts 2009*, 1627–1631.doi: 10.1190/1.3255161

Campillo, M. (2006). Phase and Correlation in `Random' Seismic Fields and the Reconstruction of the Green Function. *Pure and Applied Geophysics*, *163*(2–3), 475–502. doi: 10.1007/s00024-005-0032-8

Casto, D. W., Luke, B., Calderón-Macías, C., & Kaufmann, R. (2009). Interpreting surface-wave data for a site with shallow bedrock. *Journal of Environmental & Engineering Geophysics*, *14*(3), 115–127.

Cercato, M., Cara, F., Cardarelli, E., Di Filippo, G., Di Giulio, G., & Milana, G. (2010). Shear-wave velocity profiling at sites with high stiffness contrasts: A comparison between invasive and non-invasive methods. *Near Surface Geophysics*, *8*(1), 75–94. doi: 10.3997/1873-0604.2009053

Chalabiyev, E. (2020). *Validation of automatic dispersion curve picking in exploration data*. MSc Thesis, Politecnico di Torino.

Cheraghi, S., Malehmir, A., Bellefleur, G., Bongajum, E., & Bastani, M. (2013). Scaling behavior and the effects of heterogeneity on shallow seismic imaging of mineral deposits: A case study from Brunswick No. 6 mining area, Canada. *Journal of Applied Geophysics*, *90*, 1–18. doi: 10.1016/j.jappgeo.2012.12.003

Colombero, C., Comina, C., & Valentina Socco, L. (2019). Imaging near-surface sharp lateral variations with surface-wave methods — Part 1: Detection and location. *Geopysics*, *84*(6), EN93–EN111. doi: 10.1190/geo2019-0149.1

Comina, C., Foti, S., Boiero, D., & Socco, L. V. (2011). Reliability of VS,30 Evaluation from Surface-Wave Tests. *Journal of Geotechnical and*

Geoenvironmental Engineering, *137*(6), 579–586. doi: 10.1061/(ASCE)GT.1943-5606.0000452

Cox, M. J. G. (1999). *Static Corrections for Seismic Reflection Surveys* (Vol. 9). Society of Exploration Geophysicists.

Da Col, F., Papadopoulou, M., Koivisto, E., Sito, Ł., Savolainen, M., & Socco, L. V. (2020). Application of surface-wave tomography to mineral exploration: A case study from Siilinjärvi, Finland. *Geophysical Prospecting*, *68*(1), 254–269. doi: 10.1111/1365-2478.12903

Dal Moro, G., Pipan, M., Forte, E., & Finetti, I. (2003). Determination of Rayleigh wave dispersion curves for near surface applications in unconsolidated sediments. *SEG Technical Program Expanded Abstracts 2003*, 1247–1250. doi: 10.1190/1.1817508

Decrée, S., & Robb, L. (2019). Developments in the Continuing Search for New Mineral Deposits. *Eos*, *100*. doi: 10.1029/2019EO128347

Diaz-Segura, E. G. (2020). Influences of variations in the sledgehammer trajectory and collinearity of the geophone array in an MASW survey on the shear-wave velocity profile. *International Journal of Geo-Engineering*, *11*(1), 5. doi: 10.1186/s40703-020-00112-5

Donnelly, L. (2018). Mining Hazards. In P. T. Bobrowsky & B. Marker (Eds.), *Encyclopedia of Engineering Geology* (pp. 649–656). Springer International Publishing. doi: 10.1007/978-3-319-73568-9_202

Douma, H., & Haney, M. (2011). Surface-wave inversion for near-surface shear-wave velocity estimation at Coronation field. *SEG Technical Program Expanded Abstracts 2011*, 1411–1415. doi: 10.1190/1.3627466

Draganov, D., Campman, X., Thorbecke, J., Verdel, A., & Wapenaar, K. (2009). Reflection images from ambient seismic noise. *Geophysics*, *74*(5), A63–A67. doi: 10.1190/1.3193529

Dubiński, J. (2013). Sustainable Development of Mining Mineral Resources. *Journal of Sustainable Mining*, *12*(1), 1–6. doi: 10.7424/jsm130102

Dunkin, J. W. (1965). Computation of modal solutions in layered, elastic media at high frequencies. *Bulletin of the Seismological Society of America*, *55*(2), 335–358.

Dziewonski, A. M., & Hales, A. L. (1972). Numerical Analysis of Dispersed Seismic Waves. In *Methods in Computational Physics: Advances in Research and Applications* (Vol. 11, pp. 39–85). Elsevier. doi: 0.1016/B978-0-12-460811-5.50007-6

Eaton, D. W. (1999). Weak elastic-wave scattering from massive sulfide orebodies. *Geophysics*, *64*(1), 289–299. doi: 10.1190/1.1444525

Eaton, D. W., Milkereit, B., & Salisbury, M. H. (Eds.). (2003). *Hardrock Seismic Exploration*. Society of Exploration Geophysicists. doi: 10.1190/1.9781560802396

European Commission. (2008). *The raw materials initiative—Meeting our critical needs for growth and jobs in Europe*. COM.

European Commission. (2017). *Study on the review of the list of critical raw materials: Critical raw materials factsheets.* http://dx.publications.europa.eu/10.2873/398823

Evangelista, L., & Santucci de Magistris, F. (2015). Some Limits in the Use of the MASW Technique in Soils with Inclined Layers. *Geotechnical and Geological Engineering*, *33*(3), 701–711. doi: 10.1007/s10706-015-9852-1

Fang, H., Yao, H., Zhang, H., Huang, Y.-C., & van der Hilst, R. D. (2015). Direct inversion of surface wave dispersion for three-dimensional shallow crustal structure based on ray tracing: Methodology and application. *Geophysical Journal International*, *201*(3), 1251–1263. doi: 10.1093/gji/ggv080

Foti, S. (2002). Numerical and experimental comparison between two-station and multistation methods for spectral analysis of surface waves. *RIVISTA ITALIANA DI GEOTECNICA*, *36*(1), 11–22.

Foti, S., Hollender, F., Garofalo, F., Albarello, D., Asten, M., Bard, P.-Y., Comina, C., Cornou, C., Cox, B., Di Giulio, G., Forbriger, T., Hayashi, K., Lunedei, E., Martin, A., Mercerat, D., Ohrnberger, M., Poggi, V., Renalier, F., Sicilia, D., & Socco, V. (2018). Guidelines for the good practice of surface wave analysis: A product of the InterPACIFIC project. *Bulletin of Earthquake Engineering*, *16*(6), 2367–2420. doi: 10.1007/s10518-017-0206-7

Foti, S., Lai, C. G., Rix, G. J., & Strobbia, C. (2015). *Surface wave methods for near-surface site characterization*. CRC Press, Taylor & Francis Group.

Foti, S., Parolai, S., Albarello, D., & Picozzi, M. (2011). Application of Surface-Wave Methods for Seismic Site Characterization. *Surveys in Geophysics*, *32*(6), 777–825. doi: 10.1007/s10712-011-9134-2

Foti, S., Sambuelli, L., Socco, L. V., & Strobbia, C. (2002). Spatial Sampling Issues in FK Analysis of Surface Waves. *Symposium on the Application of Geophysics to Engineering and Environmental Problems 2002*, SEI8–SEI8. doi: 10.4133/1.2927181

Foti, S., & Strobbia, C. (2002). Some notes on model parameters for surface wave data inversion. *Symposium on the Application of Geophysics to Engineering and Environmental Problems 2002*, SEI6–SEI6.

Fry, B., Deschamps, F., Kissling, E., Stehly, L., & Giardini, D. (2010). Layered azimuthal anisotropy of Rayleigh wave phase velocities in the European Alpine lithosphere inferred from ambient noise. *Earth and Planetary Science Letters*, *297*(1–2), 95–102. doi: 10.1016/j.epsl.2010.06.008

Ganji, V., Gucunski, N., & Nazarian, S. (1998). Automated inversion procedure for spectral analysis of surface waves. *Journal of Geotechnical and Geoenvironmental Engineering*, *124*(8), 757–770.

García Nieto, M. C., Martínez Segura, M. A., García Jerez, A., Navarro López, J. F., Navarro, M., Arrien, M., & Seivane, H. (2018). Application of Multichannel Analisis of Surface Waves to Obtain Soil Classification of El Ejido Town. *24th European Meeting of Environmental and Engineering Geophysics*. doi: 10.3997/2214-4609.201802623

Garofalo, F., Foti, S., Hollender, F., Bard, P. Y., Cornou, C., Cox, B. R., Ohrnberger, M., Sicilia, D., Asten, M., Di Giulio, G., Forbriger, T., Guillier, B., Hayashi, K., Martin, A., Matsushima, S., Mercerat, D., Poggi, V., & Yamanaka, H. (2016). InterPACIFIC project: Comparison of invasive and non-invasive methods for seismic site characterization. Part I: Intra-comparison of surface wave methods. *Soil Dynamics and Earthquake Engineering*, *82*, 222–240. doi: 10.1016/j.soildyn.2015.12.010

Garofalo, Flora. (2016). *Physically constrained joint inversion of seismic and electrical data for near-surface application*. Ph. D. thesis, Politecnico di Torino.

Geijer, P., & Magnusson, N. H. (1944). *De Mellansvenska Jarnmalmernas Geologi*. Geological Survey of Sweden.

Gercek, H. (2007). Poisson's ratio values for rocks. *International Journal of Rock Mechanics and Mining Sciences*, *44*(1), 1–13.

Gouédard, P., Stehly, L., Brenguier, F., Campillo, M., Colin de Verdière, Y., Larose, E., Margerin, L., Roux, P., Sánchez-Sesma, F. J., Shapiro, N. M., & Weaver, R. L. (2008). Cross-correlation of random fields: Mathematical approach and applications. *Geophysical Prospecting*, *56*(3), 375–393. doi: 10.1111/j.1365-2478.2007.00684.x

Gucunski, N., & Woods, R. (1991). Use of Rayleigh modes in interpretation of SASW test. *International Conferences on Recent Advances in Geotechnical Earthquake Engineering and Soil Dynamics*, 10.

Halliday, D. F., Curtis, A., Vermeer, P., Strobbia, C., Glushchenko, A., van Manen, D.-J., & Robertsson, J. O. (2010). Interferometric ground-roll removal: Attenuation of scattered surface waves in single-sensor data. *Geophysics*, *75*(2), SA15–SA25. doi: 10.1190/1.3360948

Harrison, C. B. (2009). *Feasibility of Rock Characterization for Mineral Exploration Using Seismic Data*. Ph. D Thesis, Curtin University of Technology.

Harvey, D. J. (1981). Seismogram synthesis using normal mode superposition: The locked mode approximation. *Geophysical Journal International*, *66*(1), 37–69. doi: 10.1190/1.3360948

Haskell, N. A. (1953). The dispersion of surface waves on multilayered media. *Bulletin of the Seismological Society of America*, *43*(1), 17–34.

Heisey, J. S., Stokoe, K. H., Hudson, W. R., & Meyer, A. H. (1982). Determination of in situ shear wave velocities from spectral analysis of surface waves. In *Res. Rep. 256-2*. Ctr. for Transp. Res., Univ. of Texas at Austin.

Hobbs, R. W. (2003). 3D Modeling of Seismic-Wave Propagation Using Complex Elastic Screens, with Application to Mineral Exploration. In *Hardrock Seismic Exploration* (Vol. 1–0, pp. 59–69). Society of Exploration Geophysicists. doi: 10.1190/1.9781560802396.ch4

Hollender, F., Cornou, C., Dechamp, A., Renalier, F., Thomassin, S., & Bard, P. Y. (2017). Characterization of French accelerometric permanent network stations with surface-wave based methods: Importance of joint use of active and passive methods, Love and Rayleigh waves. *16th World Conference on Earthquake Engineering, 16WCEE 2017*.

Holliger, K. (1997). Seismic scattering in the upper crystalline crust based on evidence from sonic logs. *Geophysical Journal International*, *128*(1), 65–72. doi: 10.1111/j.1365-246X.1997.tb04071.x

Hollis, D., McBride, J., Good, D., Arndt, N., Brenguier, F., & Olivier, G. (2018). Use of ambient noise surface wave tomography in mineral resource exploration and evaluation. In *SEG Technical Program Expanded Abstracts 2018*, 1937-1940.

Hons, M. S., & Stewart, R. R. (2008). *Comparison of MEMS accelerometers and geophones at Spring Coulee, Alberta*. doi: 10.13140/RG.2.2.27635.12325

Hyslop, C., & Stewart, R. R. (2015). Imaging lateral heterogeneity using reflected surface waves. *Geophysics*, *80*(3), EN69–EN82. doi: 10.1190/geo2014-0066.1

Ikeda, T., & Tsuji, T. (2020). Two-station continuous wavelet transform cross-coherence analysis for surface-wave tomography using active-source seismic data. *Geophysics*, *85*(1), EN17–EN28. doi: 10.1190/geo2019-0054.1

Ikeda, T., & Tsuji, T. (2018). Surface-wave tomography for near-surface characterization with continuous-wavelet transform for two-station crosscorrelation. *SEG Technical Program Expanded Abstracts 2018*, 2531–2535. doi: 10.1190/segam2018-2996939.1

Ivanov, J., D. Miller, R., & Tsoflias, G. (2008). Some Practical Aspects Of Masw Analysis And Processing. *21st EEGS Symposium on the Application of Geophysics to Engineering and Environmental Problems*. doi: 10.3997/2214-4609-pdb.177.142

Ivanov, J., Miller, R. D., Hoch, A. M., Peterie, S. L., & Morton, S. (2019). Surface wave analysis sensitivity to a-priori information assumptions. *SEG Technical Program Expanded Abstracts 2019*, 5030–5034. doi: 10.1190/segam2019-3216657.1

Ivanov, J., Miller, R., & Peterie, S. (2016). Detecting and delineating voids and mines using surface-wave methods in Galena, Kansas. *SEG Technical Program Expanded Abstracts 2016*, 2344–2350.

Ivanov, J., Park, C. B., Miller, R. D., & Xia, J. (2000). Mapping Poisson's Ratio of Unconsolidated Materials from a Joint Analysis of Surface-Wave and Refraction Events. *Symposium on the Application of Geophysics to Engineering and Environmental Problems 2000*, 11–19. doi: 10.4133/1.2922727

Johnson, D. H., & Dudgeon, D. E. (1993). *Array Signal Processing: Concepts and Techniques* (1st ed.). Prentice Hall.

Kanlı, A. I., Tildy, P., Prónay, Z., Pınar, A., & Hermann, L. (2006). $V_{S}{}^{30}$ mapping and soil classification for seismic site effect evaluation in Dinar region, SW Turkey. *Geophysical Journal International*, *165*(1), 223–235. doi: 10.1111/j.1365-246X.2006.02882.x

Karimpour, M. (2018). *Processing workflow for estimation of dispersion curves from seismic data and QC.* MSc Thesis, Politecnico di Torino.

Karray, M., & Lefebvre, G. (2008). Significance and evaluation of Poisson's ratio in Rayleigh wave testing. *Canadian Geotechnical Journal*, *45*(5), 624–635.

Kästle, E. D., Soomro, R., Weemstra, C., Boschi, L., & Meier, T. (2016). Two-receiver measurements of phase velocity: Cross-validation of ambient-noise and earthquake-based observations. *Geophysical Journal International*, *207*(3), 1493–1512.

Kausel, E., & Roësset, J. M. (1981). Stiffness matrices for layered soils. *Bulletin of the Seismological Society of America*, *71*(6), 1743–1761.

Kauti, T., Skyttä, P., Koivisto, E., & Savolainen, M. (2019). 3D modelling of the dolerite dyke network within the Siilinjärvi phosphate deposit. *Visual3D Conference*. https://ltu.diva-portal.org/smash/get/diva2:1360188/FULLTEXT01.pdf

Ke, G., Dong, H., Kristensen, A., & Thompson, M. (2011). Modified Thomson-Haskell Matrix Methods for Surface-Wave Dispersion-Curve Calculation and Their Accelerated Root-Searching Schemes. *Bulletin of the Seismological Society of America*, *101*(4), 1692–1703. doi: 10.1785/0120100187

Kennett, B. L. N. (1974). Reflections, rays, and reverberations. *Bulletin of the Seismological Society of America*, *64*(6), 1685–1696.

Kennett, B. L. N., & Yoshizawa, K. (2002). A reappraisal of regional surface wave tomography. *Geophysical Journal International*, *150*(1), 37–44. doi: 10.1046/j.1365-246X.2002.01682.x

Khosro Anjom, F., Arabi, A., Socco, L. V., & Comina, C. (2017). Application of a method to determine S and P wave velocities from surface waves data analysis in presence of sharp lateral variations. *GNGTS 2017*.

Khosro Anjom, F., Browaeys, T. J., & Socco, L. V. (2021). Multi-modal surface wave tomography to obtain S- and P-wave velocities applied to the recordings of UAV deployed sensors. *Geophysics*, 1–56. doi: 10.1190/geo2020-0703.1

Khosro Anjom, F., Teodor, D., Comina, C., Brossier, R., Virieux, J., & Socco, L. V. (2019). Full waveform matching of vp and vs models from surface waves. *Geophysical Journal International*, *218*, 1873-1891. doi: 10.1093/gji/ggz279.

Knopoff, L. (1964). A matrix method for elastic wave problems. *Bulletin of the Seismological Society of America*, *54*(1), 431–438.

Laakso, V. (2019). *Testing of reflection seismic, GPR and magnetic methods for mineral exploration and mine planning at the Siilinjärvi Phosphate mine site in Finland*, MSc thesis, University of Helsinki. http://hdl.handle.net/10138/308248

Ladak, S. (2020). *Earthquake site characterization of rock sites in Eastern Canada and stiff ground sites in Vancouver, British Columbia*, MSc thesis, The Western University of Ontario. https://ir.lib.uwo.ca/etd/6972/

Lanaro, F., & Fredriksson, A. (2005). *Rock Mechanics Model—Summary of the primary data Preliminary site description Forsmark area—Version 12*, 1402–3091, 41. http://inis.iaea.org/search/search.aspx?orig_q=RN:37055113

Le Feuvre, M., Joubert, A., Leparoux, D., & Côte, P. (2015). Passive multi-channel analysis of surface waves with cross-correlations and beamforming. Application to a sea dike. *Journal of Applied Geophysics*, *114*, 36–51. doi: 10.1016/j.jappgeo.2014.12.014

Lehujeur, M., Vergne, J., Maggi, A., & Schmittbuhl, J. (2017). Ambient noise tomography with non-uniform noise sources and low aperture networks: Case study of deep geothermal reservoirs in northern Alsace, France. *Geophysical Journal International*, *208*(1), 193–210. doi: 10.1093/gji/ggw373

Levander, A., Hobbs, R. W., Smith, S. K., England, R. W., Snyder, D. B., & Holliger, K. (1994). The crust as a heterogeneous "optical" medium, or "crocodiles in the mist." *Tectonophysics*, *232*(1–4), 281–297. doi: 10.1016/0040-1951(94)90090-6

L'Heureux, E., Milkereit, B., & Vasudevan, K. (2009). Heterogeneity and seismic scattering in exploration environments. *Tectonophysics*, *472*(1–4), 264–272. doi: 10.1016/j.tecto.2008.04.001

Lin, C.-P., & Chang, T.-S. (2004). Multi-station analysis of surface wave dispersion. *Soil Dynamics and Earthquake Engineering*, *24*(11), 877–886. doi: 10.1016/j.soildyn.2003.11.011

Lin, C.-P., & Lin, C.-H. (2007). Effect of lateral heterogeneity on surface wave testing: Numerical simulations and a countermeasure. *Soil Dynamics and Earthquake Engineering*, *27*(6), 541–552. doi: 10.1016/j.soildyn.2006.10.008

Lin, C.-P., Lin, C.-H., & Chien, C.-J. (2017). Dispersion analysis of surface wave testing – SASW vs. MASW. *Journal of Applied Geophysics*, *143*, 223–230. doi: 10.1016/j.jappgeo.2017.05.008

Lin, F.-C., Moschetti, M. P., & Ritzwoller, M. H. (2008). Surface wave tomography of the western United States from ambient seismic noise: Rayleigh and Love wave phase velocity maps. *Geophysical Journal International*, *173*(1), 281–298. doi: 10.1111/j.1365-246X.2008.03720.x

Lin, F.-C., Ritzwoller, M. H., & Snieder, R. (2009). Eikonal tomography: Surface wave tomography by phase front tracking across a regional broad-band seismic array. *Geophysical Journal International*, *177*(3), 1091–1110.

Liu, T. (2010). Efficient Reformulation of the Thomson-Haskell Method for Computation of Surface Waves in Layered Half-Space. *Bulletin of the Seismological Society of America*, *100*(5A), 2310–2316. doi: 10.1785/0120090331

Luke, B., Taylor, W., Calderón-Macías, C., Jin, X., Murvosh, H., & Wagoner, J. (2008). Characterizing anomalous ground for engineering applications using surface-based seismic methods. *The Leading Edge*, *27*(11), 1544–1549. doi: 10.1190/1.3011027

Lynch, R., Hollis, D., McBride, J., Arndt, N., Brenguier, F., Mordret, A., Boué, P., Beaupretre, S., Santaguida, F., & Chisolm, D. (2019). Passive seismic ambient noise surface wave tomography applied to two exploration targets in Ontario, Canada. *SEG Technical Program Expanded Abstracts 2019*, 5390–5392

Malehmir, A., Heinonen, S., Dehghannejad, M., Heino, P., Maries, G., Karell, F., Suikkanen, M., & Salo, A. (2017). Landstreamer seismics and physical property measurements in the Siilinjärvi open-pit apatite (phosphate) mine, central Finland. *Geophysics*, *82*(2), B29–B48. doi: 10.1190/geo2016-0443.1

Malehmir, A., Markovic, M., Marsden, P., Gil, A., Buske, S., Sito, L., Bäckström, E., Sadeghi, M., & Luth, S. (2021). Sparse 3D reflection seismic survey

for deep-targeting iron oxide deposits and their host rocks, Ludvika Mines, Sweden. *Solid Earth*, *12*(2), 483–502. doi: 10.5194/se-12-483-2021

Malehmir, A., Urosevic, M., Bellefleur, G., Juhlin, C., & Milkereit, B. (2012). Seismic methods in mineral exploration and mine planning—Introduction. *Geophysics*, *77*(5), WC1–WC2. doi: 10.1190/2012-0724-SPSEIN.1

Maries, G., Malehmir, A., Bäckström, E., Schön, M., & Marsden, P. (2017). Downhole physical property logging for iron-oxide exploration, rock quality, and mining: An example from central Sweden. *Ore Geology Reviews*, *90*, 1–13. doi: 10.1016/j.oregeorev.2017.10.012

Markovic, M., Maries, G., Malehmir, A., Ketelhodt, J., Bäckström, E., Schön, M., & Marsden, P. (2020). Deep reflection seismic imaging of iron-oxide deposits in the Ludvika mining area of central Sweden. *Geophysical Prospecting*, *68*(1), 7–23. doi: 10.1111/1365-2478.12855

Marquardt, D. W. (1963). An Algorithm for Least-Squares Estimation of Nonlinear Parameters. *Journal of the Society for Industrial and Applied Mathematics*, *11*(2), 431–441. doi: 10.1137/0111030

Marsden, D. (1993a). Static corrections—A review, Part 1. *The Leading Edge*, *12*(1), 43–49. doi: 10.1190/1.1436912

Marsden, D. (1993b). Static corrections—A review, Part III. *The Leading Edge*, *12*(3), 210–216. doi: 10.1190/1.1436944

Martin, A. J. (2011). Analysis of SASW, MASW, and Passive Surface Wave Data Collected at the National Geotechnical Experimentation Site at Texas A&M University. *GeoRisk 2011*, 886–893. doi: 10.1061/41183(418)94

Martins, J. E., Weemstra, C., Ruigrok, E., Verdel, A., Jousset, P., & Hersir, G. P. (2020). 3D S-wave velocity imaging of Reykjanes Peninsula high-enthalpy geothermal fields with ambient-noise tomography. *Journal of Volcanology and Geothermal Research*, *391*, 106685. doi: 10.1016/j.jvolgeores.2019.106685

Mattsson, H. B., Högdahl, K., Carlsson, M., & Malehmir, A. (2019). The role of mafic dykes in the petrogenesis of the Archean Siilinjärvi carbonatite complex, east-central Finland. *Lithos*, *342–343*, 468–479. doi: 10.1016/j.lithos.2019.06.011

McKevitt, B. (2020). *Southern continuation of the Siilinjärvi carbonatite complex at the Siilinjärvi phosphate mine in Finland, based on geophysical data*. MSc thesis, University of Helsinki.

McMechan, G. A., & Yedlin, M. J. (1981). Analysis of dispersive waves by wave field transformation. *Geophysics*, *46*(6), 832–958. doi: 10.1190/1.1441225

Meier, T., Dietrich, K., Stöckhert, B., & Harjes, H.-P. (2004). One-dimensional models of shear wave velocity for the eastern Mediterranean obtained from the inversion of Rayleigh wave phase velocities and tectonic implications. *Geophysical Journal International*, *156*(1), 45–58. doi: 10.1111/j.1365-246X.2004.02121.x

Miao, X., Zheng, D., Zi, L., Zhou, Z., & Gao, M. (2016). Robust multimodal surface-wave inversion for shallow velocity and shear statics. *SEG Technical Program Expanded Abstracts 2016*, 4956–4960. doi: 10.1190/segam2016-13822744.1

Miller, R. D., Xia, J., Park, C. B., & Ivanov, J. M. (1999). Multichannel analysis of surface waves to map bedrock. *The Leading Edge*, *18*(12), 1392–1396. doi: 10.1190/1.1438226

Mohammadi, N., Gholami, A., Rahimi, H., & Aoudia, A. (2020). Simultaneous tomography of all periods in surface wave analysis. *Physics of the Earth and Planetary Interiors*, *298*, 106338. doi: 10.1016/j.pepi.2019.106338

Nasseri-Moghaddam, A., Cascante, G., & Hutchinson, J. (2005). A New Quantitative Procedure to Determine the Location and Embedment Depth of a Void Using Surface Waves. *Journal of Environmental & Engineering Geophysics*, *10*(1), 51–64. doi: 10.2113/JEEG10.1.51

Nazarian, S., & Stokoe, K. H. (1984). *In situ shear wave velocities from spectral analysis of surface wave*. *3*, 31–38.

Nolet, G., & Panza, G. F. (1976). Array analysis of seismic surface waves: Limits and possibilities. *Pure and Applied Geophysics, 114*(5), 775–790. doi: 10.1007/BF00875787

O'Brien, H., Heilimo, E., & Heino, P. (2015). The Archean Siilinjärvi Carbonatite Complex. In *Mineral Deposits of Finland*, 327–343. Elsevier. doi: 10.1016/B978-0-12-410438-9.00013-3

O'Connell, D. R. H., & Turner, J. P. (2011). Interferometric Multichannel Analysis of Surface Waves (IMASW). *Bulletin of the Seismological Society of America*, *101*(5), 2122–2141. doi: 10.1785/0120100230

OECD. (2019). *Global Material Resources Outlook to 2060: Economic Drivers and Environmental Consequences*. OECD. doi: 10.1787/9789264307452-en

Olafsdottir, E. A., Bessason, B., & Erlingsson, S. (2018). Combination of dispersion curves from MASW measurements. *Soil Dynamics and Earthquake Engineering*, *113*, 473–487. doi: 10.1016/j.soildyn.2018.05.025

O'Neill, A. (2003). *Full-waveform reflectivity for modelling, inversion and appraisal of seismic surface wave dispersion in shallow site investigation*, PhD Thesis, University of Western Australia.

Park, C. B. (2011). Imaging Dispersion of MASW Data—Full vs. Selective Offset Scheme. *Journal of Environmental & Engineering Geophysics*, *16*(1), 13–23. doi: 10.2113/JEEG16.1.13

Park, C., Cirone, A., & Rodrigues, R. (2019). Roadside Active-Passive MASW Surveys to Evaluate Soil Grouting. *Geo-Congress 2019: Engineering Geology, Site Characterization, and Geophysics*, 354–366.

Park, C., Miller, R., Laflen, D., Neb, C., Ivanov, J., Bennett, B., & Huggins, R. (2004). Imaging dispersion curves of passive surface waves. *SEG Technical Program Expanded Abstracts 2004*, 1357–1360. doi: 10.1190/1.1851112

Park, C., Richter, J., Rodrigues, R., & Cirone, A. (2018). MASW applications for road construction and maintenance. *The Leading Edge*, *37*(10), 724–730. doi: 10.1190/tle37100724.1

Park, C.B., Miller, R. D., Ryden, N., Xia, J., & Ivanov, J. (2005). Combined Use of Active and Passive Surface Waves. *Journal of Environmental & Engineering Geophysics*, *10*(3), 323–334. doi: 10.2113/JEEG10.3.323

Park, Choon B., & Carnevale, M. (2010). Optimum MASW Survey—Revisit after a Decade of Use. *GeoFlorida 2010*, 1303–1312. doi: 10.1061/41095(365)130

Park, Choon B., Miller, R. D., & Xia, J. (1999). Multichannel analysis of surface waves. *Geophysics*, *64*(3), 800–808. doi: 10.1190/1.1444590

Park, Choon B., & Ryden, N. (2007). Historical Overview of the Surface Wave Method. *Symposium on the Application of Geophysics to Engineering and Environmental Problems 2007*, 897–909. doi: 10.4133/1.2924752

Park, Choon Byong, Miller, R. D., & Xia, J. (1998). Imaging dispersion curves of surface waves on multi-channel record. *SEG Technical Program Expanded Abstracts 1998*, 1377–1380. doi: 10.1190/1.1820161

Park, Choon Byong, Miller, R. D., & Xia, J. (1999). Multimodal Analysis of High Frequency Surface Waves. *Symposium on the Application of Geophysics to Engineering and Environmental Problems 1999*, 115–121. doi: 10.4133/1.2922596

Pelekis, P. C., & Athanasopoulos, G. A. (2011). An overview of surface wave methods and a reliability study of a simplified inversion technique. *Soil Dynamics and Earthquake Engineering*, *31*(12), 1654–1668. doi: 10.1016/j.soildyn.2011.06.012

Picozzi, M., Parolai, S., Bindi, D., & Strollo, A. (2009). Characterization of shallow geology by high-frequency seismic noise tomography. *Geophysical Journal International*, *176*(1), 164–174.

Pileggi, D., Rossi, D., Lunedei, E., & Albarello, D. (2011). Seismic characterization of rigid sites in the ITACA database by ambient vibration monitoring and geological surveys. *Bulletin of Earthquake Engineering*, *9*(6), 1839–1854. doi: 10.1007/s10518-011-9292-0

Planès, T., Obermann, A., Antunes, V., & Lupi, M. (2020). Ambient-noise tomography of the Greater Geneva Basin in a geothermal exploration context. *Geophysical Journal International*, *220*(1), 370–383. doi: 10.1093/gji/ggz457

Rahman, Md. Z., Siddiqua, S., & Kamal, A. S. M. M. (2016). Shear wave velocity estimation of the near-surface materials of Chittagong City, Bangladesh for seismic site characterization. *Journal of Applied Geophysics*, *134*, 210–225. doi: 10.1016/j.jappgeo.2016.09.006

Rector, J., Pfeiffe, J., Hodges, S., Kingman, J., & Sprott, E. (2015). Tomographic imaging of surface waves: A case study from the Phoenix Mine, Battle Mountain, Nevada. *The Leading Edge*, *34*(11), 1360–1364.

Richart, F. E., Hall, J. R., & Woods, R. D. (1970). *Vibrations of soils and foundations*. Prentice-Hall.

Ritchie, H. (2019). *The death of UK coal in five charts*. Www.Ourworldindata.Org. https://ourworldindata.org/death-uk-coal

Ritzwoller, M. H., & Levshin, A. L. (1998). Eurasian surface wave tomography: Group velocities. *Journal of Geophysical Research: Solid Earth*, *103*(B3), 4839–4878.

Ritzwoller, M. H., Shapiro, N. M., Levshin, A. L., & Leahy, G. M. (2001). Crustal and upper mantle structure beneath Antarctica and surrounding oceans.

Journal of Geophysical Research: Solid Earth, *106*(B12), 30645–30670. doi: 10.1029/2001JB000179

Rosenblad, B. L., & Bertel, J. D. (2008). Potential Phase Unwrapping Errors Associated with SASW Measurements at Soft-Over-Stiff Sites. *Geotechnical Testing Journal*, *31*(5), 101411. doi: 10.1520/GTJ101411

Roux, P. (2009). Passive seismic imaging with directive ambient noise: Application to surface waves and the San Andreas Fault in Parkfield, CA. *Geophysical Journal International*, *179*(1), 367–373. doi: 10.1111/j.1365-246X.2009.04282.x

Roy, S., Kocel, E., Dyaur, N., & Stewart, R. R. (2013). Lateral heterogeneity and surface-wave inversion (MASW). *SEG Technical Program Expanded Abstracts 2013*, 1909–1913. doi: 10.1190/segam2013-1084.1

Roy, S., Stewart, R. R., & Al Dulaijan, K. (2010). S-wave velocity and statics from ground-roll inversion. *The Leading Edge*, *29*(10), 1250–1257. doi: 10.1190/1.3496915

Ryden, N., & Park, C. B. (2004). Surface waves in inversely dispersive media. *Near Surface Geophysics*, *2*(4), 187–197. doi: 10.3997/1873-0604.2004016

Ryden, Nils, Park, C. B., Ulriksen, P., & Miller, R. D. (2003). Lamb Wave Analysis for Non-Destructive Testing of Concrete Plate Structures. *Symposium on the Application of Geophysics to Engineering and Environmental Problems 2003*, 782–793. doi: 10.4133/1.2923224

Sabra, K. G., Gerstoft, P., Roux, P., Kuperman, W., & Fehler, M. C. (2005). Surface wave tomography from microseisms in Southern California. *Geophysical Research Letters*, *32*(14).

Sadeghisorkhani, H., Gudmundsson, Ó., & Tryggvason, A. (2018). GSpecDisp: A matlab GUI package for phase-velocity dispersion measurements from ambient-noise correlations. *Computers & Geosciences*, *110*, 41–53. doi: 10.1016/j.cageo.2017.09.006

Salisbury, M., Harvey, C., & Matthews, L. (2003). *1. The Acoustic Properties of Ores and Host Rocks in Hardrock Terranes*.

Sánchez-Salinero, I. (1987). *Analytical Investigation of Seismic Methods Used for Engineering Applications*. PhD Thesis, University of Texas at Austin.

Sasanakul, I., Gassman, S., Ruttithivaphanich, P., Dejphumee, S., & Department Civil and Environmental Engineering, University of South Carolina, Columbia, SC, 29208, USA. (2019). Characterization of shear wave velocity profiles for South Carolina Coastal Plain. *AIMS Geosciences*, *5*(2), 303–324. doi: 10.3934/geosci.2019.2.303

Schmidt, R. (1986). Multiple emitter location and signal parameter estimation. *IEEE Transactions on Antennas and Propagation*, *34*(3), 276–280. doi: 10.1109/TAP.1986.1143830

Schüler, D., Degreif, S., Dolega, P., Hay, D., Manhart, A., & Buchert, M. (2017). *EU raw material import flows – acknowledging non-EU environmental and social footprints*.

http://www.stradeproject.eu/fileadmin/user_upload/pdf/STRADEPolBrf_02-2017_RawMaterialFlows_Mar2017_FINAL.pdf

Serdyukov, A. S., Yablokov, A. V., Duchkov, A. A., Azarov, A. A., & Baranov, V. D. (2019). Slant *f—K* transform of multichannel seismic surface wave data. *Geophysics*, *84*(1), A19–A24. doi: 10.1190/geo2018-0430.1

Shapiro, N. M., & Campillo, M. (2004). Emergence of broadband Rayleigh waves from correlations of the ambient seismic noise: CORRELATIONS OF THE SEISMIC NOISE. *Geophysical Research Letters*, *31*(7), doi: 10.1029/2004GL019491

Shapiro, Nikolai M, Campillo, M., Stehly, L., & Ritzwoller, M. H. (2005). High-resolution surface-wave tomography from ambient seismic noise. *Science*, *307*(5715), 1615–1618.

Sharma, H., Molnar, S., Hollis, D., & McBride, J. (2018). Application of ambient-noise analysis and velocity modeling in mineral exploration. *SEG Technical Program Expanded Abstracts 2018*, 3072–3076.

Sheriff, R. E. (2002). *Encyclopedic Dictionary of Applied Geophysics, Fourth edition*. SEG. doi: 10.1190/1.9781560802969

Sherman*, C., Rector, J., Dreger, D., & Glaser, S. (2014). Seismic tunnel detection at Black Diamond Mines Regional Preserve. *SEG Technical Program Expanded Abstracts 2014*, 2078–2082.

Socco, Laura Valentina, & Boiero, D. (2008). Improved Monte Carlo inversion of surface wave data. *Geophysical Prospecting*, *56*(3), 357–371. doi: 10.1111/j.1365-2478.2007.00678.x

Socco, Laura Valentina, Boiero, D., Bergamo, P., Garofalo, F., Yao, H., Hilst, R. D. van der, & Col, F. D. (2014). Surface wave tomography to retrieve near surface velocity models. *SEG Technical Program Expanded Abstracts 2014*, 2013–2018.

Socco, Laura Valentina, Boiero, D., Foti, S., & Wisén, R. (2009). Laterally constrained inversion of ground roll from seismic reflection records. *Geophysics*, *74*(6), G35–G45. doi: 10.1190/1.3223636

Socco, Laura Valentina, & Comina, C. (2017). Time-average velocity estimation through surface-wave analysis: Part 2 — P-wave velocity. *Geophysics*, *82*(3), U61–U73. doi: 10.1190/geo2016-0368.1

Socco, Laura Valentina, Comina, C., & Khosro Anjom, F. (2017). Time-average velocity estimation through surface-wave analysis: Part 1 — S-wave velocity. *Geophysics*, *82*(3), U49–U59. doi: 10.1190/geo2016-0367.1

Socco, Laura Valentina, Foti, S., & Boiero, D. (2010). Surface-wave analysis for building near-surface velocity models—Established approaches and new perspectives. *Geophysics*, *75*(5), 75A83-75A102. doi: 10.1190/1.3479491

Socco, L.V., & Strobbia, C. (2004). Surface-wave method for near-surface characterization: A tutorial. *Near Surface Geophysics*, *2*(4), 165–185. doi: 10.3997/1873-0604.2004015

Strobbia, C., El-Emam, A., Al-Genai, J., & Roth, J. (2010). Rayleigh Wave Inversion for the Near-surface Characterization of Shallow Targets in Kuwait. *72nd*

EAGE Conference and Exhibition Incorporating SPE EUROPEC 2010. doi: 10.3997/2214-4609.201401020

Strobbia, C., & Foti, S. (2006). Multi-offset phase analysis of surface wave data (MOPA). *Journal of Applied Geophysics*, *59*(4), 300–313. doi: 10.1016/j.jappgeo.2005.10.009

Swoboda, U., Uchtmann, S., Limbrock, K., Elsen, R., Orlowsky, D., Telenga, K., Koschare, A., & Wollnik, F. (2013). Seismic and Geoelectric Investigation of Historical Mining Structures-A Case Study. *Near Surface Geoscience 2013-19th EAGE European Meeting of Environmental and Engineering Geophysics*.

The Rise and Fall of Germany's Coal Mining Industry. (2007, January 31). *DW*. https://p.dw.com/p/9mXZ

Thomson, W. T. (1950). Transmission of Elastic Waves through a Stratified Solid Medium. *Journal of Applied Physics*, *21*(2), 89–93. doi: 10.1063/1.1699629

Tran, K. T. (2008). *An appraisal of Surface Wave methods for soil characterization*, MSc thesis, University of Florida.

Tremblay, S.-P., & Karray, M. (2019). Practical considerations for array-based surface-wave testing methods with respect to near-field effects and shear-wave velocity profiles. *Journal of Applied Geophysics*, *171*. doi: 10.1016/j.jappgeo.2019.103871

Tselentis, G.-A., & Delis, G. (1998). Rapid assessment of S-wave profiles from the inversion of multichannel. *Annals of Geophysics*, *41*(1).

Van Der Neut, J. (2013). Downhole interferometric illumination diagnosis and balancing. *Geophysical Prospecting*, *61*, 352–367.

Vidal, C. A., Draganov, D., Van der Neut, J., Drijkoningen, G., & Wapenaar, K. (2014). Retrieval of reflections from ambient noise using illumination diagnosis. *Geophysical Journal International*, *198*(3), 1572–1584.

Vidal, C. A., Draganov, D., van der Neut, J., Drijkoningen, G., & Wapenaar, K. (2014). Retrieval of reflections from ambient noise using illumination diagnosis. *Geophysical Journal International*, *198*(3), 1572–1584. doi: 10.1093/gji/ggu164

Wang, L., & Rokhlin, S. I. (2001). Stable reformulation of transfer matrix method for wave propagation in layered anisotropic media. *Ultrasonics*, *39*(6), 413–424. doi: 10.1016/S0041-624X(01)00082-8

Wang, Limin, Xia, J., Xu, Y., & Luo, Y. (2015). Numerical investigation of 3D MASW technique. *Near-Surface Asia Pacific Conference*, 269–272. doi: 10.1190/nsapc2015-071

Wapenaar, K. (2004). Retrieving the Elastodynamic Green's Function of an Arbitrary Inhomogeneous Medium by Cross Correlation. *Phys. Rev. Lett.*, *93*(25), 254301. doi: PhysRevLett.93.254301

Wapenaar, K., & Fokkema, J. (2006). Green's function representations for seismic interferometry. *Geophysics*, *71*(4), SI33–SI46.

Weaver, R. L., & Lobkis, O. I. (2001). Ultrasonics without a Source: Thermal Fluctuation Correlations at MHz Frequencies. *Phys. Rev. Lett.*, *87*(13), 134301. doi: 10.1103/PhysRevLett.87.134301

Wielandt, E. (1993). Propagation and Structural Interpretation of Non-Plane Waves. *Geophysical Journal International*, *113*(1), 45–53. doi: 10.1111/j.1365-246X.1993.tb02527.x

Xia, J., Chen, C., Li, P. H., & Lewis, M. J. (2004). Delineation of a collapse feature in a noisy environment using a multichannel surface wave technique. *Géotechnique*, *54*(1), 17–27. doi: 10.1680/geot.2004.54.1.17

Xia, Jianghai, Miller, R. D., & Park, C. B. (1999). Estimation of near-surface shear-wave velocity by inversion of Rayleigh waves. *Geophysics*, *64*(3), 691–700. doi: 10.1190/1.1444578

Yang, Y., Ritzwoller, M. H., Levshin, A. L., & Shapiro, N. M. (2007). Ambient noise Rayleigh wave tomography across Europe. *Geophysical Journal International*, *168*(1), 259–274.

Yao, H., van der Hilst, R. D., & de Hoop, M. V. (2006). Surface-wave array tomography in SE Tibet from ambient seismic noise and two-station analysis—I. Phase velocity maps. *Geophysical Journal International*, *166*(2), 732–744. doi: 10.1111/j.1365-246X.2006.03028.x

Yao, H., Xu, G., Zhu, L., & Xiao, X. (2005). Mantle structure from inter-station Rayleigh wave dispersion and its tectonic implication in western China and neighboring regions. *Physics of the Earth and Planetary Interiors*, *148*(1), 39–54. doi: 10.1016/j.pepi.2004.08.006

Yin, X., Xu, H., Wang, L., Hu, Y., Shen, C., & Sun, S. (2016). Improving horizontal resolution of high-frequency surface-wave methods using travel-time tomography. *Journal of Applied Geophysics*, *126*, 42–51. doi: 10.1016/j.jappgeo.2016.01.007

Yoon, S. (2005). *Array-Based Measurements of Surface Wave Dispersion and Attenuation Using Frequency-Wavenumber Analysis*, Ph. D Thesis, Georgia Institute of Technology.

Yoon, S., & J. Rix, G. (2004). Combined Active-Passive Surface Wave Measurements For Near-Surface Site Characterization. *17th EEGS Symposium on the Application of Geophysics to Engineering and Environmental Problems*. doi: 10.3997/2214-4609-pdb.186.SUR03

Zahedi, B. (2020). *Automatic Quality control and outlier removal of DCs extracted by two-station method*, MSc thesis, Politecnico di Torino.

Zerwer, A., Polak, M. A., & Santamarina, J. C. (2005). Detection of Surface Breaking Cracks in Concrete Members Using Rayleigh Waves. *Journal of Environmental & Engineering Geophysics*, *10*(3), 295–306. doi: 10.2113/JEEG10.3.295

Zhang, X. (2020). *Bayesian inference in seismic tomography*. PhD Thesis, The University of Edinburgh.

Zhao, D. (2012). Comparison of FV, FP, and FK for Dispersion Analysis of Surface Waves. *Symposium on the Application of Geophysics to Engineering and Environmental Problems 2012*, 194–194. doi: 10.4133/1.4721741

Zywicki, D. J. (1999). *Advanced signal processing methods applied to engineering analysis of seismic surface waves.* Ph. D Thesis, Georgia Institute of Technology.

Zywicki, D. J., & Rix, G. J. (2005). Mitigation of Near-Field Effects for Seismic Surface Wave Velocity Estimation with Cylindrical Beamformers. *Journal of Geotechnical and Geoenvironmental Engineering*, *131*(8), 970–977. doi: 10.1061/(ASCE)1090-0241(2005)131:8(970)